Journal of Nanomaterials

# Applications of Nanobiomaterials in Tissue Repair

Lead Guest Editor: Xiaoming Li
Guest Editors: Hui-Qi Xie, Nicholas Dunne, and Katerina E. Aifantis

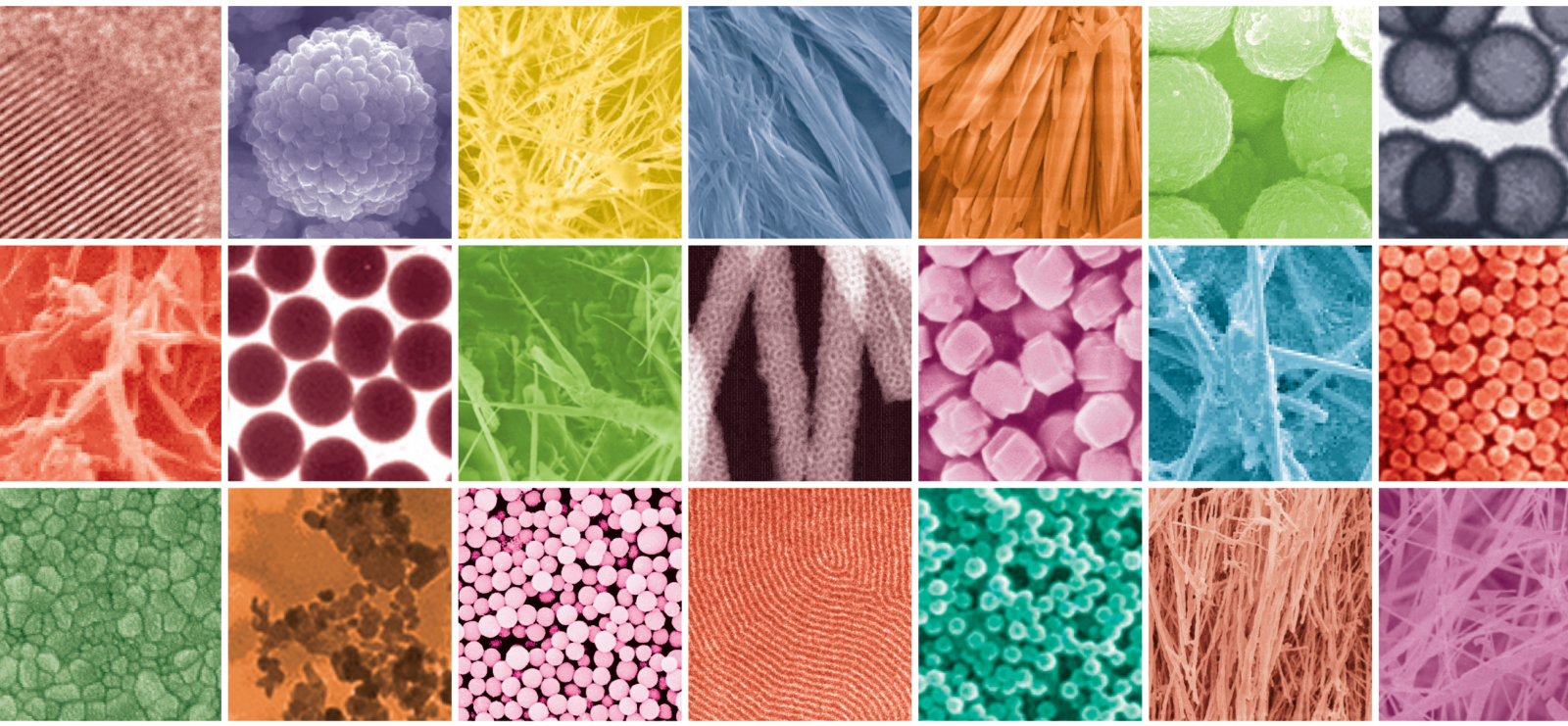

# Applications of Nanobiomaterials in Tissue Repair

Journal of Nanomaterials

# Applications of Nanobiomaterials in Tissue Repair

Lead Guest Editor: Xiaoming Li
Guest Editors: Hui-Qi Xie, Nicholas Dunne, and Katerina E. Aifantis

# Contents

**Printability Optimization of Gelatin-Alginate Bioinks by Cellulose Nanofiber Modification for Potential Meniscus Bioprinting**
Wenbin Luo, Zhengyi Song, Zhonghan Wang, Zhenguo Wang, Zuhao Li, Chenyu Wang, He Liu, Qingping Liu, and Jincheng Wang
Research Article (13 pages), Article ID 3863428, Volume 2020 (2020)

**Surface-Modified Graphene Oxide with Compatible Interface Enhances Poly-L-Lactic Acid Bone Scaffold**
Guoyong Wang, Chongxian He, Wengjing Yang, Fangwei Qi, Guowen Qian, Shuping Peng, and Cijun Shuai
Research Article (11 pages), Article ID 5634096, Volume 2020 (2020)

Hindawi
Journal of Nanomaterials
Volume 2020, Article ID 1852946, 24 pages
https://doi.org/10.1155/2020/1852946

*Review Article*

# 3D Nanostructures for Tissue Engineering, Cancer Therapy, and Gene Delivery

**Ahmad Gholami**,[1] **Seyyed Alireza Hashemi**,[2] **Khadije Yousefi**,[3] **Seyyed Mojtaba Mousavi**,[1] **Wei-Hung Chiang**,[4] **Seeram Ramakrishna**,[2] **Sargol Mazraedoost**,[1] **Ali Alizadeh**,[5] **Navid Omidifar**,[6] **Gity Behbudi**,[1] **and Aziz Babapoor**[7]

[1]*Biotechnology Research Center, Shiraz University of Medical Sciences, Shiraz, Iran*
[2]*Department of Mechanical Engineering, Center for Nanofibers and Nanotechnology, National University of Singapore, Singapore*
[3]*Department of Materials Science and Engineering, School of Engineering, Shiraz University, Shiraz, Iran*
[4]*Department of Chemical Engineering, National Taiwan University of Science and Technology, Taiwan*
[5]*Nanobiology and Nanomedicine Research Center, Shiraz University of Medical Sciences, Shiraz, Iran*
[6]*Department of Pathology, Shiraz University of Medical Sciences, Shiraz, Iran*
[7]*Department of Chemical Engineering, University of Mohaghegh Ardabili, Ardabil, Iran*

Correspondence should be addressed to Seyyed Mojtaba Mousavi; mousavi.nano@gmail.com
and Wei-Hung Chiang; whchiang@mail.ntust.edu.tw

Received 26 June 2020; Revised 31 October 2020; Accepted 12 November 2020; Published 1 December 2020

Academic Editor: Xiaoming Li



The self-assembling is a spontaneous progression through which objects of nanophase/molecules materialize into prepared collections. Several biomolecules can interact and assemble into highly structured supramolecular structures, for instance, proteins and peptides, with fibrous scaffolds, helical ribbons, and many other functionalities. Various self-assembly systems have been established, from copolymers in blocks to three-dimensional (3D) cell culture scaffolds. Another advantage of self-assembly is its ability to manage a large variety of materials, including metals, oxides, inorganic salts, polymers, semiconductors, and various organic semiconductors. The most basic self-assembly of 3D nanomaterials is three primary forms of nanostructured carbon-based materials that perform a critical role in the progress of modern nanotechnologies, such as carbon nanotubes (CNTs), graphene, and fullerene. This review summarized important information on the 3D self-assembly nanostructure, such as peptide hydrogel, graphene, carbon nanotubes (CNTs), and fullerene for application in gene delivery, cancer therapy, and tissue engineering.

## 1. Introduction

Nanostructure materials are those materials which have their dimensionality in the range of nanometers [1, 2]. Nanomaterials are synthesized using two major approaches: top-down and bottom-up techniques. Self-assembly is spontaneous assembly of constituents to form a complex nanostructure in the absence of significant external intervention. There are two types of self-assembly intermolecular and intramolecular self-assembly. Self-assembly is highly useful because it provides the path for the aggregation of structures, which are very small, to modify individually into the organized patterns that often give various functions to materials. Self-assembly is the result of a combination of weak forces such as noncovalent interactions, hydrogen bonds, electrostatic interactions, pi-pi stacking, hydrophobic forces, van der Waals forces, and chiral dipole-dipole interactions. Self-assembly of nanomaterials is affected by interparticle

interactions, particle size, and particle shape [3]. Self-assembled nanomaterials represent a classic of induced non-covalent interactions [4]. The cooperative association of disordered nanomaterial building blocks contributes to the spontaneous creation of more ordered (or organized) nanostructured structures [5]. A highly structural nanoparticle assembly is assessed for application in wiring, superlattice creation, and rings. Several self-assembly systems were created, from copolymers in blocks to three-dimensional (3D) cell culture scaffolds. Because of its applications in optical materials, nanoelectronics, computing, photonics, medical imaging, and diagnostics, the functional material assembly draws attention. Interactions between the materials, particle size, and particle composition affect nanomaterial self-assembly [4–6].

There are several standard features of the various types of self-assembly developments in nanoscience that allow for the adoption of a conceptual framework in the context of the following three phases (Figure 1).

Spontaneous self-assembly of spherical and nonspherical nanoparticles is distinguished from one another. Polydispersed spherical nanoparticles, 5% self-assembled 2D or 3D compact structures, and nonspherical nanoparticles exhibit different ways of self-assembly [8].

Significant instances of the self-assembly mechanism are originated in biomaterials, where the combination of different macromolecular components and the coordination of their activities allow for extremely complex functions of biological interest [9–11]. For instance, folding polypeptide chains within different functional types of proteins or conformation nucleic acids are essential instances of procedures of self-assembly in numerous biological functions [12, 13]. Proteins are an excellent instrument for modern nanotechnology and serve as building blocks for quaternary frameworks and functional self-assembled nanostructures [14]. These nanoassemblies were used to generate hierarchical protein nanostructures, counting 1D (tubules/strings/nanowires), 2D (nanorings/-networks), and 3D (hydrogels and crystalline frames) [15]. There are also three main forms of carbon-based nanostructured materials amongst the utmost common organic nanomaterials, which play an important role in the development of modern nanotechnologies, specifically graphene, carbon nanotubes (CNTs), and fullerene (Figure 2). Such nanomaterials are significant nanoplatforms in the creation of emerging nanotechnologies, with good mechanical properties, high aspect ratio, outstanding optical activity, and multifunctional surface properties [7, 16, 17]. Of particular interest is the use of self-assembling CNTs in biomedical applications. Single-layer carbon nanotubes (SL/CNTs) are capable of transferring imaging agents (radioisotopes or fluorophores) or medicines to certain tumors and provide major recompenses over other methods based on nanoplatforms [18, 19]. A fullerene-based nanocarrier tool for doxorubicin drugs has recently been designed to treat potential lung cancers [20]. Fullerene derivatives with well-established functional properties are also capable of nanostructures for bioactive macromolecules that are optimally distributed [21]. Graphene is used as a matrix that interferes with various cells and biomolecules [2, 22]. The peculiar characteristics of graphene, such as excellent physicochemical, electrical, large surface area, and biocompatibility, have been revealed in the past decade, leading to ongoing research into the use of graphene nanomaterial in various clinical applications and regenerative medicine [22]. The graphene-based materials can appear as nanomaterials of the next decade [23]. Graphene promotes interest in biosensing and bioimaging as two-dimensional, three-dimensional, and hybrid. The researchers should find the use of graphene nanomaterials in different tissue scaffolds as a significant field of interest shortly [2, 24–26].

The mechanisms of self-assembly of biomolecules to different nanostructures have been extensively studied, and some reviews of the synthesis, design, and applications of self-assembled biomolecular nanomaterials have been recorded [27–29]. For example, Yang and colleagues presented a summary of the self-assembly of proteins into different supramolecular products, in which the design techniques for the self-assembly of proteins were applied and discussed in detail [30]. Willner and Willner reviewed the applications of nanostructures and nanomaterials constructed on biomolecules for sensing and nanodevice manufacturing [31]. After studying these reports, we realized that contributing a review on the self-assembled 3D poly functionalized nanostructures is still valuable for us. Therefore, in this study, application of 3D self-assembly (such as hydrogels, CNTs, graphene oxide, nanodiamonds, and buckminsterfullerene) was explained in gene delivery, small molecule drug delivery, cancer therapy, and tissue engineering.

## 2. 3D Self-Assembled Nanostructures for Tissue Engineering

Tissue engineering celebrates the ability to reconstruct and remove damaged sections of the body by developments in the medical industry. The significant growing need for organ and tissue transplants has sparked ongoing research into the cell's rejuvenating properties. It promoted the development of a new tissue engineering approach, as the primary response to tissue and organ destruction. The key factors to be discussed in cell regeneration include the structure and origin of the cells, the scaffolding materials used, scaffolding design, the cell, and the outer tissue forming environment [32, 33]. Because of the nanoscale structure of human tissues (Figure 3), advances in nanotechnology have led to advances in regenerative medicine with the potential to replicate nanoscale composition and function of human tissues and organs [34].

Peptide amphiphiles, carbon nanotubes (CNTs), self-assembled peptides, electrospun fibers, and layer structures are among the most widely used nanomaterials [21]. The development of new nanostructures composed of bioactive molecules capable of directly and reproductively interacting with cell receptors and proteins to control procedures such as cell proliferation, cell differentiation, cell production, and tissue and organ regeneration dedifferentiation has called natural attention to this. Various studies using

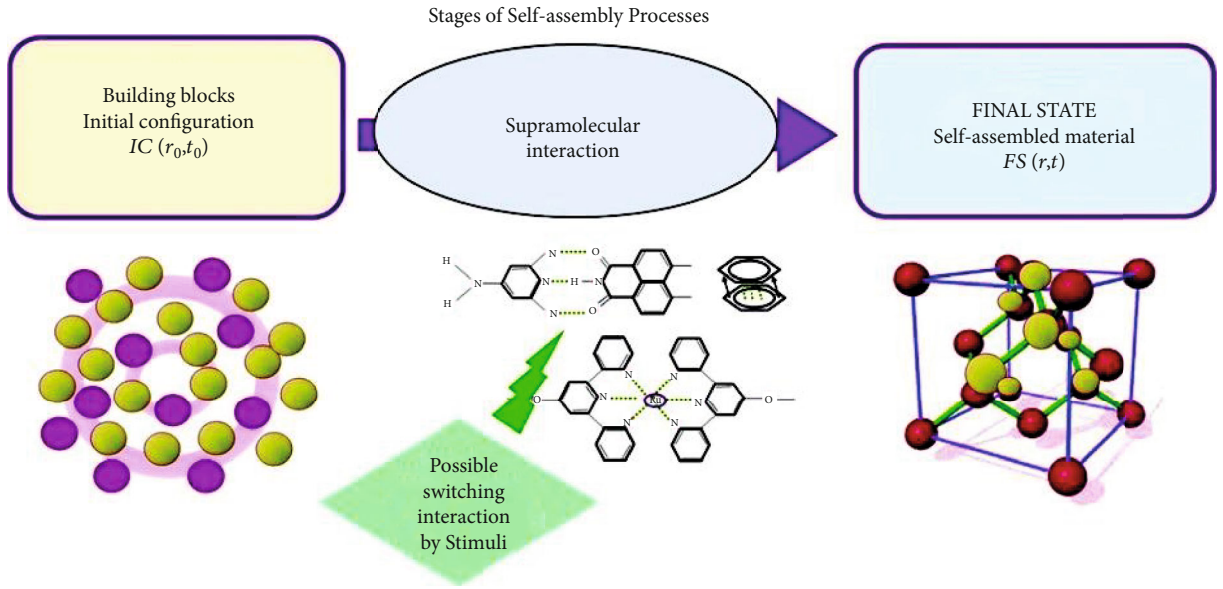


Figure 1: Conceptual structure showing the significant phases of the self-assembly procedure in nanoscience. IC: initial configuration; FS: final state; $r_0$: initial radius; $t_0$: initial time; $r$: radius; $t$: time [7].

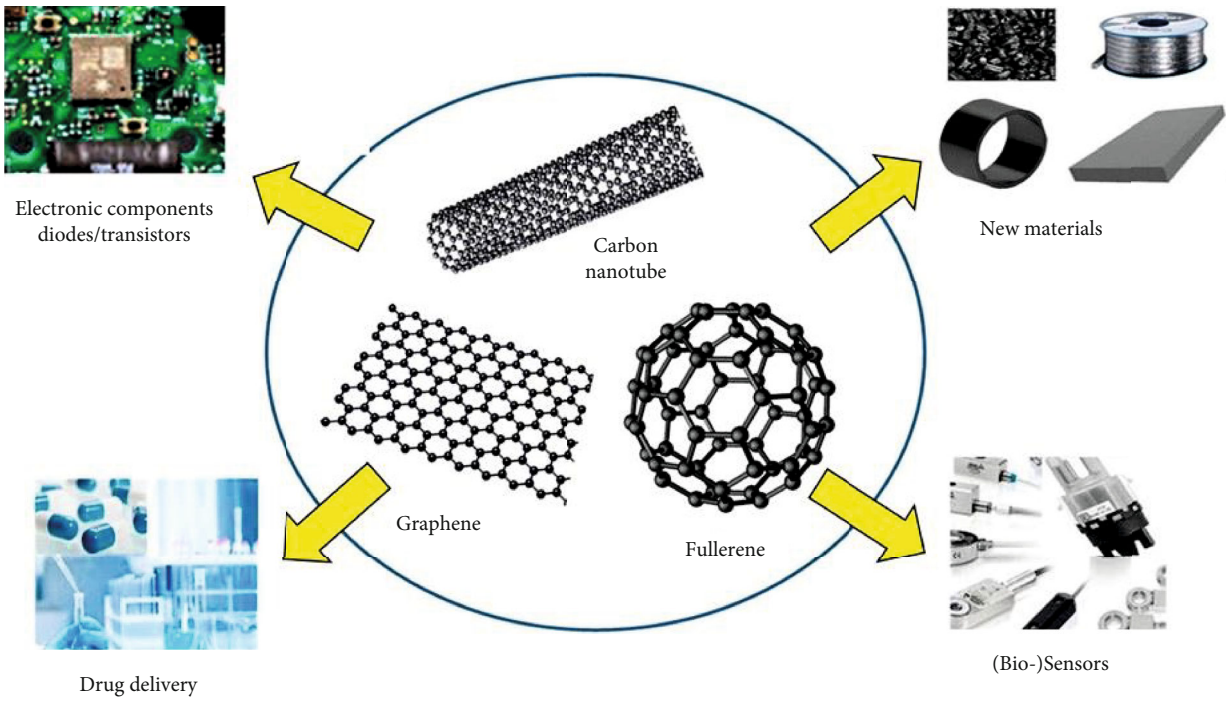


Figure 2: Morphology and critical uses of certain carbon-dependent nanoplatforms for nanotechnology development (carbon nanotubes, graphene, and fullerene) [7].

nanostructured materials have shown the feasibility of this method and its use in the regeneration of various tissues (such as the heart, bone, nerve, cartilage, lung, skin, and vascular) by improving the biological properties of cells such as cell adhesion, proliferation, and cell differentiation [3, 37–40], respectively. In the in vivo framework, the cells are located in three-dimensional (3D) microenvironments, encompassed by certain cells and the extracellular matrix (ECM) whose elements, such as elastin, laminin, and collagen, are organized into nanostructures (i.e., triple helixes, fibers) with various bioactive reasons for cell homeostasis regulation in three-dimensional (3D) microenvironments; the cells are in vivo surrounded by other cells and an extracellular matrix (ECM) whose components, such as

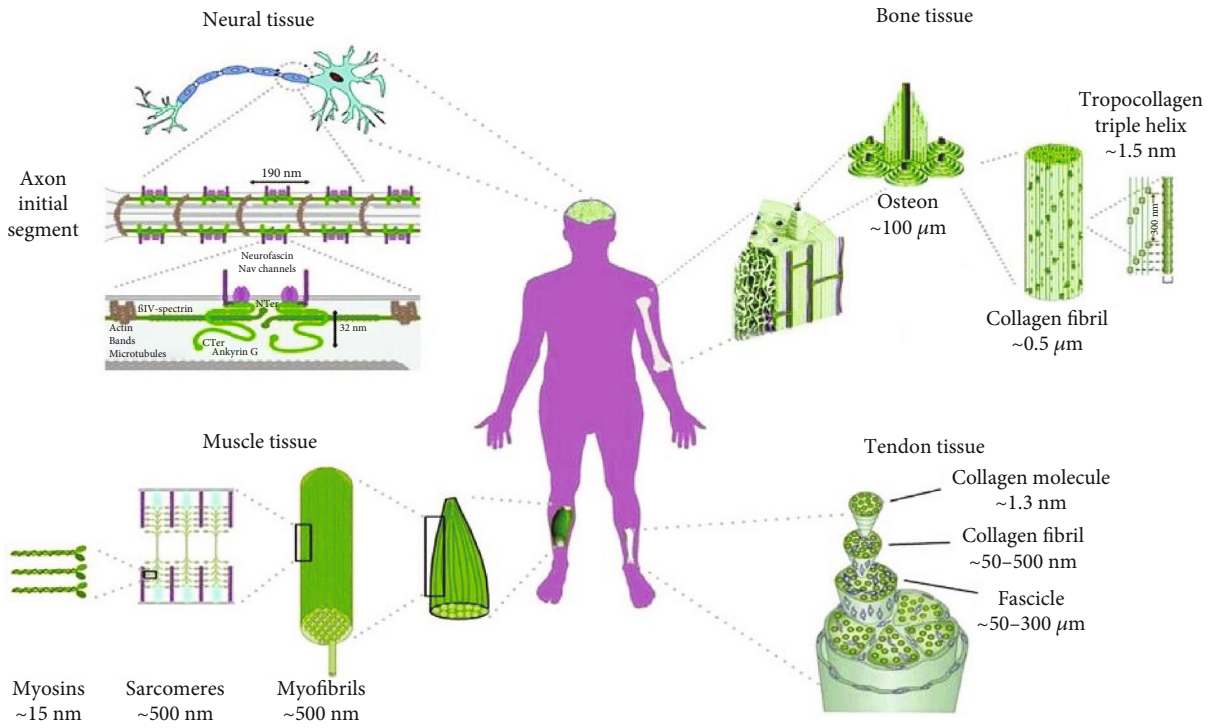


Figure 3: Characteristics of nanoscale human tissue. Within neural tissue, the axon's initial portion is responsible for producing future neuronal behavior and is organized on a nanoscale. This system is arranged regularly in a longitudinal direction and is placed radially. That architecture is essential for neuronal activity on a nanoscale [35]. The compact bone tissue comprises of osteons (100 mm), which are strengthened fibers shaped by aggregated type I collagen and calcium phosphate nanoparticles [34]. Myofibrils are produced in parallel, creating sarcomeres in the muscle tissue. The sarcomeres are made up of actin-consistent protein filaments and organized in conjunction with dense filaments made up of myosin aggregates. Nanoscale may be the dimensions of myofibrils, sarcomeres, and myosin. A tendon fiber comprises of a complex network of tendon fibers in the tendon tissue (50–500 nm), composed moreover of molecules of collagen (w1.3 nm) [36].

collagen, elastin, and laminin, are organized into nanostructures (i.e., fibers, triple helixes) with different bioactive motives regulating the homeostasis cell [41, 42].

*2.1. 3D Self-Assembled Peptide Hydrogels in Tissue Engineering.* Bone tissue is a particularly complex example of such a composite because it contains multiple levels of hierarchical organization. Various nanoscale protein filaments (e.g., peptides) can be inserted into high-aspect nanofibers, which can replicate the in vivo cells' internal microenvironment. Such nanofibers wrap round body cells that stretch long distances across their surfaces and act as cables that mechanically link and sustain adjacent cells through the creation of three-dimensional networks (Figure 4(a)) [43]. For example, one form of peptide amphiphiles has been investigated to produce nanofibers for bone tissue engineering via a pH-induced self-assembly process [44]. These peptide amphiphiles contain several main structural features, including long hydrophobic alkyl tails that accumulate in aqueous solution to drive self-assembly, four consecutive cysteine residues forming disulfide bonds to polymerize self-assembled structures, a bonding region of three glycine residues to provide flexibility for the hydrophilic head group, a single phosphorylated serine residue that strongly interacts with calcium ions to improve mineralization, and an Arg-Gly-Asp peptide ligand to enhance cell adhesion [37] (Figure 4(b)). Dithiothreitol-treated peptide amphiphiles at pH 8 are soluble in aqueous solution and begin self-assembled at pH 4. Fibers with an average diameter of 7 nm and a duration of up to many micrometers are produced and can be analyzed using electron microscopy with cryotransmission (Figure 4(c)).

In addition, a family of peptide amphiphiles has been shown to self-assemble into nanofiber networks by modifying both the concentration of pH and salt ion (e.g., sodium and potassium) in aqueous solutions. Due to their amphiphilic nature, separate model oligopeptides can also be self-assembled into nanofibers [38]. The first of the oligopeptides creators, EAK 16-II, a 16-amino acid peptide, was contained in zuotin, a yeast protein that was initially described as binding to left-handed Z-DNA [39]. This natural peptide had an AEAEAKA amino acid sequence—KAEAEAKAK, which can form a stable $\beta$-sheet structure and self-assemble into hydrogels in various shapes when the sodium/potassium concentration in aqueous solution is balanced. These peptide scaffolds can boost the adhesion, proliferation, and differentiation of mammalian cells [40]. Holmes [41] researched neuronal cell adhesion and differentiation using Ac-RADARADARADARADA-NH2 (RAD16-I).

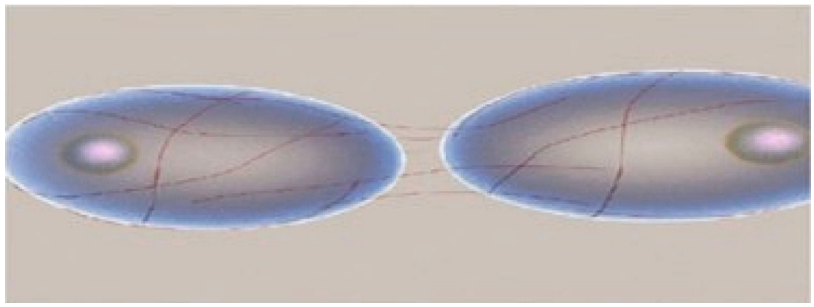

(a)

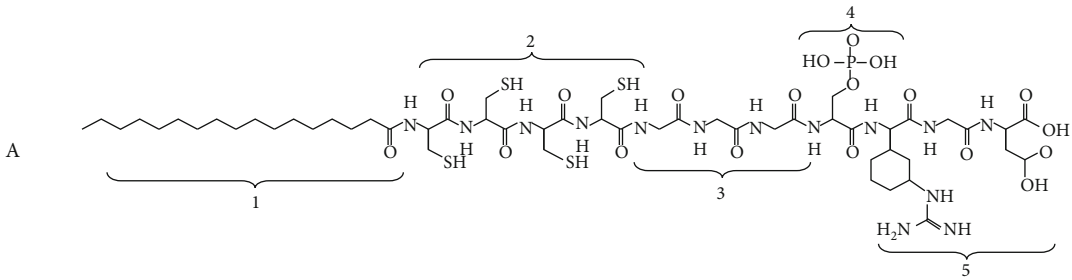


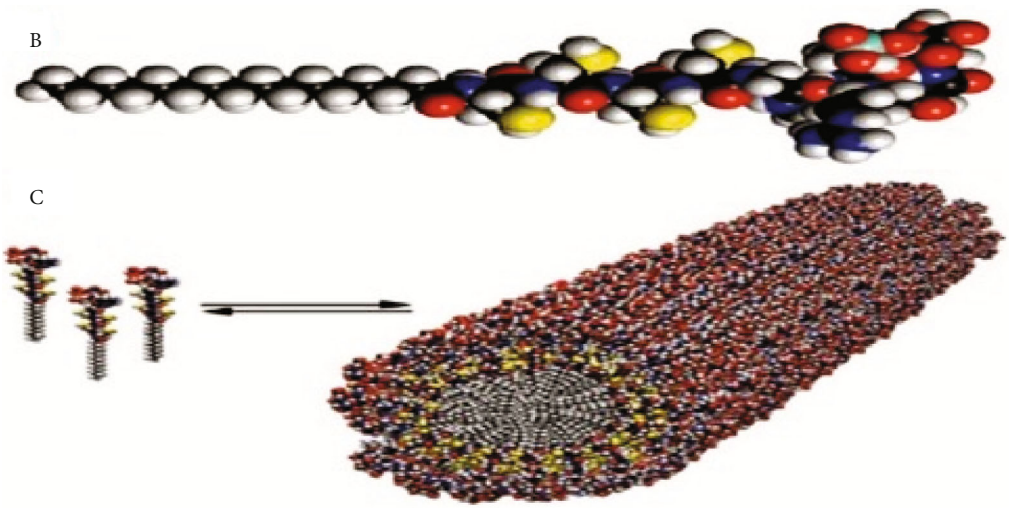


(b)

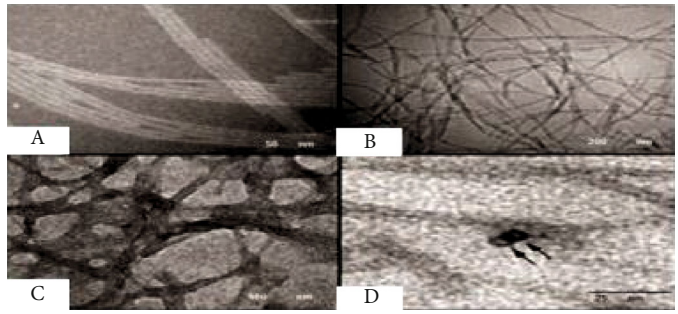


(c)

Figure 4: Self-assembly process used in developing 3D scaffolds. (a) An overview of the filamentous receptor cell nanostructures [43]. )b) Chemical composition of (A) amphiphilic peptides and (B) molecular sequence. Collection of colours: C, black; H, white; O, red; N, blue; P, cyan; and S, yellow. (C) Amphiphilic peptide self-assembly schemes into a cylindrical micelle. (c) Microscopic images of (A) negative stain (phosphotungstic acid) TEM of the self-assembled nanofibers before covalent capture, (B) vitreous ice cryo-TEM of the fibers reveals the diameter of the fibers, (C) positive stain (uranyl acetate) TEM of the self-assembled nanofibers after oxidative crosslinking, and (D) thin section TEM of positively stained (uranyl acetate) nanofibers after oxidative crosslinking and embedding in epoxy resin [37].

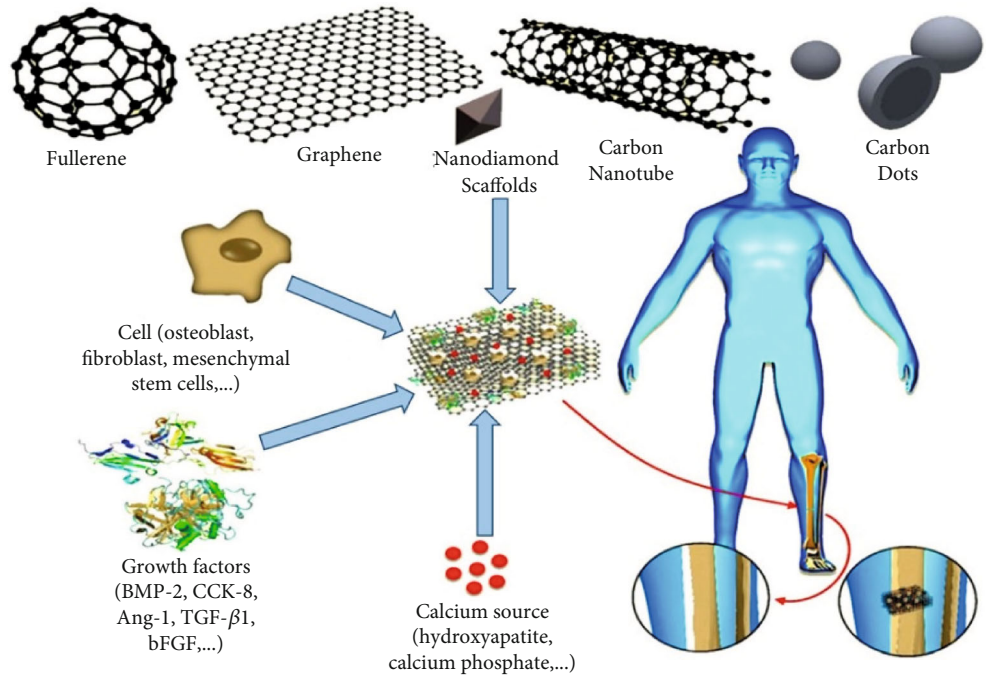


Figure 5: Use of carbon-dependent nanomaterials as scaffolds in the engineering of bone tissues [45].

Two small self-assembling peptide hydrogel scaffolds, and Ac-RARADARADADADA-NH2 (RAD16-II), showed that mouse neurons can develop active dendrites on these scaffolds.

*2.2. Carbon-Based Nanomaterials in Tissue Engineering.* All the carbon nanomaterials on one or more ends are bioactive. Most exhibit high bone tissue engineering capabilities with acceptable mechanical possessions, no osteoblast cytotoxicity, and endogenous antibacterial activity (deprived of the use of exogenous antibiotics) [42] (Figure 5).

*2.2.1. Tissue Engineering by Graphene-Based Nanomaterials.* GO-based systems provide a wide variety of applications for engineering bone and tissue regeneration. GO nanomaterials' remarkable advantages are the wide surface area, adequate wettability, excellent mechanical properties, strong adhesion power, and quick start of stimulation performance. Besides, these materials may solve the weak interaction between bioceramics and biopolymers by incorporating strong electrostatic and p-p stacking interactions [46, 47]. GO would also definitely start to draw experts from prospective bone regeneration fields and other tissue engineering programs. Below are three items related to the usage of GO for scaffolding bone tissue. First, the existence of GO in natural biopolymer-based scaffolds has more potent stimulating effects on the bone tissue mineralization cycle than synthetic polymers. Second, the presence of GO in the matrix of polymer scaffolds will stimulate the growth and spread of bone cells on both natural and synthetic polymer scaffolding surfaces. However, on the GO synthetic polymer scaffold, the fraction of dead cells was higher than that of the natural biopolymer scaffold from the GO. Third, while the proportion of dead cells on the GO synthetic polymer scaffold was higher than that of the GO natural biopolymer, GO natural biopolymer scaffolds can produce better mechanically resistant bone tissue. Table 1 summarizes the results of GO nanomaterials and their application in bone tissue engineering.

Omidi et al. made a carbon dot/chitosan hydrogel and found it to be biocompatible with Staphylococcus aureus and have antibacterial efficacy [56]. It has been shown that chitosan hydrogel composites filled with carbon dots composed of citrate-conjugate ammonium hydrogen have enhanced mechanical properties. These nanomaterials were extremely pH-reactive and found to be highly successful for wound cure. Consequently, carbon dots/chitosan nanocomposite both have pH responsiveness and antibacterial rial properties. In tissue engineering, this study has the potential to improve wound healing. GQDs have been used in recent research for regenerative, and stem cell-based uses in tissue engineering. Many researchers have used stem cells to organize them across a variety of categories, utilizing several techniques. GQDs can be used to promote stem cell differentiation in the right conditions. Qiu et al. looked at how GQDs perform an important osteogenic differentiation function [57]. In particular, GQDs have been shown to affect the early activation of osteogenesis. This nanomaterial increases the abundance of calcium, too. Due to their low toxicity, differentiation, and excellent mechanical properties, these particles are highly valuable in the regenerative medicine field. Tissue engineering's future depends on the three-dimensional (3D) scaffolds created by exciting new biomaterials. Recent advances in tissue engineering for applications in 3D graphene scaffolds are shown in Figure 6 [58].

*2.2.2. Carbon Nanotubes in Tissue Engineering.* Due to its exceptional biocompatibility, carbon nanotubes/nanofibers (CNTs/CNFs) are seen as potential candidates for

Table 1: GO-based nanoparticle application in the engineering of bone tissue.

| Method of NP synthesis | Cell type | Mechanical strength (MPa) | Application | Ref. |
|---|---|---|---|---|
| Modified Hummers' method | mMSCs | 53 | In vivo | [48] |
| Modified "Hummers' and Offeman's" method | Osteogenesis of MC3T3-E1 preosteoblasts | — | In vivo | [49] |
| Modified Hummers' method | MC3T3 cells | 10.0 | In vitro | [50] |
| Modified Hummers' method | Rat mesenchymal stem cell line | 14 ± 0.7 | In vivo and in vitro | [51] |
| Modified Hummers' method | Mesenchymal stem cells | 134.4 ± 26.5 | N/A | [51] |
| Electrostatic LBL assembly followed by electrochemical deposition | MC3T3-E1 osteoblast | 85.94 ± 10.76 | N/A | [52] |
| Prepared by chemical oxidation of graphite flakes following a modified Hummers' process | Human osteoblast cell line Saos-2 | 12.69 ± 0.86 | N/A | [53] |
| Modified Hummers' and Offeman's method | Osteoblastic MC3T3 E1 cell | 0.125 | In vitro and in vivo | [53] |
| Modified Hummers' method | Human periodontal ligament stem cells | — | In vitro | [54] |
| Biomineralization of GO/C scaffolds | Bone marrow stromal cells | 0.65 | In vivo and in vitro | [55] |

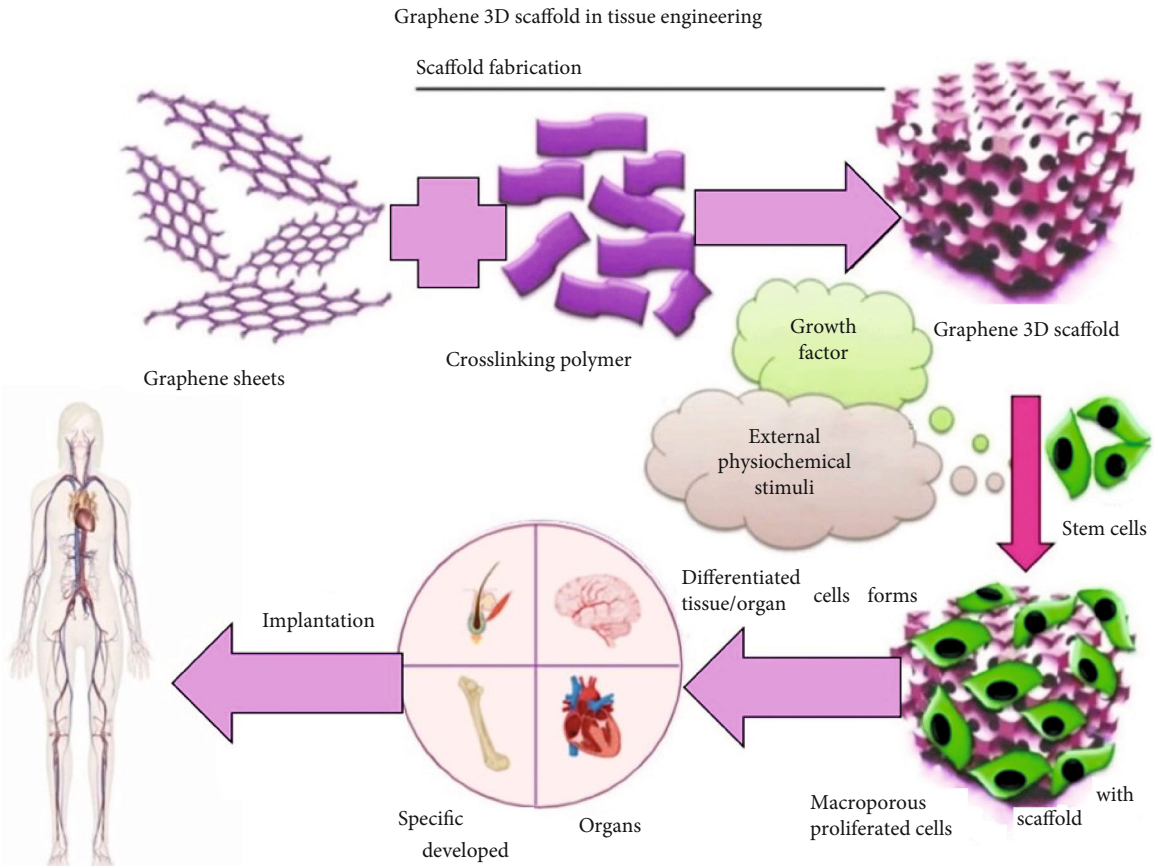


Figure 6: Schematic diagram of 3D graphene scaffolding in tissue engineering [58].

applications in bone tissue engineering, electrical and mechanical possessions [59]. In a new study by Price et al., osteoblast adherence by a diameter of 60 nm CNF significantly improved and, at the same time, diminished competitive cells (smooth muscle cells and fibroblasts) in order to induce sufficient osseointegration [60].

Sitharaman et al. recently published an in vivo study of the ultrashort SWCNT polymer nanocomposites (single-

walled carbon nanotubes), following up to 12 weeks of implantation in rabbit femoral condyles and subcutaneous pockets. For 4 to 12 weeks, nanocomposites had intense hard and soft tissue reactions [61]. Hirata et al. studied MWCNT-coated 3D-C scaffolds and checked the adhesion of the cells to MWCNT-coated C sponges. Their study of actin stress fibers showed that the tension in Saos2 cells, which developed on materials covered with CNT, became more apparent after seven days of growth. MWCNT coating gives the cell culture a 3D scaffold, which is more fitting than SWCNT [62].

The structural and molecular dynamics of the scaffold microenvironments can be discussed in the interaction between different types of CNTs and their effect on bone cell growth and attachment. Because of its wide specific surface area, SWCNTs can give more space for efficient cell adhesion to the scaffold. At the same time, MWCNTs will manage the positive contact between the cells and the scaffold surface due to the more aggregated condition of the MWCNTs. While the cytotoxicity of CNTs continues to be a problem in bone tissue engineering because of the complicated interactions between CNTs and cellular processes, the inclusion of CNTs in the scaffold matrix may enhance cell interactions. Due to the smaller number of oxygen atoms in functional groups of functionalized CNT, the spreading and aggregation of cells within the scaffold microenvironments is less successful than GO-based scaffolds. Table 2 summarizes some of the observations regarding the use of CNT-based materials in bone tissue engineering.

*2.2.3. Fullerenes in Bone Tissue Engineering.* Fullerenes are closed-cage structures consisting of roughly spherical carbon atoms and hybridized by sp2. The fullerenes C60 and C70 are more widespread than the whole of other types. A natural application of the fullerene compounds provides alternative types of development in bone tissue. The spherical molecular structure of the fullerenes allows their use in biomedicine as free radical scavenger agents [70]. For instance, because neuroprotective agents are HIV particle inhibitors, fullerene materials incorporate new behavior.

As a consequence of findings of enhanced cell adhesion to fullerene biomaterials, advances in bone tissue engineering have drawn significant attention in recent years [71]. Bacakova et al. developed fullerene-coated carbon nanofibers capable of increasing the adhesion of osteoblastic MG 63 cells and increasing cell proliferation by up to 4.5 times in 7 days [72]. This work recorded fullerene-based microarrays which were prepared using a metallic "nanomask" to improve the growth and adhesion of MG 63 osteoblast bone cells. Hierarchical surface morphology has played a crucial role in the formation of cells because the cells are almost entirely located between the prominences of the grooves. However, fullerene-based biomaterial did not allow the cells to extend by more than 1 mm in height. That is explained by the hydrophobic nature of the materials fullerene [73]. In another research, this group proposed that complements and other carbon nanoparticles could be therapeutic agents for arthritic bone diseases. Their consequences showed that fullerene materials were stable and did not cause DNA damage or alter osteoblastic MG 63 and U-2 OS cells morphology. However, they could increase the biological function of bone cells [74].

*2.3. 3D Self-Assembled Nanostructures for Use in Scaffolds.* Scaffolds can be called the tissue engineering field's "beating heart." Without proper scaffolding, the cells cannot expand in an artificial setting. Bone cells are perhaps the essential forms among all the separate cells in the human body, providing a well-designed scaffold for constructed living bones. Research has shown that nanostructured materials through desirable cell surface possessions can enable more protein interactions than conventional materials to support more effective new bone development [75, 76].

*2.3.1. Graphene Family Materials as Scaffold or a Reinforcement Material in Scaffold.* In bone tissue engineering, the most common technique is to reproduce the bone remolding and regeneration processes as natural. Biocompatible scaffold, biodegradable, and osteoinductive or osteoconductive techniques must reach three dimensions [77]. This form of scaffold would provide an ideal microenvironment for imitating the extracellular matrix (ECM) for osteogenic cell binding, division, differentiation and proliferation, and growth factor carriers [78]. Graphene should make the full surface area of the substratum suitable as a flexible biocompatible scaffold for cell differentiation and osteogenic differentiation [79]. For example, 3D graphene foams used as substrates for human mesenchymal stem cells (hMSC) have shown their capacity to preserve stem cell viability and facilitate osteogenic differentiation [80]. In addition, 3D graphene (3DGp) scaffolding and 2D graphene (2DGp) coating have been shown to induce the differentiation of periodontal ligament stem cells (PDLSC) into mature osteoblasts by higher rates of mineralization and graphene-related upregulated bone-related genes and proteins with or without chemical inductors [81]. GO was placed by Han et al. on Ti scaffolds, modified with polydopamine (PDA). After that, a separate form of gelatin microspheres (GelMS) was encapsulated in BMP-2 and vancomycin. The drug-containing GelMS were subsequently placed on GO/Ti scaffolds and stabilized by usable GO groups (Figure 7). The novel scaffolds play an essential role in bone recovery and tolerance for bacterial infections [82]. Substance P (SP) is a neuropeptide containing 11 strictly retained amino acids [83]. It includes, for example, inflammatory wound healing, control, and angiogenesis in many procedures, and is necessary to facilitate the recruitment of MSC implants [84]. So apart from the BMP-2, this peptide, SP, was applied to the GO-coated Ti surface by La et al. The dual delivery mechanism of GO-coated Ti has demonstrated the continuous release of BMP-2 and SP, and the ability of SP to activate MSC mi-integration. In vivo, the Ti/SP/GO/BMP-2 group showed more magnificent new bone formation in the mouse calvary relative to implant recruitment by SP for the Ti/GO/BMP-2 population [85].

A significant factor in the design of tissue engineering scaffolds is the mechanical strength and longevity of the

Table 2: Carbon nanotubes used in the manufacture of bone tissues.

| Method of NP synthesis | Type of NPs | Cell type | Mechanical strength (MPa) | Application | Ref. |
|---|---|---|---|---|---|
| In situ hybrid CNTs with bacterial cellulose (BC) | BC | Osteogenic cells | 0.474 | In situ | [63] |
| Chemical vapor deposition (CVD) | Hydroxyapatite | Osteoblastic and fibroblast (L-929) cells | 89 | In situ | [64] |
| Thermal | Hydroxyapatite | Human osteoblast sarcoma cell lines | — | In vitro | [65] |
| CVD | Graphene (G) nanosheets and HAp-polyether ether ketone (PEEK) | MG-63 cells and human bone marrow stromal cells (hBMSCs) | 78.65 | In vitro | [66] |
| Freeze-drying method | Polyvinyl alcohol (PVA) | Osteoblast cells | 215.00 ± 9.20 | In vitro | [67] |
| Freeze-drying method | Polysaccharide HAp | MG 63 cell line | 0.222 | In vitro | [68] |
| Thermal | Poly (butylene adipate-co-terephthalate) (PBAT) | MG63 osteoblast-like cells | 3.5 | In vitro | [69] |

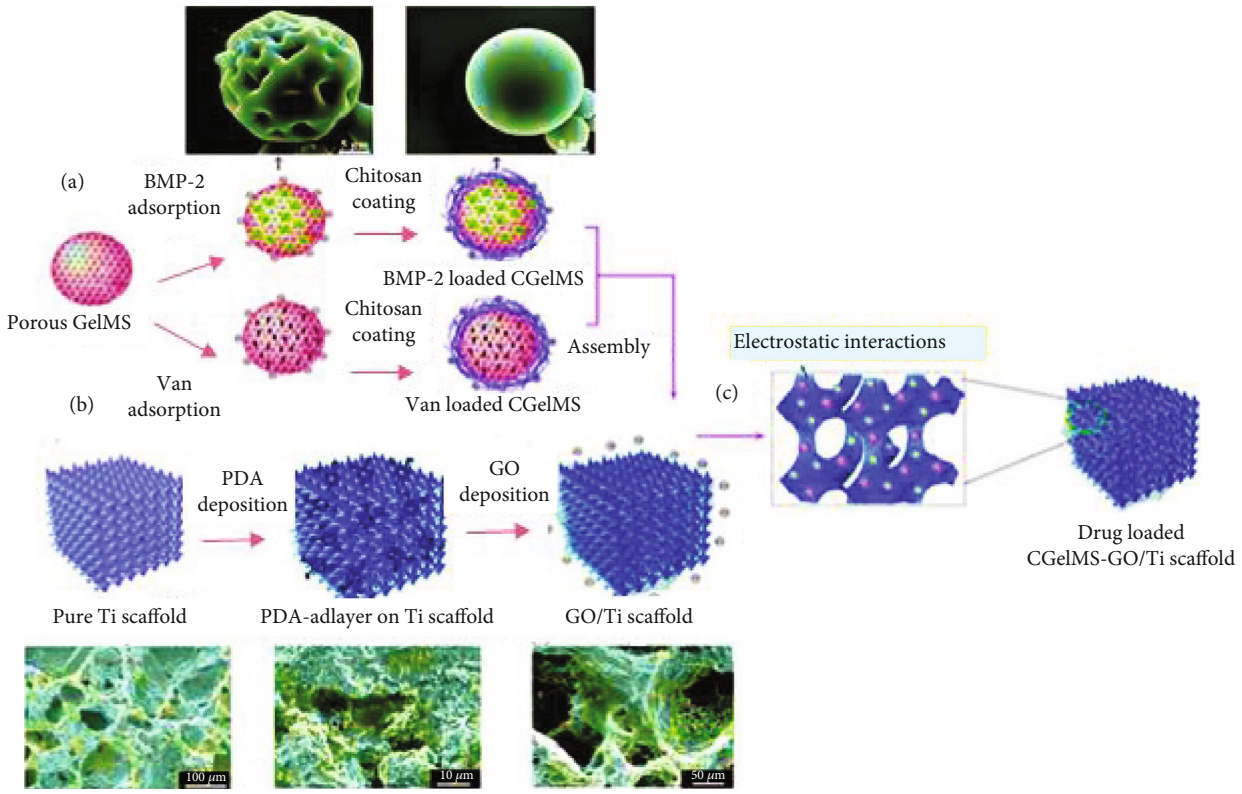


Figure 7: Schematics and electron micrograph examination of the preparation of the new GO/Ti scaffold: BMP2- and Van-loaded CGelMS are immobilized by electrostatic interactions on the GO/Ti scaffold between functional GO and CGelMS groups [82].

material. GO-based composites have very porous structures and high mechanical strength, which give strong prospects for regeneration to Liang et al. scaffolds. It is reported that composite scaffolds HAp/collagen (C)/poly(lactic-co-glycolic acid)/GO (nHAp/C/PLGA/GO) facilitate the proliferation of MC3T3-E1 cells (Figure 8), [86]. For scaffold preparation, they formulated nHAp/C/PLGA/GO nanomaterials with a particular percentage of GO weight and measured the mechanical properties of the scaffold. The findings showed that the dynamics would raise the mechanical strength of the scaffold by 1.5 wt. percent of GO and provide a good cell adhesion and propagation substratum.

One of the critical factors influencing the mechanical possessions of the bone-shaped in tissue engineering is the adhesion of bone cells to the substrate at the center [88]. A variety of work has focused on this subject over the last few years—for example, Mahmoudi and Simchi. A nanofibrous matrix was developed using electrospun material to improve

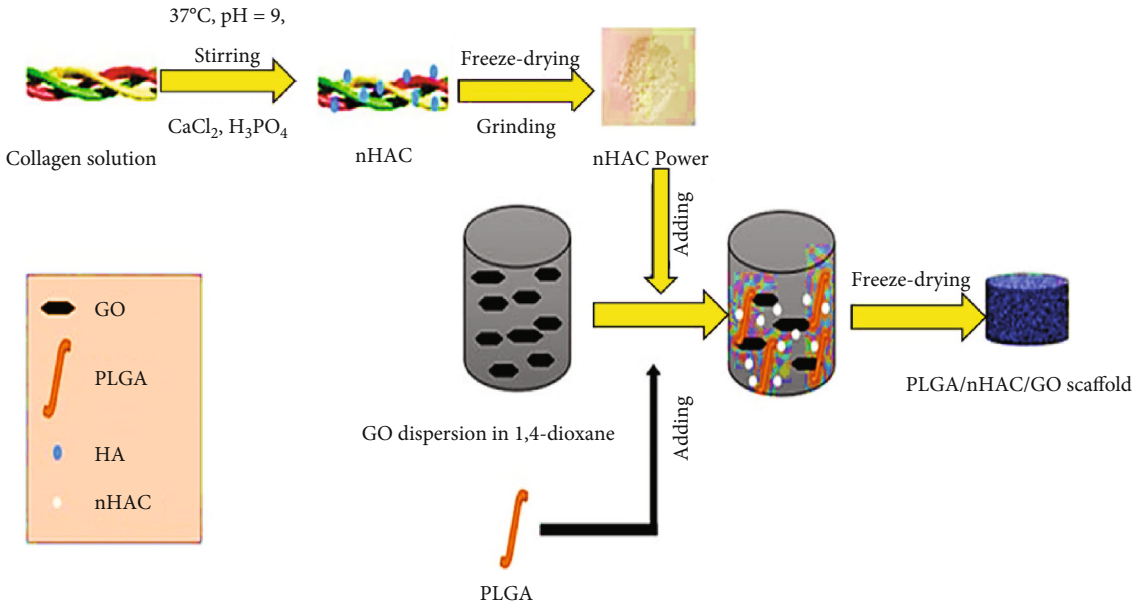


Figure 8: Experimental schematic techniques for the preparation of nHAp/C/PLGA/GO scaffold [87].

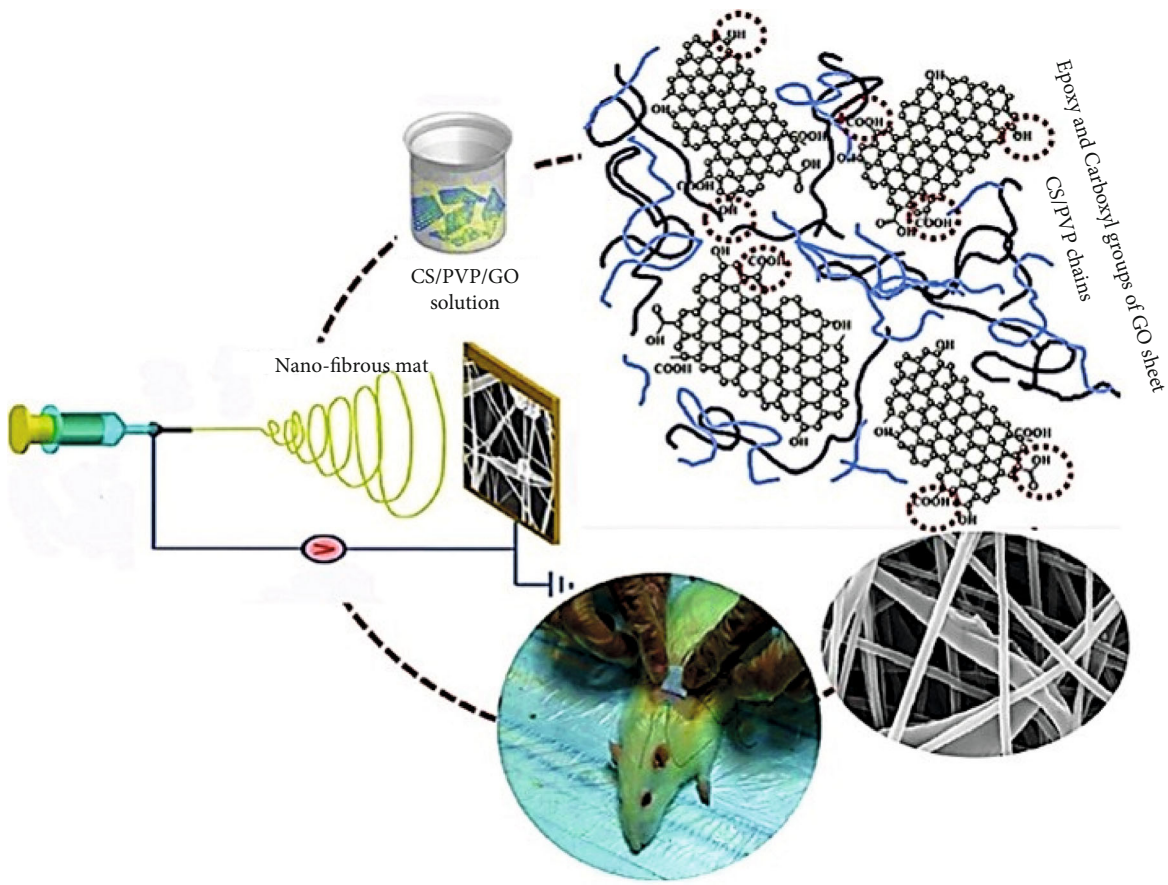


Figure 9: Biopolymer-GO composites are made using chitosan (CS), poly (vinyl pyrrolidone) (PVP), and GO using a process of electrospinning [89].

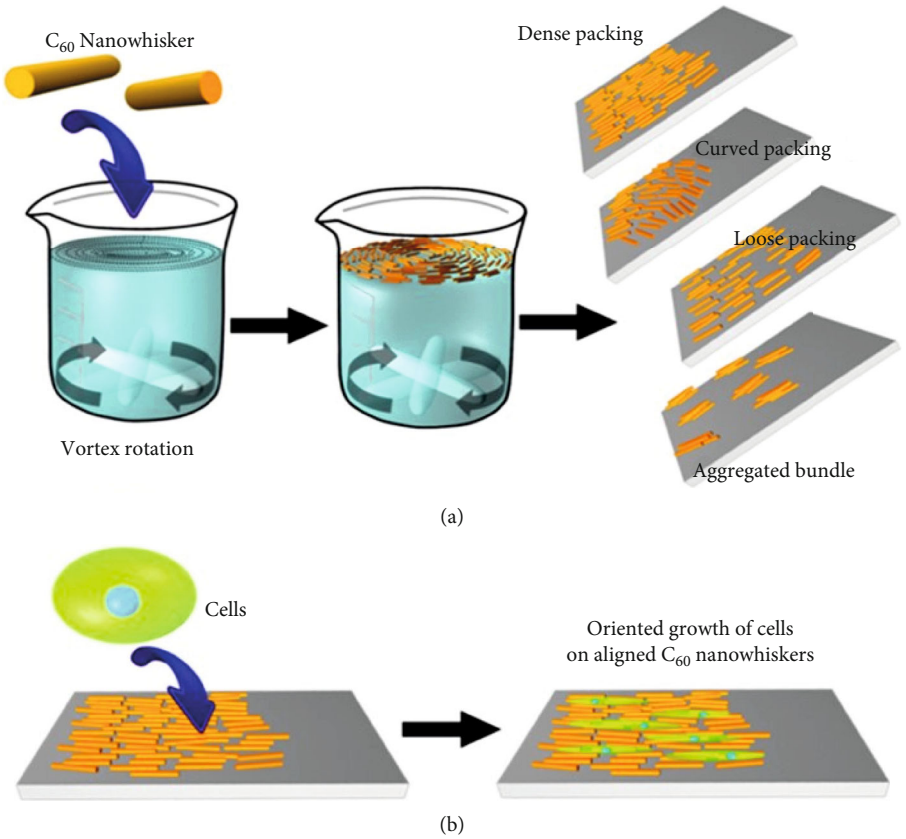


FIGURE 10: Schemes for (a) the alignment of C60NWs at an air–water interface by vortex flow and (b) aligned C60NWs as scaffold for directing cell growth [74].

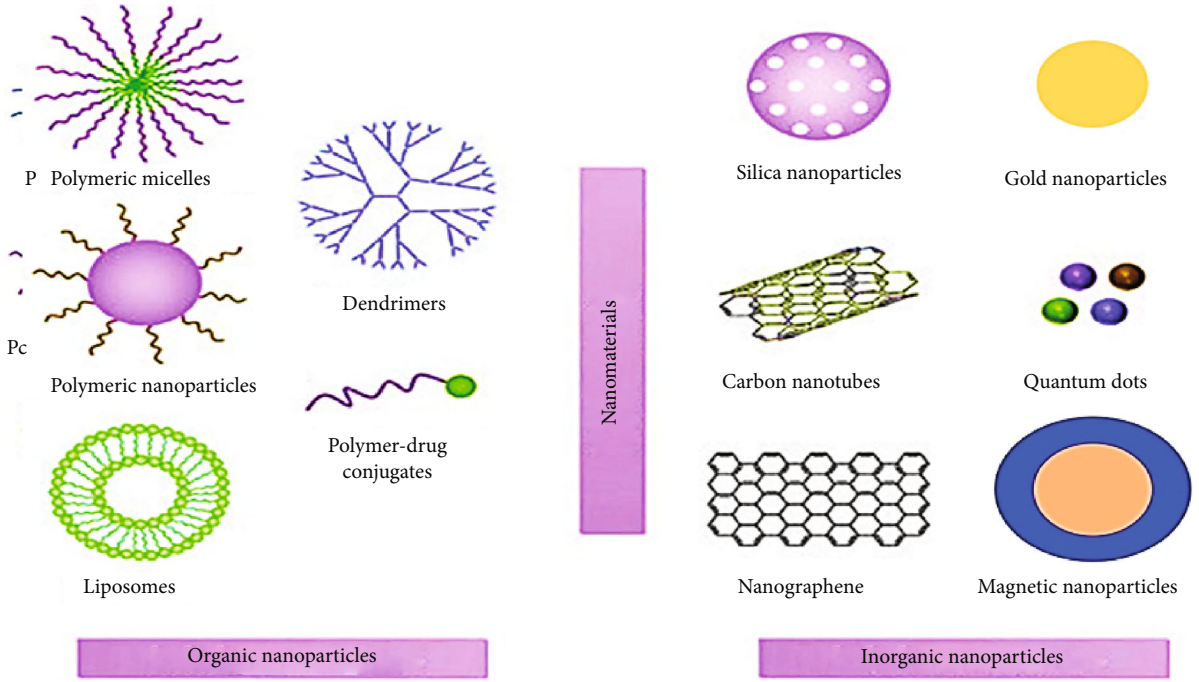


FIGURE 11: Representation of nanomaterials used for cancer therapy, including organic and inorganic nanoparticles [91].

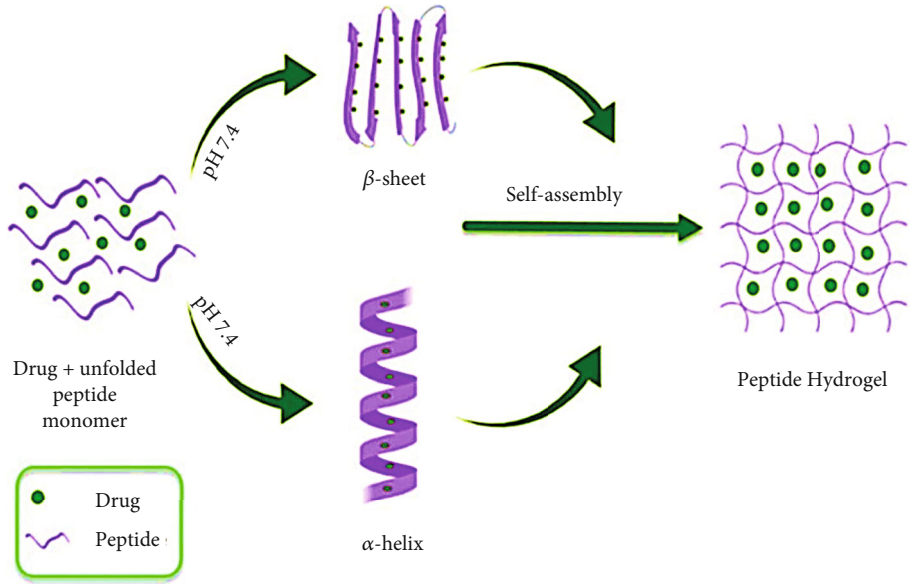


Figure 12: Peptides are self-assembled into hydrogels for drug delivery [93].

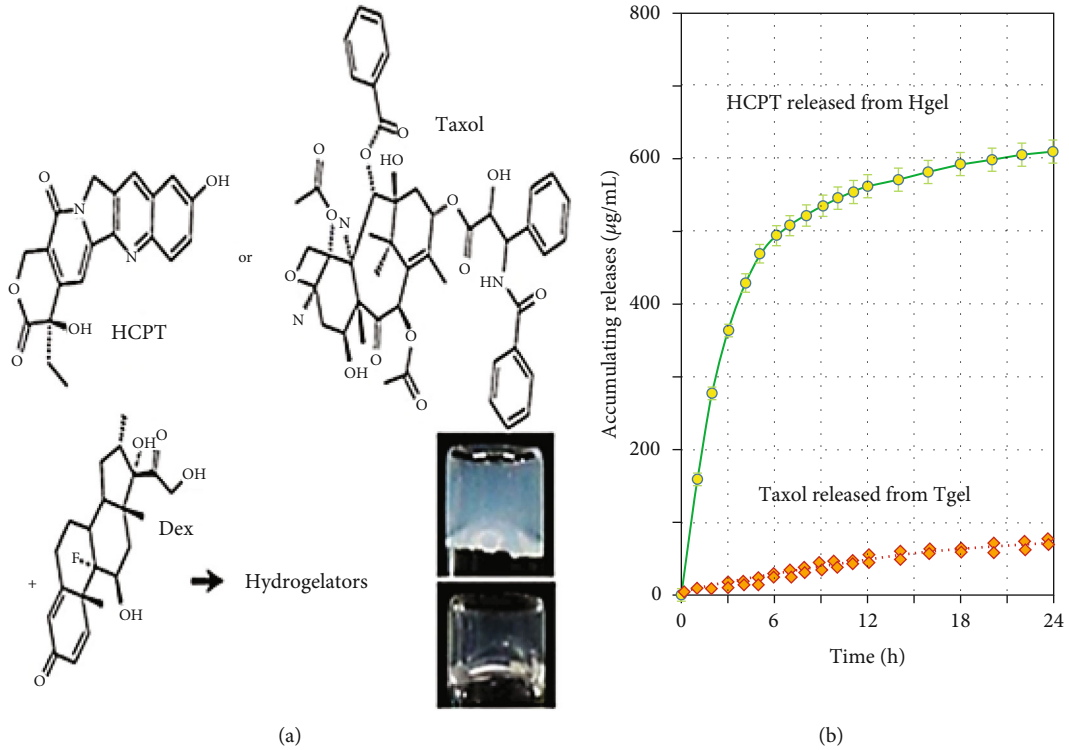


Figure 13: Codelivery of two anticancer drugs via a peptide-based hydrogel system [93].

the bonding forces within the bone cells. Because of this, they used high mechanical resistance and biocompatibility biopolymers and GO hybrids, and then a natural closure rate for wounds. The experimental design approach to this material are shown in Figure 9 [89].

*2.3.2. Scaffolds of Fullerene Materials.* Scaffolds of fullerene materials have specific situations in various and broad ranges of scaffolds in bone tissue engineering. These have strong calming effects on bone cell proliferation, with minimal cytotoxicity. Scaffolds dependent on fullerenes have more roughness and hydrophobicity. It would improve the potential for controlling the cell connection and strengthen the bone tissue thickness, and then the mineralization phase, which is an entirely remarkable feature of carbon nanomaterials. The fullerene molecule structure enables the anatomy of the final bone tissue to be organized and regulated [45]. In order to stimulate the growth of osteoblastic MG 63 bone cells,

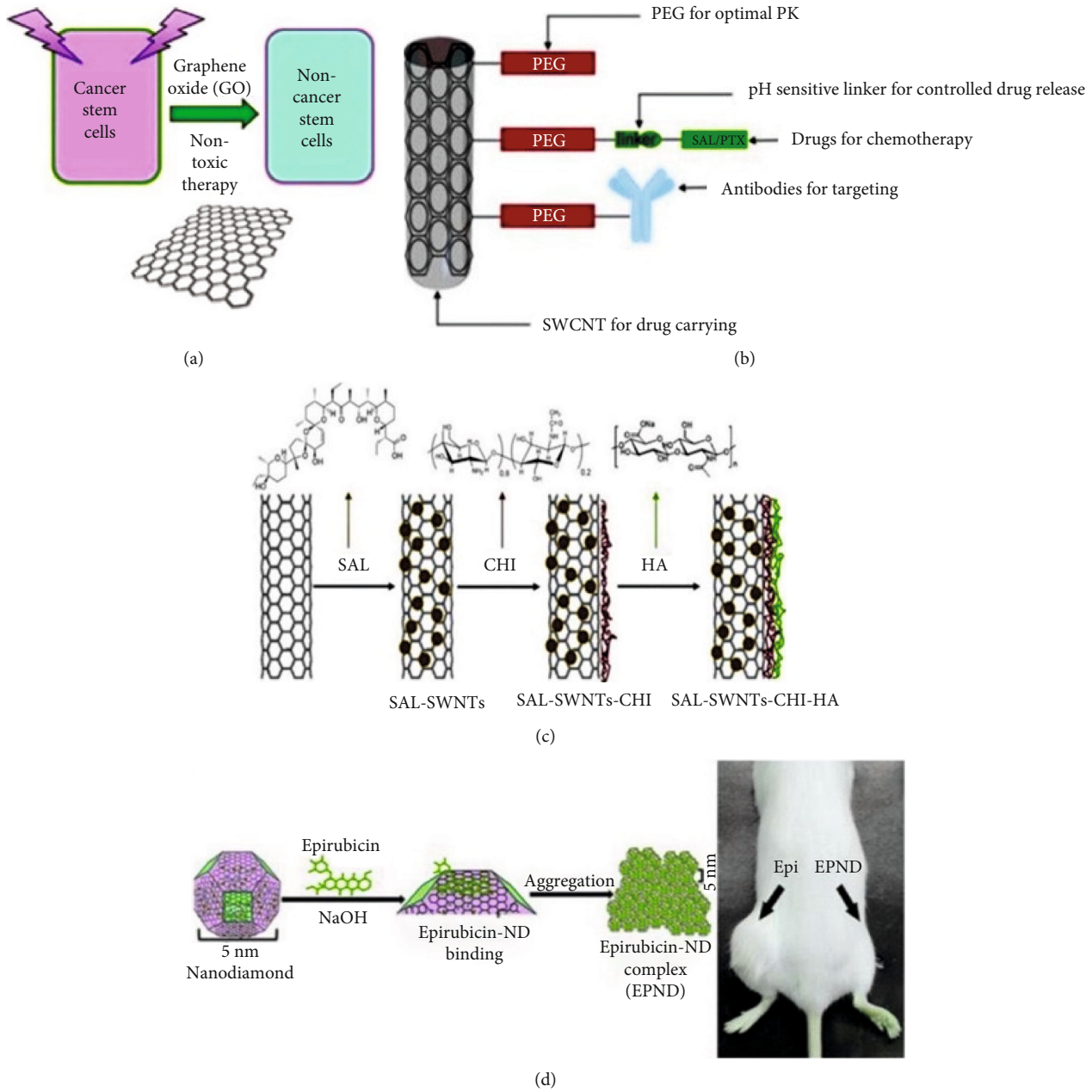


Figure 14: (a) Graphene oxide (GO): cancer stem cells targeted at the difference with nanotherapy [71]. (b) Schematic illustration of a processing method for SAL-SWNTs-CHI-HA (chitosan- (CHI-) coated single-wall carbon nanotubes (SWCNTs) treated with hyaluronic acid (HA) salinomycin (SAL)) [102]. (c) Schematic diagram showing the concept of drug carriers as operational SWCNTs [103]. (d) Left: a graphical model demonstrating the surface and chemical composition of (ND) and epirubicin (Epi). Epirubicin-nanodiamond (EPND) complex synthesis and aggregation. [104].

Krishnan et al. described a new method for making and depositing fullerene nanowhiskers on scaffolds. This was achieved by rotational flow of solutions that comprise fullerene nanowhiskers, allowing normal arranged arrays to be deposited on a glass substrate. They observed that fullerene nanowhiskers' normal, coordinated deposition had better biological activity than a random deposition. The distance from the vortex core of the glass substratum played a vital role in morphology of the formation. Samples produced at the edge of the vortex fluid had a more normal morphology than samples from core vortex sections. A processing schematic for this sample is shown in Figure 10 [74].

Cancer accounts for millions of deaths per year, and the number of new confirmed cases is increasingly growing due to the rise and aging of the world's population. While several advancements in early detection and novel therapy procedures have now been established in clinical practice, several important issues still need to be resolved in order to treat cancer efficiently and to reduce many drawbacks created by traditional therapies. Nanomedicine appeared as an up-

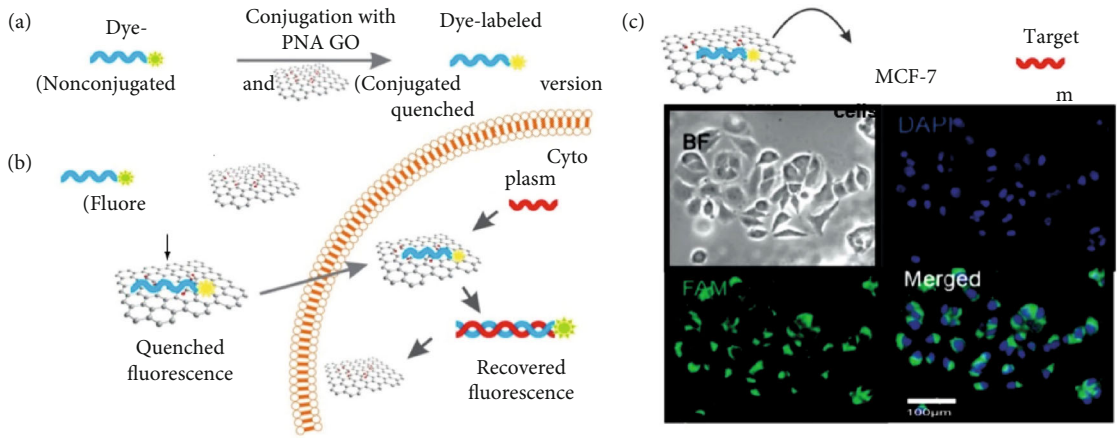


Figure 15: Nanotechnology focused on graphene used to identify miRNAs. (a) The dye-labeled PNA becomes fluorescent when nonconjugated; however, fluorescence becomes quenched after contact with GO. (b) Nanoparticle graphene oxide technique for intracellular miRNA identification has been used as a fluorescence quencher for the identification and tracking of dye-labeled nucleic acid probes in living cells by miRNA multiplex in vitro. Dye-labeled PNA fluorescence is quenched when interacting with GO, and further hybridization of the PNA with the target miRNA has helped activate the GO surface PNA sample and recovery of fluorescence. The ability of the PNA-GO probe to enter cells and the minimization of nonspecific fluorescence signal allows sensitive monitoring of multiple miRNA targets even in living cells with low basal fluorescence. (c) GO-sample fluorescent microscopy of MCF-7 cancer cells for quantitative miR-21 detection. MCF-7 cells had substantial fluorescence due to the strong expression of miR-21. GO: graphene oxide; PNA: peptide nucleic acid [118].

and-coming method to promote both early detection and successful tumor therapy. A plethora of various inorganic and organic multifunctional nanomaterials was ad hoc developed to satisfy the increasing need for new cancer treatment solutions [90] As shown in Figure 11, a wide variety of nanomaterials were produced using organic, inorganic, lipid, and protein compounds usually within 1–100 nm varieties and delivering various antitumor drugs by fine-tuning the chemical structure, size, and form (morphology) capable of regulating nanomaterial functionality.

*2.4. 3D Self-Assembled Peptide Hydrogels in Cancer Therapy.* Peptide hydrogels are leading carriers in many medical applications because of their exceptional structural and behavioral properties [92]. Numerous self-assembled peptides have been developed which have the potential to be an antitumor drug delivery nanocarriers. Figure 12 shows the peptides that are self-assembled into hydrogels.

By self-assembling its molecules, the peptide produces structures identical to nanotubes. With adequate mechanical power, stability, and biocompatibility, the microscale length of these nanotubes is calculated. It was also found that its thermal and chemical properties were within the appropriate range [94]. Self-assembled hydrogels based on peptides have significant effects in stabilizing and regulating the release of anticancer drugs. Some examples of self-assembled peptide-based hydrogels in tumor cells were receptive to microenvironmental conditions [95]. Mao et al. first advanced a drug delivery device focused on a self-assembled peptide hydrogel. The study group integrated two chemotherapeutic drugs and reported a significant increase in medication safety, as seen in Figure 13 [96]. The device showed a controlled release of medicinal products through hydrolysis of the ester bond, thus demonstrating the potential for targeted antitumor delivery. Due to their lower cost and tunable properties, small peptide hydrogels are reported to be more beneficial for the delivery of drugs [97].

*2.5. Graphene Oxide for Cancer Therapy.* Previous research has shown that GO can be used to monitor targeted cancer, to stop tumor growth, and to prevent tumor cell movement [2, 98, 99]. Phototherapy focused on transdermal nanographene oxide-hyaluronic acid (NGO-HA) conjugates recorded for skin cancer melanoma using a near-infrared (NIR) laser in 2014; however, studies which used GO in CSC therapy for cancer treatment are uncommon. Fiorillo et al. have shown that GO prevents tumors from growing in six separate lines of cancer cells (prostate, pancreatic, breast, vaginal, lung, and brain cancer) through different types of tumors. They used the tumorsphere method to evaluate GO-targeted therapy and clinically measured the production and extension of tumorspheres from individual CSCs under conditions independent of anchorage. The results suggested that GO specifically targets a phenotypic worldwide property of CSCs, which may decrease the amount of bonafide CSCs by splitting which inhibiting them (Figure 14(a)) [100, 101]. The author here, in a nutshell, presents evidence that GO-based therapy may be successful in reducing CSCs by inhibiting several main signal pathways and then splitting CSCs.

*2.6. Carbon Nanotubes in Cancer Therapy.* Carbon nanotubes are nanostructures of cylindrical graphene with advanced nanotechnologies and clinical research, for example, water solubility, cell membrane penetration, strong drug load performance, photothermal, low toxicity, tumor selectivity, photoacoustic, and radiant properties [105, 106].

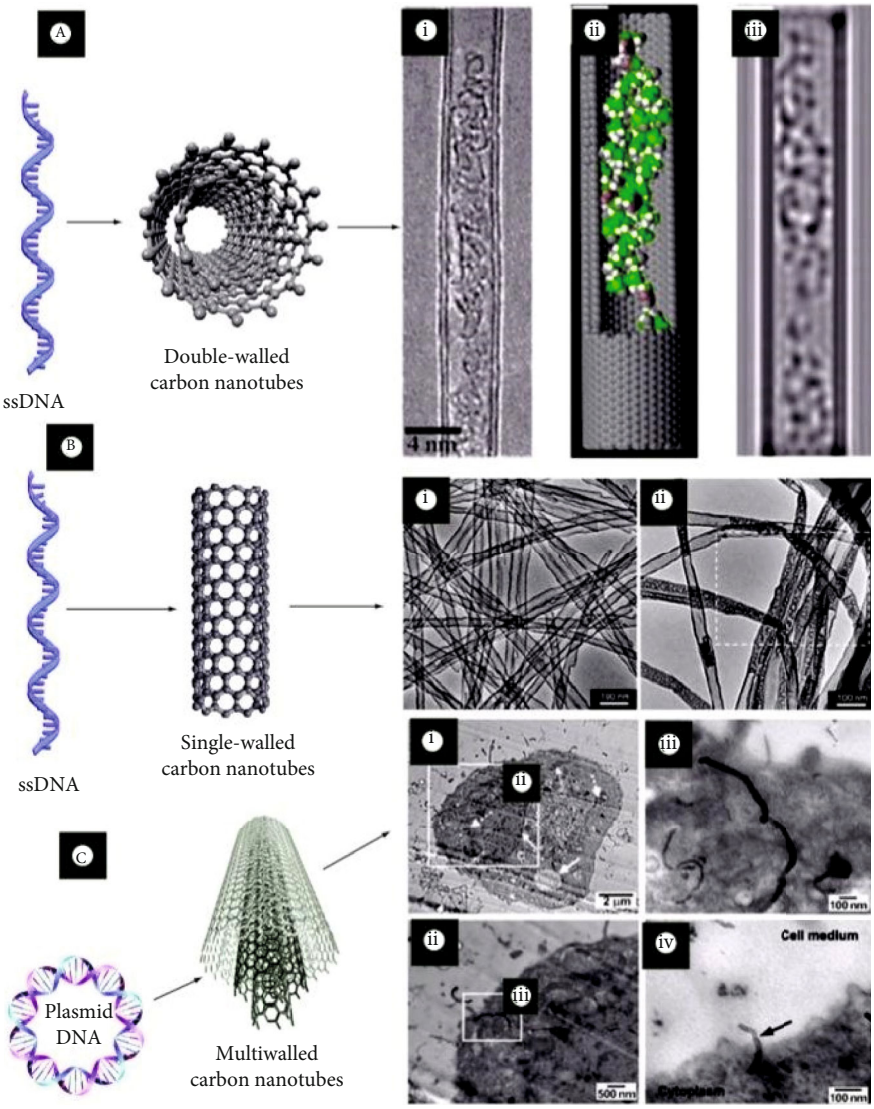


Figure 16: DNA encapsulation and gene transition. (a) Double-walled nanotubes of carbon, which encapsulate ssDNA. (i) A transmission image of ssDNA molecules composed of 30-base cytosine homopolymers (defined as C30) encapsulated double-walled carbon nanotubes by an electron microscope (TEM). (ii) Layout TEM image structure and (iii) simulation of TEM image. (b) A single-walled carbon nanotube encapsulated with ssDNA. TEM photographs, after soaking, of a solution ssDNA (i) without $CaCl_2$ and (ii) $CaCl_2$ (DNA-$CaCl_2$). The ssDNA internalization happened at (iii). (c) Multiwalled carbon nanotubes which are used for strong plasmid DNA encapsulation. The cells in HeLa were treated with DNA-multiwalled carbon plasmid nanotubes during the encapsulation process. Box magnifications for each cell are given (ii and iii). (iv) A multiwalled carbon nanotube which separates the cell membrane. White dotted arrow: chromatin; white dotted arrow: mitochondria; white dotted arrow: atomic membrane; white arrow: vacuole. To: ssDNA [118].

Burke et al., in 2012, mentioned that breast cancer stem cells (BCSCs) were found to be immune to thermal carbon nanotube therapy and loss of proliferative capacity after thermal nanotube therapy [107]. Thus, nanotube-assisted thermal therapy will destroy all the isolated cells that form the bulk of a tumor simultaneously. In 2014, Yao et al. developed a gastric CSC-specific drug delivery system (SAL-SWNT-CHI-HA complexes) centered on single-wall chitosan-coated carbon nanotubes (SWChNTs) packed with the hyaluronic acid (HA) and salinomycin (SAL) structure. The designed system can extract gastric CSCs selectively (Figure 14(b)) [108]. Al Faraj et al. suggested a technique utilizing biocompatible multimodal SWCNTs that were functionalized with CD44 antibodies and enhanced direct anti-CD44 targeting, resulting in promising breast targeting findings for CSCs and potential for further clinical trials [103]. Shortly afterward, the same community combined paclitaxel and salinomycin drugs in the murine xenograft model combined SWCNTs (Figure 14(c)) similarly to fight breast cancer and CSCs simultaneously, and the results revealed an increased therapeutic effect of combination therapy compared to care for independent nanocarriers or free suspension of medication. Consequently, the optimized drug delivery mechanism for conjugated SWCNTs has enormous potential to effectively treat breast cancer by attacking both CSCs and cancer cells [103].

Table 3: Graphene-based nanocarriers used for gene delivery.

| Graphene-based nanomaterial | Gene | Target cell in the study | Ref. |
|---|---|---|---|
| Graphene oxide low-molecular-weight branched polyethyleneimine | Luciferase reporter gene | HeLa and PC-3 cell lines | [116] |
| Graphene-polyethyleneimine (25 kDa) | EGFP | HeLa cells | [123] |
| Graphene oxide-chitosan | Luciferase reporter gene | HeLa cells | [129] |
| Grafted ultrasmall graphene oxide-polyethyleneimine | EGFP | H293T and U2Os cell lines | [124] |
| Graphene-polyethyleneimine (25 kDa) | Luciferase reporter gene | HeLa cells | [123] |
| Graphene oxide-gold nanorods-polyethyleneimine | EGFP and luciferase reporter gene | HeLa cells | [125] |
| Graphene oxide-gold nanoparticles-polyethyleneimine | EGFP and luciferase reporter gene | HeLa cells | [125] |
| Reduced graphene oxide PEG low-molecular-weight branched polyethyleneimine | Luciferase reporter gene | PC-3 and NIH/3T3 cell lines | [128] |

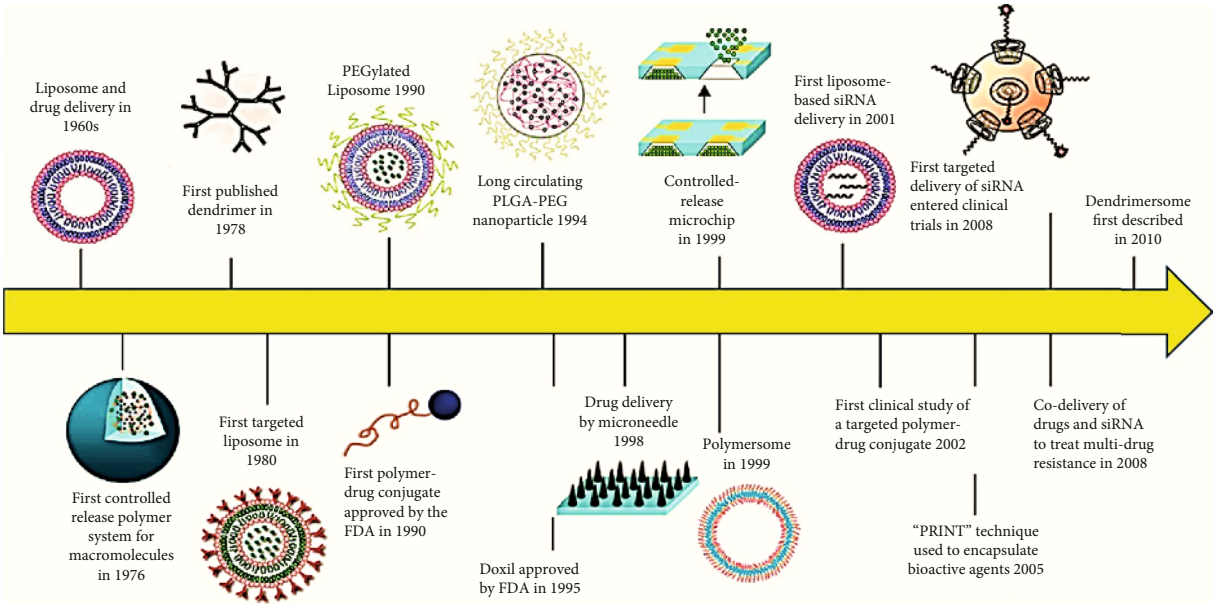


Figure 17: Delivery of nanotechnology-based drugs in the timeline. Here, we highlight those delivery systems which serve as essential milestones in drug delivery history [131].

*2.7. Nanodiamonds in Cancer Therapy.* Nanodiamonds are carbon semioctahedral systems with a wide variety of biological and chemical elements, as well as small molecules, genetic content, biomolecules, and imaging agents [109]. Nanodiamonds (NDs) have shown excellent delivery capacity and excellent biocompatibility among a wide range of vehicles based on nanomaterials [110]. Zhao et al. showed that detonation of nanodiamond with hyperbranched polyglycerol (dND-PG) coating charged with an anticancer drug and conducted by an active targeting moiety might lead to tumor cells becoming highly preferential toxic via different absorption mechanisms while minimizing macrophage absorption and toxicity [111]. The nanodiamond drug complex, also developed by physical adsorption of epirubicin on nanodiamonds, has proven to be a highly successful nanomedicine-based solution for overcoming chemoresistance in hepatic CSC. As shown in Figure 14(d), the resultant EPND complex, Epirubicin@nanodiamonds, has improved care over unmodified epirubicin [104] The probability of binding different bioactive molecules to carbon molecules such as cell-specific ligands makes carbon-dependent nanomaterials an important option for cancer therapy through targeting CSCs.

*2.7.1. 3D Self-Assembled Nanostructures for Gene Delivery.* Despite recent advancements in multiple nucleotide-based therapies, the efficacy of gene therapy in clinical procedures remains limited due to less efficient delivery routes to the targeted tissue or cells [112]. Nanotechnology has rendered a significant advance in the production of healthy and efficient gene carriers in recent decades [113]. Nonviral gene delivery carriers can be made from several materials, including

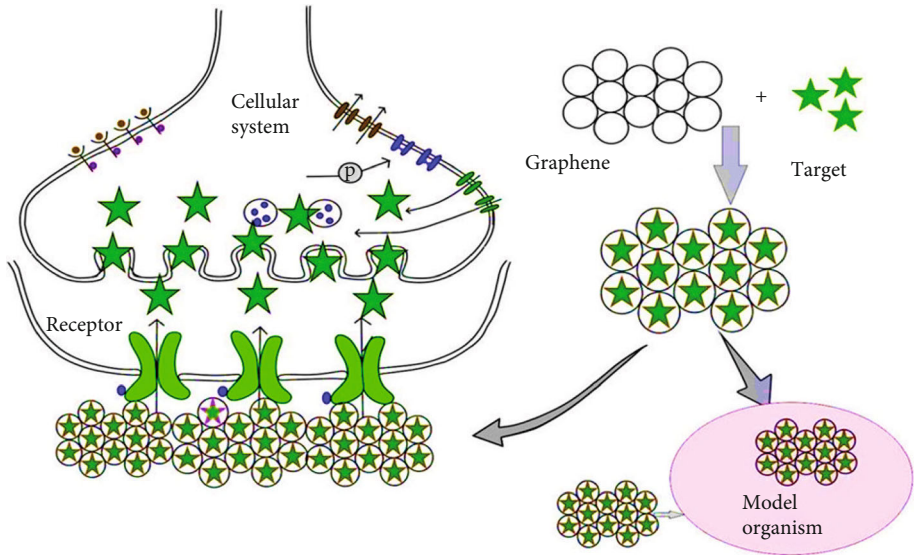


Figure 18: Graphene as target carrier (gene or small molecular drug) [134].

inorganic nanoparticles, carbon nanotubes, liposomes, protein-based nanoparticles, and peptides, as well as nanoscale polymeric materials, and have gained popularity in recent years due to their protection, versatility in nucleic acid packaging, and ease of processing. Significant attempts were made to increase the efficiency of nonviral gene transmission by fair and semirational design as an ideal gene carrier that should have many functions to resolve the obstacles in the gene transfection process at different levels.

*2.7.2. Gene Delivery with Graphene-Based Nanomaterials.* Graphene and its derivatives have been increasingly used in many biomedical fields as sheet-like carbonic nanomaterials [114, 115]. Graphene-based platform applications currently apply to the distribution of genes as a nanocarrier. Provided the unique structure and chemistry of graphite nanoparticles, they have a high potential for gene processing. Biostability, cellular uptake, and improved efficiency of gene processing, graphene surfaces, and their derivatives have been adjusted with various polymers or ligands to boost biocompatibility [114, 116]. Graphene-based nanosheets with a vast hybridized sp2 carbon region may interact with further molecules, including DNA and RNA nucleic acids, as well as with drugs. They may also be used as moving genes or as protectors and carriers of specimens involved in miRNA detection (Figures 15 and 16) [117].

DNA can also interact with nanomaterials based on graphenes [119]. Low pH and strong ionic resistance DNA adsorption can be built with tiny fragments [120], in which they are covered sterically from nuclease (DNase) attacks [121]. One of the advantages of preserving DNA is that a robust gene transfer vector will thus be proficient in successful cellular uptake. Graphene is, therefore, an exciting option for plasmid transmission, uniquely when it is functionalized with cationic polyethyleneimine that interacts well with DNA phosphate groupings [119]. Kim et al. combined low-molecular-weight polyethylenimine branched to GO to provide the cytomegalovirus promoter with a plasmid that controls luciferase gene expression [116]. Feng and Liu initially delivered a plasmid to HeLa cells carrying the enhanced green fluorescent protein (EGFP) encoding gene, using a different nanocarrier [122]. Chen et al. used a higher-molecular-weight polyethyleneimine [123] in which cytotoxicity to polyethyleneimine decreased with GO presence. In the presence of 10% fetal bovine serum (FBS), they also transmitted the luciferase reporter gene to HeLa cells using this gene delivery mechanism. They demonstrated that the transfection efficiency of serum proteins did not decrease [108]. Zhou and his colleagues recently transferred ultrasmall GO plasmid DNA (pEGFP) to mammalian cell lines and zebrafish embryos [124]. By contrast, Xu et al. encapsulated inorganic nanoparticles and gold nanorods in GO nanosheets that not only decreased cytotoxicity dramatically, allowing polyethyleneimine to work better, yet also achieved high transfection efficiency and improved viability of HeLa cells [125]. Although polyethyleneimine is not the only gene transmission component that can be added to the nanomaterials based on graphene, in this experiment, Bao et al. used a chitosan-like GO (a nanosystem frequently administered to HeLa cells for A plasmid containing the luciferase gene) and demonstrated that this complex could condense DNA for rapid cell absorption through agarose gel electrophoresis [126]. Additionally, the use of PEG and polyethylenimine, for example, to improve the efficiency of plasmid DNA transfection, can also be performed in GO. This gene carrier was also found to be light-responsive, as described by Feng et al. [127]. Another example of an environmentally sensitive nanosystem is Kim et al.'s photothermally regulated gene delivery carrier, which integrates branched low-molecular-weight polyethylenimine and reduced GO through PEG. The increased efficacy of the gene transfection of this nanocarrier was due to a rapid endosomal escape through locally mediated heat [128]. Table 3 reviews several of the graphene-based nanocarriers used for the gene delivery.

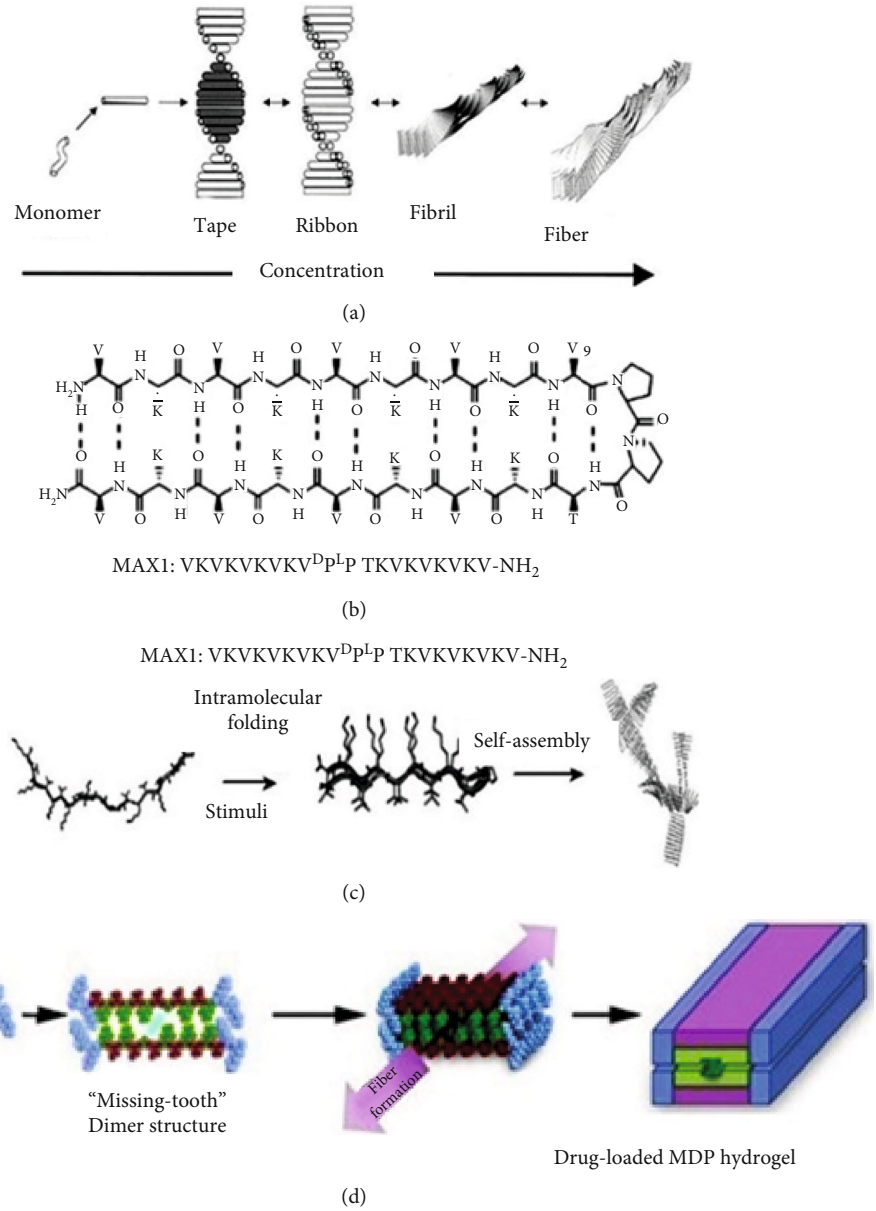


Figure 19: (a) Hierarchical model of self-assembly, from monomer to fiber. (b) MAX1 and (c) $\beta$-hairpin sequence intramolecular random-coil folding of the MAX1 peptide followed by self-assembly. (d) The MDP assembly named "broken tooth" exposes the vacuum produced during fiber packaging. MDP: multidomain peptides [143].

## 3. 3D Self-Assembled Nanostructures for Small Molecule Drug Delivery

Small molecules are amongst the most vital biological function molecules found in most medicines to date. Many organic molecules exhibit low solubility in aqueous media and insufficient delivery of products as the primary cause of around 40 percent of all medication failures. While high-profile strategies continue to improve a variety of chemical agents for the treatment of complicated disease processes, there is an increasing need for suitable methods of molecular delivery to be established, which are useful and practical. Precise spatiotemporal regulation of a large variety of hydrophobic and neutral small molecules is therefore essential. Recent developments in nanotechnology have introduced smart and new therapeutic nanomaterials using various targeted approaches [130]. The application of nanotechnology in medicine and, more specifically, the drug market is expected to expand even more than it has over the last two decades. As delivery vehicles, a range of organic/inorganic nanomaterials and technologies were used to develop effective therapeutic methods (Figure 17) [131].

*3.1. Graphene and Graphene Oxide as Nanomaterials for Small Molecule Drug Delivery.* Mechanisms of drug delivery utilizing graphene-dependent nanosources have been researched since 2008 [132, 133]. Proteolytic enzyme development within the cytoplasm often interferes with the drug delivery process. GO is used to provide the carrier genes and medicines with efficacy (Figure 18). The GO biological

community (COOH and OH) allows for the mixing of numerous polymers and biomolecules (DNA, ligand, and protein) [134]. Methods contain its cationic polymer functionality, like PEI [24]. It is known as a nonviral gene vector, as it intensively communicates with negatively charged DNA and RNA phosphate ions [24]. Its varieties of transfection are simple and effective boost cell selectivity and decrease cell toxicity. The use of PEI-functional GO transmission of the Bcl-2-target antiapoptotic family protein siRNA and anticancer drug DOX exhibited a synergistic impact providing enhanced transfection ability with reduced PEI cytotoxicity and enhanced anticancer effectiveness [135]. Also established was a photochemically regulated gene delivery carrier in which low-molecular-weight PEI and rGO were combined with hydrophilic polyethylene glycol (PEG) and plasmid DNA and physiochemical assays were found to be stable [136]. FeO nanoparticles offer multifunctional and multimodal GO for broad organic and medicinal applications [128]. The delivery of anti-inflammatory ibuprofen drugs utilizing chitosan-containing GOs has been reported [137].

Graphene's unmodified basal plane sites with free surface $\pi$ electrons are hydrophobic and can create interactions for charging drugs and covalent modifications [123]. Part of drug delivery is due to differences in the concentration of temperature, pH, light, and salt. Polymers sense the fundamental changes, and the medication is released. GO biopolymers are pH sensitive and are, therefore, often used as smart transporters for the delivery of drugs [138]. In this respect, the use of folic acid containing of nano-GO (NGO) called FA–NGO for the treatment of tumors has conclusively demonstrated pH-sensitive delivery in the case of DOX and camptothecin [139]. Ibuprofen and 5-fluorouracil anti-inflammatory drugs with distinctive hydrophilicity were also administered utilizing a pH-dependent CS–GO complex [140]. GO is being modified to carry a carrier of water-soluble cancer drugs. The functionalized PEG NGO can allow more soluble physiological and aqueous solutions [141].

*3.2. Self-Assembled Peptide and Protein Nanofibers for Small Molecule Drug Delivery.* Hydrogels offer a commonly employed and efficient tool for the distribution of small molecule medications and biological therapies self-assembly as shown in Figure 19 (e.g., proteins and DNA), as their physical and chemical properties may be adjusted to suit the release profile of the encapsulated cargo and are treated under moderate conditions conducive to cargo survival [142].

Soil-based hydrogels can be used for the delivery of small medicinal molecules. For instance, hydrogels that consist either of a high-molecular-mass silk protein (SPH) or an SPH composite and a low-molecular-mass silk protein (SPL) release the drug buprenorphine at concentration-related SPH levels [144]. This concentration of SPH was hypothesized as leading to a denser network of nanofiber and, in turn, a more tortuous route through which buprenorphine moves to avoid the hydrogel. This was also confirmed by SPH/SPL composite hydrogels, where 10% SPH with 6% SPL had a higher diffusion rate than 10% SPH with 2% SPL, respectively. RADA16 gels, for example, published small-molecule encapsulated colors such as phenol red, bromophenol blue, 3-PSA, 4-PSA, and Coomassie Brilliant Brown G-250 (CBBG) at levels associated with chemical coloring [145]. In particular, after seven days, bromophenol blue and CBBG did not elute out of the gels, indicating that they had not adsorbed nanofibers directly into RADA16. Besides, 3-PSA has eluted the more electrostatically charged 4-PSA at a faster pace, indicating the net charge of the drugs that affect their release kinetics. The diffusivity of red, 3-PSA, and 4-PSA phenols decreased as the RADA16 concentration increased similarly to the SPH/SPL gels mentioned above.

## 4. Conclusion and Future Perspectives

This research summarized the application of 3D self-assembled polyfunctional nanostructures such as carbon nanotubes (CNTs), graphene fullerene, and peptide hydrogels that are used successfully in tissue engineering, gene delivery, and cancer therapy. Some nanocarbon allotropes, such as GO, CNTs, fullerenes, CDs, NDs, and their derivatives, have high potential as bone cell proliferation scaffolds and can be used to rebuild bones. Also, nanotube-assisted thermal therapy can kill all of the specialized cells that form the bulk of a tumor simultaneously. Because of their nanoscale size, photoluminescence properties, large specific surface area, and antibacterial activity, graphene family materials possess significant potential for bone tissue engineering, drug/gene delivery, and cancer treatment.

Self-assembly of nanostructural materials is theoretically valuable and has produced new resources to revolutionize the biological and biomedical sciences. In this study, application of 3D self-assembled nanostructures such as carbon nanotubes (CNTs), graphene and fullerene, peptide hydrogels for use in tissue engineering, gene delivery, and cancer therapy has been summarized. Besides, they have applications in drug delivery, vaccine delivery, and photothermal therapy. Therefore, their application can be examined in these cases as well. Also, there are other categories of 3D self-assembled nanostructures that have exciting applications in medicine, which are essential and practical to study.

## Conflicts of Interest

The authors declare that they have no conflicts of interest.

## References

[1] Y. Khadijeh, D. Habib, and K. Alireza, "Optimization of physical and mechanical properties of calcium silicate nanocomposite by Taguchi method," *Journal of New Materials*, vol. 10, no. 39, pp. 77–90, 2020.

[2] S. M. Mousavi, S. A. Hashemi, Y. Ghasemi, A. M. Amani, A. Babapoor, and O. Arjmand, "Applications of graphene oxide in case of nanomedicines and nanocarriers for biomolecules: review study," *Drug Metabolism Reviews*, vol. 51, no. 1, pp. 12–41, 2019.

[3] G. M. Whitesides, "Self-assembling materials," *Scientific American*, vol. 273, no. 3, pp. 146–149, 1995.

[4] J. H. Fendler, "Self-assembled nanostructured materials," *Chemistry of Materials*, vol. 8, no. 8, pp. 1616–1624, 1996.

[5] A. Klinkova, R. M. Choueiri, and E. Kumacheva, "Self-assembled plasmonic nanostructures," *Chemical Society Reviews*, vol. 43, no. 11, pp. 3976–3991, 2014.

[6] J. Y. Cheng, A. M. Mayes, and C. A. Ross, "Nanostructure engineering by templated self-assembly of block copolymers," *Nature Materials*, vol. 3, no. 11, pp. 823–828, 2004.

[7] D. Lombardo, P. Calandra, L. Pasqua, and S. Magazù, "Self-assembly of organic nanomaterials and biomaterials: the bottom-up approach for functional nanostructures formation and advanced applications," *Materials*, vol. 13, no. 5, p. 1048, 2020.

[8] A. Joshi, N. Singh, and G. Verma, "Preparation and applications of self-assembled natural and synthetic nanostructures," in *Fabrication and Self-Assembly of Nanobiomaterials*, pp. 29–55, Elsevier, 2016.

[9] M. Lazzari, C. Rodríguez-Abreu, J. Rivas, and M. A. López-Quintela, "Self-assembly: a minimalist route to the fabrication of nanomaterials," *Journal of Nanoscience and Nanotechnology*, vol. 6, no. 4, pp. 892–905, 2006.

[10] D. Lombardo, M. A. Kiselev, and M. T. Caccamo, "Smart nanoparticles for drug delivery application: development of versatile nanocarrier platforms in biotechnology and nanomedicine," *Journal of Nanomaterials*, vol. 2019, 26 pages, 2019.

[11] K. Yousefi, H. D. Manesh, A. R. Khalifeh, F. Moazami, and M. R. Sanaee, "Nanocement/poly (vinyl alcohol) composites for endodontic applications," *Materials Chemistry and Physics*, vol. 254, article 123337, 2020.

[12] Y. Wan and D. Zhao, "On the controllable soft-templating approach to mesoporous silicates," *Chemical Reviews*, vol. 107, no. 7, pp. 2821–2860, 2007.

[13] T. Xu, Y. Ding, Z. Liang et al., "Three-dimensional monolithic porous structures assembled from fragmented electrospun nanofiber mats/membranes: methods, properties, and applications," *Progress in Materials Science*, vol. 112, article 100656, 2020.

[14] Y. Bai, Q. Luo, and J. Liu, "Protein self-assembly via supramolecular strategies," *Chemical Society Reviews*, vol. 45, no. 10, pp. 2756–2767, 2016.

[15] T. O. Mason and U. Shimanovich, "Fibrous protein self-assembly in biomimetic materials," *Advanced Materials*, vol. 30, no. 41, article 1706462, 2018.

[16] G. Liao, F. He, Q. Li et al., "Emerging graphitic carbon nitride-based materials for biomedical applications," *Progress in Materials Science*, vol. 112, article 100666, 2020.

[17] A. M. Amani, S. A. Hashemi, S. M. Mousavi, H. Pouya, and V. Arash, "Electric field induced alignment of carbon nanotubes: methodology and outcomes," in *Carbon Nanotubes-Recent Progress*, IntechOpen, 2018.

[18] H. Yi, H. Song, and X. Chen, "Carbon nanotube capsules self-assembled by W/O emulsion technique," *Langmuir*, vol. 23, no. 6, pp. 3199–3204, 2007.

[19] J. J. Mulvey, C. H. Villa, M. R. McDevitt, F. E. Escorcia, E. Casey, and D. A. Scheinberg, "Self-assembly of carbon nanotubes and antibodies on tumours for targeted amplified delivery," *Nature Nanotechnology*, vol. 8, no. 10, pp. 763–771, 2013.

[20] L. Zhao, H. Li, and L. Tan, "A novel fullerene-based drug delivery system delivering doxorubicin for potential lung cancer therapy," *Journal of Nanoscience and Nanotechnology*, vol. 17, no. 8, pp. 5147–5154, 2017.

[21] C. H. Hung, W. W. Chang, S. C. Liu et al., "Self-aggregation of amphiphilic [60] fullerenyl focal point functionalized PAMAM dendrons into pseudodendrimers: DNA binding involving dendriplex formation," *Journal of Biomedical Materials Research Part A*, vol. 103, no. 5, pp. 1595–1604, 2014.

[22] S. M. Mousavi, S. Soroshnia, S. A. Hashemi et al., "Graphene nano-ribbon based high potential and efficiency for DNA, cancer therapy and drug delivery applications," *Drug Metabolism Reviews*, vol. 51, no. 1, pp. 91–104, 2019.

[23] S. M. Mousavi, F. W. Low, S. A. Hashemi et al., "Development of hydrophobic reduced graphene oxide as a new efficient approach for photochemotherapy," *RSC Advances*, vol. 10, no. 22, pp. 12851–12863, 2020.

[24] S. Goenka, V. Sant, and S. Sant, "Graphene-based nanomaterials for drug delivery and tissue engineering," *Journal of Controlled Release*, vol. 173, pp. 75–88, 2014.

[25] A. C. Ferrari, F. Bonaccorso, V. Fal'ko et al., "Science and technology roadmap for graphene, related two-dimensional crystals, and hybrid systems," *Nanoscale*, vol. 7, no. 11, pp. 4598–4810, 2015.

[26] S. Mousavi, A. Aghili, S. A. Hashemi, N. Goudarzian, Z. Bakhoda, and S. Baseri, "Improved morphology and properties of nanocomposites, linear low density polyethylene, ethylene-co-vinyl acetate and nano clay particles by electron beam," *Polymers from Renewable Resources*, vol. 7, no. 4, pp. 135–153, 2018.

[27] S. Zhang, "Fabrication of novel biomaterials through molecular self-assembly," *Nature Biotechnology*, vol. 21, no. 10, pp. 1171–1178, 2003.

[28] C. Gröger, K. Lutz, and E. Brunner, "Biomolecular self-assembly and its relevance in silica biomineralization," *Cell Biochemistry and Biophysics*, vol. 50, no. 1, pp. 23–39, 2008.

[29] S. Zhang, D. M. Marini, W. Hwang, and S. Santoso, "Design of nanostructured biological materials through self-assembly of peptides and proteins," *Current Opinion in Chemical Biology*, vol. 6, no. 6, pp. 865–871, 2002.

[30] L. Yang, A. Liu, S. Cao, R. M. Putri, P. Jonkheijm, and J. J. L. M. Cornelissen, "Self-assembly of proteins: towards supramolecular materials," *Chemistry–A European Journal*, vol. 22, no. 44, pp. 15570–15582, 2016.

[31] I. Willner and B. Willner, "Biomolecule-based nanomaterials and nanostructures," *Nano Letters*, vol. 10, no. 10, pp. 3805–3815, 2010.

[32] E. Lavik and R. Langer, "Tissue engineering: current state and perspectives," *Applied Microbiology and Biotechnology*, vol. 65, no. 1, pp. 1–8, 2004.

[33] R. M. Nerem and A. Sambanis, "Tissue engineering: from biology to biological substitutes," *Tissue Engineering*, vol. 1, no. 1, pp. 3–13, 1995.

[34] U. G. Wegst, H. Bai, E. Saiz, A. P. Tomsia, and R. O. Ritchie, "Bioinspired structural materials," *Nature Materials*, vol. 14, no. 1, pp. 23–36, 2015.

[35] C. Leterrier, J. Potier, G. Caillol, C. Debarnot, F. Rueda Boroni, and B. Dargent, "Nanoscale architecture of the axon initial segment reveals an organized and robust scaffold," *Cell Reports*, vol. 13, no. 12, pp. 2781–2793, 2015.

[36] G. Nourissat, F. Berenbaum, and D. Duprez, "Tendon injury: from biology to tendon repair," *Nature Reviews Rheumatology*, vol. 11, no. 4, pp. 223–233, 2015.

[37] J. D. Hartgerink, E. Beniash, and S. I. Stupp, "Self-assembly and mineralization of peptide-amphiphile nanofibers," *Science*, vol. 294, no. 5547, pp. 1684–1688, 2001.

[38] I. Hamley, "Self-assembly of amphiphilic peptides," *Soft Matter*, vol. 7, no. 9, pp. 4122–4138, 2011.

[39] S. Zhang, C. Lockshin, A. Herbert, E. Winter, and A. Rich, "Zuotin, a putative Z-DNA binding protein in Saccharomyces cerevisiae," *The EMBO Journal*, vol. 11, no. 10, pp. 3787–3796, 1992.

[40] J. Liu, H. Song, L. Zhang, H. Xu, and X. Zhao, "Self-assembly-peptide hydrogels as tissue-engineering scaffolds for three-dimensional culture of chondrocytes in vitro," *Macromolecular Bioscience*, vol. 10, no. 10, pp. 1164–1170, 2010.

[41] T. C. Holmes, "Novel peptide-based biomaterial scaffolds for tissue engineering," *Trends in Biotechnology*, vol. 20, no. 1, pp. 16–21, 2002.

[42] T. Umeyama and H. Imahori, "Photofunctional hybrid nanocarbon materials," *The Journal of Physical Chemistry C*, vol. 117, no. 7, pp. 3195–3209, 2013.

[43] S. I. Stupp, "Self-assembly and biomaterials," *Nano Letters*, vol. 10, no. 12, pp. 4783–4786, 2010.

[44] J. D. Hartgerink, E. Beniash, and S. I. Stupp, "Peptide-amphiphile nanofibers: a versatile scaffold for the preparation of self-assembling materials," *Proceedings of the National Academy of Sciences*, vol. 99, no. 8, pp. 5133–5138, 2002.

[45] R. Eivazzadeh-Keihan, A. Maleki, M. de la Guardia et al., "Carbon based nanomaterials for tissue engineering of bone: building new bone on small black scaffolds: a review," *Journal of Advanced Research*, vol. 18, pp. 185–201, 2019.

[46] R. Geetha Bai, N. Ninan, K. Muthoosamy, and S. Manickam, "Graphene: a versatile platform for nanotheranostics and tissue engineering," *Progress in Materials Science*, vol. 91, pp. 24–69, 2018.

[47] S. M. Mousavi, S. A. Hashemi, M. Arjmand, A. M. Amani, F. Sharif, and S. Jahandideh, "Octadecyl amine functionalized graphene oxide towards hydrophobic chemical resistant epoxy nanocomposites," *ChemistrySelect*, vol. 3, no. 25, pp. 7200–7207, 2018.

[48] W. Shao, J. He, F. Sang et al., "Enhanced bone formation in electrospun poly (l-lactic-co-glycolic acid)–tussah silk fibroin ultrafine nanofiber scaffolds incorporated with graphene oxide," *Materials Science and Engineering: C*, vol. 62, pp. 823–834, 2016.

[49] J. H. Lee, Y. C. Shin, S. M. Lee et al., "Enhanced osteogenesis by reduced graphene oxide/hydroxyapatite nanocomposites," *Scientific Reports*, vol. 5, no. 1, article BFsrep18833, pp. 1–13, 2015.

[50] A. Rajan Unnithan, A. Ramachandra Kurup Sasikala, C. H. Park, and C. S. Kim, "A unique scaffold for bone tissue engineering: an osteogenic combination of graphene oxide–hyaluronic acid–chitosan with simvastatin," *Journal of Industrial and Engineering Chemistry*, vol. 46, pp. 182–191, 2017.

[51] Y. Luo, H. Shen, Y. Fang et al., "Enhanced proliferation and osteogenic differentiation of mesenchymal stem cells on graphene oxide-incorporated electrospun poly (lactic-co-glycolic acid) nanofibrous mats," *ACS Applied Materials & Interfaces*, vol. 7, no. 11, pp. 6331–6339, 2015.

[52] F. Song, W. Jie, T. Zhang et al., "Room-temperature fabrication of a three-dimensional reduced-graphene oxide/polypyrrole/hydroxyapatite composite scaffold for bone tissue engineering," *RSC Advances*, vol. 6, no. 95, pp. 92804–92812, 2016.

[53] C.-Y. Liu and F.-C. Lin, "Geometric effect on photonic nanojet generated by dielectric microcylinders with non-cylindrical cross-sections," *Optics Communications*, vol. 380, pp. 287–296, 2016.

[54] Q. Zhou, P. Yang, X. Li, H. Liu, and S. Ge, "Bioactivity of periodontal ligament stem cells on sodium titanate coated with graphene oxide," *Scientific Reports*, vol. 6, no. 1, article 19343, 2016.

[55] C. Xie, X. Lu, L. Han et al., "Biomimetic mineralized hierarchical graphene oxide/chitosan scaffolds with adsorbability for immobilization of nanoparticles for biomedical applications," *ACS Applied Materials & Interfaces*, vol. 8, no. 3, pp. 1707–1717, 2016.

[56] M. Omidi, A. Yadegari, and L. Tayebi, "Wound dressing application of pH-sensitive carbon dots/chitosan hydrogel," *RSC Advances*, vol. 7, no. 18, pp. 10638–10649, 2017.

[57] J. Qiu, D. Li, X. Mou et al., "Effects of graphene quantum dots on the self-renewal and differentiation of mesenchymal stem cells," *Advanced Healthcare Materials*, vol. 5, no. 6, pp. 702–710, 2016.

[58] R. Geetha Bai, K. Muthoosamy, S. Manickam, and A. Hilal-Alnaqbi, "Graphene-based 3D scaffolds in tissue engineering: fabrication, applications, and future scope in liver tissue engineering," *International Journal of Nanomedicine*, vol. 14, pp. 5753–5783, 2019.

[59] S. Smart, A. I. Cassady, G. Q. Lu, and D. J. Martin, "The biocompatibility of carbon nanotubes," *Carbon*, vol. 44, no. 6, pp. 1034–1047, 2006.

[60] R. L. Price, M. C. Waid, K. M. Haberstroh, and T. J. Webster, "Selective bone cell adhesion on formulations containing carbon nanofibers," *Biomaterials*, vol. 24, no. 11, pp. 1877–1887, 2003.

[61] B. Sitharaman, X. Shi, X. F. Walboomers et al., "In vivo biocompatibility of ultra-short single-walled carbon nanotube/-biodegradable polymer nanocomposites for bone tissue engineering," *Bone*, vol. 43, no. 2, pp. 362–370, 2008.

[62] E. Hirata, M. Uo, Y. Nodasaka et al., "3D collagen scaffolds coated with multiwalled carbon nanotubes: initial cell attachment to internal surface," *Journal of Biomedical Materials Research Part B: Applied Biomaterials*, vol. 93B, no. 2, pp. 544–550, 2010.

[63] S. Park, J. Park, I. Jo et al., "In situ hybridization of carbon nanotubes with bacterial cellulose for three-dimensional hybrid bioscaffolds," *Biomaterials*, vol. 58, pp. 93–102, 2015.

[64] H. Li, Q. Zhao, B. Li et al., "Fabrication and properties of carbon nanotube-reinforced hydroxyapatite composites by a double in situ synthesis process," *Carbon*, vol. 101, pp. 159–167, 2016.

[65] P. Khalid, M. A. Hussain, P. D. Rekha, and A. B. Arun, "Carbon nanotube-reinforced hydroxyapatite composite and their interaction with human osteoblast in vitro," *Human & Experimental Toxicology*, vol. 34, no. 5, pp. 548–556, 2015.

[66] C. Shuai, S. Peng, P. Wu et al., "A nano-sandwich construct built with graphene nanosheets and carbon nanotubes enhances mechanical properties of hydroxyapatite–polyetheretherketone scaffolds," *International Journal of Nanomedicine*, vol. 11, pp. 3487–3500, 2016.

[67] T. Kaur and A. Thirugnanam, "Tailoring in vitro biological and mechanical properties of polyvinyl alcohol reinforced

with threshold carbon nanotube concentration for improved cellular response," *RSC Advances*, vol. 6, no. 46, pp. 39982–39992, 2016.

[68] R. Rajesh, Y. Dominic Ravichandran, M. Jeevan Kumar Reddy, S. H. Ryu, and A. M. Shanmugharaj, "Development of functionalized multi-walled carbon nanotube-based polysaccharide–hydroxyapatite scaffolds for bone tissue engineering," *RSC Advances*, vol. 6, no. 85, pp. 82385–82393, 2016.

[69] B. V. Rodrigues, A. S. Silva, G. F. S. Melo, L. M. R. Vasconscellos, F. R. Marciano, and A. O. Lobo, "Influence of low contents of superhydrophilic MWCNT on the properties and cell viability of electrospun poly (butylene adipate-co-terephthalate) fibers," *Materials Science and Engineering: C*, vol. 59, pp. 782–791, 2016.

[70] J. Grebowski, P. Kazmierska, and A. Krokosz, "Fullerenols as a new therapeutic approach in nanomedicine," *BioMed Research International*, vol. 2013, 9 pages, 2013.

[71] R. Sijbesma, G. Srdanov, F. Wudl et al., "Synthesis of a fullerene derivative for the inhibition of HIV enzymes," *Journal of the American Chemical Society*, vol. 115, no. 15, pp. 6510–6512, 1993.

[72] L. Bacakova, L. Grausova, J. Vacik et al., "Improved adhesion and growth of human osteoblast-like MG 63 cells on biomaterials modified with carbon nanoparticles," *Diamond and Related Materials*, vol. 16, no. 12, pp. 2133–2140, 2007.

[73] K. Sadeghi, "Document details," in *Proceedings First International Conference on Concrete and Development C and D*, Iran, 2001.

[74] V. Krishnan, Y. Kasuya, Q. Ji et al., "Vortex-aligned fullerene nanowhiskers as a scaffold for orienting cell growth," *ACS Applied Materials & Interfaces*, vol. 7, no. 28, pp. 15667–15673, 2015.

[75] A. Khademhosseini and R. Langer, "A decade of progress in tissue engineering," *Nature Protocols*, vol. 11, no. 10, pp. 1775–1781, 2016.

[76] S. Van Vlierberghe, P. Dubruel, and E. Schacht, "Biopolymer-based hydrogels as scaffolds for tissue engineering applications: a review," *Biomacromolecules*, vol. 12, no. 5, pp. 1387–1408, 2011.

[77] J. R. Porter, T. T. Ruckh, and K. C. Popat, "Bone tissue engineering: a review in bone biomimetics and drug delivery strategies," *Biotechnology Progress*, vol. 25, no. 6, pp. 1539–1560, 2009.

[78] A. I. Alford, K. M. Kozloff, and K. D. Hankenson, "Extracellular matrix networks in bone remodeling," *The International Journal of Biochemistry & Cell Biology*, vol. 65, pp. 20–31, 2015.

[79] M. Gu, Y. Liu, T. Chen et al., "Is graphene a promising nanomaterial for promoting surface modification of implants or scaffold materials in bone tissue engineering?," *Tissue Engineering Part B: Reviews*, vol. 20, no. 5, pp. 477–491, 2014.

[80] S. W. Crowder, D. Prasai, R. Rath et al., "Three-dimensional graphene foams promote osteogenic differentiation of human mesenchymal stem cells," *Nanoscale*, vol. 5, no. 10, pp. 4171–4176, 2013.

[81] H. Xie, T. Cao, J. V. Gomes, A. H. Castro Neto, and V. Rosa, "Two and three-dimensional graphene substrates to magnify osteogenic differentiation of periodontal ligament stem cells," *Carbon*, vol. 93, pp. 266–275, 2015.

[82] L. Han, H. Sun, P. Tang et al., "Mussel-inspired graphene oxide nanosheet-enwrapped Ti scaffolds with drug-encapsulated gelatin microspheres for bone regeneration," *Biomaterials Science*, vol. 6, no. 3, pp. 538–549, 2018.

[83] S. Peng, P. Feng, P. Wu et al., "Graphene oxide as an interface phase between polyetheretherketone and hydroxyapatite for tissue engineering scaffolds," *Scientific Reports*, vol. 7, no. 1, article 46604, 2017.

[84] H. S. Hong, J. Lee, E. A. Lee et al., "A new role of substance P as an injury-inducible messenger for mobilization of CD29+ stromal-like cells," *Nature Medicine*, vol. 15, no. 4, pp. 425–435, 2009.

[85] O. Akhavan and E. Ghaderi, "Toxicity of graphene and graphene oxide nanowalls against bacteria," *ACS Nano*, vol. 4, no. 10, pp. 5731–5736, 2010.

[86] G. CanforaHarman and M. Di Penta, "New frontiers of reverse engineering," in *In Future of Software Engineering (FOSE'07)*, Minneapolis, MN, USA, 2007.

[87] J. Natarajan, G. Madras, and K. Chatterjee, "Development of graphene oxide-/galactitol polyester-based biodegradable composites for biomedical applications," *ACS Omega*, vol. 2, no. 9, pp. 5545–5556, 2017.

[88] S. Samavedi, A. R. Whittington, and A. S. Goldstein, "Calcium phosphate ceramics in bone tissue engineering: a review of properties and their influence on cell behavior," *Acta Biomaterialia*, vol. 9, no. 9, pp. 8037–8045, 2013.

[89] N. Mahmoudi and A. Simchi, "On the biological performance of graphene oxide-modified chitosan/polyvinyl pyrrolidone nanocomposite membranes: in vitro and in vivo effects of graphene oxide," *Materials Science and Engineering: C*, vol. 70, no. 1, pp. 121–131, 2017.

[90] C. Martinelli, C. Pucci, and G. Ciofani, "Nanostructured carriers as innovative tools for cancer diagnosis and therapy," *APL Bioengineering*, vol. 3, no. 1, article 011502, 2019.

[91] K. H. Bae, H. J. Chung, and T. G. Park, "Nanomaterials for cancer therapy and imaging," *Molecules and Cells*, vol. 31, no. 4, pp. 295–302, 2011.

[92] F. Raza, H. Zafar, Y. Zhu et al., "A review on recent advances in stabilizing peptides/proteins upon fabrication in hydrogels from biodegradable polymers," *Pharmaceutics*, vol. 10, no. 1, p. 16, 2018.

[93] F. Raza, H. Zafar, X. You, A. Khan, J. Wu, and L. Ge, "Cancer nanomedicine: focus on recent developments and self-assembled peptide nanocarriers," *Journal of Materials Chemistry B*, vol. 7, no. 48, pp. 7639–7655, 2019.

[94] C. Tang, A. M. Smith, R. F. Collins, R. V. Ulijn, and A. Saiani, "Fmoc-diphenylalanine self-assembly mechanism induces apparent pKa shifts," *Langmuir*, vol. 25, no. 16, pp. 9447–9453, 2009.

[95] Y. Li, T. Wen, R. Zhao et al., "Localized electric field of plasmonic nanoplatform enhanced photodynamic tumor therapy," *ACS Nano*, vol. 8, no. 11, pp. 11529–11542, 2014.

[96] L. Mao, H. Wang, M. Tan, L. Ou, D. Kong, and Z. Yang, "Conjugation of two complementary anti-cancer drugs confers molecular hydrogels as a co-delivery system," *Chemical Communications*, vol. 48, no. 3, pp. 395–397, 2012.

[97] E. K. Johnson, D. J. Adams, and P. J. Cameron, "Peptide based low molecular weight gelators," *Journal of Materials Chemistry*, vol. 21, no. 7, pp. 2024–2027, 2011.

[98] B. Tian, C. Wang, S. Zhang, L. Feng, and Z. Liu, "Photothermally enhanced photodynamic therapy delivered by nano-graphene oxide," *ACS Nano*, vol. 5, no. 9, pp. 7000–7009, 2011.

[99] G. Gonçalves, M. Vila, M. T. Portolés, M. Vallet-Regi, J. Gracio, and P. A. A. P. Marques, "Nano-graphene oxide: a potential multifunctional platform for cancer therapy," *Advanced Healthcare Materials*, vol. 2, no. 8, pp. 1072–1090, 2013.

[100] M. Fiorillo, A. F. Verre, M. Iliut et al., "Graphene oxide selectively targets cancer stem cells, across multiple tumor types: implications for non-toxic cancer treatment, via "differentiation-based nano-therapy"," *Oncotarget*, vol. 6, no. 6, pp. 3553–3562, 2015.

[101] R. Masoumzade, G. Behbudi, and S. Mazraedoost, "A medical encyclopedia with new approach graphene quantum dots for anti-breast cancer applications: mini review," *Advances in Applied NanoBio-Technologies*, vol. 1, no. 4, pp. 84–90, 2020.

[102] J. You, J. Zhao, X. Wen et al., "Chemoradiation therapy using cyclopamine-loaded liquid–lipid nanoparticles and lutetium-177-labeled core-crosslinked polymeric micelles," *Journal of Controlled Release*, vol. 202, pp. 40–48, 2015.

[103] A. al Faraj, A. S. Shaik, E. Ratemi, and R. Halwani, "Combination of drug-conjugated SWCNT nanocarriers for efficient therapy of cancer stem cells in a breast cancer animal model," *Journal of Controlled Release*, vol. 225, pp. 240–251, 2016.

[104] X. Wang, X. C. Low, W. Hou et al., "Epirubicin-adsorbed nanodiamonds kill chemoresistant hepatic cancer stem cells," *ACS Nano*, vol. 8, no. 12, pp. 12151–12166, 2014.

[105] W. Shao, A. Paul, B. Zhao, C. Lee, L. Rodes, and S. Prakash, "Carbon nanotube lipid drug approach for targeted delivery of a chemotherapy drug in a human breast cancer xenograft animal model," *Biomaterials*, vol. 34, no. 38, pp. 10109–10119, 2013.

[106] H. Wu, H. Shi, H. Zhang et al., "Prostate stem cell antigen antibody-conjugated multiwalled carbon nanotubes for targeted ultrasound imaging and drug delivery," *Biomaterials*, vol. 35, no. 20, pp. 5369–5380, 2014.

[107] A. R. Burke, R. N. Singh, D. L. Carroll et al., "The resistance of breast cancer stem cells to conventional hyperthermia and their sensitivity to nanoparticle-mediated photothermal therapy," *Biomaterials*, vol. 33, no. 10, pp. 2961–2970, 2012.

[108] H. -j. Yao, Y. G. Zhang, L. Sun, and Y. Liu, "The effect of hyaluronic acid functionalized carbon nanotubes loaded with salinomycin on gastric cancer stem cells," *Biomaterials*, vol. 35, no. 33, pp. 9208–9223, 2014.

[109] K.-K. Liu, C. C. Wang, C. L. Cheng, and J. I. Chao, "Endocytic carboxylated nanodiamond for the labeling and tracking of cell division and differentiation in cancer and stem cells," *Biomaterials*, vol. 30, no. 26, pp. 4249–4259, 2009.

[110] Y. Zhang, Z. Cui, H. Kong et al., "One-shot immunomodulatory nanodiamond agents for cancer immunotherapy," *Advanced Materials*, vol. 28, no. 14, pp. 2699–2708, 2016.

[111] L. Zhao, Y. H. Xu, T. Akasaka et al., "Polyglycerol-coated nanodiamond as a macrophage-evading platform for selective drug delivery in cancer cells," *Biomaterials*, vol. 35, no. 20, pp. 5393–5406, 2014.

[112] V. Gaspar, D. . Melo-Diogo, E. Costa et al., "Minicircle DNA vectors for gene therapy: advances and applications," *Expert Opinion on Biological Therapy*, vol. 15, no. 3, pp. 353–379, 2015.

[113] K. Luo, B. He, Y. Wu, Y. Shen, and Z. Gu, "Functional and biodegradable dendritic macromolecules with controlled architectures as nontoxic and efficient nanoscale gene vectors," *Biotechnology Advances*, vol. 32, no. 4, pp. 818–830, 2014.

[114] R. Imani, F. Mohabatpour, and F. Mostafavi, "Graphene-based nano-carrier modifications for gene delivery applications," *Carbon*, vol. 140, pp. 569–591, 2018.

[115] G. Behbudi, "Mini review of graphene oxide for medical detection and applications," *Advances in Applied NanoBio-Technologies*, vol. 1, no. 3, pp. 63–66, 2020.

[116] H. Kim, R. Namgung, K. Singha, I. K. Oh, and W. J. Kim, "Graphene oxide–polyethylenimine nanoconstruct as a gene delivery vector and bioimaging tool," *Bioconjugate Chemistry*, vol. 22, no. 12, pp. 2558–2567, 2011.

[117] N. Druesne-Pecollo, Y. Keita, M. Touvier et al., "Alcohol drinking and second primary cancer risk in patients with upper aerodigestive tract cancers: a systematic review and meta-analysis of observational studies," *Cancer Epidemiology and Prevention Biomarkers*, vol. 23, no. 2, pp. 324–331, 2014.

[118] F. M. Tonelli, V. A. M. Goulart, K. N. Gomes et al., "Graphene-based nanomaterials: biological and medical applications and toxicity," *Nanomedicine*, vol. 10, no. 15, pp. 2423–2450, 2015.

[119] Y. Zhang, T. R. Nayak, H. Hong, and W. Cai, "Graphene: a versatile nanoplatform for biomedical applications," *Nanoscale*, vol. 4, no. 13, pp. 3833–3842, 2012.

[120] D. Wu, F. Zhang, P. Liu, and X. Feng, "Two-dimensional nanocomposites based on chemically modified graphene," *Chemistry–A European Journal*, vol. 17, no. 39, pp. 10804–10812, 2011.

[121] H. Lei, L. Mi, X. Zhou et al., "Adsorption of double-stranded DNA to graphene oxide preventing enzymatic digestion," *Nanoscale*, vol. 3, no. 9, pp. 3888–3892, 2011.

[122] L. Feng and Z. Liu, "Graphene in biomedicine: opportunities and challenges," *Nanomedicine*, vol. 6, no. 2, pp. 317–324, 2011.

[123] B. Chen, M. Liu, L. Zhang, J. Huang, J. Yao, and Z. Zhang, "Polyethylenimine-functionalized graphene oxide as an efficient gene delivery vector," *Journal of Materials Chemistry*, vol. 21, no. 21, pp. 7736–7741, 2011.

[124] X. Zhou, F. Laroche, G. E. M. Lamers et al., "Ultra-small graphene oxide functionalized with polyethylenimine (PEI) for very efficient gene delivery in cell and zebrafish embryos," *Nano Research*, vol. 5, no. 10, pp. 703–709, 2012.

[125] C. Xu, D. Yang, L. Mei et al., "Encapsulating gold nanoparticles or nanorods in graphene oxide shells as a novel gene vector," *ACS Applied Materials & Interfaces*, vol. 5, no. 7, pp. 2715–2724, 2013.

[126] H. Bao, Y. Pan, Y. Ping et al., "Chitosan-functionalized graphene oxide as a nanocarrier for drug and gene delivery," *Small*, vol. 7, no. 11, pp. 1569–1578, 2011.

[127] L. Feng, X. Yang, X. Shi et al., "Polyethylene glycol and polyethylenimine dual-functionalized nano-graphene oxide for photothermally enhanced gene delivery," *Small*, vol. 9, no. 11, pp. 1989–1997, 2013.

[128] H. Kim and W. J. Kim, "Photothermally controlled gene delivery by reduced graphene oxide–polyethylenimine nanocomposite," *Small*, vol. 10, no. 1, pp. 117–126, 2014.

[129] Y. Yang, Y. M. Zhang, Y. Chen, D. Zhao, J. T. Chen, and Y. Liu, "Construction of a graphene oxide based noncovalent multiple nanosupramolecular assembly as a scaffold for drug delivery," *Chemistry–A European Journal*, vol. 18, no. 14, pp. 4208–4215, 2012.

[130] H. Jahangirian, K. Kalantari, Z. Izadiyan, R. Rafiee-Moghaddam, K. Shameli, and T. J. Webster, "A review of small molecules and drug delivery applications using gold and iron nanoparticles," *International Journal of Nanomedicine*, vol. - Volume 14, pp. 1633–1657, 2019.

[131] J. Shi, A. R. Votruba, O. C. Farokhzad, and R. Langer, "Nanotechnology in drug delivery and tissue engineering: from discovery to applications," *Nano Letters*, vol. 10, no. 9, pp. 3223–3230, 2010.

[132] S. Zhu, J. Zhang, C. Qiao et al., "Strongly green-photoluminescent graphene quantum dots for bioimaging applications," *Chemical Communications*, vol. 47, no. 24, pp. 6858–6860, 2011.

[133] S. Garayemi and F. Raeisi, "Graphene oxide as a docking station for modern drug delivery system. by Ulva lactuca species study its antimicrobial, anti-fungal and anti-blood cancer activity," *Advances in Applied NanoBio-Technologies*, vol. 1, no. 2, pp. 53–62, 2020.

[134] S. Priyadarsini, S. Mohanty, S. Mukherjee, S. Basu, and M. Mishra, "Graphene and graphene oxide as nanomaterials for medicine and biology application," *Journal of Nanostructure in Chemistry*, vol. 8, no. 2, pp. 123–137, 2018.

[135] M. Jäger, S. Schubert, S. Ochrimenko, D. Fischer, and U. S. Schubert, "Branched and linear poly (ethylene imine)-based conjugates: synthetic modification, characterization, and application," *Chemical Society Reviews*, vol. 41, no. 13, pp. 4755–4767, 2012.

[136] S. Gurunathan, J. Woong Han, E. Kim, D. N. Kwon, J. K. Park, and J. H. Kim, "Enhanced green fluorescent protein-mediated synthesis of biocompatible graphene," *Journal of Nanobiotechnology*, vol. 12, no. 1, p. 41, 2014.

[137] N. Li, Q. Zhang, S. Gao et al., "Three-dimensional graphene foam as a biocompatible and conductive scaffold for neural stem cells," *Scientific Reports*, vol. 3, no. 1, p. 1604, 2013.

[138] X. Yang, X. Zhang, Z. Liu, Y. Ma, Y. Huang, and Y. Chen, "High-efficiency loading and controlled release of doxorubicin hydrochloride on graphene oxide," *The Journal of Physical Chemistry C*, vol. 112, no. 45, pp. 17554–17558, 2008.

[139] J. Zhang, Y. Sun, B. Xu et al., "A novel surface plasmon resonance biosensor based on graphene oxide decorated with gold nanorod–antibody conjugates for determination of transferrin," *Biosensors and Bioelectronics*, vol. 45, pp. 230–236, 2013.

[140] M. Acik, C. Mattevi, C. Gong et al., "The role of intercalated water in multilayered graphene oxide," *ACS Nano*, vol. 4, no. 10, pp. 5861–5868, 2010.

[141] M. Zhang, B. C. Yin, X. F. Wang, and B. C. Ye, "Interaction of peptides with graphene oxide and its application for real-time monitoring of protease activity," *Chemical Communications*, vol. 47, no. 8, pp. 2399–2401, 2011.

[142] T. R. Hoare and D. S. Kohane, "Hydrogels in drug delivery: progress and challenges," *Polymer*, vol. 49, no. 8, pp. 1993–2007, 2008.

[143] D. T. Seroski and G. A. Hudalla, "Self-assembled peptide and protein nanofibers for biomedical applications," in *Biomedical Applications of Functionalized Nanomaterials*, pp. 569–598, Elsevier, 2018.

[144] J.-Y. Fang, J. P. Chen, Y. L. Leu, and H. Y. Wang, "Characterization and evaluation of silk protein hydrogels for drug delivery," *Chemical and Pharmaceutical Bulletin*, vol. 54, no. 2, pp. 156–162, 2006.

[145] Y. Nagai, L. D. Unsworth, S. Koutsopoulos, and S. Zhang, "Slow release of molecules in self-assembling peptide nanofiber scaffold," *Journal of Controlled Release*, vol. 115, no. 1, pp. 18–25, 2006.

Hindawi
Journal of Nanomaterials
Volume 2020, Article ID 1072765, 14 pages
https://doi.org/10.1155/2020/1072765

*Research Article*

# Simvastatin-Loaded Nanomicelles Enhance the Osteogenic Effect of Simvastatin

**Xianling Feng**,[1] **Xinxin Yue**,[2] **and Mao Niu**[3]

[1]*School of Medicine, Shenzhen University, Shenzhen 518060, China*
[2]*Department of Dental Implantology, Beijing Stomatological Hospital, School of Stomatology, Capital Medical University, Beijing 100050, China*
[3]*School of Medical Technology and Nursing, Shenzhen Polytechnic, Shenzhen 518055, China*

Correspondence should be addressed to Mao Niu; niu1037@szpt.edu.cn

Received 26 June 2020; Revised 30 October 2020; Accepted 5 November 2020; Published 19 November 2020

Academic Editor: Xiaoming Li



*Objectives*. The present study intended to further verify that simvastatin-loaded nanomicelles (SVNs) enhanced the role of simvastatin (SV) in promoting osteoblast differentiation in vitro and to evaluate the effect of SVNs on bone defect repair in vivo. *Methods*. SVNs were synthesized by dialysis. MG63 cells were subjected to intervention with 0.25 $\mu$mol/l of SVNs and SV. A 3-(4,5-dimethylthiazol-2-yl)-5-(3-carboxymethoxyphenyl)-2-(4-sulfophenyl)-2H-tetrazolium (MTS) assay kit and flow cytometry were used to determine cell proliferation activity, cell cycle distribution, and apoptosis. The osteoblastic differentiation of MG 63 cells was evaluated by measuring alkaline phosphatase (ALP) activity, ALP staining, and the expression levels of the osterix (Osx) and osteocalcin (OC) proteins. In addition, 0.5 mg of SVNs or SV was applied to the skull defect area of rabbits. Micro-CT, hematoxylin and eosin (HE) staining, and Masson's trichrome staining were used for qualitative and quantitative evaluation of new bone in three dimensions and two dimensions. *Results*. The SVNs had a mean diameter of 38.97 nm. The encapsulation and drug-loading efficiencies were $54.57 \pm 3.15\%$ and $10.91 \pm 0.63\%$, respectively. In vitro, SVNs and SV can inhibit the proliferation activity and promote osteogenic differentiation of MG63 cells by arresting MG63 cells at the G0/G1 phase without increasing the apoptosis rate. In vivo quantitative results showed that the bone mineral density (BMD), bone volume (BV)/total volume (TV) ratio, and trabecular number (Tb.N) in the gelatin sponge with SVNs (SVNs-GS) group and gelatin sponge with SV (SV-GS) group were 362.1%, 292.0%; 181.3%, 158.0%; and 215.2%, 181.8% of those in the blank control (BC) group, respectively. Histological results identified the new bone tissue in each group as irregular fibrous bone, and the arrangement of trabecular bone was disordered. There were significantly more osteoblasts and new capillaries around the trabecular bone in the SVNs-GS group and SV-GS group than in both the BC and drug-free nanomicelle (DFNs) groups. Both in vitro and in vivo, SVNs exhibited greater osteogenic efficacy than SV. *Conclusion*. SVNs significantly improved the osteogenic efficacy of SV.

## 1. Introduction

Trauma, infection, and tumors can all cause bone defects. Due to mineral deposits and an insufficient blood supply in bone defect areas, the rate of new bone formation is very slow, and large bone defects cannot self-heal [1, 2]. Methods such as bone grafting, bone tissue engineering, and membrane-guided bone regeneration are commonly used to promote bone defect repair, and the materials used include autogenic bone, allogenic bone, synthetic bone replacement materials, stem cells, and exogenous growth factors [3, 4]. Among these materials, autogenic bone is the gold standard of bone repair materials due to its superior osteoconduction, osteoinduction, and osteogenesis [5]. However, autogenic bone grafting is associated with considerable trauma and increased patient suffering, which substantially limits its clinical application [6]. Allogenic bone, which is mainly derived from human cadavers derived, has been applied in clinical practice and has yielded good results [7]. However, the potential risks of spreading viruses and immunological rejection limit the application of allogenic bone in clinical practice [8]. Synthetic biodegradable bone replacement materials

overcome the limitations of the above two materials but have the disadvantages of fast degradation, low strength, and localized inflammation caused by degraded products [9, 10]. The addition of exogenous osteogenic growth factors (such as bone morphogenetic protein 2 (BMP-2)) to the above materials can significantly improve the osteoinductive ability and promote the proliferation and differentiation of osteoblasts [11–14]. However, exogenous osteogenic growth factors are expensive, have a short half-life, are difficult to store, and have low cell-targeting properties [15]. Therefore, some scholars have attempted to identify specific drugs to accelerate the formation of new bone in the bone defect area by regulating endogenous osteogenic growth factors.

Simvastatin (SV), which is commonly used in clinical practice, is inexpensive, safe, and reliable. SV can specifically bind to HMG-CoA reductase, a key enzyme in cholesterol synthesis, to inhibit cholesterol synthesis and prevent cardiovascular diseases [16]. In 1999, Mundy et al. first reported that subcutaneous injection of SV and lovastatin could significantly promote the formation of new bone in a mouse cranial bone defect area [17]. Studies have shown that SV can promote osteogenesis mainly through the induction of BMP-2 and VEGF gene expression, thereby promoting angiogenesis and the differentiation of osteoblasts [17, 18]. In addition, SV inhibits the RANKL expression to suppress the differentiation of osteoclasts and promote osteogenesis [19, 20]. The osteogenesis-promoting effect of SV is closely associated with the regulatory functions of osteogenesis-related signaling pathways, such as the Smad pathway, the Erk1/2 pathway, and the Pi3k/Akt pathway [21–26].

SV is liposoluble and poorly soluble in water. When used systemically, most drugs are metabolized by the liver. Only small amounts of drugs can reach bone defect areas. An extremely low available drug concentration seriously impacts the promoting effect of SV [27]. Increasing the dose of SV for systemic administration can effectively increase the drug concentration in the bone defect area, but high doses can also increase the systemic side effects of SV, such as liver and kidney damage and rhabdomyolysis [28, 29]. Therefore, the extremely low bioavailability in bone defect areas and the potential side effects of SV are urgent problems requiring resolution.

Nano-based drug carriers include nanoparticles, nanoliposomes, solid lipid nanoparticles, magnetic nanoparticles, and polymeric nanomicelles. Among these carriers, polymeric nanomicelles, which were first proposed by Ringsdorf et al. to be used as a drug carrier, have become a research focus of drug delivery systems. Amphiphilic polymeric nanomicelles are self-assembled nanostructures formed by hydrophilic shells and a hydrophobic core. Polymeric nanomicelles are mostly spherical in shape and are mainly used for encapsulation and delivery of lipophilic small-molecule drugs [30, 31]. The particle sizes of polymeric nanomicelles are relatively small, mostly ranging between 10 and 80 nm [32]. Currently, polyethylene glycol (PEG), polyethylene oxide (PEO), and chitosan (CTS) are commonly used in the synthesis of the hydrophilic segments of polymeric nanomicelles [33, 34]. PEG has good water solubility and a large exclusion volume, which can effectively prevent aggregation of micelles. PEG can also reduce the capture of the reticuloendothelial system (RES) and extend the half-life of polymeric nanomicelles [33, 34]. The hydrophobic segments of polymeric nanomicelles are usually synthesized using polylactic acid (PLA) and polycaprolactone (PCL), which mainly serve the functions of encapsulating hydrophobic drugs [30, 34]. Polymeric nanomicelles prepared with these materials have excellent biocompatibility and biodegradability [35]. Polymeric nanomicelles can be excreted through the kidneys and will not accumulate in the body. Therefore, polymer micelles have great application prospects as drug carriers.

We hypothesized that the encapsulation of SV using polymer nanomicelles can significantly improve the in vitro and in vivo osteogenic effect of SV. In previous studies, we applied methoxy-PEG (mPEG-) PLA to encapsulate SV, successfully synthesized simvastatin-loaded nanomicelles (SVNs) by dialysis, and preliminarily verified that an appropriate concentration of SVNs can significantly improve the osteoblast differentiation-promoting effect of SV in vitro [24]. In the present study, we not only further verified the role of SVNs in promoting osteoblast differentiation in vitro but also evaluated the in vivo osteogenesis-promoting effects of SVNs.

## 2. Materials and Methods

*2.1. Preparation and Characterization of SVNs.* Based on previous experience in preparing nanomicelles in our group [24], SVNs (mPEG-PLA-SV) were prepared using a dialysis method. In short, 10 mg of mPEG-PLA (Mn = 5000 – 3000) (Jinan Daigang Biomaterial Co., Ltd., Shandong, China) and 2 mg of SV (National Institutes for Food and Drug Control, Beijing, China) were dissolved in 2 ml of acetonitrile (Fisher Scientific, Waltham, MA, USA) and slowly added dropwise into 12 ml of purified water. The mixture was stirred for 1 h at room temperature and then dispersed via ultrasonication for 5 min. Finally, the above solution was dialyzed for 7 h. The drug-free nanomicelles (DFNs) were also prepared in a similar way in the absence of SV.

The particle sizes of SVNs and DFNs were measured using a Zetasizer instrument (Mastersizer 2000, Malvern Instruments Ltd., Malvern, UK). Nanomicelle morphology was observed with a transmission electron microscope (TEM; HT7700, Hitachi Limited, Tokyo, Japan). High-performance liquid chromatography (HPLC; LC-20AD, Shimazu Corporation, Kyoto, Japan) was used to determine the drug-loading content and drug entrapment efficiency.

*2.1.1. In Vitro Simvastatin Release.* SVNs were sealed in a dialysis bag and incubated in 4% HAS solution at 37°C and 50 rpm. The same amount of free SV was dialyzed under the same conditions as a control. At predetermined time intervals, 12 ml of the samples was withdrawn and replaced with 12 ml of fresh release medium. The SV concentration was analyzed using the HPLC system.

*2.2. Cell Experiment*

*2.2.1. Cell Culture and Experimental Group.* The human osteoblast-like MG63 cells were purchased from the Cell

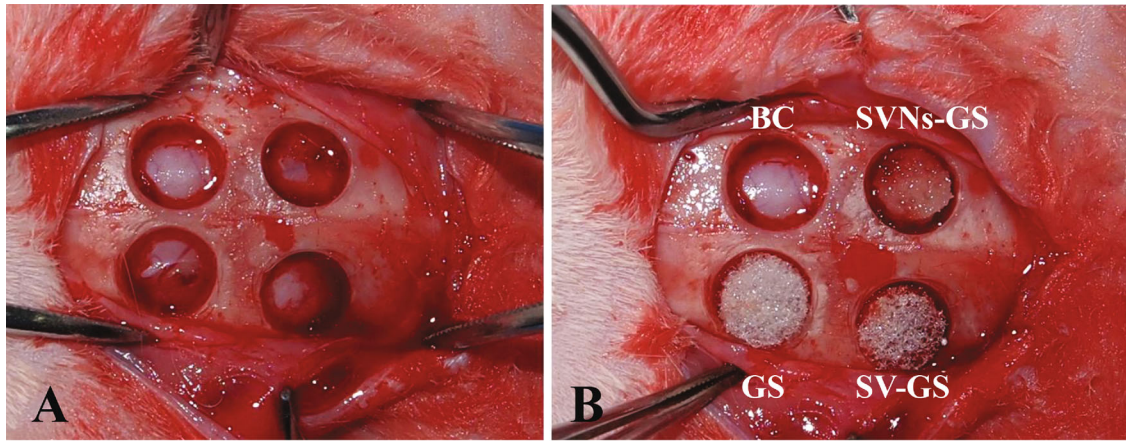


FIGURE 1: The surgical procedures with rabbit calvaria. (a) A mucoperiosteal flap was raised, and four critical bone defects (6.5 mm in diameter) were created at the top of the skull. (b) The defects were divided into the following four groups: no augmentation (blank control, BC) group, gelatin sponge (GS) group, gelatin sponge with 0.5 mg SV (SV-GS) group, and gelatin sponge with 5 mg SVNs (0.5 mg SV) (SVNs-GS) group.

Bank of the Chinese Academy of Sciences, Shanghai, People's Republic of China. The MG63 cells were cultured in Dulbecco's modified Eagle's medium (DMEM; Thermo Fisher Scientific, Waltham, MA, USA) with 10% fetal bovine serum (FBS; Thermo Fisher Scientific, Waltham, MA, USA) and 1% penicillin-streptomycin (HyClone, Logan, UT, USA) at 37°C in a humidified incubator with 5% $CO_2$. The medium was refreshed every three days.

The experiment was divided into four groups: SVNs group, SV group as the positive control, DFNs group, and blank control (BC) group as the negative control. According to the preliminary results of our group, the SV in the SVNs group and in the SV group was dissolved and diluted to 0.25 $\mu$mol/l in the complete medium. Equal concentrations of DFNs were also prepared.

*2.2.2. Cell Proliferation.* MG63 cells were seeded onto 24-well plates at $10^4$ cells per well and cultured with the drug formulations (500 $\mu$l/well) for 72 h. Then, culture medium was replaced with serum-free medium. The plate was incubated for 2 h at 37°C in a humidified atmosphere with 5% $CO_2$. An MTS assay kit (MTS; Biovision Inc., CA, USA) was used to measure cell proliferation. One hundred microliters of MTS solution was mixed with culture medium per well. One hundred microliters of the mixture was pipetted into each well of a 96-well plate, and absorbance was measured at 30 min intervals at 490 nm using a microplate reader (Tecan, Tecan Trading AG, Switzerland).

*2.2.3. Cell Cycle and Apoptosis.* MG63 cells were seeded in 6 cm Petri dishes at $1 \times 10^6$/dish. The experiment was terminated at 72 h after dosing, and the effects of drugs on the cell cycle and apoptosis of MG63 cells were measured by flow cytometry.

*(1) Cell Cycle.* A cell cycle detection kit (keygen, Keygen biotech, Jiangsu, China) was used to detect the cell cycle. The cells were digested and collected by centrifugation at 1,000 × g at 4°C for 5 min. With the supernatant removed, the cells were resuspended with 1 ml of precooled Buffer A and collected by centrifugation again. Then, the cells were resuspended with 100 $\mu$l of precooled Buffer A, slowly dripped into 900 $\mu$l of precooled 70% ethanol, and fixed at -20°C for at least 12 h. The cells were collected by centrifugation again, washed with precooled Buffer A to remove ethanol, and resuspended in 500 $\mu$l of Buffer A; then, RNase A was added, and the solution was further incubated at 37°C for 30 min. The samples were stained with propidium iodide (PI) at room temperature for 30 min in the dark and analyzed by flow cytometry.

*(2) Cell Apoptosis.* An Annexin V-FITC/PI Apoptosis Detection Kit (BD, Becton, Dickinson and Company, NJ, USA) was used to detect the apoptotic cells. The cells were collected using trypsin without EDTA by centrifugation and resuspended with 300 $\mu$l 1× binding buffer. One hundred microliters of cell suspension was pipetted into culture tubes; then, 5 $\mu$l of Annexin V-FITC was added to each tube, followed by incubation for 15 min at room temperature. Five microliters of PI stain was added to the cells for 5 min at room temperature without light. After the addition of 400 $\mu$l of 1× binding buffer to each tube, cell apoptosis was analyzed by flow cytometry.

*2.2.4. Alkaline Phosphatase (ALP) Activity.* MG63 cells were seeded onto 24-well plates at $10^4$ cells/well. After 7 d of culturing, the culture medium was removed, and 50 $\mu$l/well of Laemmli sample buffer together with protease inhibitor (50 : 1 v/v) was added to lyse the cells. Then, the samples were centrifuged at 10,000 rpm, at 4°C. Ten microliters of supernatant was pipetted to measure the protein concentration using a bicinchoninic acid protein assay kit (Thermo, Thermo Fisher Scientific, MA, USA). The absorbance of the solution was measured at 562 nm, and the amount of total protein was calculated using a generated calibration curve. In addition, 30 $\mu$l of supernatant was pipetted to measure the ALP activity, and the absorbance of the solution at 520 nm was measured. To determine the ALP activity, the amount of

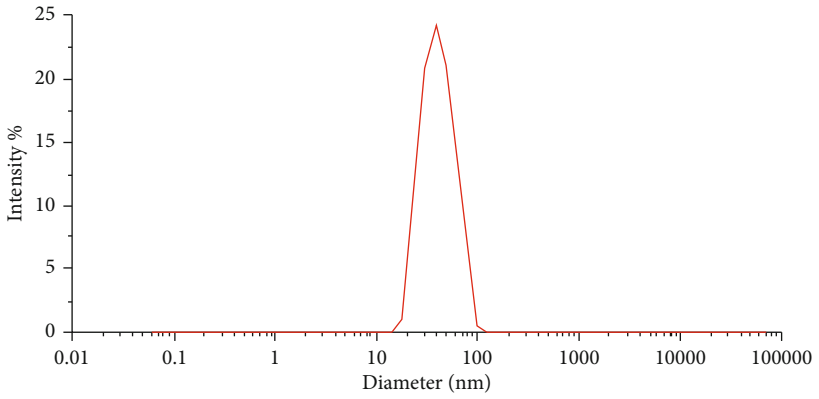


(a)

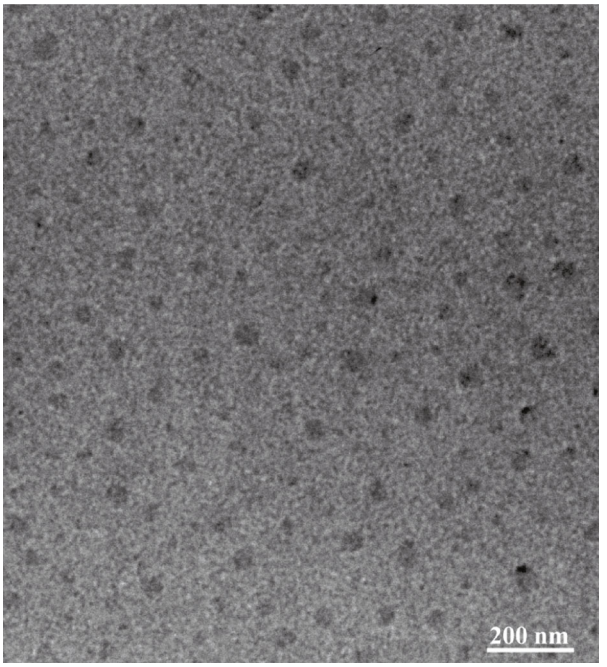


(b)

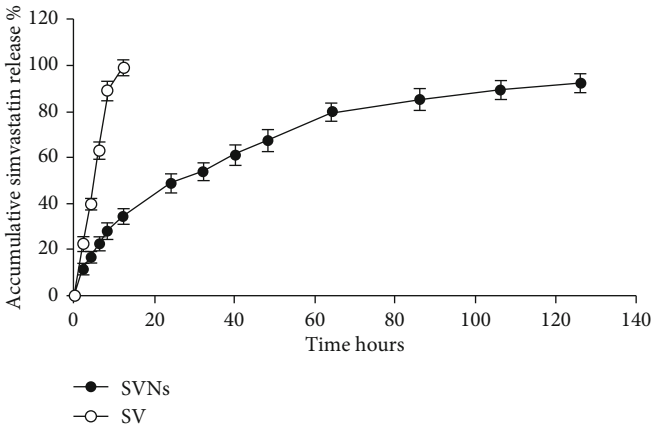


(c)

Figure 2: The characteristics of simvastatin-loaded nanomicelles. (a) The particle size of simvastatin-loaded nanomicelles was measured using a Zetasizer instrument. (b) Simvastatin-loaded nanomicelle morphology was observed with a transmission electron microscope (TEM). (c) The in vitro cumulative release profiles of simvastatin from simvastatin-loaded nanomicelles using human serum albumin as dissolution medium by a dynamic dialysis method. The simvastatin concentration was measured via the HPLC method at a UV absorbance of 238 nm. The results are the mean values of three independent measurements (±SD).

ALP was normalized to the amount of total proteins synthesized.

*2.2.5. ALP Staining.* The slides of MG63 cells were stained for the presence of ALP using an ALP assay kit (86C-1KT; Sigma-Aldrich Corp., St. Louis, USA) according to the manufacturer's instructions after incubating in various experimental media for 7 d. The cells were fixed in a citrate-acetone-formaldehyde solution for 30 s and then incubated in an ALP mixture solution containing sodium nitrite solution, fast blue BB base (FBB-) alkaline solution, and naphthol AS-BI alkaline solution as a substrate for 30 min at room temperature away from light. Stained cells were rinsed twice with deionized water and photographed.

*2.2.6. Western Blotting.* MG63 cells were seeded onto 6-well plates at 5 × 105 cells/well and cultured with the corresponding drugs according to the experimental group. The protein expression levels of osterix (OSX) and osteocalcin (OC) were determined by western blot analysis according to the following steps: cultured cells were washed twice with ice-cold PBS, and then, the total proteins were extracted from the cells using the RIPA lysis buffer containing a protease inhibitor (Cell Signaling, Cell Signaling Technology Inc., MA, USA) and phosphatase inhibitors (Cell Signaling, Cell Signaling Technology Inc., MA, USA). The protein concentrations were determined using the bicinchoninic acid (BCA) protein assay (Pierce BCA Protein Assay Kit; Thermo Fisher Scientific). An equal amount of protein (20 $\mu$g/lane) was separated by 10% sodium dodecyl sulfate-polyacrylamide gel electrophoresis, then transferred to polyvinylidene difluoride (PVDF) membranes (Millipore, Bedford, MA, USA). After blocking with 5% BSA in TBS with Tween-20 (TBST) for 60 min, the PVDF membranes were incubated with primary antibodies at 4°C overnight. Next, the membranes were incubated for 60 min at room temperature with a horseradish peroxidase-linked secondary antibody. The bands were visualized using the enhanced chemiluminescence (ECL) detection system. The quantification of protein was calculated by densitometry analysis using the ImageJ software. The primary antibodies used were specific for OSX (1 : 1500 diluted; Abcam, Cambridge, UK), OC (1 : 1500 diluted; Abcam), and GAPDH (1 : 1500 diluted; Cell Signaling, Cell Signaling Technology Inc., MA, USA).

*2.3. Animal Experiment.* Six New Zealand white rabbits (20–24 weeks, 2.3–0.3 kg) were used as experimental animals in this experiment. The experimental protocol was approved by the Animal Ethics Committee at Shenzhen University.

*2.3.1. Surgical Procedure.* All surgical procedures were performed under sterile conditions. First, the animals were anesthetized with an injection of 3% sodium pentobarbital (30 mg/kg) into the lateral ear vein. Then, the head of the rabbit was shaved and sterilized with iodine solution. Next, 2 ml of 2% lidocaine was administered to the operating site as local anesthesia. A perpendicular incision was made, and a mucoperiosteal flap was raised. Four critical bone defects (6.5 mm in diameter) were created at the top of the skull and randomly divided into the following four groups: no augmentation (blank control, BC) group, gelatin sponge (GS) group, gelatin sponge with 0.5 mg SV (SV-GS) group, and gelatin sponge with 5 mg SVNs (0.5 mg SV) (SVNs-GS) group. The surgical procedure is depicted in Figure 1. The animals were sacrificed four weeks after surgery.

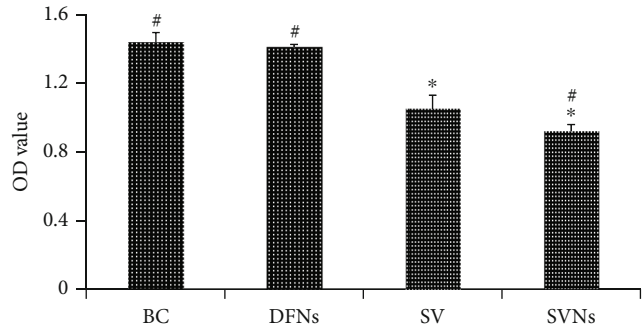


Figure 3: The effect of SVNs and SV on the proliferative activity of MG63 cells. The results are the mean values of three independent measurements (±SD). $^{*}P < 0.05$ vs. BC group; $^{\#}P < 0.05$ vs. SV group.

*2.3.2. Microcomputed Tomography (Micro-CT) Analysis.* The effects of SVNs and SV on osteogenesis were evaluated radiographically. The specimens were removed en bloc, fixed in 10% neutral formalin, and scanned with a micro-CT scanner (Skyscan-1176; Bruker, Belgium) (pixel size: 18.05 $\mu$m; source voltage: 62 kV; source current: 380 $\mu$A). Micro-CT images were reconstructed using Skyscan NRecon software (Bruker, Belgium). The bone defect area (6.5 mm in diameter) of each image was defined as the region of interest (ROI), and the volume of interest (VOI) was made up of the ROIs of 150 images. The newly formed bone volume (BV), bone mineral density (BMD), percent bone volume (bone volume/tissue volume, BV/TV), and trabecular number (Tb.N) of the newly formed bone were measured using Skyscan CTAn software (Bruker, Belgium).

*2.3.3. Histomorphometric Analysis.* After the specimens were completely fixed, they were demineralized with 10% EDTA for four weeks and paraffin-embedded after dehydration. All the specimens were sectioned into 4 $\mu$m-thick serial sections for hematoxylin and eosin (HE) and Masson's trichrome staining for observation of the newly formed bone under a microscope.

*2.4. Statistical Analysis.* Statistical analysis was performed using SPSS version 19.0 (IBM Corp., Armonk, NY, USA). All data are shown as the mean ± standard deviation (SD) from at least three independent experiments and were analyzed by repeated-measures ANOVA and Student's $t$-test.

## 3. Results

*3.1. Characterization of Simvastatin-Loaded Nanomicelles.* The mean diameter of the SVNs was determined with dynamic light scattering (DLS) and found to be approximately 38.97 ± 1.96 nm (Figure 2(a)). The SVNs were nearly spherical in shape based on the TEM results (Figure 2(b)).

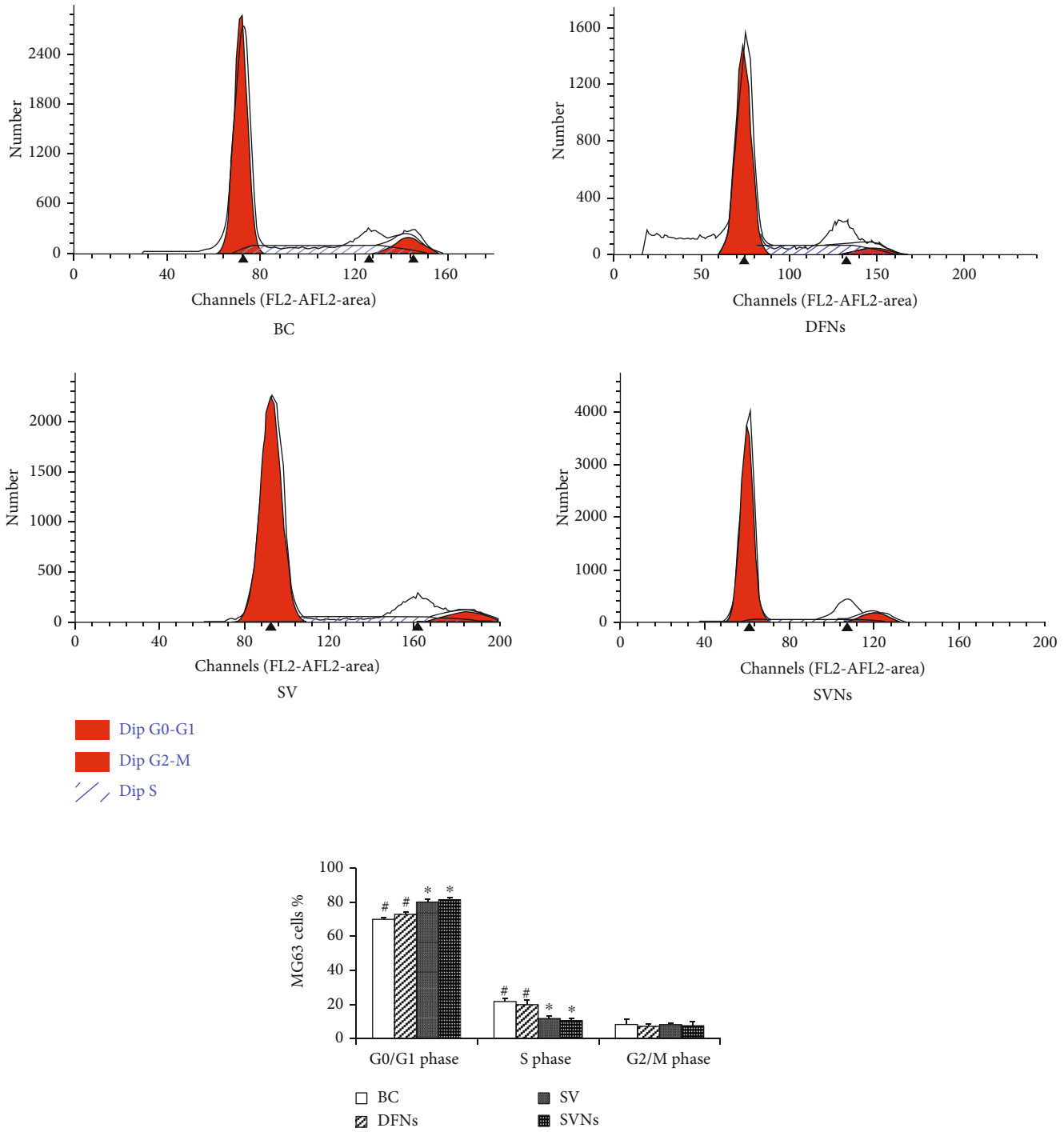


Figure 4: The effect of SVNs and SV on the cell cycle of MG63 cells. The results are the mean values of three independent measurements (±SD). $^{*}P < 0.05$ vs. BC group; $^{\#}P < 0.05$ vs. SV group.

Under 20% theoretical drug-loading capacity (DLC) conditions, the SVNs presented an encapsulation ratio and drug-loading efficiency of $54.57 \pm 3.15\%$ and $10.91 \pm 0.63\%$, respectively. These nanomicelles were selected for subsequent experiments to evaluate their osteogenic effects.

*3.1.1. In Vitro Simvastatin Release.* As shown in Figure 2(c), the free SV was nearly completely released at 12 h, whereas only approximately 35% of the total SV had been released from the nanomicelles at the same time. SVNs showed good sustained-release properties in vitro.

### 3.2. Cell Experiment Results

*3.2.1. Cell Proliferation.* Figure 3(a) shows that the number of cells significantly decreased in the SVNs group and the SV group at 3 d after administration of the drugs in comparison with the BC group. The SVNs group had fewest cells,

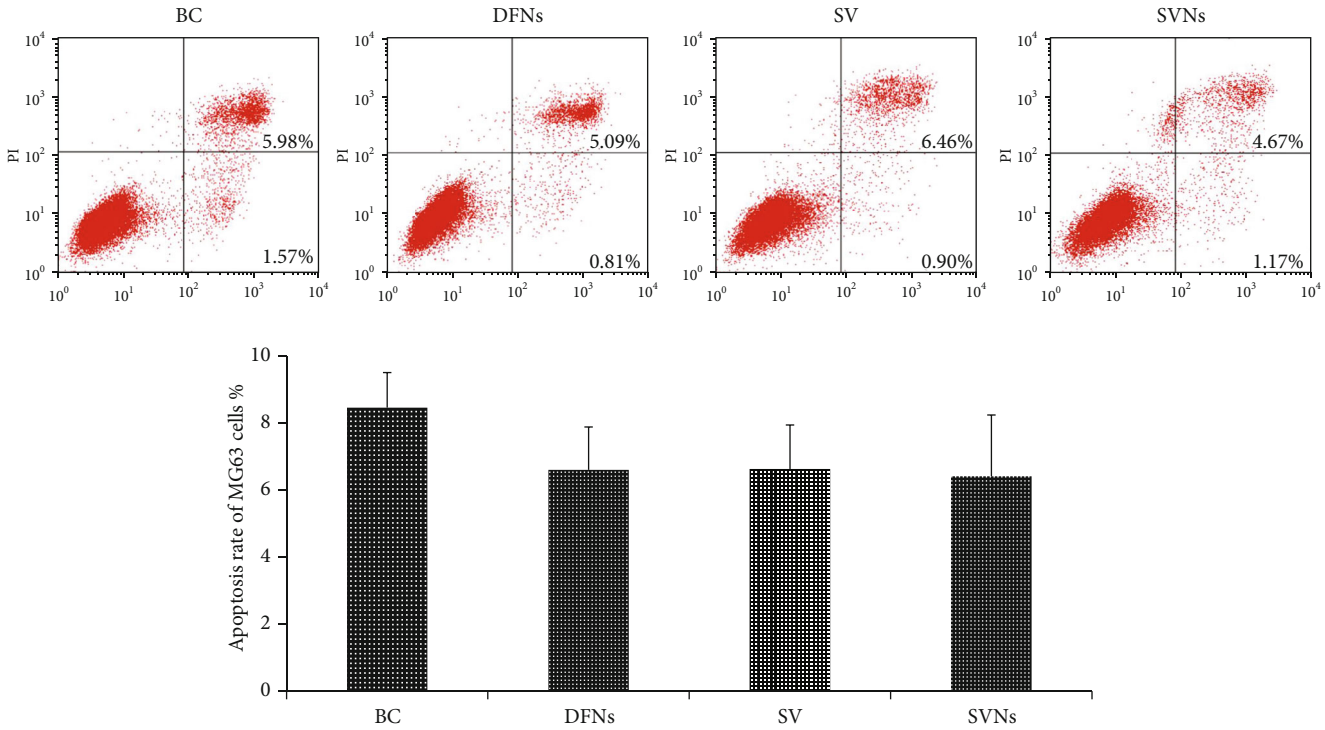


Figure 5: The effect of SVNs and SV on the apoptotic rate of MG63 cells. The results are the mean values of three independent measurements (±SD). $^{*}P < 0.05$ vs. BC group; $^{\#}P < 0.05$ vs. SV group.

indicating that SVNs exerted a significantly more potent inhibitory effect on cell proliferation than SV.

*3.2.2. Cell Cycle and Cell Apoptosis.* To clarify whether the inhibitory effect of SVNs and SV on the proliferative activity of MG63 cells is related to a drug-induced alteration of cell cycle and apoptotic rate, flow cytometry was used to analyze the cell cycle and apoptotic rate of the MG63 cells in all experimental groups.

Figure 4 shows that the percentages of the MG63 cells in the G0/G1 phases of the cell cycle were significantly increased, while the percentage of cells in the S phase of the cell cycle was markedly reduced, in the SVNs group and the SV group 3 d after administration of the drugs in comparison with the BC group. No significant changes were observed in the percentages of G2/M phase cells.

Moreover, Figure 5 shows that the apoptotic rate of MG63 cells did not increase significantly after treatment with SVNs and SV. The above cell proliferation experiment results show that SVNs and SV significantly reduced the number of MG63 cells. The decrease in the number of cells in the SVNs group and the SV group did not appear to be related to apoptosis.

*3.2.3. ALP Activity Assay.* The osteoblastic differentiation of MG63 cells was evaluated by measuring the ALP activity after culturing with different drug formulations for 7 d. As shown in Figure 6(a), the ALP activities of cells in the SVNs group and SV group were significantly higher than those of cells in the BC group, and the SVNs group exhibited the greatest cellular ALP activity. ALP staining results (Figure 6(b)) showed obvious blue areas in the SVNs group and SV group, especially in the SVNs group, and almost no blue areas were observed in the DFN group and BC group. These results are consistent with those of the quantitative analysis of ALP activity described above.

*3.2.4. Protein Levels of OSX and OC.* The protein expression levels of OSX and OC in MG63 cells were determined by the western blot analysis. At 7 d or 14 d after drug application, the protein expression levels of OSX (Figure 6(c)) and OC (Figure 6(d)) of cells in the SVNs group and SV group were significantly higher than those of the cells in the BC group. SVNs could further significantly enhance the promoting effect of SV on the expression of OSX or OC in MG63 cells.

The above results showed that SVNs and SV significantly promoted the osteogenic differentiation ability of the MG63 cells in vitro. Their osteogenesis-promoting effect in vivo requires further verification in animal experiments.

*3.3. Animal Experiment Results.* The animal experiment was executed smoothly, the experimental animals healed well after surgery, and no complications such as inflammation, infection, splitting, or exposure were noted in the surgical area. During specimen preparation, one specimen was damaged and was not included in the subsequent analysis. The number of samples in each group was $n = 5$.

*3.3.1. Microcomputed Tomography (CT) Analysis Results.* Animals were sacrificed by air injection into an ear vein 4 weeks after surgery. Under sterile conditions, the surgical

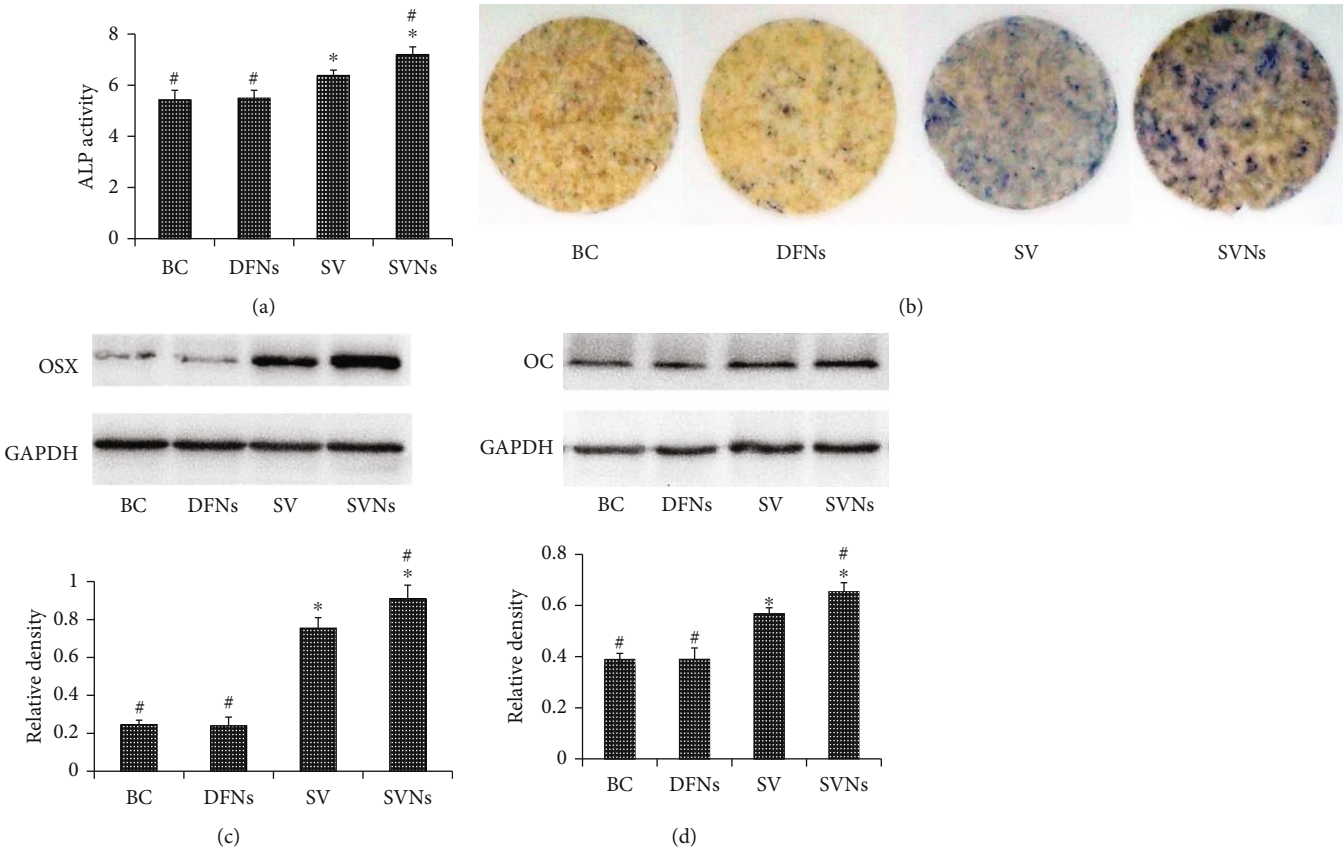


Figure 6: The effect of SVNs and SV on the osteogenic differentiation of MG63 cells. (a) ALP activity was measured in whole-cell extracts. (b) ALP staining. The ALP activity was proportional to the intensity of the blue-violet color. (c) The protein expression of OSX after treatment with different drug formulations for 7 d. (d) The protein expression of OC after treatment with different drug formulations for 14 d. The results are the mean values of three independent measurements (±SD). $^{*}P < 0.05$ vs. BC group; $^{\#}P < 0.05$ vs. SV group.

area was completely delineated at the site larger than 5 mm along the edge of the defect area. After scanning with micro-CT, the Skyscan CTAn software of the scanner was used to perform three-dimensional reconstruction of the defect area (Figure 7(a)). At 4 weeks after surgery, each experimental group had different degrees of new bone formation, and the direction of the new bone formation mainly extended from the edge of the bone defect toward the center of the defect area. New bone formation was most extensive in the SVNs-GS group, followed by the SV-GS group, while new bone formation was the least obvious in the BC group, and large defects were still present in the bone defect area. The bone defect area was further divided into VOI, and three-dimensional reconstructed images more clearly showed that the new bone formation in the SVNs-GS group was significantly more obvious than that in the other groups (Figure 7(b)). Quantitative analysis of BMD (Figure 7(c)), BV/TV ratio (Figure 7(d)), and Tb.N (Figure 7(e)) in the new bone by Skyscan CTAn software showed that the BMDs in the SVNs-GS, SV-GS, and GS groups were 362.1%, 292.0%, and 183.5% of the BMD in the BC group; the BV/TV ratios were 181.3%, 158.0%, and 133.8% of the BV/TV ratio in the BC group; and the Tb.N values were 215.2%, 181.8%, and 145.4% of the Tb.N in the BC group, respectively.

*3.3.2. Histological Evaluation Results.* At 4 weeks after surgery, sagittal primary bone slices obtained from the centers of the bone defect areas were subjected to HE staining (Figure 8). The results showed that the bone defect areas of each group were covered by new fibrous tissue and immature bone tissue, with a small amount of irregular cancellous bone at the edge of the primary bone defect. The SVNs-GS group had the most newly formed irregular cancellous bone and the smallest remaining bone defect areas. The new bone formation in the SVNs-GS group and SV-GS group was significantly greater than that in the BC group and GS group. Under high magnification, the new bone tissue in each group was identified as irregular fibrous bone, and the arrangement of trabecular bone was disordered; a large number of spindle-shaped osteoblasts were attached to the surface of the primary trabecular bone, and some osteoblasts had transformed into immature bone cells and were buried in the bone lacunae. The extensive new capillary formation was evident around the primary trabecular bone, especially in the SVNs-GS group.

Adjacent blank sections were subjected to Masson trichrome staining (Figure 9). The results showed that the new fibrous tissues in the bone defect areas of all groups were stained blue, the new bone tissue at the edge of the bone

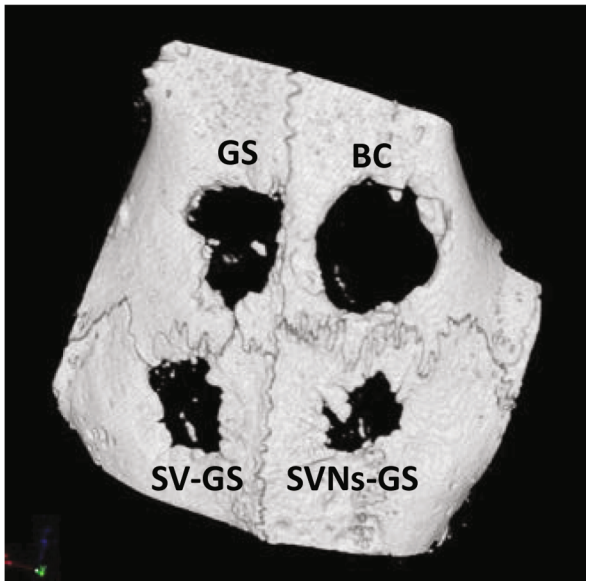


(a)

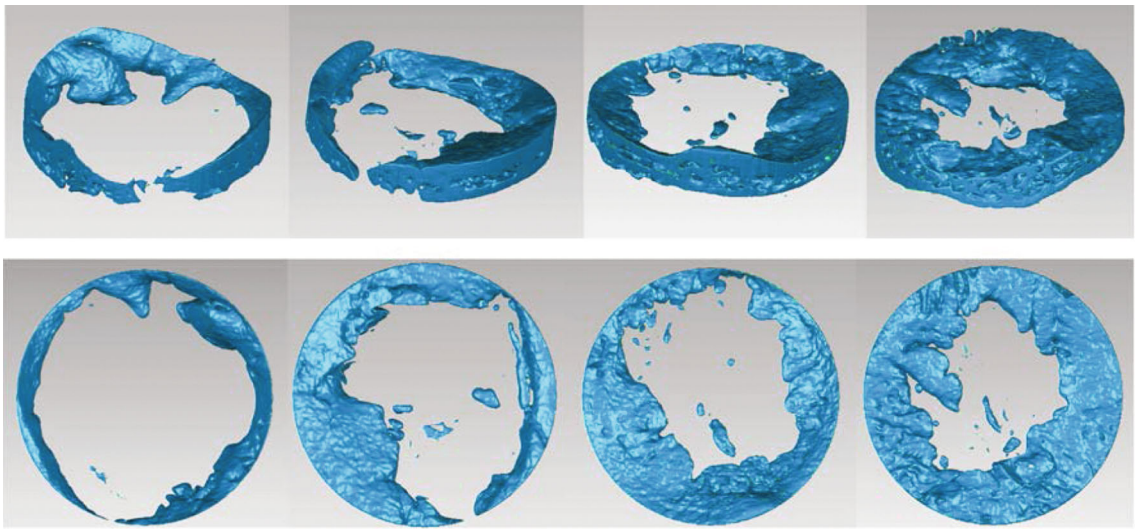


(b)

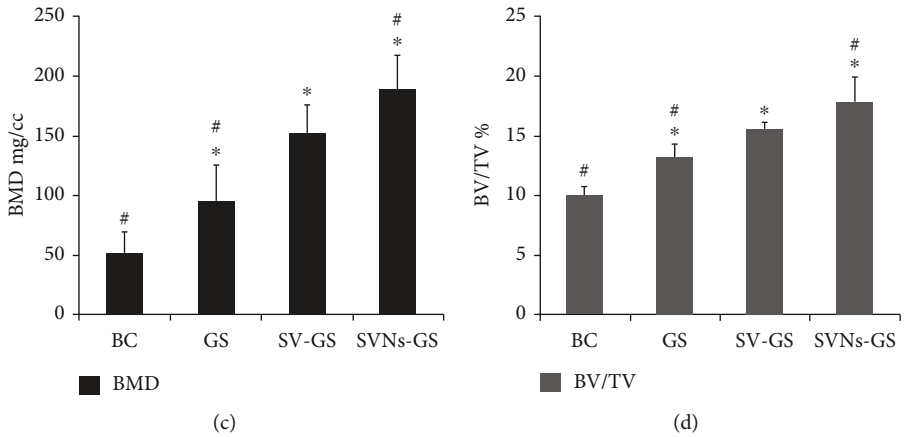


(c) (d)

Figure 7: Continued.

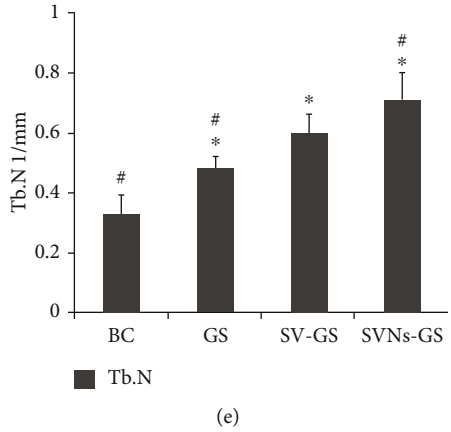


Figure 7: Evaluation of new bone formation in the surgical defect area with micro-CT scanning at 4 weeks after surgery. (a) Three-dimensional reconstruction of the defect area. (b) Three-dimensional reconstruction of VOI. Quantitative analysis of BMD (c), BV/TV ratio (d), and Tb.N (e) in the new bone. The results are the mean values of five independent measurements (±SD). $^{*}P < 0.05$ vs. BC group; $^{\#}P < 0.05$ vs. SV group.

defect area was stained blue or red and blue, and the surrounding old bone was stained red. In the BC and GS groups, the arrangement of collagen fibers in the new fibrosis tissues, which showed lighter staining, was sparse and slightly disordered; only a small amount of new bone formation was noted on the edge of the defect, the bone defect area was large, trabecular bone was scarce, and no obvious mature red lamellar bone tissue was observed. In the SVNs-GS and SV-GS groups, the arrangement of collagen fibers in the new fibrosis tissues, which showed darker staining, was regular and dense; a large number of blue or red-blue primary trabecular bones had formed at the edge of the defect area and extended to the center of the defect area, the bone defect area was significantly reduced, and the trabecular bones at the proximal end of the bone defect appeared to be almost mature and exhibited red-stained lamellar bone. These observations were especially obvious in the SVNs-GS group. Under high magnification, the SVNs-GS group and SV-GS group had a large amount of osteoblasts with blue-violet nuclei attached to new trabecular bones that were gradually surrounded by newly formed osteoid, which were buried inside a new trabecular bone to form lacunae, and osteoblasts had gradually transformed into bone cells. The BC and GS groups had formed few new trabecular bones, osteoblasts were mainly located in the newly formed collagen fibers, and no apparent mature bone tissue structure was noted.

## 4. Discussion

Autogenic bone, allogeneic bone, and artificial bone replacement materials are often used in the repair of large bone defects [3–7]. Adding exogenous osteogenic growth factors such as BMP-2 to these materials can increase the osteoinductivity of the materials, thereby enhancing the osteogenesis-promoting effect [11–14]. However, the high cost and short half-life of exogenous osteogenic growth factors largely limit their clinical application [15]. SV, a commonly used lipid-lowering agent, has been found to increase the expression of BMP-2 in osteoblasts in vivo to promote the formation of new bone in bone defect areas [28, 36]. Therefore, SV is expected to replace exogenous BMP-2 for bone formation promotion since the cost of SV is 16,000-times lower than that of BMP-2 [17].

The local concentration of SV in the treatment area is closely related to whether SV can exert its osteogenesis-promoting effect. In animal experiments, SV is mainly administered systemically, and oral administration is the most common route of administration [28]. SV is a lipid-soluble drug with a low affinity for bone. After oral administration, most drugs will be metabolized by the liver, and eventually, only very small amounts of drugs can reach the treatment area [27]. The low concentration of SV in the treatment area results in a negligible promoting effect on new bone formation. Increasing the oral dose and repeated drug administration can enhance the osteogenic effect of SV. However, an excessive dose also substantially increases the likelihood of systemic side effects [28, 29]. Local administration of SV is an effective approach to avoid the above problems [28, 37].

Local administration of SV has the advantages of avoiding liver metabolism and improving the bioavailability of SV. Many methods can be used for local SV administration [38–40]. The simplest method is to combine SV directly with bone scaffold materials. The disadvantage of this method is that due to the burst release effect, a large amount of SV can be released from the stent into the blood and be quickly cleared from the body [28]. As a result, SV can act only for a short time, resulting in a limited osteogenic effect. Therefore, the goal of local SV administration should be slow and sustained drug release to the bone defect area to promote bone formation and to effectively improve the bioavailability of SV [40].

In previous studies, some scholars synthesized SV-loaded microspheres or nanospheres and confirmed that SV could be slowly released from the microspheres or nanospheres [41–44]. The present study used mPEG-PLA polymeric nanomicelles to encapsulate SV using the preferred dialysis method developed in a previous study. The prepared SVNs

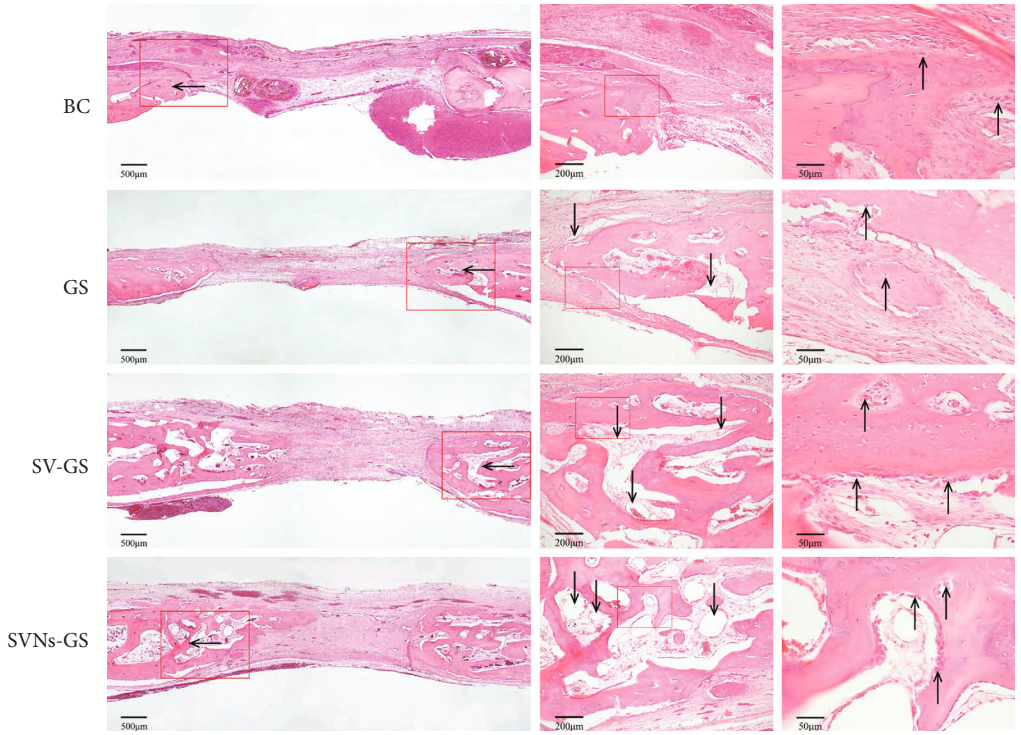


Figure 8: Histologic images of the surgical defects at four weeks (HE stain, ×40, ×100, ×400). The "←" arrows point to the original defect margins, the "↓" arrows indicate newly formed capillary, and the "↑" arrows indicate osteoblasts.

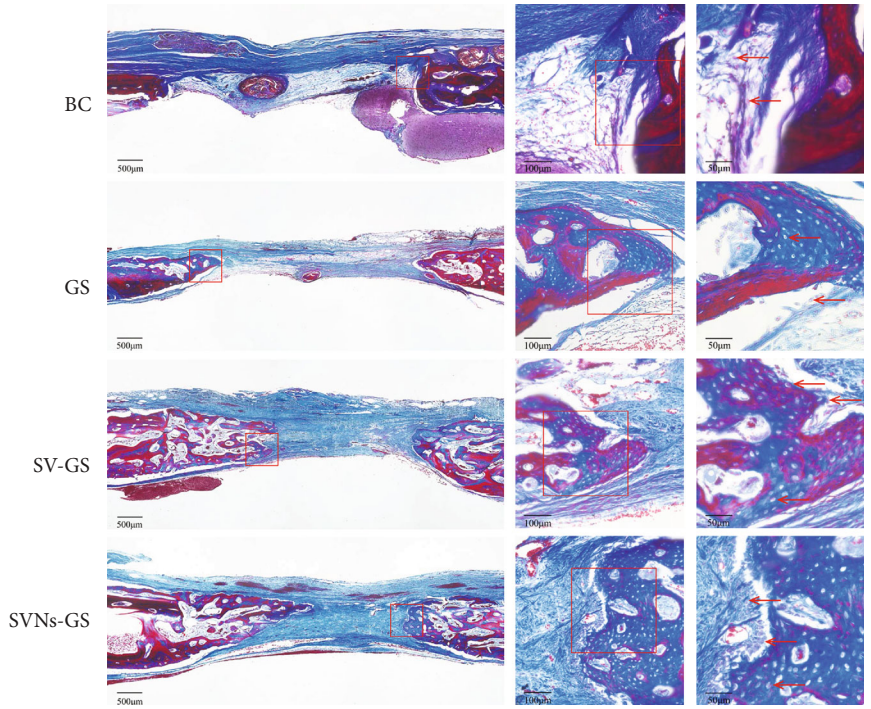


Figure 9: Histologic images of the surgical defects at four weeks (Masson stain, ×40, ×100, ×400). The "←" arrows indicate osteoblasts.

had a small size and a spherical shape, which extended the release time of the same amount of SV from 12 h to over 100 h, reflecting excellent sustained-release properties.

Few studies related to the osteogenesis-promoting effect of SV are available. Existing studies have shown that nano-based drug carriers can significantly improve the osteogenesis-promoting effect of SV in vivo and in vitro [41–44]. Our previous in vitro study preliminarily confirmed these findings [24]. In the present study, we detected the ALP activity and protein expression levels of OSX and OC in MG63 cells and

again confirmed that SVNs can significantly improve the osteoblast differentiation-promoting effect of SV in vitro. In previous studies, we found that after adding SVNs and SV, the number of MG63 cells was significantly decreased compared with that in the control group, and cell proliferation activity was inhibited. The premise of cell differentiation is currently believed to be that cells stop proliferation. Whether the reduced number of cells after drug application is the result of cell differentiation or drug-induced apoptosis requires further investigation. The results of the present study showed that SVNs and SV can block MG63 cells in the G0/G1 phase and thus inhibit cell proliferation; however, SVNs and SV did not increase the cell apoptosis rate. These results suggest that the osteoblast differentiation-promoting effects of SVNs and SV are closely related to changes in the osteoblast cell cycle.

We also evaluated the in vivo osteogenic effects of SVNs and SV through a rabbit skull defect model. To avoid the drawbacks of systemic administration, local SV administration was used in the study. Because micro-CT scans of specimens were needed in the later stage to observe and analyze the new bone formation, we loaded SVNs and SV on gelatin sponges, which do not interfere with X-rays. The amount of SV used in the animal experiments had a significant impact on the experimental results. SV at a low concentration cannot promote the formation of new bone, while excessively high doses of SV can trigger inflammation in the bone defect area and affect bone healing [45]. In animal experiments, doses of 0.1 mg to 0.5 mg of SV have been suggested to be suitable [46]. Within this range, the bone healing-promoting effect of SV was directly proportional to the amount of SV used [47, 48]. Therefore, we selected 0.5 mg as the dose of SV in the present study. Micro-CT quantitative analysis results showed that SVNs and SV both significantly promoted the formation of new bone and significantly increased the BMD and the amount of new trabecular bone in the bone defect area. It is well known that the formation of new bone mainly depends on the number of osteoblasts. Histomorphology qualitative results showed that both SVNs and SV significantly increased the number of osteoblasts in the bone defect area. In addition, both SVNs and SV increased the number of new blood vessels in the bone defect area, which may be related to the promotion of the expression of vascular endothelial growth factor by SVNs and SV, thus stimulating the differentiation of endothelial progenitor cells and ultimately stimulating angiogenesis. The increases in the number of osteoblasts and new blood vessels both promoted the formation and maturation of new bones in the bone defect area. The above quantitative and qualitative results showed that compared with the same amount of SV, SVNs had a greater effect on the promotion of new bone formation in the bone defect area, which may be due to the slow and sustained release of SV by SVNs. SVNs continuously and slowly release SV into the bone defect area to maintain a high local concentration while substantially prolonging the duration of SV action, resulting in a stronger osteogenic effect. In addition, due to their small size, nano-based drug carriers have physical and chemical properties (such as surface effects and small-size effects) that traditional materials do not have. Therefore, SVNs and SV may have significantly different effects on cellular uptake, intracellular distribution, and regulation of osteogenesis-related signaling pathways. Compared with SV, SVNs have a stronger osteogenic effect.

This study has certain limitations. This study did not elucidate the possible mechanism through which SVNs significantly improve the in vivo and in vitro osteogenesis-promoting effect of SV. In addition, this study mainly focused on the effects of SVNs and SV on the early stage of osteogenesis, and further studies are needed to investigate their roles in the late stage of osteogenesis. Finally, porous scaffolds play an important role in bone tissue engineering [49]. In the future, we will try to prepare porous scaffolds combined with SVNs in order to achieve better bone defect repair effects.

## 5. Conclusion

This study showed that polymeric nanomicelles can be used to encapsulate SV to prepare SVNs. In vitro, SVNs can promote the differentiation of osteoblasts by arresting osteoblasts at the G0/G1 phase and significantly increase the ALP activity and protein expression levels of markers associated with osteogenesis. In vivo, SVNs can promote the formation and mineralization of new bones in bone defect areas by increasing the number of osteoblasts and new blood vessels and accelerating the repair process of bone defects. Therefore, polymeric nanomicelles can be used as SV carriers to enhance the osteogenic effect of SV.

## Data Availability

The data used to support the findings of this study are available from the corresponding author upon request.

## Conflicts of Interest

The authors report no conflicts of interest in this work.

## Authors' Contributions

Xianling Feng and Xinxin Yue contributed equally to this article.

## Acknowledgments

This work was supported by grants from the Characteristic Innovation Project of Guangdong Province (No. 2018GKTSCX028), the Medical Science and Technology Research Foundation of Guangdong Province (No. A2018170), and the Innovative Engineering Project of Shenzhen Polytechnic (cxgc2019c0004).

## References

[1] A. A. El-Rashidy, J. A. Roether, L. Harhaus, U. Kneser, and A. R. Boccaccini, "Regenerating bone with bioactive glass scaffolds: a review of in vivo studies in bone defect models," *Acta Biomaterialia*, vol. 62, pp. 1–28, 2017.

[2] A. Noori, S. J. Ashrafi, R. Vaez-Ghaemi, A. Hatamian-Zaremi, and T. J. Webster, "A review of fibrin and fibrin composites for

bone tissue engineering," *International Journal of Nanomedicine*, vol. Volume 12, pp. 4937–4961, 2017.

[3] A. R. Amini, C. T. Laurencin, and S. P. Nukavarapu, "Bone tissue engineering: recent advances and challenges," *Critical Reviews in Biomedical Engineering*, vol. 40, no. 5, pp. 363–408, 2012.

[4] Z. P. Du, X. X. Feng, G. X. Cao et al., "The effect of carbon nanotubes on osteogenic functions of adipose-derived mesenchymal stem cells in vitro and bone formation in vivo compared with that of nano-hydroxyapatite and the possible mechanism," *Bioactive Materials*, vol. 6, no. 2, pp. 333–345, 2021.

[5] Y. Li, S. K. Chen, L. Li, L. Qin, X. L. Wang, and Y. X. Lai, "Bone defect animal models for testing efficacy of bone substitute biomaterials," *Journal of Orthopaedic Translation*, vol. 3, no. 3, pp. 95–104, 2015.

[6] A. Bow, D. E. Anderson, and M. Dhar, "Commercially available bone graft substitutes: the impact of origin and processing on graft functionality," *Drug Metabolism Reviews*, vol. 51, no. 4, pp. 533–544, 2019.

[7] D. J. Hall, T. M. Turner, and R. M. Urban, "Healing bone lesion defects using injectable CaSO4 /CaPO4 -TCP bone graft substitute compared to cancellous allograft bone chips in a canine model," *Journal of Biomedical Materials Research. Part B, Applied Biomaterials*, vol. 107, no. 2, pp. 408–414, 2019.

[8] A. Kadam, P. W. Millhouse, C. K. Kepler et al., "Bone substitutes and expanders in spine surgery: a review of their fusion efficacies," *International Journal of Spine Surgery*, vol. 10, p. 33, 2016.

[9] T. Rolvien, M. Barbeck, S. Wenisch, M. Amling, and M. Krause, "Cellular mechanisms responsible for success and failure of bone substitute materials," *International Journal of Molecular Sciences*, vol. 19, no. 10, p. 2893, 2018.

[10] M. Yamada and H. Egusa, "Current bone substitutes for implant dentistry," *Journal of Prosthodontic Research*, vol. 62, no. 2, pp. 152–161, 2018.

[11] Z. P. Du, G. X. Cao, K. Li, R. H. Zhang, and X. M. Li, "Nanocomposites for the delivery of bioactive molecules in tissue repair: vital structural features, application mechanisms, updated progress and future perspectives," *Journal of Materials Chemistry B*, 2020.

[12] A. Decambron, A. Fournet, M. Bensidhoum et al., "Low-dose BMP-2 and MSC dual delivery onto coral scaffold for critical-size bone defect regeneration in sheep," *Journal of Orthopaedic Research*, vol. 35, no. 12, pp. 2637–2645, 2017.

[13] M. Koolen, A. Longoni, J. van der Stok, O. Van der Jagt, D. Gawlitta, and H. Weinans, "Complete regeneration of large bone defects in rats with commercially available fibrin loaded with BMP-2," *European Cells & Materials*, vol. 38, pp. 94–105, 2019.

[14] L. Wei, F. Teng, L. Deng et al., "Periodontal regeneration using bone morphogenetic protein 2 incorporated biomimetic calcium phosphate in conjunction with barrier membrane: a pre-clinical study in dogs," *Journal of Clinical Periodontology*, vol. 46, no. 12, pp. 1254–1263, 2019.

[15] P. J. Boyne, S. Salina, A. Nakamura, F. Audia, and S. Shabahang, "Bone regeneration using rhBMP-2 induction in hemimandibulectomy type defects of elderly sub-human primates," *Cell and Tissue Banking*, vol. 7, no. 1, pp. 1–10, 2006.

[16] J. Lewandowski, M. Sinski, L. Puchalska, B. Symonides, and Z. Gaciong, "Simvastatin but not ezetimibe reduces sympathetic activity despite similar reductions in cholesterol levels," *Journal of the American Society of Hypertension*, vol. 8, no. 10, pp. 715–723, 2014.

[17] G. Mundy, R. Garrett, S. Harris et al., "Stimulation of bone formation in vitro and in rodents by statins," *Science*, vol. 286, no. 5446, pp. 1946–1949, 1999.

[18] M. Takenaka, K. Hirade, K. Tanabe et al., "Simvastatin stimulates VEGF release via p44/p42 MAP kinase in vascular smooth muscle cells," *Biochemical and Biophysical Research Communications*, vol. 301, no. 1, pp. 198–203, 2003.

[19] S. N. Raafat, R. M. Amin, M. M. Elmazar, M. M. Khattab, and A. S. El-Khatib, "The sole and combined effect of simvastatin and platelet rich fibrin as a filling material in induced bone defect in tibia of albino rats," *Bone*, vol. 117, pp. 60–69, 2018.

[20] J. Zhou, X. Gao, S. Huang et al., "Simvastatin improves the jaw bone microstructural defect induced by high cholesterol diet in rats by regulating autophagic flux," *BioMed Research International*, vol. 2018, Article ID 4147932, 9 pages, 2018.

[21] M. Yamashita, F. Otsuka, T. Mukai et al., "Simvastatin antagonizes tumor necrosis factor-alpha inhibition of bone morphogenetic proteins-2-induced osteoblast differentiation by regulating Smad signaling and Ras/Rho-mitogen–activated protein kinase pathway," *The Journal of Endocrinology*, vol. 196, no. 3, pp. 601–613, 2008.

[22] A. Neve, A. Corrado, and F. P. Cantatore, "Osteoblast physiology in normal and pathological conditions," *Cell and Tissue Research*, vol. 343, no. 2, pp. 289–302, 2011.

[23] A. N. Tsartsalis, C. Dokos, G. D. Kaiafa et al., "Statins, bone formation and osteoporosis: hope or hype?," *Hormones (Athens, Greece)*, vol. 11, no. 2, pp. 126–139, 2012.

[24] M. Niu, X. Feng, and L. Zhou, "The role of the ERK1/2 pathway in simvastatin-loaded nanomicelles and simvastatin in regulating the osteogenic effect in MG63 cells," *International Journal of Nanomedicine*, vol. Volume 13, pp. 8165–8178, 2018.

[25] P. Y. Chen, J. S. Sun, Y. H. Tsuang, M. H. Chen, P. W. Weng, and F. H. Lin, "Simvastatin promotes osteoblast viability and differentiation via Ras/Smad/Erk/BMP-2 signaling pathway," *Nutrition Research*, vol. 30, no. 3, pp. 191–199, 2010.

[26] N. Ghosh-Choudhury, C. C. Mandal, and G. G. Choudhury, "Statin-induced Ras activation integrates the phosphatidylinositol 3-kinase signal to Akt and MAPK for bone morphogenetic protein-2 expression in osteoblast differentiation," *The Journal of Biological Chemistry*, vol. 282, no. 7, pp. 4983–4993, 2007.

[27] P. Gazzerro, M. C. Proto, G. Gangemi et al., "Pharmacological actions of statins: a critical appraisal in the management of cancer," *Pharmacological Reviews*, vol. 64, no. 1, pp. 102–146, 2011.

[28] A. Moshiri, A. M. Sharifi, and A. Oryan, "Role of simvastatin on fracture healing and osteoporosis: a systematic review on in vivo investigations," *Clinical and Experimental Pharmacology & Physiology*, vol. 43, no. 7, pp. 659–684, 2016.

[29] M. Schachter, "Chemical, pharmacokinetic and pharmacodynamic properties of statins: an update," *Fundamental & Clinical Pharmacology*, vol. 19, no. 1, pp. 117–125, 2005.

[30] G. G. Walmsley, A. McArdle, R. Tevlin et al., "Nanotechnology in bone tissue engineering," *Nanomedicine: Nanotechnology, Biology and Medicine*, vol. 11, no. 5, pp. 1253–1263, 2015.

[31] G. Gaucher, R. H. Marchessault, and J. C. Leroux, "Polyester-based micelles and nanoparticles for the parenteral delivery

of taxanes," *Journal of Controlled Release*, vol. 143, no. 1, pp. 2–12, 2010.

[32] V. P. Torchilin, "Structure and design of polymeric surfactant-based drug delivery systems," *Journal of Controlled Release*, vol. 73, no. 2-3, pp. 137–172, 2001.

[33] H. Danafar, A. Sharafi, M. H. Kheiri, and S. Andalib, "Sulforaphane delivery using mPEG-PCL co-polymer nanoparticles to breast cancer cells," *Pharmaceutical Development and Technology*, vol. 22, no. 5, pp. 642–651, 2017.

[34] Z. Karami, S. Sadighian, K. Rostamizadeh, M. Parsa, and S. Rezaee, "Naproxen conjugated mPEG-PCL micelles for dual triggered drug delivery," *Materials Science & Engineering. C, Materials for Biological Applications*, vol. 61, pp. 665–673, 2016.

[35] D. T. Pham, A. Chokamonsirikun, V. Phattaravorakarn, and W. Tiyaboonchai, "Polymeric micelles for pulmonary drug delivery: a comprehensive review," *Journal of Materials Science*, vol. 56, no. 3, pp. 2016–2036, 2021.

[36] W. L. Yu, T. W. Sun, C. Qi et al., "Enhanced osteogenesis and angiogenesis by mesoporous hydroxyapatite microspheres-derived simvastatin sustained release system for superior bone regeneration," *Scientific Reports*, vol. 7, no. 1, article 44129, 2017.

[37] A. Oryan, A. Kamali, and A. Moshiri, "Potential mechanisms and applications of statins on osteogenesis: current modalities, conflicts and future directions," *Journal of Controlled Release*, vol. 215, pp. 12–24, 2015.

[38] A. S. Chauhan, A. Maria, and A. Managutti, "Efficacy of simvastatin in bone regeneration after surgical removal of mandibular third molars: a clinical pilot study," *Journal of Maxillofacial and Oral Surgery*, vol. 14, no. 3, pp. 578–585, 2015.

[39] A. Gouda, E. Helal, S. Ali, S. Bakry, and S. Yassin, "Maxillary sinus lift using osteoinductive simvastatin combined with $\beta$-TCP versus $\beta$-TCP - a comparative pilot study to evaluate simvastatin enhanced and accelerated bone formation," *Acta Odontologica Scandinavica*, vol. 76, no. 1, pp. 39–47, 2018.

[40] S. Gupta, M. del Fabbro, and J. Chang, "The impact of simvastatin intervention on the healing of bone, soft tissue, and TMJ cartilage in dentistry: a systematic review and meta-analysis," *International Journal of Implant Dentistry*, vol. 5, no. 1, p. 17, 2019.

[41] M. L. Ho, Y. C. Fu, Y. H. Wang, C. H. Chen, G. J. Wang, and G. J. Wang, "Combination of calcium sulfate and simvastatin-controlled release microspheres enhances bone repair in critical-sized rat calvarial bone defects," *International Journal of Nanomedicine*, vol. 10, p. 7231, 2015.

[42] X. Liu, X. Li, L. Zhou et al., "Effects of simvastatin-loaded polymeric micelles on human osteoblast-like MG-63 cells," *Colloids and Surfaces. B, Biointerfaces*, vol. 102, pp. 420–427, 2013.

[43] L. B. Ferreira, V. Bradaschia-Correa, M. M. Moreira, N. D. Marques, and V. E. Arana-Chavez, "Evaluation of bone repair of critical size defects treated with simvastatin-loaded poly(lactic-co-glycolic acid) microspheres in rat calvaria," *Journal of Biomaterials Applications*, vol. 29, no. 7, pp. 965–976, 2014.

[44] I. C. Tai, Y. C. Fu, C. K. Wang, J. K. Chang, and M. L. Ho, "Local delivery of controlled-release simvastatin/PLGA/HAp microspheres enhances bone repair," *International Journal of Nanomedicine*, vol. 8, p. 3895, 2013.

[45] M. Nyan, T. Miyahara, K. Noritake et al., "Molecular and tissue responses in the healing of rat calvarial defects after local application of simvastatin combined with alpha tricalcium phosphate," *Journal of Biomedical Materials Research. Part B, Applied Biomaterials*, vol. 9999B, 2009.

[46] S. Chen, J. Y. Yang, S. Y. Zhang, L. Feng, and J. Ren, "Effects of simvastatin gel on bone regeneration in alveolar defects in miniature pigs," *Chinese Medical Journal*, vol. 124, p. 3953, 2011.

[47] X. Yue, M. Niu, T. Zhang et al., "In vivo evaluation of a simvastatin-loaded nanostructured lipid carrier for bone tissue regeneration," *Nanotechnology*, vol. 27, no. 11, article 115708, 2016.

[48] Y. Lee, M. J. Schmid, D. B. Marx et al., "The effect of local simvastatin delivery strategies on mandibular bone formation in vivo," *Biomaterials*, vol. 29, no. 12, pp. 1940–1949, 2008.

[49] K. Zhang, Y. B. Fan, N. Dunne, and X. M. Li, "Effect of microporosity on scaffolds for bone tissue engineering," *Regenerative Biomaterials*, vol. 5, no. 2, pp. 115–124, 2018.

Hindawi
Journal of Nanomaterials
Volume 2020, Article ID 8887323, 13 pages
https://doi.org/10.1155/2020/8887323

*Research Article*

# Evaluation of Osteogenic Potentials of Titanium Dioxide Nanoparticles with Different Sizes and Shapes

**Yixing Ren,[1] Xinxing Feng,[2] Xinhua Lang,[1] Jianbo Wang,[3] Zhipo Du,[3] and Xufeng Niu[4]**

[1]*Department of Joint Surgery, The Fourth Central Hospital of Baoding City, Baoding 072350, China*
[2]*Endocrinology and Cardiovascular Disease Centre, Fuwai Hospital, National Center for Cardiovascular Diseases, Chinese Academy of Medical Sciences and Peking Union Medical College, Beijing 100037, China*
[3]*Department of Orthopaedics, The Fourth Central Hospital of Baoding City, Baoding 072350, China*
[4]*Research Institute of Beihang University in Shenzhen, Shenzhen 518057, China*

Correspondence should be addressed to Zhipo Du; duzhipo@163.com and Xufeng Niu; niuxf1979@163.com

Received 26 August 2020; Revised 22 September 2020; Accepted 7 October 2020; Published 11 November 2020

Academic Editor: Xiaoming Li



$TiO_2$ nanoparticles (NPs) have the potential to be used in the human body as an artificial implant because of their special physicochemical properties. However, information about the effects of $TiO_2$ NPs on preosteoblast proliferation and osteogenic differentiation is not clear. In this work, we focus on the impact of $TiO_2$ NPs with different shapes and sizes on the proliferation and differentiation of MC3T3-E1 cells. The morphology and physicochemical properties of $TiO_2$ NPs are analyzed by scanning electron microscopy, transmission electron microscopy, Quadrasorb SI analyzer, dynamic light scattering, and zeta potential. The MTT results indicate that when the concentration of $TiO_2$ NPs is less than 20 $\mu$g/mL, the proliferation of osteoblasts is preserved the most. The expression of alkaline phosphatase and osteocalcin is detected by BCA and enzyme-linked immunosorbent assay to analyze the differentiation of osteoblasts. The results indicate that both rutile and anatase $TiO_2$ NPs have a significant inhibiting influence on the differentiation of osteoblasts. Alizarin Red staining is performed on cells to detect the mineralized nodules. The results show that $TiO_2$ NPs can promote the mineralization of MC3T3-E1 cells. Then, we study the oxidative stress response of MC3T3-E1 cells by flow cytometry analysis, and all $TiO_2$ NPs induce the excessive generation of reactive oxide species. On the other hand, our study also shows that the early apoptotic cells increase significantly. $TiO_2$ NPs are swallowed by cells, and then the agglomerated particles enter mitochondria, causing the shape of mitochondria to change and vacuolation to appear. All these results show that $TiO_2$ NPs have certain cytotoxicity to cells, but they also promote the mineralization and maturation of osteoblasts.

## 1. Introduction

With the development of nanotechnology, there is a tremendous growth in the application of nanoparticles (NPs) to drug delivery systems, healthcare, antibacterial materials, optics, and electronics [1, 2]. Compared with fine particles, the interest in NPs is mostly due to their special physicochemical properties like higher specific surface area, which enhances their reactivity. Since surface properties, such as energy level, electronic structure, and reactivity, are quite different from interior states, the bioactivity of NPs is considered different from that of the fine size analogue [3]. Therefore, the potential impacts of NPs on cells and tissue have been investigated by many researchers [4–10].

As a member of NPs, $TiO_2$ NPs possess similar surface properties to the general NPs. Due to their unique physicochemical properties, $TiO_2$ NPs are widely used as a photocatalyst in solar cells, pigment in paints, corrosion-protective coating in bone implants, etc. [11–14]. Recently, concerns have been raised on the biological response of $TiO_2$ NPs. Ferin et al. [15] reported that ultrafine $TiO_2$ (~20 nm) accessed the pulmonary interstitium in rat lung and caused

inflammatory response compared with fine $TiO_2$ at the same mass burden. Kumazawa et al. [16] observed that fine Ti particles (1-3 $\mu$m) were phagocytized by the neutrophils (about 5 $\mu$m) both *in vitro* and *in vivo*, and they concluded that the cytotoxicity of Ti particles was dependent on the particle size. Thereafter, $TiO_2$ NPs have been widely investigated to identify the potential toxicity to various cells, such as human fibroblasts, macrophages, and dermal microvascular endothelial cells [17, 18]. These studies tried to illustrate the cell toxicological influence of $TiO_2$ NPs based on particle sizes [19], surface coatings [20], crystal structures, and doses [21]. However, few studies investigated the impact of $TiO_2$ NPs on cell osteogenic differentiation.

Bone tissue is an extremely dynamic and diverse tissue in the human body. Trauma, injury, infections, and bone extracellular matrix loss are among the most health-threatening problems for humans [22]. Bone tissue engineering is an exciting approach to directly repair bone defects or engineer bone tissue transplantation [23]. A large number of studies on bone tissue engineering have verified the influence of various materials, stress, and other factors on cell proliferation, differentiation [24–29], and mineralization [30–33] in bone tissue. During bone reconstruction, several cell types, especially osteoblasts, colonize the bone defect. Osteoblasts are mostly responsible for bone regeneration because of their ability to secrete a large amount of proteins on the bone matrix surface by their large Golgi apparatus [34]. Owing to the important role osteoblasts play in bone formation, it is of great interest to investigate whether $TiO_2$ NPs could promote cell osteogenic differentiation. In this study, we investigate the influence of concentration, shape, and size of NPs on preosteoblast proliferation and its osteogenic differentiation by coculturing MC3T3-E1 cells with $TiO_2$ NPs. MC3T3-E1 cell proliferation is detected by the CCK-8 kit. Cell apoptosis and reactive oxidative species (ROS) are analyzed by flow cytometry. ALP and OCN are detected to evaluate the differentiation and proliferation of osteoblasts, and the mineralized nodules are stained using Alizarin Red to estimate the mineralization of osteoblasts.

## 2. Materials and Methods

*2.1. Materials.* The commercial pure $TiO_2$ NPs (A1, R1, and R2; Wan Jing New Material Co. Ltd.; purity > 99.8%) and rutile $TiO_2$ NPs (A2, Beijing Nanchen Technology Development Co. Ltd.) without any coating were used in this study, as shown in Table 1. Minimum Essential Medium Eagle (MEM) was purchased from Gibco Invitrogen (USA). Fetal bovine serum (FBS) was purchased from MDgenics (New Zealand). Penicillin G and streptomycin were purchased from INALCO (USA). Cell counting kit-8 (CCK-8); ALP assay kit; 2,7-dichlorodihydrofluorescein diacetate (DCFH-DA) assay kit; total glutathione assay kit; superoxide assay kit; total superoxide dismutase (SOD) assay kit with WST-1; lipid peroxidation product (malondialdehyde, MDA) assay kit; cell lysis buffer; and BCA protein assay kit were all obtained from Beyotime Institute of Biotechnology (Jiangsu, China). Phenylmethanesulfonyl fluoride (PMSF) was provided by Roche Co. Ltd. The trypsin was purchased from AMRESCO (USA). The mouse bone gla protein/osteocalcin (BGP/OCN) ELISA kit was provided by Nanjing Jiancheng Bioengineering Institute. Alizarin Red S was obtained from Bellancom Chemistry. Dexamethasone and $\beta$-glycerophosphate were obtained from Sigma-Fluka. L-ascorbic acid was purchased from AMRESCO (USA). All other reagents used in this study were analytical grade.

*2.2. Characterization of $TiO_2$ NPs.* $TiO_2$ NPs were suspended in anhydrous ethanol and ultrasonicated for 5 s × 10 circles at 200 W. The suspension was dipped on the cleaned silicon wafer. The size and shape of $TiO_2$ NPs were detected by SEM (Hitachi S-4800 SEM). TEM (FEI Tecnai G2 F20 S-Twin) was used to characterize the microstructure profile of $TiO_2$ NPs. The surface properties for $TiO_2$ NPs such as surface area, average pore diameter, and pore volume were determined under the Quadrasorb SI analyzer (Quantachrome Instruments, USA) by $N_2$ absorption at 77.3 K. To evaluate the dispersion and aggregation status of $TiO_2$ NPs in aqueous solution, the DLS method was performed by a particle size and zeta potential analyzer (Zetasizer Nano ZS90, Malvern Instruments, UK).

*2.3. Sedimental Observation of $TiO_2$ NPs Suspended in PBS.* A series of experiments were set to observe the sediment of the $TiO_2$ NP suspension. The $TiO_2$ NPs were dispersed in fresh sterilized PBS solution at the concentrations of 10, 30, and 100 $\mu$g/mL, respectively. To disperse the $TiO_2$ NPs, the suspension was ultrasonicated for 5 s with a 7 s interval at 200 W for 10 times (ultrasonic cell disruptor system, Jiangsu, China). Then, the $TiO_2$ NP suspension was left standing for 12 h. The sediment status was recorded by digital camera (Canon PowerShot S95, Japan). Then, 5, 10, 20, and 30 $\mu$g/mL nano-$TiO_2$ suspensions were prepared in PBS. To increase the dispersion of NPs, bovine serum albumin (BSA) was added in PBS with a concentration of 2 mg/mL (40 : 1 compared with the weight of $TiO_2$ NPs). The 20 $\mu$g/mL $TiO_2$ NPs in MEM was used as a contrast. All $TiO_2$ NP suspensions were standing for 48 h to record the status of the sediment.

*2.4. Cell Culture.* The mouse preosteoblast MC3T3-E1 cells were obtained from the National Platform of Experimental Cell Resources for Sci-Tech (Beijing, China). The cells were incubated in MEM supplemented with 10% FBS, 100 U/mL penicillin, and 100 $\mu$g/mL streptomycin at 37°C in a fully humidified atmosphere containing 5% $CO_2$ in air. The culture medium was changed every 3 d until the cells reached 80-100% confluence. The cells were seeded in 96-well plates at a density of $8.0 \times 10^3$ cells per well in 100 $\mu$L culture medium to evaluate the cell activity. For other analyses, the cells were seeded in 6-well plates at a density of $2.5 \times 10^5$ cells per well in 2 mL of culture medium. After 70% confluence, the cells were exposed to four types of nano-$TiO_2$ suspensions. The $TiO_2$ NP suspension (1 mg/mL) was freshly dispersed in PBS solution containing 2 mg/mL BSA. To avoid aggregation, the suspensions were ultrasonicated for 30 min in sealed sterile tubes. Then, the suspension was diluted by MEM to 20 $\mu$g/mL. After adding 10% FBS, 20 $\mu$g/mL $TiO_2$ NP suspension was

Table 1: Characterization of $TiO_2$ NPs.

| Original no. | No. | Crystal | Shape | Size (nm) | Specific surface area ($m^2$/g) | Average pore diameter (nm) | Total pore volume (cc/g) | *Z*-Ave (d·nm) | Zeta potential (mV) |
|---|---|---|---|---|---|---|---|---|---|
| 1 | A1 | Anatase | Red blood cell like | D: 45.87 ± 7.75 | 97.75 | 1.79 | 0.56 | 166.6 | 5.7 |
| 6 | A2 | Anatase | Sphere | D: 79.39 ± 22.58 | 10.37 | 1.93 | 0.05 | 653.3 | -18.7 |
| 2 | R1 | Rutile | Long rod | D: 52.37 ± 7.35 L: 86.55 ± 12.13 | 21.51 | 2.17 | 0.22 | 408.7 | 2.3 |
| 4 | R2 | Rutile | Long rod | D: 25.46 ± 9.65 L: 75.34 ± 13.28 | 28.27 | 2.44 | 0.17 | 183.6 | -22.0 |

cultured with MC3T3-E1 cells. Culture media without $TiO_2$ NPs served as the control in each experiment.

*2.5. CCK-8 Assay.* The MC3T3-E1 cells were exposed to four types of nano-$TiO_2$ for 24 h, and the concentration of NPs was 20 $\mu$g/mL. Then, the cells were washed with PBS for 2 times and incubated with 100 $\mu$L MEM medium and 10 $\mu$L CCK-8 at 37°C for 2 h. MEM and CCK-8 without cells were set as the negative control. The intensity was detected using the Varioskan Flash microplate reader (3001, Thermo Fisher Scientific, USA) at 450 nm. Cell viability was expressed as the percentage of viable cells relative to control. All experiments were performed at least in triplicate.

*2.6. Determination of ROS Production and Superoxide.* The production of ROS was determined by the fluorescence probe DCFH-DA. After being cocultured with four types of 20 $\mu$g/mL $TiO_2$ NPs for 24 h, MC3T3-E1 cells were collected. Then, the cells were incubated with 10 $\mu$M DCFH-DA in the dark for 20 min at 37°C and reverse mixed every 3-5 min to prove the full reaction of the probe with cells. Then, the cells were washed 3 times with serum-free culture medium. The cells cultured with 1 $\mu$L Rosup served as positive control. The oxidation of DCFH by ROS yields a highly fluorescent compound, 2′,7′-dichlorofluorescein (DCF), which can be analyzed by flow cytometry (BD FACSCalibur, USA). The mean intensity of DCF fluorescence was obtained from 20,000 cells in each experiment group under 488 nm excitation and 530 nm emission settings. WST-1 was reduced by superoxide to orange soluble formazan, which was detected at 450 nm. In this kit, the catalase enzyme was added to eliminate the interruption of $H_2O_2$, and SOD was used to exclude the interference and correct the result.

*2.7. TEM of MC3T3-E1 Cells.* For the TEM study, MC3T3-E1 cells cocultured with or without $TiO_2$ NPs were collected by a cell scraper, then immediately immersed in 2.5% glutaraldehyde at 4°C overnight. After washing with PBS sufficiently, the samples were fixed with 1% osmium tetroxide, dehydrated in a graded series of ethanol, embedded in araldite, and polymerized for 24 h at 37°C. The ultrathin sections (60 nm) were cut, stained with uranyl acetate and lead citrate, and then observed with a TEM (Hitachi H-600, Japan) at 50 kV.

*2.8. Cell Apoptosis Assay.* Apoptosis was assessed by Annexin V-FITC and PI staining followed by analysis with flow cytometry. The methodology followed the procedures as described in the Annexin V-FITC/PI detection kit. The cultured cells were exposed to four types of $TiO_2$ NPs at a concentration of 20 $\mu$g/mL for 24 h. Then, the cells were collected by trypsinization, washed with PBS, and centrifuged at 1,000 rpm for 5 min. The cells were resuspended at $1 \times 10^6$ cells/mL in Annexin V binding buffer solution eventually. Aliquots of cells (100 $\mu$L/tube) were incubated with 5 $\mu$L Annexin V-FITC, then mixed and incubated for 15 min at room temperature in the dark. PI was added to distinguish necrotic cells. Finally, 400 $\mu$L binding buffer was added to each tube, and the cells were analyzed by flow cytometry within 1 h of staining.

*2.9. Determination of ALP Activity and OCN.* ALP was assayed as the release of *p*-nitrophenol from *p*-nitrophenyl phosphate (pNPP) in alkaline buffer as mentioned before. Briefly, cell layers in a 6-well plate were washed 3 times with PBS and then incubated with 100 $\mu$L cell lysis buffer with 1% Triton X-100 for 40 min on ice. The cell lysates were removed with a cell scraper placed into an EP tube. After centrifugation at 12,000 rpm for 10 min at 4°C, the supernatant was used to determine the enzyme activity. At the same time, the protein content was also detected according to the BCA method. The products of OCN in the culture medium was measured using the method of ELISA. The assays were performed strictly according to the manufacturer's instruction. Briefly, a purified anti-mouse OCN antibody was precoated onto an ELISA microplate. The culture media was concentrated by lyophilization and reconstituted in PBS and pipetted into the wells. All OCN present was bound by the

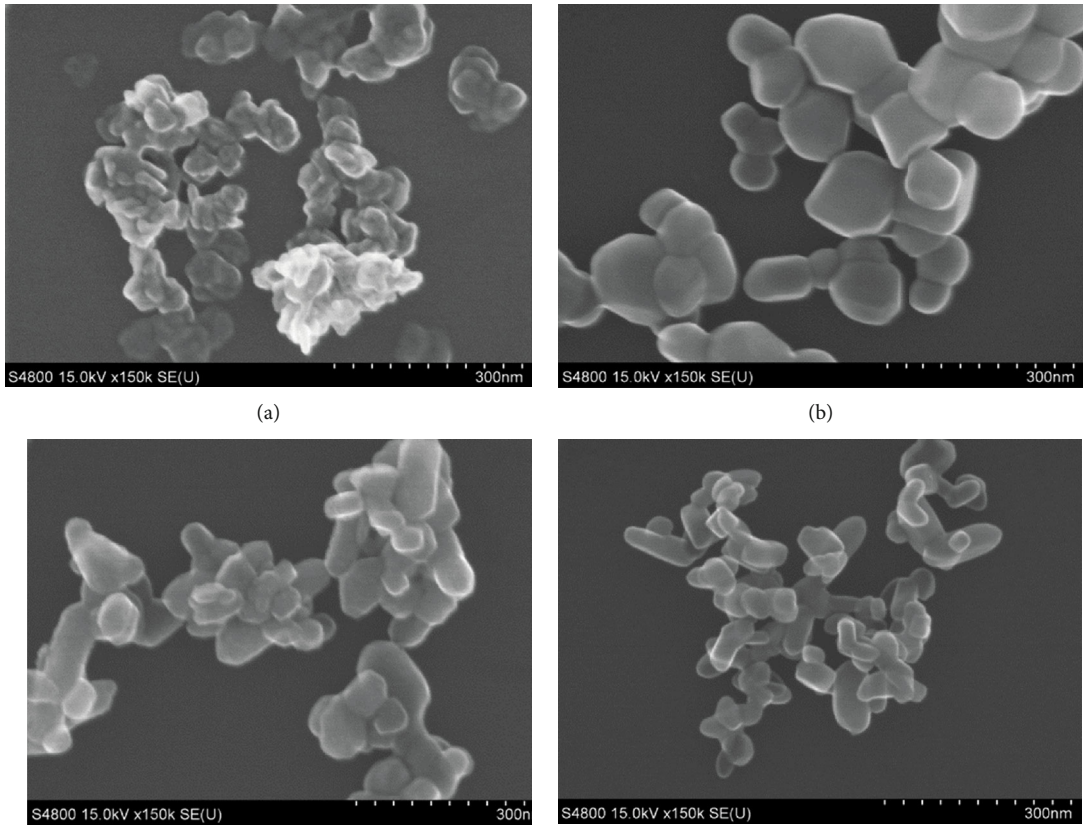


FIGURE 1: Micrographs of $TiO_2$ NPs by SEM. (a) The diameter of A1 $TiO_2$ NPs is $45.87 \pm 7.75$ nm. (b) The diameter of A2 $TiO_2$ NPs is $79.39 \pm 22.58$ nm. (c) The diameter and length of R1 $TiO_2$ NPs are $52.37 \pm 7.35$ nm and $86.55 \pm 12.13$ nm, respectively. (d) The diameter and length of R2 $TiO_2$ NPs are $25.46 \pm 9.65$ nm and $75.34 \pm 13.28$ nm, respectively.

immobilized antibody. Polyclonal HRP-conjugated avidin was used to measure the fixation of primary Abs.

*2.10. Mineralized Nodule Staining.* Alizarin Red S staining was used to evaluate the influence of $TiO_2$ NPs on MC3T3-E1 cell mineralization. Briefly, the cells were cultured to 100% confluence in MEM medium and exposed to four types of $TiO_2$ NPs in the osteogenic medium containing MEM medium and 10 mmol/L $\beta$-glycerophosphate and 0.05 mmol/L-ascorbic acid. The osteogenic medium was changed every 3 d. At 28 d, the cell layers were washed 3 times with PBS and fixed in 95% ethanol for 10 min. After being washed 3 times with water, the cells were stained by 0.1% Alizarin Red S for 30 min. The mineralized nodules were imaged and counted by microscopy.

*2.11. Statistical Analysis.* All data were reported as mean ± standard deviation (SD) and analyzed using the SPSS 13.0 (SPSS Inc., USA). Statistical analysis was performed for the experimental data using one-way analysis of variance (ANOVA). Results with $p < 0.05$ were considered statistically significant.

## 3. Results

*3.1. Characterization of $TiO_2$ NPs.* In this study, anatase and rutile $TiO_2$ were provided and characterized in detail. The SEM and TEM micrographs of $TiO_2$ NPs are shown in Figures 1 and 2. For the anatase $TiO_2$, A1 was like red blood cells (Figure 2(a)) with an average diameter of $45.87 \pm 7.75$ nm (Figure 1(a)). A2 was spherical (Figure 2(b)) with an average diameter of $79.39 \pm 22.58$ nm (Figure 1(b)). For the rutile $TiO_2$, R1 and R2 were long rods with different sizes (Figures 2(c) and 2(d)). The average length of R1 was $86.55 \pm 12.13$ nm and the average diameter was $52.37 \pm 7.35$ nm (Figure 1(c)), whereas the average length of R2 was $75.34 \pm 13.28$ nm and the average diameter was $25.46 \pm 9.65$ nm (Figure 1(d)). The physical properties of $TiO_2$ NPs are well summarized and listed in Table 1.

DLS was used to analyze the aggregation ability of $TiO_2$ NPs in solution. The hydrodynamic diameter distribution of $TiO_2$ NPs in an aqueous solution is shown in Figure 3. For the rutile $TiO_2$, R1 showed a peak at 408.7 nm (size distribution from 141 to 1106 nm) with a zeta potential of 2.3 mV, which suggested that R1 was agglomerated and aggregated easily in solution. R2 showed a narrow peak at 183.6 nm (size distribution from 105 to 396 nm), which indicated that the R2 suspension was stable owing to the zeta potential of -22.0 mV (Table 1). For anatase, the average diameter of A1 at the peak was 166.6 nm, and A2 showed a high, narrow peak at 235.3 nm with a low peak at 5.1 $\mu$m. The zeta potentials of the anatase and rutile suspensions are determined and listed in Table 1.

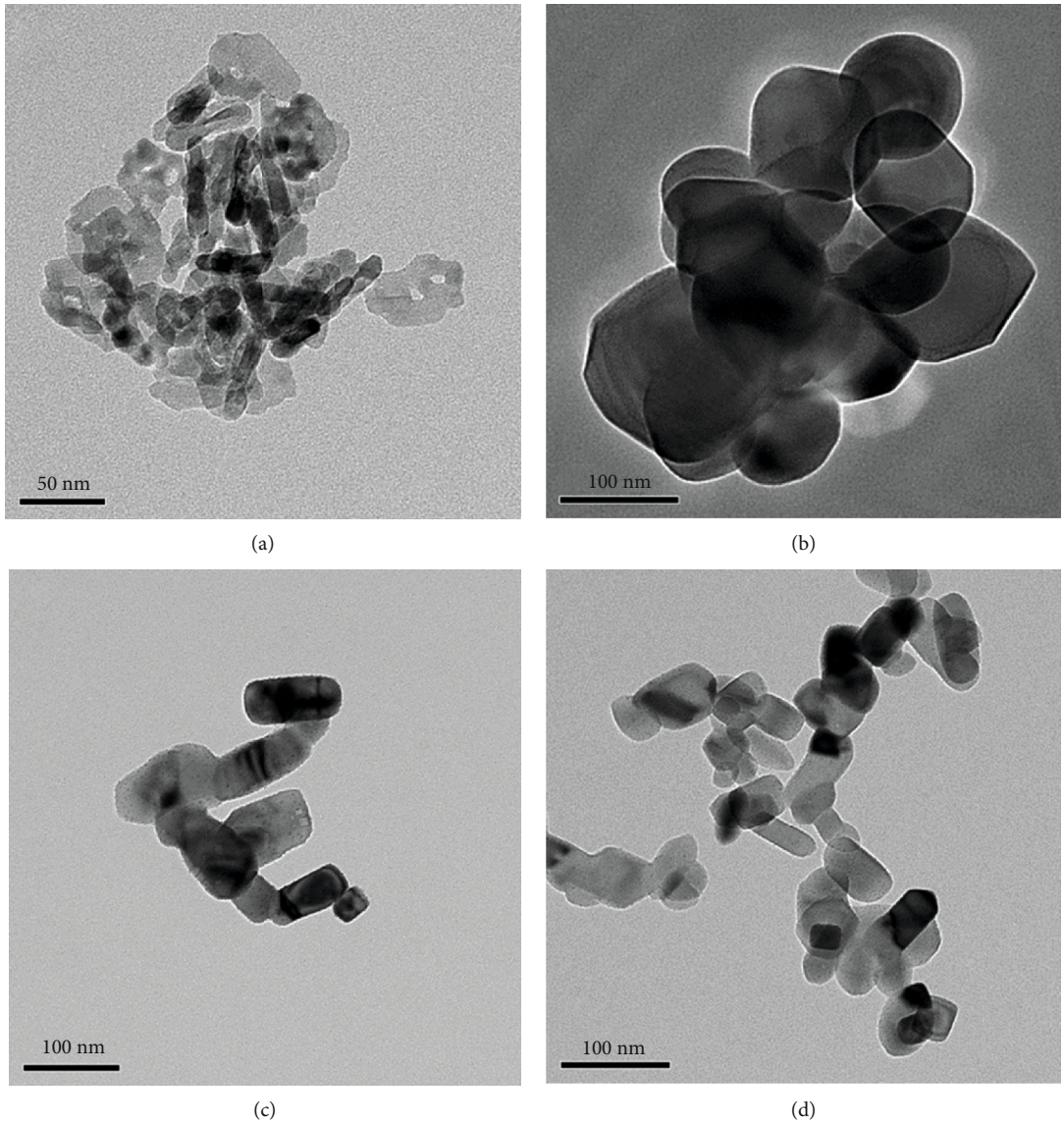


Figure 2: Micrographs of $TiO_2$ NPs by TEM: (a) A1 is erythrocyte like; (b) A2 is spherical; (c) R1 is a long rod; (d) R2 is a long rod.

*3.2. Determination of $TiO_2$ NP Concentration.* The sedimentation of $TiO_2$ NPs was recorded by camera to select the appropriate concentration used in the experiment. Figure S1 shows the sedimentation of $TiO_2$ at concentrations of 10, 30, and 100 $\mu$g/mL in PBS containing BSA for 12 h. The 100 $\mu$g/mL $TiO_2$ NP group was allowed to settle after standing for 2 h. There were some flocculated precipitates in 30 $\mu$g/mL $TiO_2$ NPs at 6.5 h, and the precipitates became obvious at 12 h. However, no sediment was observed in the suspension at the concentration of 10 $\mu$g/mL by settling for 12 h.

Figure S2 is the sedimentation of $TiO_2$ NPs lower than 30 $\mu$g/mL in PBS and culture medium for 48 h. The 20 $\mu$g/mL $TiO_2$ NPs in culture medium was set as control. The 30 $\mu$g/mL group showed flocculated precipitates at 12 h, whereas no precipitate could be found in $TiO_2$ NP suspension at a concentration of less than 20 $\mu$g/mL after 48 h. This indicated that the suspension with a concentration of less than 20 $\mu$g/mL showed good stability and dispersion both in PBS and in culture medium.

*3.3. Viability of MC3T3-E1 Cells Cocultured with $TiO_2$ NPs.* The cell viability was determined by coculturing MC3T3-E1 preosteoblast cells with A1 and R2 $TiO_2$ NPs at different concentrations (Figure 4). After 24 h incubation, cell viability was decreased over 50% when the concentration of $TiO_2$ NPs was higher than 50 $\mu$g/mL, and this group also exhibited high cytotoxicity (Figure 4(a)). The cells showed about 80% viability when the concentration of $TiO_2$ NPs was between 30 and 50 $\mu$g/mL, which was significantly lower than the control group (Figure 4(c)). However, when the concentration of $TiO_2$ NPs was lower than 10 $\mu$g/mL, it had no influence on cell viability (Figure 4(b)). At 20 $\mu$g/mL, $TiO_2$ NPs also

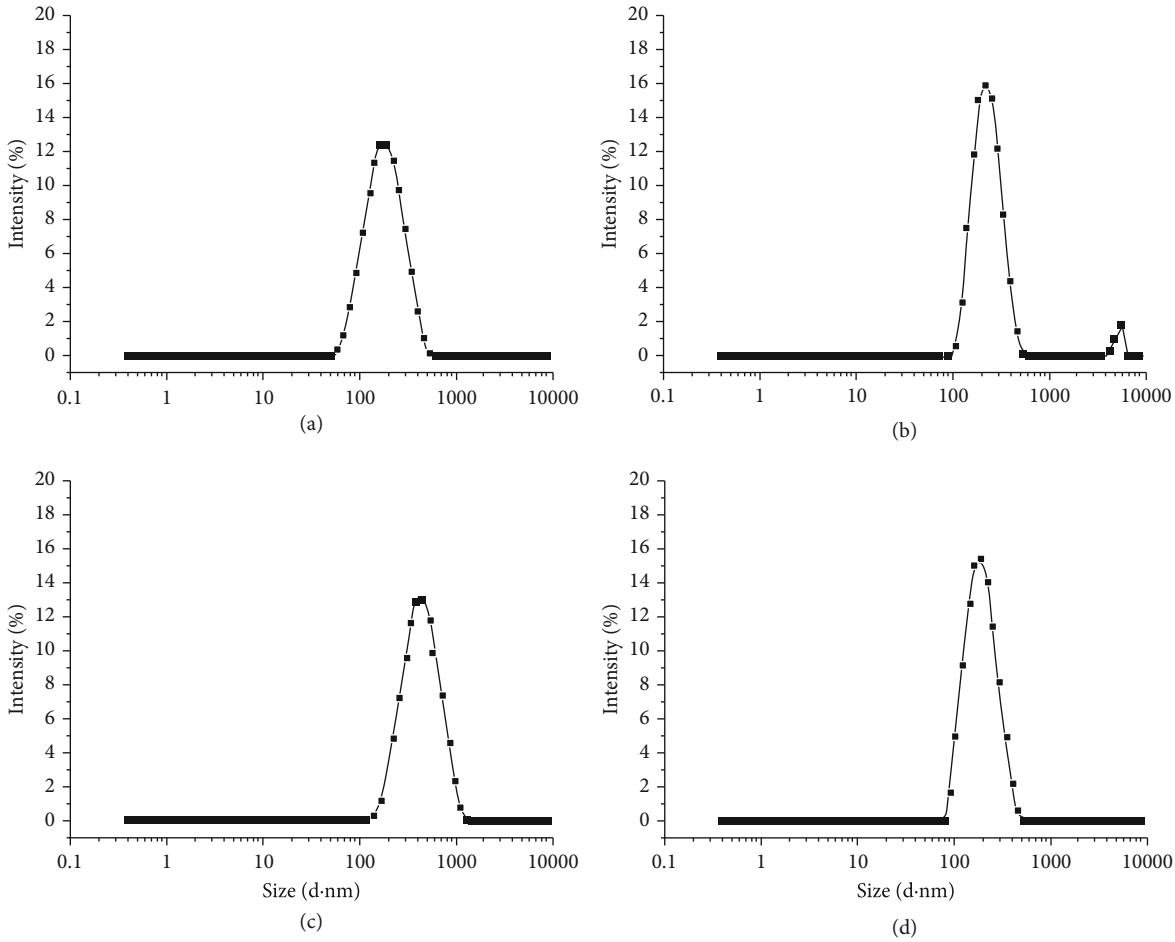


Figure 3: Hydrodynamic diameter distribution of nano-$TiO_2$ in aqueous solution analyzed by the DLS method. (a) The average diameter of A1 at the peak is 166.6 nm. (b) A2 shows a high, narrow peak at 235.3 nm. (c) R1 shows a peak at 408.7 nm. (d) R2 shows a narrow peak at 183.6 nm.

showed no obvious effect on cell viability. These results indicated that 20 $\mu$g/mL was a critical value for the cell viability of $TiO_2$ NPs, and different levels of cytotoxicity were shown over this concentration.

*3.4. ALP and OCN Expression of MC3T3-E1 Cells.* To find out the influence of NPs on ALP expression, the MC3T3-E1 cells were cocultured with A1 and R1 $TiO_2$ NPs at concentrations of 20, 50, and 100 $\mu$g/mL for 7 and 14 d. Compared with the blank control group, the osteogenic differentiation ability of all experimental groups was significantly decreased (Figure 5(a)). Moreover, A1 and R1 $TiO_2$ NPs had different degrees of influence on osteoblast differentiation. When the concentration is low, the inhibitory effect on cell differentiation of R1 is less than that of A1. However, with the increase of NP concentration, the inhibitory effect of rutile materials on cell differentiation was gradually stronger than that of anatase materials. The ALP level of cells cocultured with A1 and R1 materials for 14 d is shown in Figure 5(b). When the concentration of A1 was 20 $\mu$g/mL, the ALP level was reduced by 64.30% compared with the control. When the concentration was 50 and 100 $\mu$g/mL, the ALP level decreased by 43.01% and 47.69%, respectively. The inhibition effect of R1 on cell differentiation was similar with that of A1. These results indicated that both A1 and R1 had negative impacts on the differentiation of preosteoblast cells. As for the results of OCN, there was no significant difference between the experiments groups and the control group (Figure S3).

*3.5. Determination of ROS Production and the Antioxidant Level.* Lots of evidence pointed out that ROS production represented a hallmark in $TiO_2$ NP toxicity. In this study, ROS production and the antioxidant level in MC3T3-E1 cells were tested and the results are shown in Figure 6. The fluorescence intensity of oxidized DCF increased in cells when treated with $TiO_2$ NPs (Figure 6(a)), which was especially obvious in the A1, R1, and R2 groups ($p < 0.05$). This meant that ROS was generated in response to the treatment of 20 $\mu$g/mL $TiO_2$ NPs. In addition, WST-1 was used to detect the level of superoxide production in cells. Compared to the control group, four types of $TiO_2$ NPs induced significantly higher superoxide production (Figure 6(b)). Total glutathione (T-GSH), the main

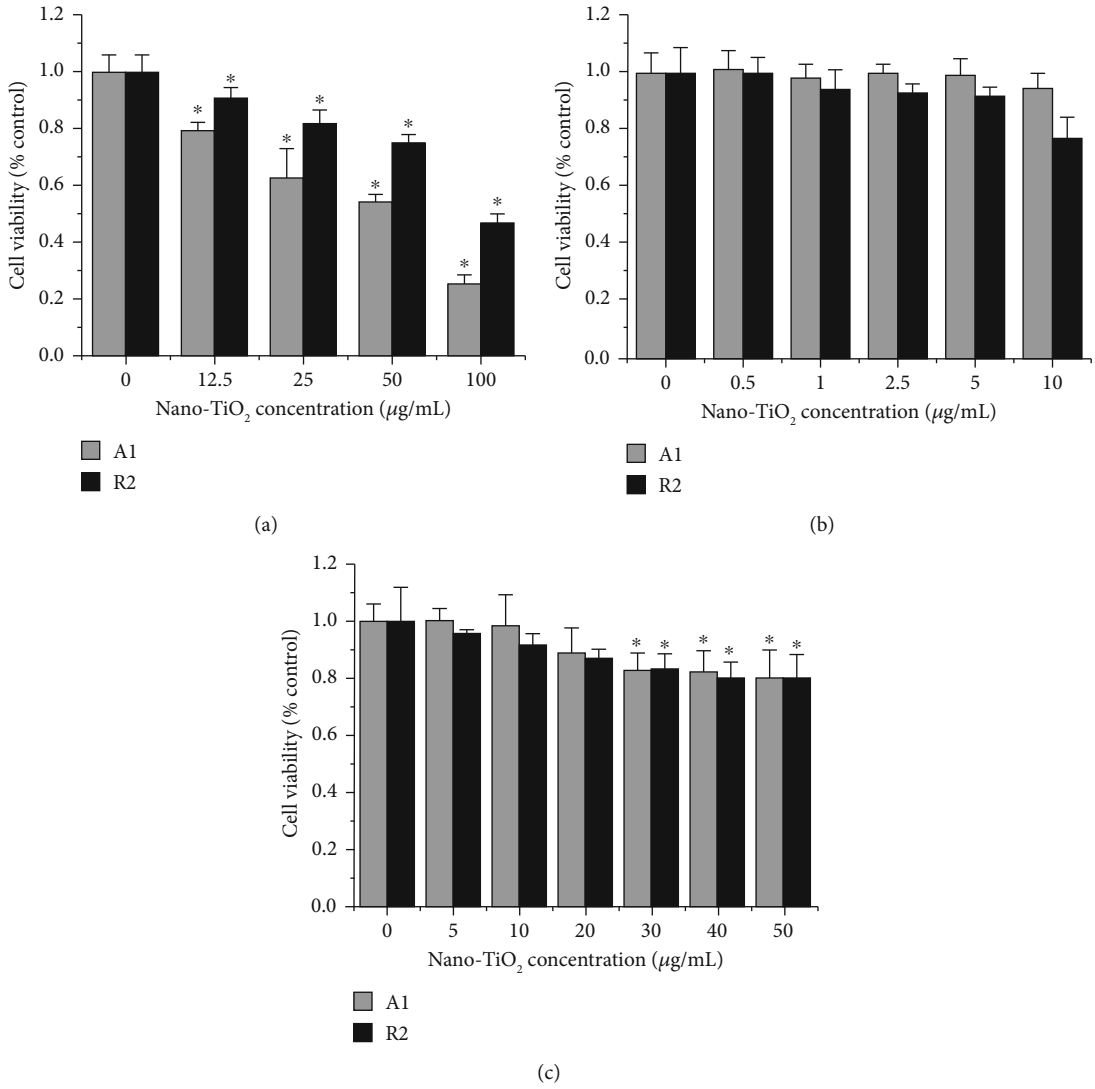


Figure 4: Cell viability of MC3T3-E1 cells cocultured with different concentrations of $TiO_2$ NPs. $^*p < 0.05$ significantly different from the corresponding control group.

antioxidant, decreased in $TiO_2$ NP-treated cells, and the significantly downregulated T-GSH was detected in the A1 and R1 groups (Figure 6(c)). SOD and MDA were also detected to show the level of oxidative stress in MC3T3-E1 cells. After treatment with $TiO_2$ NPs, SOD and MDA activity was slightly higher than that in the control, which was especially obvious for the R1 group ($p < 0.05$) (Figures 6(d) and 6(e)).

*3.6. TEM Characterization of MC3T3-E1 Cells Cocultured with $TiO_2$ NPs.* After coculturing with $TiO_2$ NPs, the membrane of MC3T3-E1 cells was distorted and caved in, enclosing the aggregated $TiO_2$ NPs (Figure 7(a)). The clustered $TiO_2$ NPs were enclosed by the plasma membrane of cells and internalized into the cytoplasm around cell nucleus (Figure 7(b)). Some NPs were located in the mitochondria, and the internalization of $TiO_2$ NPs caused the ultrastructural change of MC3T3-E1 cells. The nuclear envelope was distorted though the cell nucleus was clear and intact. Meanwhile, the nuclear chromatin was condensed and distributed over the fringe of the nucleus. The number of mitochondria and lysosome increased, and the lamellar cristae became irregular and disordered. At the same time, mitochondrial structures became swollen and vacuous, suggesting that the storage of nano-$TiO_2$ within mitochondria resulted in some damage to the organelle. The swelling of the golgi complex was also observed (Figure 7(c)), which suggested the injury of the golgi complex. After exposure to A2 and R2 for 24 h, cell disintegration and an apoptotic body appeared (Figures 7(d) and 7(e)). The TEM results indicated that $TiO_2$ NPs were absorbed in the cells and induced some injury at the subcellular level.

*3.7. Cell Apoptosis and Mineralized Nodules of MC3T3-E1 Cells Cocultured with $TiO_2$ NPs.* MC3T3-E1 cell apoptosis and necrosis were observed by flow cytometry

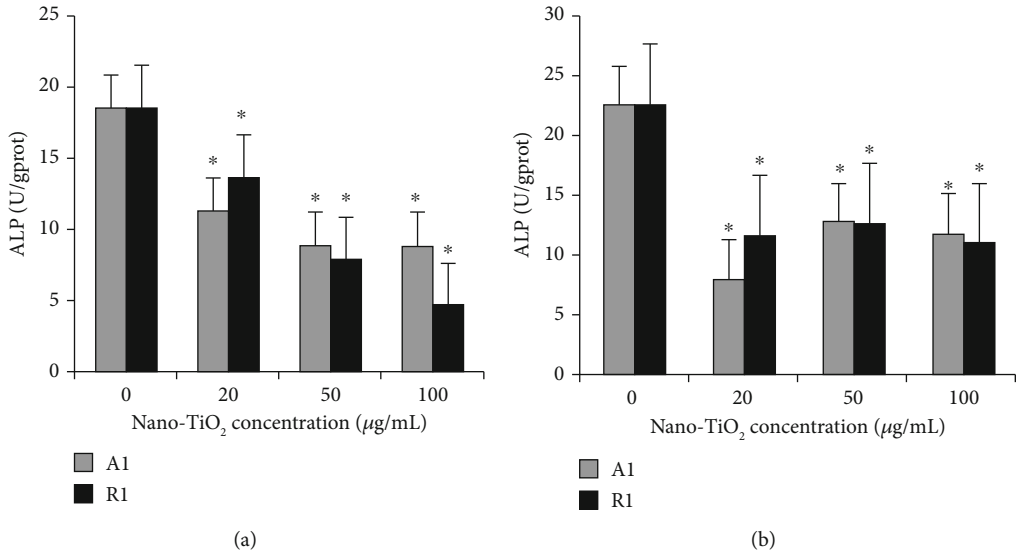


Figure 5: ALP expression of MC3T3-E1 cells cocultured with $TiO_2$ NPs for 7 d (a) and 14 d (b). $^*p < 0.05$ significantly different from the corresponding control group.

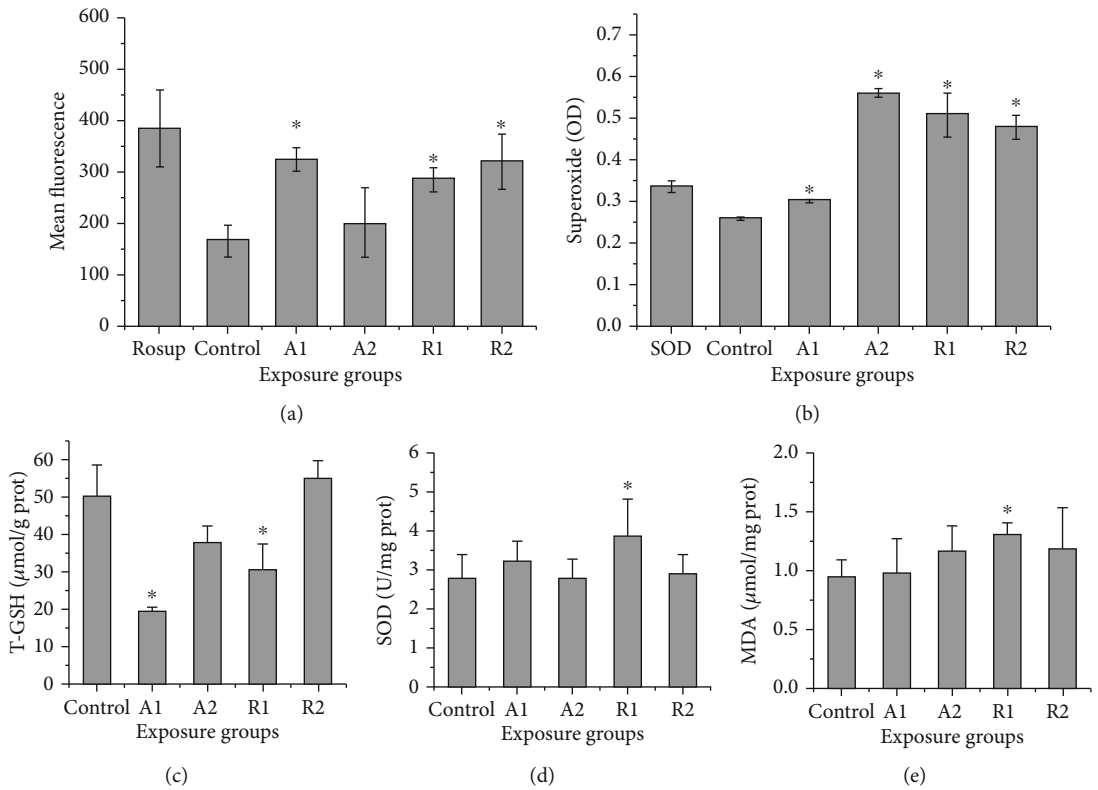


Figure 6: Oxidative stress in MC3T3-E1 cells treated with nano-$TiO_2$ for 24 h by measuring the levels of (a) ROS, (b) superoxide production, (c) total glutathione (T-GSH), (d) SOD, and (e) MDA. Data are expressed as mean ± SD of three repeated experiments. $^*p < 0.05$; significantly different from the control group.

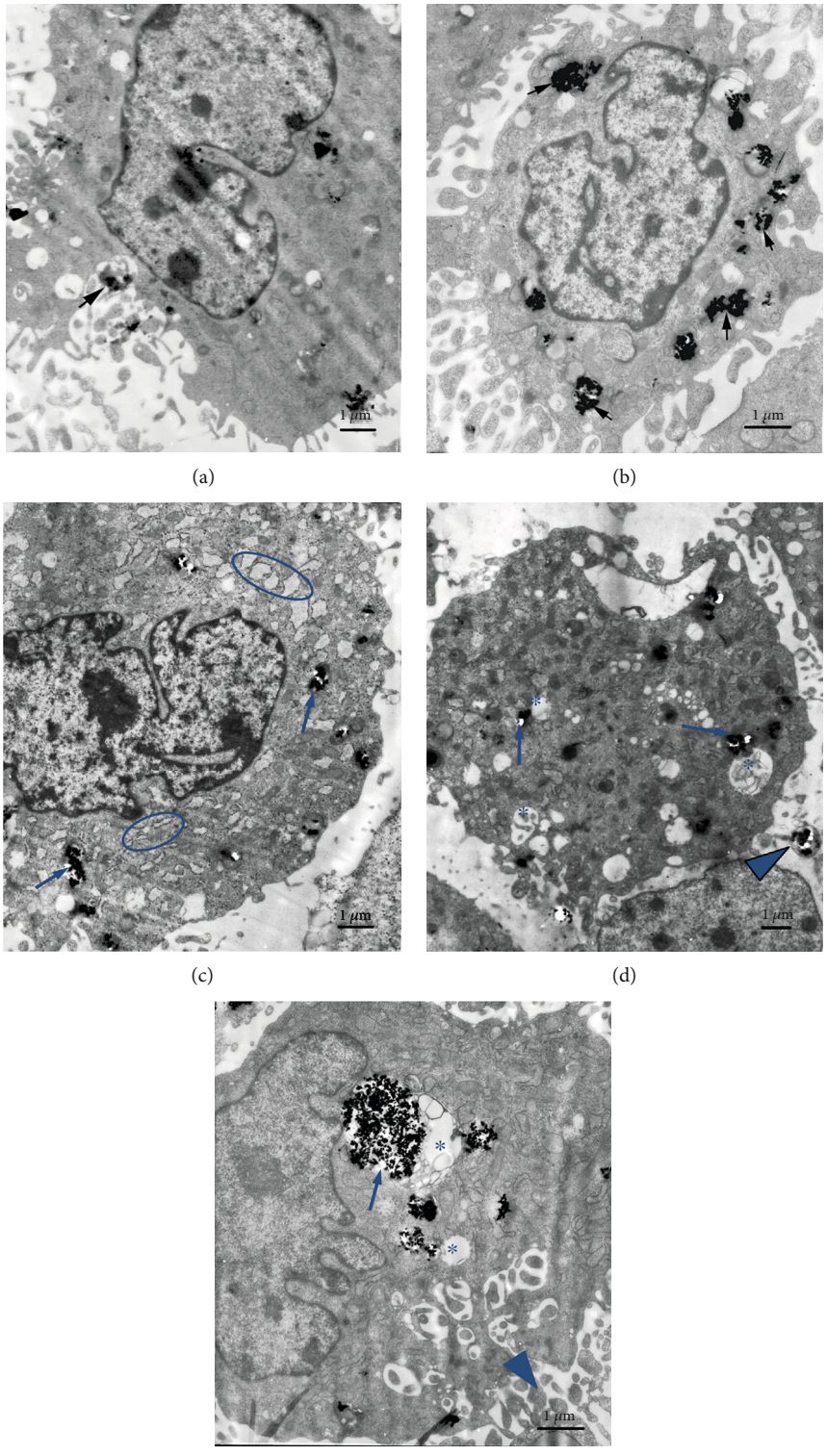


FIGURE 7: The ultrastructure morphology of MC3T3-E1 cells after exposure to $TiO_2$ NPs for 24 h. ∗ indicates the swelling of mitochondria and vacuolization. ↗ indicates the internalization of $TiO_2$ NPs and aggregation in the cytoplasm. *O* indicates the swelling of the golgi complex. ▲ indicates the apoptotic body.

quantitatively. As shown in Figure 8, after exposure to the four types of $TiO_2$ NPs, the percentage of cells in early apoptosis increased by 130.37% (A1), 81.38% (A2), 99.63% (R1), and 116.11% (R2) compared to the control group, respectively. Moreover, the percentage of cells in late apoptosis and necrosis in the exposure groups was significantly higher than that in the control group. However, it is worth noting that the majority of the cells were alive. The percentage of live cells was 88.64% in the control group, and the percentage in the exposure groups remained at the level of about 80%. This was consistent with the result obtained by the CCK-8 method.

After 28 d of culture with differential medium, the mineralized nodules were stained with Alizarin Red S (Figure 9). The mineralized nodules could be found in all groups, which increased significantly in $TiO_2$ NP-exposed groups. These results indicated that $TiO_2$ NPs promoted osteoblast mineralization and maturation.

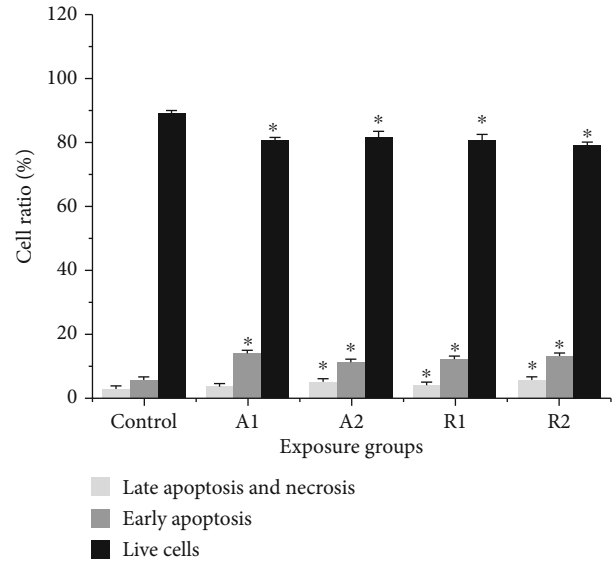


Figure 8: Cell apoptosis and necrosis detected by flow cytometry after being treated with nano-$TiO_2$ for 24 h. $^*p < 0.05$; significantly different from the control group.

## 4. Discussion

In this study, we selected anatase and rutile $TiO_2$ NPs as test nanomaterials. MC3T3-E1 preosteoblast cells were used as tested cells to evaluate the influence of $TiO_2$ NPs with different sizes and shapes on bone formation. Firstly, the sizes and shapes of $TiO_2$ NPs were evaluated by SEM and TEM. The anatase nanomaterials were like red blood cells with a diameter of $45.87 \pm 7.75$ nm and had a spherical shape with a diameter of $79.39 \pm 22.58$ nm. Some studies found that the same materials with different sizes have a different influence on cell formation [35]. It is generally believed that the particles with sizes smaller than 10 $\mu$m are easily swallowed by cells, while those with sizes bigger than 10 $\mu$m are more likely to be circumvoluted by macrophages. Based on this, we predicted that the nanomaterials can be swallowed by preosteoblasts and influence the cells. According to the results of the NP suspension precipitation experiment, we found that material concentrations below 30 $\mu$g/mL can guarantee no precipitation for 24 h. By measuring the effects of different concentrations of $TiO_2$ NPs on cell proliferation, we determined that the optimum material concentration for experiments is 20 $\mu$g/mL, which not only conforms with the actual range of material concentration in the physical environment but also ensures that $TiO_2$ NP precipitation does not occur after 24 h.

Osteoblast is the main cell type participating in bone formation, which is responsible for synthesis, secretion, and mineralization of the bone matrix. Bone is constantly reconstructed, and the bone reconstruction process is maintained by the cooperation of osteoblasts and osteoclasts. The balance between osteoblasts and osteoclasts is the key to maintaining normal bone mass. It was found that particles from high molecular polyethylene wear can inhibit the proliferation and differentiation of osteoblasts [36]. We find the same trend in the process of cocultivation of $TiO_2$ NPs and osteoblasts. By cell proliferation tests, we can find that if the concentration of $TiO_2$ NPs is lower than 50 $\mu$g/mL, the osteoblast proliferation is significantly impaired as the particle concentration increases. Once the concentration of $TiO_2$ NPs is less than 10 $\mu$g/mL, the NPs do not produce a dose effect on cells. We reckon that cell proliferation ability does not show an obvious change when the material concentration is too low. Besides, when the concentration of $TiO_2$ NPs is in the range of 10-50 $\mu$g/mL, the dose effect on cells appears at a slower trend. The comprehensive results show that $TiO_2$ NPs can affect cell growth and metabolism, seriously reducing the number of living cells. This is probably because NPs are recognized as foreign bodies, and the exogenous substances block cell endocytosis and metabolism.

We selected 20 $\mu$g/mL as the test concentration to observe the effect of coculture time with different types of $TiO_2$ NPs on osteoblast differentiation and intracellular mineralization. The results showed that at short coculture times, the NPs had little effect on osteoblasts, but when the coculture time was prolonged to 7 or 14 d, it showed a significant difference. All experimental groups inhibited the expression of ALP, which means that $TiO_2$ NPs inhibit the proliferation and differentiation of MC3T3-E1 cells, and anatase NPs inhibited the expression of ALP more than rutile NPs. The results of oxidative stress also indicated that $TiO_2$ NPs can induce cells to produce ROS and superoxide, leading to cell apoptosis or necrosis. Some studies reveal that metallic ions have a significant influence on the cell cycle distribution of osteoblasts, inhibiting their proliferation and leaving most cells dormant [37, 38]. From the TEM micrograph of MC3T3-E1 cells, we can also see that NPs are prone to reuniting in the solution, then entering mitochondria after being swallowed, causing mitochondrial degeneration, necrosis, cavitation, and even an intracellular material leakage phenomenon which reduces the activity and differentiation ability of cells. At the same time, the apoptosis rate increased and the ALP expression was inhibited by $TiO_2$ NPs, which reduce the vitality of osteoblasts. Thereafter, we can conclude that though $TiO_2$ NPs can

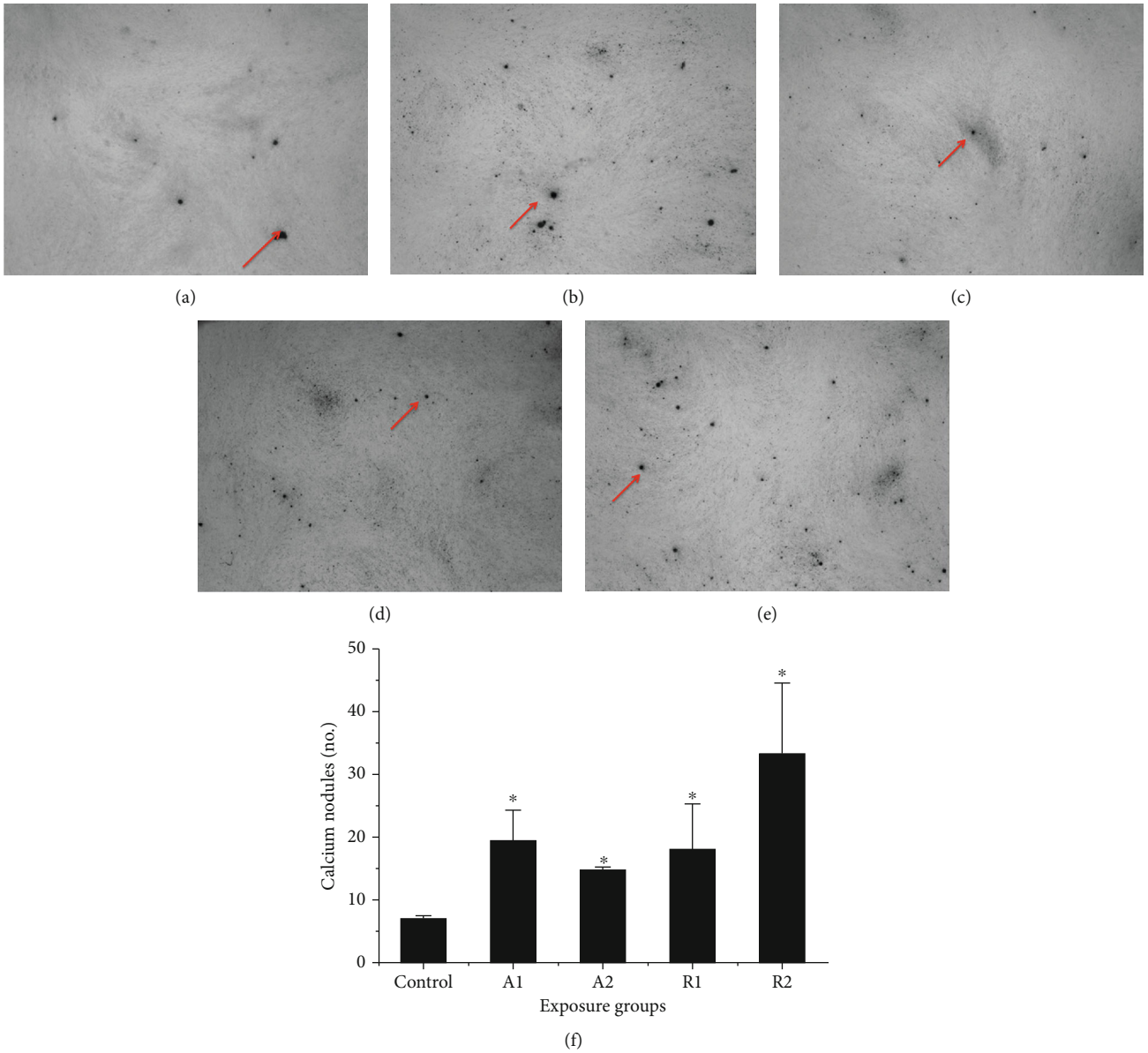


Figure 9: Alizarin Red S-stained mineralized nodules after coculture with differentiation medium for 28 d (arrows). There were more mineralized nodules in the experimental groups (b, c, d, e) compared with the control group (a). (f) Statistical graph of the quantity of mineralized nodules in different groups. There were significant differences between four experimental groups and the control group.

promote the maturation and mineralization of osteoblasts, they are not absolutely safe biomedical materials, and even a low dose of 20 $\mu$g/mL for short periods of stimulation has influence on cells.

## 5. Conclusion

$TiO_2$ NPs have a certain negative influence on bone formation. Here, we find that all the concentrations, shapes, and coculture times of nano-$TiO_2$ have different influence on the proliferation and differentiation of bone cells. In general, the presence of nano-$TiO_2$ in tissues can accelerate cell senescence and apoptosis, leading to decreased osteoblast activity and obstructed bone formation.

## Data Availability

The data used to support the findings of this study are available from the corresponding authors upon request.

## Conflicts of Interest

The authors declare that they have no conflicts of interest.

## Authors' Contributions

Yixing Ren and Xinxing Feng contributed equally to this work.

## Acknowledgments

This study was supported financially by the Shenzhen Science and Technology Project (JCYJ20170817140537062).

## Supplementary Materials

Supplementary 1 Sedimentation of nano-$TiO_2$ with different concentrations in PBS. Supplementary 2 Sedimentation of nano-$TiO_2$ in PBS (the first 4 tubes) compared with that in MEM (the last tube) ($TiO_2$ : BSA = 1 : 40). Supplementary 3 The results of OCN measured by ELISA. There was no significant difference between the experimental groups and the control group. *(Supplementary Materials)*

## References

[1] J. Jeevanandam, A. Barhoum, Y. S. Chan, A. Dufresne, and M. K. Danquah, "Review on nanoparticles and nanostructured materials: history, sources, toxicity and regulations," *Beilstein Journal of Nanotechnology*, vol. 9, pp. 1050–1074, 2018.

[2] H. Shi, R. Magaye, V. Castranova, and J. Zhao, "Titanium dioxide nanoparticles: a review of current toxicological data," *Particle and Fibre Toxicology*, vol. 10, no. 1, p. 15, 2013.

[3] S. Silva, H. Oliveira, A. M. S. Silva, and C. Santos, "The cytotoxic targets of anatase or rutile + anatase nanoparticles depend on the plant species," *Biologia Plantarum*, vol. 61, no. 4, pp. 717–725, 2017.

[4] A. Hasan, M. Morshed, A. Memic, S. Hassan, T. Webster, and H. Marei, "Nanoparticles in tissue engineering: applications, challenges and prospects," *International Journal of Nanomedicine*, vol. Volume 13, pp. 5637–5655, 2018.

[5] X. Li, J. Wei, K. E. Aifantis et al., "Current investigations into magnetic nanoparticles for biomedical applications," *Journal of Biomedical Materials Research Part A*, vol. 104, no. 5, pp. 1285–1296, 2016.

[6] A. Jimeno-Romero, M. Oron, M. P. Cajaraville, M. Soto, and I. Marigomez, "Nanoparticle size and combined toxicity of $TiO_2$ and DSLS (surfactant) contribute to lysosomal responses in digestive cells of mussels exposed to $TiO_2$ nanoparticles," *Nanotoxicology*, vol. 10, no. 8, pp. 1168–1176, 2016.

[7] T. H. Kim, M. S. Kang, N. Mandakhbayar, A. El-Fiqi, and H. W. Kim, "Anti-inflammatory actions of folate-functionalized bioactive ion-releasing nanoparticles imply drug-free nanotherapy of inflamed tissues," *Biomaterials*, vol. 207, pp. 23–38, 2019.

[8] I. Pujalte, D. Dieme, S. Haddad, A. M. Serventi, and M. Bouchard, "Toxicokinetics of titanium dioxide ($TiO_2$) nanoparticles after inhalation in rats," *Toxicology Letters*, vol. 265, pp. 77–85, 2017.

[9] S. Vial, R. L. Reis, and J. M. Oliveira, "Recent advances using gold nanoparticles as a promising multimodal tool for tissue engineering and regenerative medicine," *Current Opinion in Solid State & Materials Science*, vol. 21, no. 2, pp. 92–112, 2017.

[10] K. Zhang, Y. Fan, N. Dunne, and X. Li, "Effect of microporosity on scaffolds for bone tissue engineering," *Regenerative Biomaterials*, vol. 5, no. 2, pp. 115–124, 2018.

[11] A. J. Haider, Z. N. Jameel, and I. H. M. Al-Hussaini, "Review on: titanium dioxide applications," *Energy Procedia*, vol. 157, pp. 17–29, 2019.

[12] M. H. Hamzah, S. Eavani, and E. Rafiee, "CoAl2O4/TiO2 nano composite as an anti-corrosion pigment," *Materials Chemistry and Physics*, vol. 242, p. 122495, 2020.

[13] I. Narkevica, L. Stradina, L. Stipniece, E. Jakobsons, and J. Ozolins, "Electrophoretic deposition of nanocrystalline $TiO_2$ particles on porous $TiO_{2-X}$ ceramic scaffolds for biomedical applications," *Journal of the European Ceramic Society*, vol. 37, no. 9, pp. 3185–3193, 2017.

[14] T. V. S. S. P. Sashank, B. Manikanta, and A. Pasula, "Fabrication and experimental investigation on dye sensitized solar cells using titanium dioxide nano particles," *Materials Today: Proceedings*, vol. 4, no. 2, pp. 3918–3925, 2017.

[15] J. Ferin, G. Oberdörster, and D. P. Penney, "Pulmonary retention of ultrafine and fine particles in rats," *American Journal of Respiratory Cell and Molecular Biology*, vol. 6, no. 5, pp. 535–542, 1992.

[16] R. Kumazawa, F. Watari, N. Takashi, Y. Tanimura, M. Uo, and Y. Totsuka, "Effects of Ti ions and particles on neutrophil function and morphology," *Biomaterials*, vol. 23, no. 17, pp. 3757–3764, 2002.

[17] T. Brzicova, J. Sikorova, A. Milcova et al., "Nano-$TiO_2$ stability in medium and size as important factors of toxicity in macrophage-like cells," *Toxicology In Vitro*, vol. 54, pp. 178–188, 2019.

[18] M. Ibrahim, J. Schoelermann, K. Mustafa, and M. R. Cimpan, "$TiO_2$ nanoparticles disrupt cell adhesion and the architecture of cytoskeletal networks of human osteoblast-like cells in a size dependent manner," *Journal of Biomedical Materials Research Part A*, vol. 106, no. 10, pp. 2582–2593, 2018.

[19] K. Hattori, K. Nakadate, A. Morii, T. Noguchi, Y. Ogasawara, and K. Ishii, "Exposure to nano-size titanium dioxide causes oxidative damages in human mesothelial cells: the crystal form rather than size of particle contributes to cytotoxicity," *Biochemical and Biophysical Research Communications*, vol. 492, no. 2, pp. 218–223, 2017.

[20] M. J. Bessa, C. Costa, J. Reinosa et al., "Toxicity of rutile $TiO_2$ nanoparticles immobilized in nanokaolin nanocomposites on $HepG_2$ cell line," *Toxicology and Applied Pharmacology*, vol. 316, pp. 114–122, 2017.

[21] V. Madhubala, A. Pugazhendhi, and K. Thirunavukarasu, "Cytotoxic and immunomodulatory effects of the low concentration of titanium dioxide nanoparticles ($TiO_2$ NPs) on human cell lines—an in vitro study," *Process Biochemistry*, vol. 86, pp. 186–195, 2019.

[22] P. Kumar, "Nano-TiO2Doped chitosan scaffold for the bone tissue engineering applications," *International Journal of Biomaterials*, vol. 2018, Article ID 6576157, 7 pages, 2018.

[23] M. Dang, L. Saunders, X. Niu, Y. Fan, and P. X. Ma, "Biomimetic delivery of signals for bone tissue engineering," *Bone Research*, vol. 6, no. 1, p. 25, 2018.

[24] F. Gao, Z. Xu, Q. Liang et al., "Osteochondral regeneration with 3D-printed biodegradable high-strength supramolecular polymer reinforced-gelatin hydrogel scaffolds," *Advanced Science*, vol. 6, no. 15, p. 1900867, 2019.

[25] F. Gao, Z. Xu, Q. Liang et al., "Direct 3D printing of high strength biohybrid gradient hydrogel scaffolds for efficient repair of osteochondral defect," *Advanced Functional Materials*, vol. 28, no. 13, 2018.

[26] Y. Huang, X. Niu, W. Song, C. Guan, Q. Feng, and Y. Fan, "Combined effects of mechanical strain and hydroxyapatite/-collagen composite on osteogenic differentiation of rat bone

marrow derived mesenchymal stem cells," *Journal of Nanomaterials*, vol. 2013, Article ID 343909, 7 pages, 2013.

[27] Y. Ma, N. Hu, J. Liu et al., "Three-dimensional printing of biodegradable piperazine-based polyurethane-urea scaffolds with enhanced osteogenesis for bone regeneration," *ACS Applied Materials & Interfaces*, vol. 11, no. 9, pp. 9415–9424, 2019.

[28] F. Yang, X. Niu, X. Gu, C. Xu, W. Wang, and Y. Fan, "Biodegradable magnesium-incorporated poly(L-lactic acid) microspheres for manipulation of drug release and alleviation of inflammatory response," *ACS Applied Materials & Interfaces*, vol. 11, no. 26, pp. 23546–23557, 2019.

[29] X. Zhai, C. Ruan, Y. Ma et al., "3D-bioprinted osteoblast-laden nanocomposite hydrogel constructs with induced microenvironments promote cell viability, differentiation, and osteogenesis both in vitro and in vivo," *Advanced Science*, vol. 5, no. 3, 2018.

[30] T. Du, X. Niu, S. Hou et al., "Highly aligned hierarchical intrafibrillar mineralization of collagen induced by periodic fluid shear stress," *Journal of Materials Chemistry B*, vol. 8, no. 13, pp. 2562–2572, 2020.

[31] X. Niu, S. Chen, F. Tian, L. Wang, Q. Feng, and Y. Fan, "Hydrolytic conversion of amorphous calcium phosphate into apatite accompanied by sustained calcium and orthophosphate ions release," *Materials Science & Engineering C-Materials for Biological Applications*, vol. 70, Part 2, pp. 1120–1124, 2017.

[32] X. Niu, R. Fan, X. Guo et al., "Shear-mediated orientational mineralization of bone apatite on collagen fibrils," *Journal of Materials Chemistry B*, vol. 5, no. 46, pp. 9141–9147, 2017.

[33] X. Niu, R. Fan, F. Tian et al., "Calcium concentration dependent collagen mineralization," *Materials Science & Engineering C-Materials for Biological Applications*, vol. 73, pp. 137–143, 2017.

[34] R. G. Tilkin, N. Regibeau, S. D. Lambert, and C. Grandfils, "Correlation between surface properties of polystyrene and polylactide materials and fibroblast and osteoblast cell line behavior: a critical overview of the literature," *Biomacromolecules*, vol. 21, no. 6, pp. 1995–2013, 2020.

[35] M. Sajid, M. Ilyas, C. Basheer et al., "Impact of nanoparticles on human and environment: review of toxicity factors, exposures, control strategies, and future prospects," *Environmental Science and Pollution Research*, vol. 22, no. 6, pp. 4122–4143, 2015.

[36] H. Zreiqat, T. N. Crotti, C. R. Howlett, M. Capone, B. Markovic, and D. R. Haynes, "Prosthetic particles modify the expression of bone-related proteins by human osteoblastic cells in vitro," *Biomaterials*, vol. 24, no. 2, pp. 337–346, 2003.

[37] C. E. Albers, W. Hofstetter, K. A. Siebenrock, R. Landmann, and F. M. Klenke, "In vitrocytotoxicity of silver nanoparticles on osteoblasts and osteoclasts at antibacterial concentrations," *Nanotoxicology*, vol. 7, no. 1, pp. 30–36, 2012.

[38] N. J. Hallab, C. Vermes, C. Messina, K. A. Roebuck, T. T. Glant, and J. J. Jacobs, "Concentration-and composition-dependent effects of metal ions on human MG-63 osteoblasts," *Journal of Biomedical Materials Research*, vol. 60, no. 3, pp. 420–433, 2002.

Hindawi
Journal of Nanomaterials
Volume 2020, Article ID 1257646, 14 pages
https://doi.org/10.1155/2020/1257646

*Review Article*

# Electrospun Nanofibers Containing Strontium for Bone Tissue Engineering

**Qi Zhang**[1], **Yanjing Ji**[2], **Weiping Zheng**[2], **Mingzhe Yan**[3], **Danyang Wang**[2], **Min Li**[3], **Junbo Chen**[1], **Xiao Yan**[1], **Qiang Zhang**[1], **Xiao Yuan**[1,4] and **Qihui Zhou**[1,2,3,4]

[1]*Department of Orthodontics, The Affiliated Hospital of Qingdao University, Qingdao 266003, China*
[2]*Department of Stomatology, The Affiliated Hospital of Qingdao University, Qingdao 266003, China*
[3]*Institute for Translational Medicine, Qingdao University, Qingdao 266021, China*
[4]*School of Stomatology, Qingdao University, Qingdao 266003, China*

Correspondence should be addressed to Xiao Yuan; yuanxiaoqd@163.com and Qihui Zhou; qihuizhou@qdu.edu.cn

Received 26 July 2020; Revised 10 September 2020; Accepted 22 September 2020; Published 24 October 2020

Academic Editor: Xiaoming Li



Electrospun polymer/metal composite nanofibers have received much attention in the field of bone tissue engineering and regenerative medicine (BTERM) owing to their extracellular matrix- (ECM-) like structure, sufficient mechanical strength, favorable biological properties, and bone induction. In particular, electrospun nanofibers containing strontium (Sr) can significantly promote bone repair and regeneration by mediating osteolysis and osteogenesis, which offers a promising bioactive material for BTERM. In this review, we summarized the effects of electrospun nanofibers containing Sr on stem cells, osteoblasts, and osteoclasts in BTERM. Also, current challenges and future perspectives for electrospun nanofibers containing Sr in BTERM are briefly outlined. It is hoped that the systematic overview will inspire the readers to further study Sr-containing nanofibers for BTERM and accelerate their translation from the bench to the clinic.

## 1. Introduction

*1.1. Bone Defect in Clinical Treatments.* Bone is a biological structure that can regenerate by combining with biochemical, cellular, or hormonal processes. The unique structure of natural bone confers excellent mechanical properties, which can support the body, allow movement, protect internal organs, and regulate the storage and release of minerals [1]. Also, bone is a hierarchically structured tissue, mainly composed of organic (30%) and inorganic (70%) components. Microscopically, hydroxyapatite (HAp) nanocrystals can be found to be deposited regularly in the collagen interstitial area during bone biomineralization [2]. At the macro level, the bone can be divided into the cortical bone and cancellous bone [3]. Cortical bones are mainly distributed in the long bone shaft, commonly with the elastic modulus (17~20 GPa) and compressive strength (131~224 MPa) [4]. In contrast, cancellous bone has a much lower modulus of elasticity because of its high porosity [5]. Therefore, cancellous bone is generally used as a reference to evaluate the mechanical properties of the bone. There are four types of cells in bone tissue: osteogenesis cells, osteoprogenitor cells, osteoblasts, and osteoclasts [6]. Osteoprogenitor cells, as the main cells of bone, can be differentiated into mature bone cells and then further transformed into osteoblasts through activation and proliferation during bone damage and repair. Osteoblasts can produce new bones through osteogenic differentiation, including three stages: proliferation, matrix maturation, and mineralization. The main indicators of osteoblast phenotype are collagen type I, osteopontin (OPN), osteocalcin (OCN), and alkaline phosphatase (ALP) activity detection. Osteoclasts can absorb mineralized bone matrix and degrade collagen, leading to bone destruction or bone absorption [6]. When suffering from severe bone trauma, defects, and tumors, bone grafting is considered as the standard of clinical treatment of bone defects since the bone cannot achieve self-repairing.

Bone tissue engineering and regenerative medicine (BTERM) hold great promise to repair or regenerate bone

on demand for a higher quality of human life [7–10]. There are three key elements in BTERM, i.e., cells, regulatory factors, and biomaterial scaffolds [11]. Particularly, biomaterials with micro, nano, molecular levels can regulate cell behaviors [12], induce bone formation, and thereby repair or regenerate bone [13–18]. The ideal biomaterial scaffold in BTERM should possess appropriate porosity with a similarity of natural bone structure [19], and excellent pore connectivity with the optimum range of pore size is 200~350 $\mu$m, which is conducive to cell ingrowth, the nutrient supply, and oxygen transportation. The mechanical property of the scaffold should be maintained in a certain range of Young's modulus to support bone reconstruction and repair activities [20–22]. For instance, the optimal Young's modulus of cortical bone and cancellous bone should be in the range of 15~20 GPa and 0.1~2 GPa, respectively [23]. Furthermore, it was well demonstrated that the topography and stiffness of bioscaffold have a significant effect on cell adhesion and can maintain the favorable capacities of cell proliferation and differentiation [19, 24–32]. Particularly, ECM-like ultrafine fiber structure has received much attention in the field of BTERM owing to their sufficient mechanical strength, favorable biological properties, and bone induction.

*1.2. Nanofibrous Scaffolds in BTERM.* While many advanced nanofabrication strategies, e.g., template synthesis, self-assembly, phase separation, and nanoskiving [33, 34], have provided useful technologies to prepare ECM-like nanofibers, over the past decade electrospinning has particularly demonstrated its significant impact on the preparation of nanofibers with unique physicochemical properties [35–42] (Figure 1). Electrospinning technology was first invented in 1902 by Cooley and Morton. However, it was not until the past thirty years that the research on the preparation of nanofibers by electrospinning was gradually carried out [43]. The electrospinning technology is to construct an electric field to make the polymer solution electrostatically atomized in the electric field to form a slender fluid and finally form a fiber. A complete electrospinning device consists of a high-voltage power supply, a syringe, a syringe pump, and a metal collector [44]. The fiber diameter can range from micrometer to nanometer level by changing the spinneret, collector, electric field, etc. [45]. At present, electrospinning technology is gradually being used proficiently, and the high-quality polymer nanofiber scaffolds manufactured through it have been recognized in various fields of tissue engineering. In recent years, studies have found that the nanofiber scaffold can imitate the ECM and promote cell proliferation and bone regeneration, due to its advantages of high specific surface area, high porosity, and suitable pore size [46]. Moreover, electrospinning nanofibers can be used as a promising material for drug delivery due to its high loading capacity of drugs, such as antibiotics, proteins, and anticancer drugs [47]. Although advanced fibers are constantly emerging, bone guidance material that can completely replace bone function has not been established clinically. Growth factors are not only expensive but also easily lose activity during processing when incorporated into scaffolds. In contrast, metals play a critical role in the area of biomedicine [48, 49] and provide an effective alternative to developing a composite osteoconductive scaffold, which has been proved to be effective in clinical practice [50]. In particular, the past discovered Sr in bone tissue mineralization is crucial. It is generally believed that Sr can increase ALP activity and OCN deposition and inhibit osteoclast differentiation [51, 52]. Therefore, Sr has become a potential additive in BTERM.

*1.3. Sr in BTERM.* Sr is one of the trace elements in the human body, most of which are accumulated in bones and teeth after ingestion. Sr has two metabolic effects, i.e., increasing osteoblasts and reducing osteoclast activity [53]. It has been found that adding strontium ions ($Sr^{2+}$) to biomaterials can not only change the porosity and mechanical properties of the fibers but also regulate the metabolism of cells, thereby increasing the healing process of bones [54, 55]. However, long-term and high-dose intake of Sr has side effects, which may lead to rickets [56]. At present, most researches on Sr in BTERM are doping Sr into composite materials, and there is a lack of further in-depth research on the specific dopant dosage for a certain material to have the best osteogenic effect.

Based on the introduction above, electrospun nanofibers containing strontium (Sr) can significantly promote bone repair and regeneration by mediating osteolysis and osteogenesis, which offers a promising bioactive material for BTERM. We present an overview of the effects of electrospun nanofibers containing Sr on stem cells, osteoblasts, and osteoclasts. Also, future perspectives for electrospun nanofibers containing Sr in BTERM are briefly outlined.

## 2. Sr and Its Properties

As a nonessential element, Sr accounts for approximately 0.035% of the skeletal system. Sr is usually captured from food and drinking water, and some foods such as cereals and seafood may contain up to 25 mg/kg of strontium [57]. $Sr^{2+}$ has bone-seeking behavior, and studies have shown that bone regeneration can be enhanced when incorporated in synthetic bone grafts. As the size and charge of $Sr^{2+}$ are very similar to $Ca^{2+}$, they can displace $Ca^{2+}$ during osteoblast-mediated processes [58]. Researchers have found that Sr may dually stimulate bone formation by inducing osteoblasts and preventing osteoclast activity [59]. On the one hand, Sr enhances the replication and activity of preosteoblasts, increases the synthesis of bone matrix, and can increase bone formation. On the other hand, Sr can inhibit the differentiation of osteoclasts and induce the apoptosis of osteoclasts to reduce bone resorption [60]. Ca-sensing receptor (CaSR) is a membrane-bound receptor expressed in osteoblasts and osteoclasts. Because Sr is similar to Ca, Sr mainly acts on CaSR [61, 62]. Sr not only enhances the proliferation and differentiation of mesenchymal stem cells and osteoblasts but also promotes the mineralization and deposition of extracellular matrix by activating the Wnt/catenin signaling pathway in the cell [63]. Sr can promote the combination of osteoprotegerin (OPG) and the receptor activator NF-$\kappa$B ligand (RANKL), prevent its combination with RANK, and regulate the signaling pathway of osteoclast function to reduce the

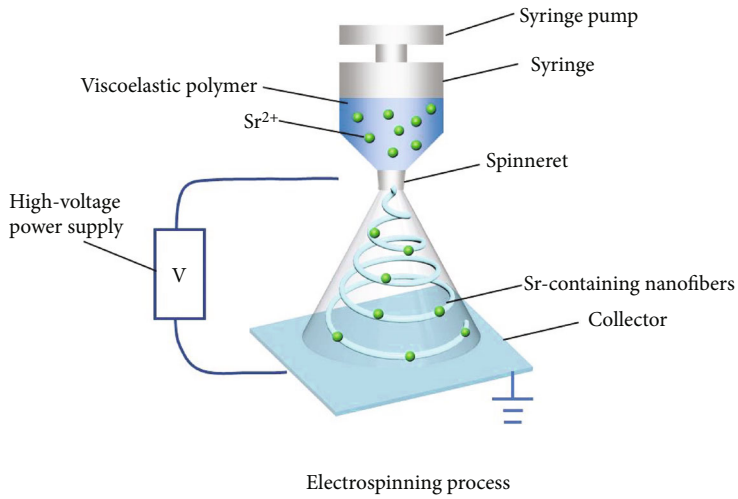


Figure 1: The schematic diagram of the preparation of electrospun nanofibers containing Sr.

formation of osteoclasts and bone resorption [64]. The mechanism of action of Sr is shown in Figure 2. The dual action has already been under extensive research both *in vitro* and *in vivo*. *In vitro*, Sr has been proved to promote the osteogenic differentiation of bone mesenchymal stem cells (BMSCs), stimulate the osteoblastic differentiation of human mesenchymal stem cells (hMSCs), increase osteoblast proliferation, reduce osteoblast apoptosis, decrease osteoclast differentiation, and increase osteoclast apoptosis [65]. Sr can also increase bone mass, density, and bone mechanical properties and reduce the risk of the vertebral, nonvertebral, and hip fractures *in vivo* [66]. Because Sr has a variety of effects on bone physiology, it provides a good treatment strategy for improving the bone-guiding ability of biomaterials to repair and regenerate human damaged lesions. However, it has been reported that there are several long-term side effects when oral Sr-containing drugs have overdosed [67]. Therefore, new methods for targeted delivery of $Sr^{2+}$ to the defect site are being explored. Several studies report the benefits of combining Sr with polymers to prepare composite scaffolds such as nanofibers for bone tissue engineering [68]. The related research of Sr-containing nanofibers on osteogenesis and osteoclast differentiation *in vitro* and *in vivo* experiments is shown in Table 1.

## 3. Applications of Sr-Containing Nanofibers in BTERM

*3.1. Sr-Containing Nanofibers and the Osteogenic Differentiation of Stem Cells.* Stem cells, such as hMSCs, BMSCs, and SHEDs, are considered as a promising cell source for bone engineering due to their unlimited self-renewal capacity and multiple differentiation potential [68–70]. As a principal player in the regenerative process, ECM provides many biological cues for cell adhesion, proliferation, and differentiation. Along with the similarity to ECM structure, various nanofiber scaffolds can promote the above cell behaviors and even induce the osteogenic differentiation of stem cells by controlling cell morphology. These scaffolds can also be improved by incorporating Sr nanoparticles which further impart osteogenic characteristics of stem cells by continuously releasing $Sr^{2+}$ [71]. As a biodegradable polymer, PCL has been widely used in the field of nanofiber spinning production and processing. The nanoscale structure of PCL nanofibers can directly induce bone formation [71] and is particularly suitable for the regeneration of bone tissue around the periosteum, which has been shown to significantly enhance the osseointegration of implants [72]. Meka et al. have studied the growth and osteogenic differentiation of hMSCs on $SrCO_3$-containing PCL nanofibers [69]. The PCL nanofibers containing 20% $nSrCO_3$ (PCL/SrC20) have been found to promote the proliferation of hMSCs *in vitro* and significantly increase mineral deposition (up to four-fold), indicating enhanced osteogenesis. Also, the mRNA and protein expression of osteogenic markers (e.g., BMP-2, Osterix, and of Runx2) was increased in PCL/SrC20 composite nanofibers [73–77]. Considering that the diameter, crystallinity, and modulus of PCL/SrC composite scaffolds have little effect, these results may be because the sustained release of $Sr^{2+}$ stimulates the differentiation of hBMSCs into osteoblasts [78]. Therefore, $nSrCO_3$ can be considered as a nonregulatory growth factor rather than bioactive cues and with a combination of nanofibers is a promising strategy for bone tissue engineering.

As a new source of pluripotent stem cells, SHEDs, which can be differentiated into osteoblasts, have recently attracted much attention [79]. However, limited information is available on the osteogenic potential of SHEDs in Sr-containing artificial nanofibers *in vitro*. Su et al. have found that both Sr-coated PCL and Sr/PCL blend nanofibers showed significant effects on the osteogenic differentiation of SHEDs *in vitro* [68]. Cell morphology and MTT analysis showed that these nanofibers effectively support cell attachment and proliferation. Compared with pure PCL nanofibers, PCL nanofibers loaded with Sr showed better ALP activity, biomineralization, and bone-related gene expression. Though nanofibers imitate ECM architecture and create a suitable microenvironment for cell adhesion, proliferation,

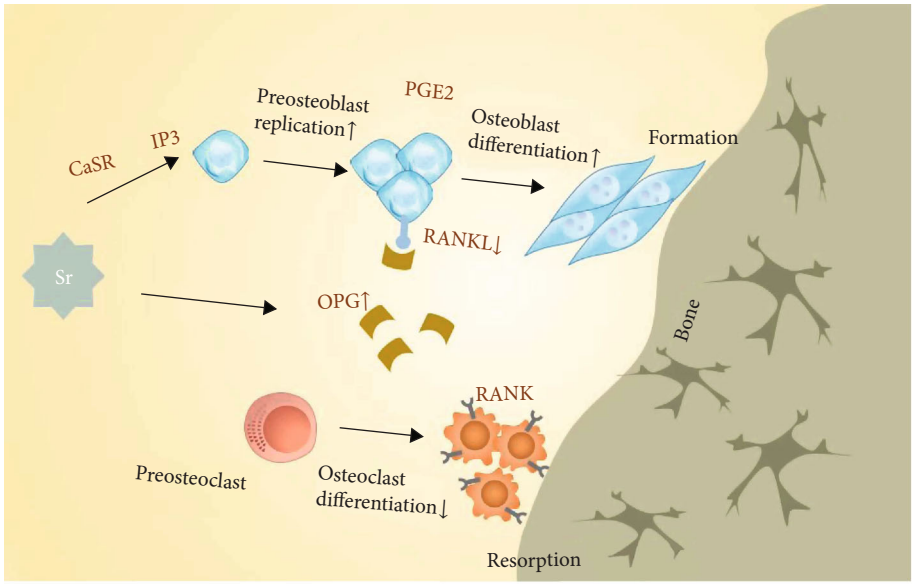


Figure 2: Mechanism of Sr at the cellular and molecular level. Sr by activating CaSR to activate 1,4,5-trisphosphate (IP3) to activate osteoblast replication. Sr can also activate osteoblast replication by inducing the expression of cyclooxygenase- (COX-) 2 and prostaglandin 2 (PGE2). For osteoclasts, Sr can increase the bait receptor OPG of RANKL to inhibit RANKL-induced osteoclast formation.

Table 1: Sr-containing nanofibers on osteogenesis and osteoclast differentiation *in vitro* and *in vivo* experiments.

| Material | Cell lines/animal model | Results | Ref. |
|---|---|---|---|
| Polycaprolactone (PCL); Sr/PCL blending; Sr-coated PCL | Stem cells of human exfoliated deciduous teeth (SHEDs) | Strontium-loaded PCL nanofibers promote osteogenic differentiation of SHEDs. | [26] |
| PCL; PCL/SrC10; PCL/SrC20 | hMSCs | PCL/SrC20 enhanced proliferation and osteogenesis of hMSCs. | [27] |
| PLLA; 5Sr/PLLA; 10Sr/PLLA; 15Sr/PLLA | BMSCs/Sprague-Dawley rats | 15Sr/PLLA promoted cell proliferation and osteogenic differentiation *in vitro* and enhanced bone regeneration *in vivo*. | [28] |
| PLLA; PLLA-BBG-Sr | BMSCs | PLLA-BBG-Sr promoted osteogenic differentiation of cells. | [49] |
| PCL/PLGA-PVA; Sr-coated PCL/PLGA-PVA | MC3T3-E1 | Sr-coated PCL/PLGA-PVA NFs increased the differentiation of preosteoblast cells. | [50] |
| PCL; PCL-SrHANF | MG63 osteoblast-like cells | PCL-SrHANF composite membrane possessed elevated osteogenic potential. | [52] |
| BGEF; 50Sr-BGNF; 50Sr/0.5Cu-BGNF; 50Sr/1Cu-BGNF | RAW264.7; human vascular endothelial cells (HUVECs); hBMSCs | Sr dopant significantly enhanced osteogenesis and suppressed osteoclastogenesis. | [65] |

and differentiation, their poor mechanical strength still limits their application. By adding Sr coating on PCL or cospinning Sr/PCL nanofiber, Sr-based PCL nanofibers can not only simulate the structure of natural bone but also improve the mechanical properties and biological response of scaffolds [80]. Furthermore, the cell viability of pure PCL and Sr/PCL blended fibers has been significantly higher than that of Sr-coated PCL fibers, which may be because of the particles on the surface of strontium phosphate coating that promote cell differentiation and inhibit cell proliferation [81]. This study suggests that Sr may be a potential inducer for SHED osteogenesis.

Poly-L-lactic acid (PLLA) is a biodegradable and biocompatible polymer, which is widely used in bone tissue engineering and has been approved by the US Federal Food and Drug Administration (FDA) for clinical applications of a variety of PLLA medical devices [82]. Owing to appropriate flexibility and deformability, PLLA can be processed and manipulated by different techniques (such as fusion, dry and wet spinning, and electrospinning) [36–38, 83, 84]. However, PLLA is generally not considered to be osteoinductive [85]. Experiments by Charles et al. have shown that the introduction of HA into PLLA can improve the interaction between material and bone [86]. Moreover, Han et al. have recently produced Sr/PLLA nanofibers *via* electrodeposition to study BMSC and nanofiber interaction. The *in vitro* results revealed that the mineralized Sr/PLLA nanofibers continuously released $Sr^{2+}$ for controlled times and showed higher release rates of $Ca^{2+}$ and $PO_4^{3-}$ and excellent ability to promote proliferation and osteogenic differentiation of BMSCs.

Importantly, *in vivo* experiments showed that the mineralized Sr/PLLA nanofibers promote bone regeneration. The $Sr^{2+}$ released from the nanofiber was thought to contribute to enhancing bone repair and regeneration, as shown in Figure 3. Thus, these findings indicate that the mineralization Sr/PLLA nanofibrous membrane has a broad application prospect in bone tissue engineering. Studies have shown that the bioactive glass (BG) can improve the biological performance of PLLA, thereby enhancing its osteoinduction [87]. Fernandes et al. fabricated a composite bioactive glass particle (BBG-Sr) (PLLA-BBG-Sr) by electrospinning [88]. BBG-Sr glass particles are uniformly distributed in PLLA films, thus improving the mechanical properties. The prepared smooth and uniform fibers (width 1~3 $\mu$m) except for BBG-Sr particles (<45 $\mu$m) have uniform distribution. Moreover, cell evaluation tests of BMSCs showed that PLLA-BBG-Sr membrane enhanced ALP activity and upregulated the expression of osteogenic genes (*Alpl*, *Sp7*, and *Bglap*), which was suggested to promote osteogenic differentiation of BMSCs. These results indicate that the use of this composite material has great potential for promoting bone regeneration.

*3.2. Sr-Containing Nanofibers and the Osteogenesis of Osteoblasts.* The manufacture of nanofibers with PCL has attracted a lot of attention in tissue engineering. Many studies have shown that adding bioactive substances such as hydroxyapatite (HAp) to PCL can increase the hydrophilicity of PCL. The study found that due to the difference in ionic radius, the solubility of Sr-substituted hydroxyapatite (SrHAp) is higher than that of pure HAp, which contributes to the perturbation of the crystal lattice [89]. Lino et al. found that the proliferation of BMSCs on polydiisopropyl fumarate (PCL-PDIPF) membrane containing 5% Sr was significantly higher than that on PCL-PDIPF membrane containing 1% Sr [90]. Moreover, the replacement of $Ca^{2+}$ for $Sr^{2+}$ led to an increase of d-space, and the dissolution of SrHAp increases with the increase of Sr dosage [91]. Tsai et al. produced a bioactive and biodegradable composite film comprising Sr-substituted hydroxyapatite nanofibers (SrHANFs) and PCL and PCL-SrHANF film to evaluate the behavior of osteoblast [92]. The effect of SrHANFs on osteoblast proliferation was not observed in this study. It has been reported that dissolved HAp particles can result in a high local concentration of $Ca^{2+}$, which may stimulate osteoblast proliferation and immediately switch from stage to stage of differentiation [93]. Lino et al. found that compared with PCL-PDIPF (polydiisopropyl fumarate) membrane containing 1% Sr, the proliferation of BMSCs on PCL-PDIPF membrane containing 5% Sr was higher [90]. Since the difference in ionic radius disturbs the lattice, the dissolution rate of SrHANFs increased with the increase of Sr doping amount [91]. Therefore, the dissolution of SrHANFs may lead to an increase in the concentration of $Ca^{2+}$ and $Sr^{2+}$, which affects cell proliferation. The detection of ALP activity, OCN gene expression, and colourimetric calcium quantitative determination showed that the presence of SrHANFs in the PCL membrane promoted the differentiation and activity of osteoblasts, as shown in Figure 4. $Sr^{2+}$ released from PCL-SrHANF membranes may interact with cells *via* calcium-sensitive receptors (CaR) to activate inositol 1,4,5-triphosphate production and mitogen-activated protein kinase (MAPK) signaling. Thus, the expression and activity of osteogenesis-related genes and proteins are enhanced, and osteogenic differentiation is regulated [94]. By incorporating fragments of Sr-substituted hydroxyapatite nanofibers into PCL, an organic-inorganic composite membrane for guided bone regeneration was first produced. Compared with the PCL membrane alone, PCL-SrHANF composite membrane had higher osteogenesis potential.

Total joint replacement (TJR) surgery is currently one of the most successful functional recovery operations in the clinical practice [95]. However, a major drawback is the lack of early osseointegration of the implant [96]. Electrospun nanofibers can be used as promising implants to improve the deficiency of early osteointegration. Some studies have shown that nanofibers can not only use their structural properties to create an osteogenic environment but also affect the attachment, proliferation, and differentiation of bone cells [97–99]. Previous research by Song et al. showed that in contaminated rat tibial implant models, oxygenated nanofiber coatings can effectively inhibit bacterial infections and enhance osteointegration [96]. These results indicate that these coated nanofibers have great potential to enhance bone integration. Also, nanofibers can be used as a drug delivery device to control release through coaxial electrospinning [100]. Local delivery of $Sr^{2+}$ from bone substitutes such as nanofibers is considered a promising approach to treat bone defects [78]. In the research of Chen et al., a coaxial PCL/PLGA-PVA nanofiber coating doped with $Sr^{2+}$ was developed to enhance osseointegration [89]. It was observed from PCL/PLGA-PVA nanofibers that $Sr^{2+}$ was continuously released for more than two months. SEM images also showed that compared with non-$Sr^{2+}$-doped nanofibers, $Sr^{2+}$-doped nanofibers have fewer dense structures and greater porosity. In addition, PCL/PLGA-PVA nanofibers doped with $Sr^{2+}$ were biocompatible and significantly enhanced the differentiation of murine osteoblast MC3T3-E1 cells through indirect and direct contact methods.

*3.3. Sr-Containing Nanofibers and the Osteolysis of Osteoclasts.* Bioactive glass is a well-known class of synthetic bone replacement materials and has been used clinically for orthopedic and dental applications since 1985 [101]. However, most of the previous bioactive glasses were block-shaped, granular, or fiber-type fused glass with a diameter of hundreds to tens of microns. To stimulate 3D structures and nanofibril structure of bone ECM, some researchers have prepared bioactive glass-based nanofibers by electrospinning and proved their bioactivity by biomineralization of hydroxyapatite crystals in simulated body fluids [102]. Sr can promote the proliferation and differentiation of osteoblasts while reducing the activity of osteoclasts [103]. Inspired by these results, researchers have incorporated Sr into a variety of calcium phosphate and porous bioactive glass to induce bone regeneration through the long-term release of $Sr^{2+}$. Wen et al. produced microactive glass nanofibers doped with Sr and Cu, and the released ions affected the viability and cell function of related cell types [104]. The

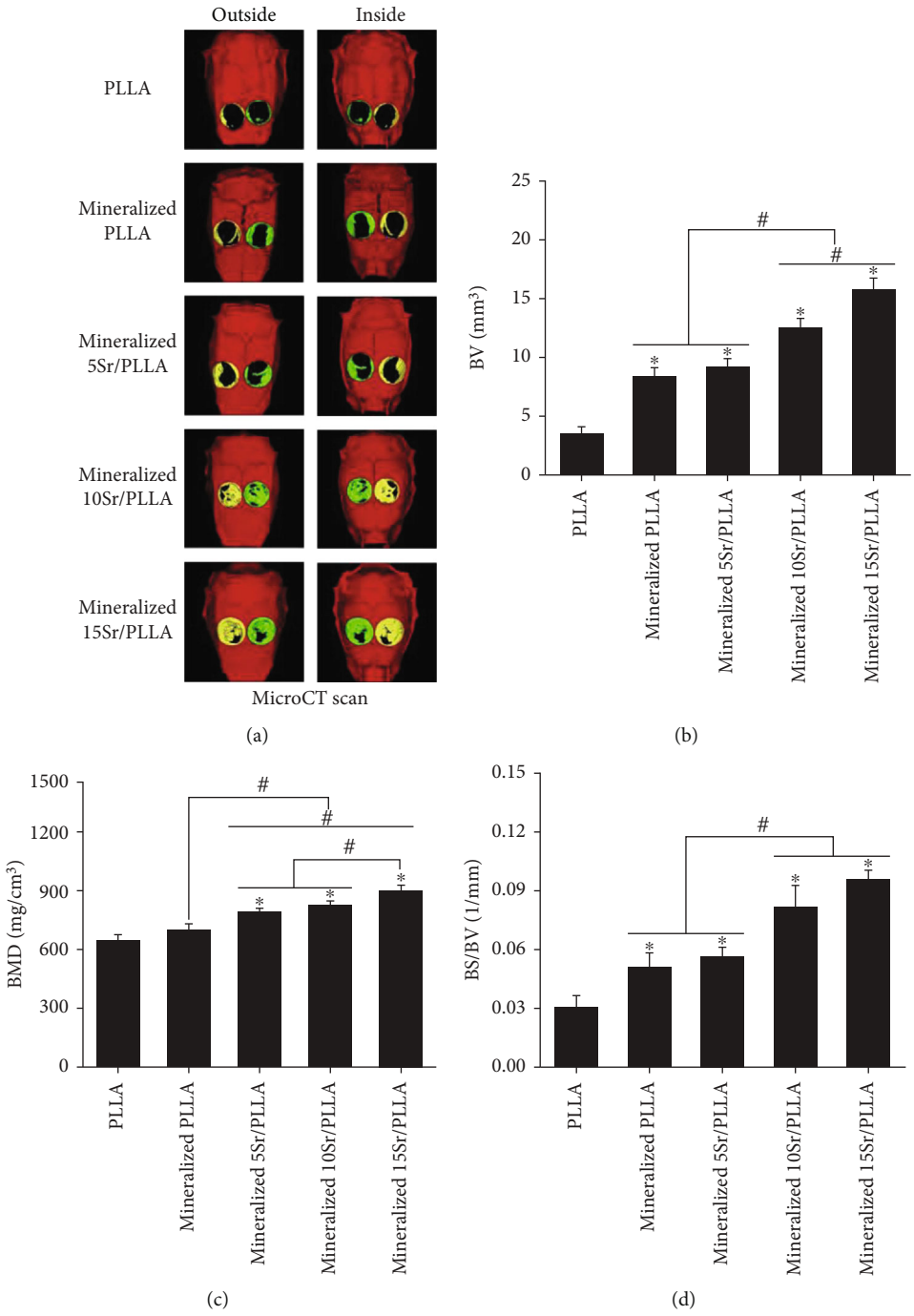


Figure 3: Continued.

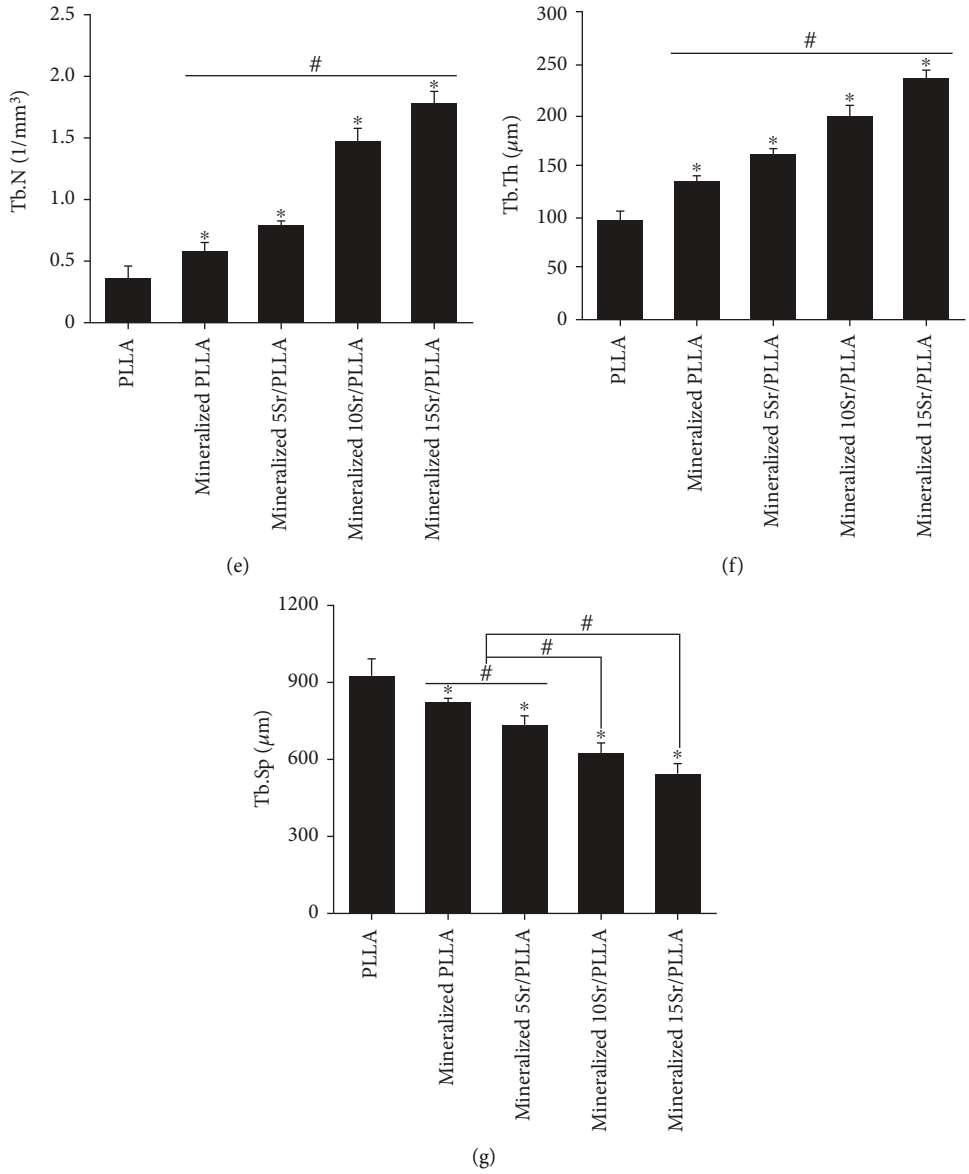


FIGURE 3: *In vivo* experiments of nanofibers with different Sr content induced bone formation. With the increase of Sr content, the osteogenic effect became stronger [60].

diameter of bioactive glass fiber can be increased by adding Sr instead of Ca. The reason may be that the conductivity of $Sr^{2+}$ is lower than that of $Ca^{2+}$, which may cause the current of glass fibers with dopants to decrease during the electric discharge process and eventually make the diameter of the electric discharge nanofibers smaller [105]. These findings indicate that the properties of dopant or substituent ions play a critical role in controlling fiber diameter. By studying the release of therapeutic ions from the doped glass nanofibers into the cell culture medium, it was found that $Sr^{2+}$ showed a rapid burst release during the first 120 h, followed by constant release kinetics. The accelerated release may be due to the fact that dopant $Sr^{2+}$ has a higher solubility [106]. The artificial Sr-containing bioactive glass fibers immersed in simulated body fluid (SBF) accelerated the formation of apatite crystals. According to previous reports, the surfaces of Sr-doped bioactive glass and Sr-doped HAp mineralized electrospun polymer nanofibers are smoother, making them a less preferred formation of apatite nuclear sites [106]. TRAP analysis is a marker of osteoclast differentiation and bone resorption activity. Through this analysis, the effect of Sr released from bioactive glass nanofibers on the differentiation and maturation of RAW264.7 macrophages into multinuclear osteoclasts was studied. Quantitative comparison of the number of TRAP-positive macrophages obtained from the solution extracted from Sr-doped bioactive glass nanofibers with RAW264.7 cells treated with lipopolysaccharide (LPS) showed that osteoclast activity was inhibited, as shown in Figure 5 [107]. Few studies illustrate $Sr^{2+}$ inhibitory effect on bone resorption. The molecular basis of this antiosteoclast effect induced by Sr revolves around the RANKL signaling pathway. Sr promoted OPG in conjunction with the relevant

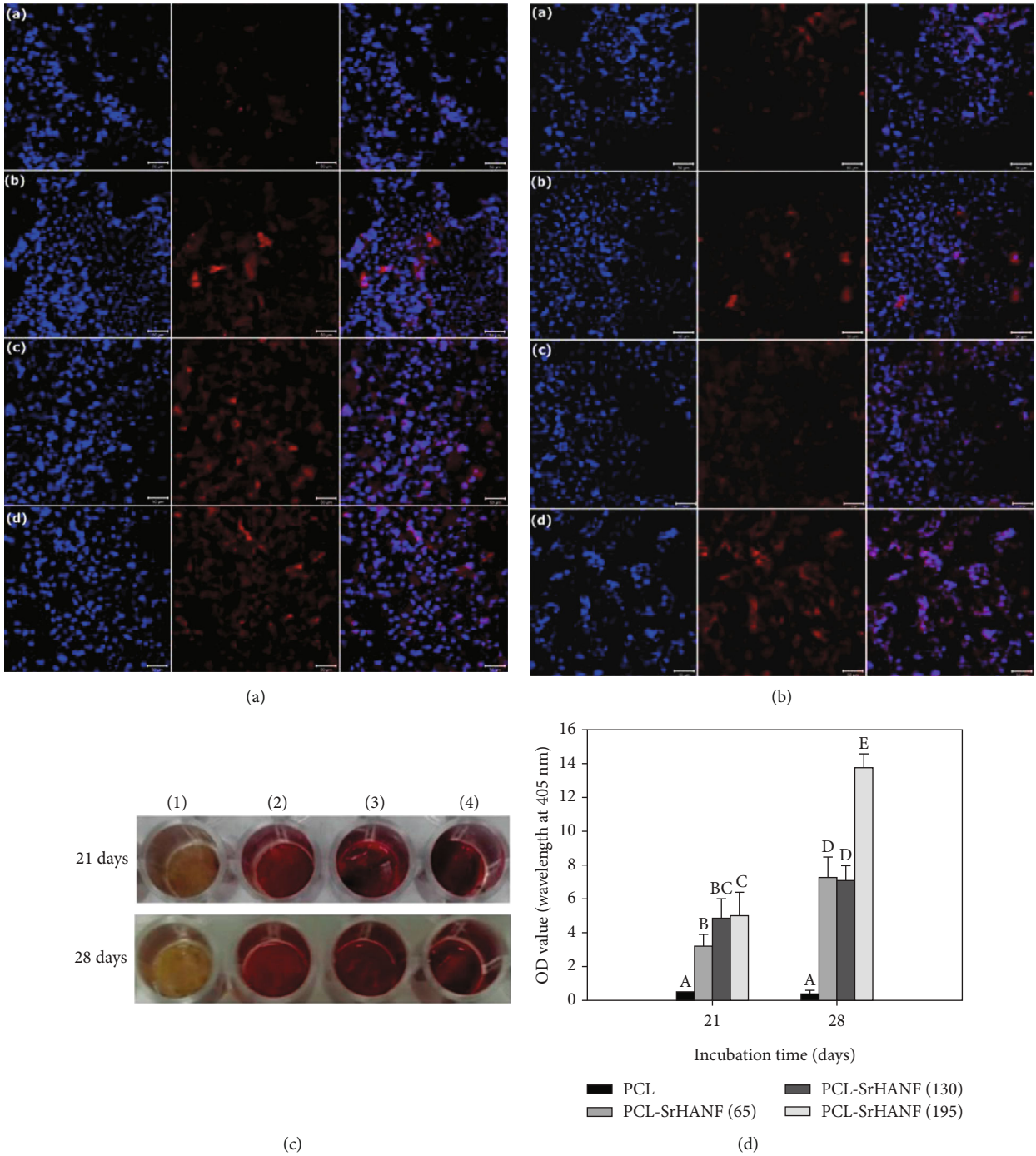


Figure 4: (a, b) BSP and OCN protein immunofluorescence staining of MG63 osteoblast-like cells on (A) PCL, (B) PCL-SrHANF (65), (C) PCL-SrHANF (130), and (D) PCL-SrHANF (195) after 14 days of culture. (c) Optical images by Alizarin Red-S (ARS) staining. (d) ARS staining for quantitative analysis of mineral deposits [82].

RANKL and prevented it from binding to RANK [64]. Therefore, $Sr^{2+}$ has a direct impact on the RANK/RANKL/OPG systems and is a key factor for bone remodeling and homeostasis. However, moderate-high concentrations of $Sr^{2+}$ are required to produce this osteoclast-resistant effect. In previous studies, low concentrations (about 200 ppb) of $Sr^{2+}$ released from $\beta$-tricalcium phosphate (Sr-doped $\beta$-TCP) bioceramics did not prevent RAW 264.7 mononuclear osteoclastogenesis to mature osteoclasts [108]. In contrast, in the study by Wen et al., the lever of $Sr^{2+}$ in the extraction medium from the doped bioactive glass nanofibers was high enough (about 0.3-0.4 mM) to sufficiently inhibit the activity of osteoclasts [104]. In short, Sr-doped bioactive glass nanofibers prepared by electrospinning accelerated the formation of apatite crystals on the surface when immersed in SBF. Ion release kinetics showed that $Sr^{2+}$ was continuously released during the test period, and Sr dopants significantly increased osteogenesis and inhibited osteoclastogenesis.

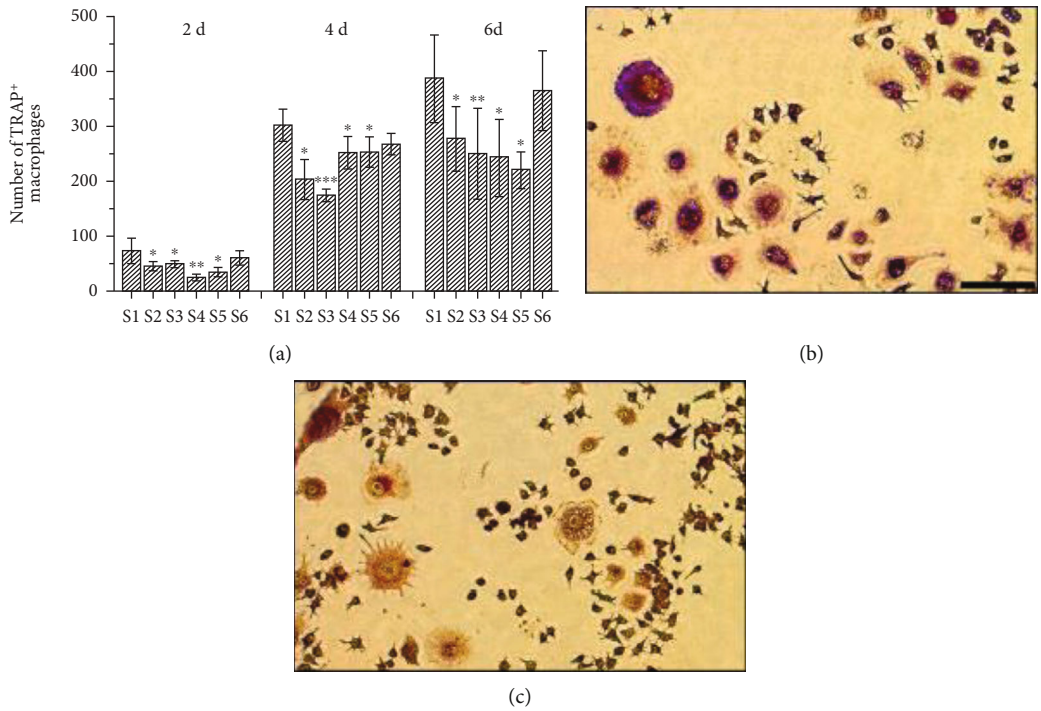


Figure 5: All groups containing released $Sr^{2+}$ showed inhibition of osteoclast activity [94].

*3.4. Sr-Containing Nanofibers with Antibacterial Properties and Drug Delivery.* Nanofiber-structured bioactive materials have excellent potential for use as bone defect fillers because they can mimic the architecture of the ECM. On this basis, endowing implants with antibacterial properties can prevent or treat implant-related infections. Bioactive glass is one of the suitable choices for antibacterial properties, depending on the composition, the concentration of the glass, the microorganisms, and their morphology [109]. In a recent study, two different components of bioactive glass nanofibers, M1/45 (45S5 Bioglass®) and ICIE 16M (bioactive glass doped with Zn and Sr), were produced using laser spinning technology to test antibacterial activity against *Staphylococcus aureus* [110, 111]. The release of $Zn^{2+}$ and $Sr^{2+}$ demonstrated the additional bactericidal effect of doped nanofibers for longer periods. ZnO and SrO may also be doped into the nanostructure as a network modifier, like the alkali metal oxide glass [112]. The difference of density between two types of laser-spun glass nanofibers indicates that $Zn^{2+}$- and $Sr^{2+}$-doped nanofibers formed a more closed structure, which limits the infiltration of the medium, thus slowing down the dissolution of the nanofibers. As a result, its biological activity is affected. The decrease in the release rate of potentially toxic ions may also affect the effectiveness of nanofibers against bacteria.

As an effective drug delivery system, nanofibers have attracted much attention as mesoporous materials due to their excellent drug loading capacity and drug release efficacy and have become drug delivery systems [113, 114]. In a previous work, Tsai et al. prepared mesoporous hydroxyapatite-CaO composite nanofibers (p-HapFs) and found that p-HapFs have good drug-loading efficiency and can delay the burst release of tetracycline (TC). However, many studies have shown that CaO plays a negative role in the biocompatibility of HAp [115, 116]. Kanchana and Sekar found that the addition of Sr during the synthesis of biphasic calcium phosphate using the sol-gel method can reduce the formation of CaO impurities [117]. In another study, Sr-substituted hydroxyapatite-CaO-$CO_3$ nanofibers (mSrHANFs) with the mesoporous structure were prepared and characterized by electrospinning, and the effects of different doping amounts on the composition of mSrHANFs were evaluated [91]. TC was selected to evaluate the drug-loading efficiency, drug release mechanism, and antibacterial activity of the model drug. It was found that as the doping amount of Sr increased, the content of CaO and $CaCO_3$ in the sample decreased. The mSrHANFs showed excellent drug-loading efficiency and TC sustained-release capacity for more than 3 weeks, which maintained the antibacterial activity well, as shown in Figure 6.

## 4. Conclusion and Future Perspectives

This review summarizes some insights on the effect of Sr-containing nanofibers in bone tissue engineering. Sr-containing nanofibers have not only good potential to imitate natural bone ECM but also special effects on cell growth and differentiation, which provides a new strategy for bone tissue regeneration and repair. Sr dopants have been confirmed that can enhance the osteogenic effect and inhibit the formation of osteoclasts. Also, the use of Sr nanoparticles can replace the biofunctionalization of biomolecules for bone tissue engineering. Sr-containing nanofibers have proved to have excellent biocompatibility with bone tissue, promote the growth of seed cells and osteogenic differentiation, were used for drug delivery in bone regeneration engineering, and have excellent

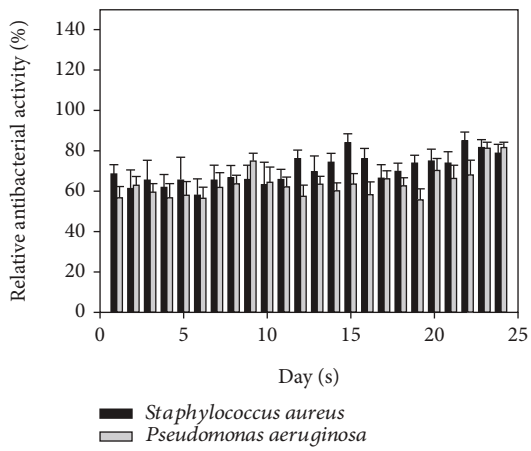


Figure 6: The solution obtained with 3mSrHANFs loaded with TC can effectively delay the growth of bacteria to day 24 [81].

antibacterial effects. Moreover, Sr-containing nanofibers have excellent drug-loading efficiency, which can delay the burst release of drugs and can continuously release drugs locally, which is very ideal for transplants. The inclusion of $Sr^{2+}$ in the nanofiber structure leads to changes in its dissolution kinetics, and the Sr-doped nanofibers show an additional bactericidal effect for a longer period. Such hybrid scaffolds with multifunctional elements that perform complementary functions are promising for the development of tissue substitutes.

Electrospinning nanofibers have broad prospects for development, because they can process various polymer materials to stimulate the hierarchical structure of ECM, which is conducive to cell infiltration and survival. Recent studies have shown that Sr-containing nanofibers can promote the differentiation of human osteoprogenitor cells into osteocytes. The future development direction of this field is to manufacture scaffolds with mechanical properties comparable to those of natural bone. Sr-containing nanofibers have become a hot spot in BTERM research in recent years. Most studies have confirmed that the incorporation of Sr can effectively improve the mechanical properties of nanofibers, improve the differentiation ability of osteoblasts, and promote the ability of bone formation *in vivo*. However, different researchers use different Sr doping methods, and the results of the research and the optimal Sr doping concentration are not consistent. With the deepening of its research, as an emerging tissue engineering material, Sr-containing nanofibers are expected to become an ideal artificial bone substitute material in the field of bone tissue repair.

## Data Availability

The data used to support the findings of this study are available from the corresponding authors upon request.

## Conflicts of Interest

The authors declare no conflict of interest.

## Acknowledgments

The authors are very grateful for the financial support of the National Natural Science Foundation of China (Grant Nos. 31900957 and 31870929), Shandong Provincial Natural Science Foundation (Grant Nos. ZR2019QC007 and ZR2019MH007), Innovation and Technology Program for the Excellent Youth Scholars of Higher Education of Shandong Province (Grant No. 2019KJE015), China Postdoctoral Science Foundation (Grant No. 2019M652326), and Scientific Research Foundation of Qingdao University (Grant No. DC1900009689).

## References

[1] Y. Liu, D. Luo, and T. Wang, "Hierarchical structures of bone and bioinspired bone tissue engineering," *Small*, vol. 12, no. 34, pp. 4611–4632, 2016.

[2] Z. Hao, Z. Song, J. Huang et al., "The scaffold microenvironment for stem cell based bone tissue engineering," *Biomaterials Science*, vol. 5, no. 8, pp. 1382–1392, 2017.

[3] N. Reznikov, R. Shahar, and S. Weiner, "Bone hierarchical structure in three dimensions," *Acta Biomaterialia*, vol. 10, no. 9, pp. 3815–3826, 2014.

[4] R. Hodgskinson and J. D. Currey, "Young's modulus, density and material properties in cancellous bone over a large density range," *Journal of Materials Science. Materials in Medicine*, vol. 3, no. 5, pp. 377–381, 1992.

[5] J. R. Porter, T. T. Ruckh, and K. C. Popat, "Bone tissue engineering: a review in bone biomimetics and drug delivery strategies," *Biotechnology Progress*, vol. 25, no. 6, pp. 1539–1560, 2009.

[6] M. Doblaré, J. M. García, and M. J. Gómez, "Modelling bone tissue fracture and healing: a review," *Engineering Fracture Mechanics*, vol. 71, no. 13-14, pp. 1809–1840, 2004.

[7] Y. Li, Y. Xiao, and C. Liu, "The horizon of materiobiology: a perspective on material-guided cell behaviors and tissue engineering," *Chemical Reviews*, vol. 117, no. 5, pp. 4376–4421, 2017.

[8] G. Huang, F. Li, X. Zhao et al., "Functional and biomimetic materials for engineering of the three-dimensional cell microenvironment," *Chemical Reviews*, vol. 117, no. 20, pp. 12764–12850, 2017.

[9] C. Wang, G. Cao, T. Zhao et al., "Terminal group modification of carbon nanotubes determines covalently bound osteogenic peptide performance," *ACS Biomaterials Science & Engineering*, vol. 6, no. 2, pp. 865–878, 2020.

[10] B. Pei, W. Wang, N. Dunne, and X. Li, "Applications of carbon nanotubes in bone tissue regeneration and engineering: superiority, concerns, current advancements, and prospects," *Nanomaterials*, vol. 9, no. 10, article 1501, 2019.

[11] M. R. Iaquinta, E. Mazzoni, M. Manfrini et al., "Innovative biomaterials for bone regrowth," *International Journal of Molecular Sciences*, vol. 20, no. 3, p. 618, 2019.

[12] S. Wang, X. Yang, L. Zhou, J. Li, and H. Chen, "2D nanostructures beyond graphene: preparation, biocompatibility and biodegradation behaviors," *Journal of Materials Chemistry B*, vol. 8, no. 15, pp. 2974–2989, 2020.

[13] M. M. Stevens, "Biomaterials for bone tissue engineering," *Materials Today*, vol. 11, no. 5, pp. 18–25, 2008.

[14] Q. Zhou, J. Chen, Y. Luan et al., "Unidirectional rotating molecular motors dynamically interact with adsorbed

proteins to direct the fate of mesenchymal stem cells," *Science Advances*, vol. 6, article eaay2756, no. 5, 2020.

[15] Z. P. Du, X. X. Feng, G. X. Cao et al., "The effect of carbon nanotubes on osteogenic functions of adipose-derived mesenchymal stem cells in vitro and bone formation in vivo compared with that of nano-hydroxyapatite and the possible mechanism," *Bioactive Materials*, vol. 6, no. 2, pp. 333–345, 2021.

[16] T. Mokabber, Q. Zhou, A. I. Vakis, P. van Rijn, and Y. T. Pei, "Mechanical and biological properties of electrodeposited calcium phosphate coatings," *Materials Science and Engineering: C*, vol. 100, pp. 475–484, 2019.

[17] X. Bi, L. Li, Z. Mao et al., "The effects of silk layer-by-layer surface modification on the mechanical and structural retention of extracellular matrix scaffolds," *Biomaterials Science*, vol. 8, no. 14, pp. 4026–4038, 2020.

[18] W. Wang, Z. Wang, Y. Fu et al., "Improved osteogenic differentiation of human amniotic mesenchymal stem cells on gradient nanostructured Ti surface," *Journal of Biomedial Materials Research Part A*, vol. 108, no. 9, pp. 1824–1833, 2020.

[19] A. Przekora, "The summary of the most important cell-biomaterial interactions that need to be considered during in vitro biocompatibility testing of bone scaffolds for tissue engineering applications," *Materials Science and Engineering: C*, vol. 97, pp. 1036–1051, 2019.

[20] L. Wang, C. Wang, S. Wu, Y. Fan, and X. Li, "Influence of the mechanical properties of biomaterials on degradability, cell behaviors and signaling pathways: current progress and challenges," *Biomaterials Science*, vol. 8, no. 10, pp. 2714–2733, 2020.

[21] L. Wang, S. Wu, G. Cao, Y. Fan, N. Dunne, and X. Li, "Biomechanical studies on biomaterial degradation and co-cultured cells: mechanisms, potential applications, challenges and prospects," *Journal of Materials Chemistry B*, vol. 7, no. 47, pp. 7439–7459, 2019.

[22] K. Zhang, X. Xiao, X. Wang, Y. Fan, and X. Li, "Topographical patterning: characteristics of current processing techniques, controllable effects on material properties and co-cultured cell fate, updated applications in tissue engineering, and improvement strategies," *Journal of Materials Chemistry B*, vol. 7, no. 45, pp. 7090–7109, 2019.

[23] S. Bose, M. Roy, and A. Bandyopadhyay, "Recent advances in bone tissue engineering scaffolds," *Trends in Biotechnology*, vol. 30, no. 10, pp. 546–554, 2012.

[24] G. R. Liguori, Q. Zhou, T. T. A. Liguori et al., "Directional topography influences adipose mesenchymal stromal cell plasticity: prospects for tissue engineering and fibrosis," *Stem Cells International*, vol. 2019, Article ID 5387850, 14 pages, 2019.

[25] P. T. Kühn, Q. Zhou, T. A. B. van der Boon, A. M. Schaap-Oziemlak, T. G. van Kooten, and P. van Rijn, "Double linear gradient biointerfaces for determining two-parameter dependent stem cell behavior," *ChemNanoMat*, vol. 2, no. 5, pp. 407–413, 2016.

[26] Q. Zhou, L. Ge, C. F. Guimarães, P. T. Kühn, L. Yang, and P. van Rijn, "Development of a novel orthogonal double gradient for high-throughput screening of mesenchymal stem cells-materials interaction," *Advanced Materials Interfaces*, vol. 5, no. 18, article 1800504, 2018.

[27] Q. Zhou, P. Wünnemann, P. T. Kühn et al., "Mechanical properties of aligned nanotopologies for directing cellular behavior," *Advanced Materials Interfaces*, vol. 3, no. 18, article 1600275, 2016.

[28] Q. Zhou, O. Castañeda Ocampo, C. F. Guimarães, P. T. Kühn, T. G. van Kooten, and P. van Rijn, "Screening platform for cell contact guidance based on inorganic biomaterial micro/nanotopographical gradients," *ACS Applied Materials & Interfaces*, vol. 9, no. 37, pp. 31433–31445, 2017.

[29] A. M. Almonacid Suarez, Q. Zhou, P. van Rijn, and M. C. Harmsen, "Directional topography gradients drive optimum alignment and differentiation of human myoblasts," *Journal of Tissue Engineering and Regenerative Medicine*, vol. 13, no. 12, pp. 2234–2245, 2019.

[30] Q. Zhou, P. T. Kühn, T. Huisman et al., "Directional nanotopographic gradients: a high-throughput screening platform for cell contact guidance," *Scientific Reports*, vol. 5, no. 1, article 16240, 2015.

[31] X. Qiu, S. Xu, Y. Hao et al., "Biological effects on tooth root surface topographies induced by various mechanical treatments," *Colloids Surfaces B Biointerfaces*, vol. 188, article 110748, 2020.

[32] Y. Hao, W. Zhao, L. Zhang et al., "Bio-multifunctional alginate/chitosan/fucoidan sponges with enhanced angiogenesis and hair follicle regeneration for promoting full-thickness wound healing," *Materials and Design*, vol. 193, article 108863, 2020.

[33] Q. Zhou, Z. Zhao, Z. Zhou, G. Zhang, R. C. Chiechi, and P. van Rijn, "Directing mesenchymal stem cells with gold nanowire arrays," *Advanced Materials Interfaces*, vol. 5, no. 14, article 1800334, 2018.

[34] Kenry and C. T. Lim, "Nanofiber technology: current status and emerging developments," *Progress in Polymer Science*, vol. 70, pp. 1–17, 2017.

[35] Y. Zhang, C. T. Lim, S. Ramakrishna, and Z. M. Huang, "Recent development of polymer nanofibers for biomedical and biotechnological applications," *Journal of Materials Science Materials in Medicine*, vol. 16, no. 10, pp. 933–946, 2005.

[36] H. Yuan, Q. Zhou, B. Li, M. Bao, X. Lou, and Y. Zhang, "Direct printing of patterned three-dimensional ultrafine fibrous scaffolds by stable jet electrospinning for cellular ingrowth," *Biofabrication*, vol. 7, no. 4, article 045004, 2015.

[37] Q. Zhou, J. Xie, M. Bao et al., "Engineering aligned electrospun PLLA microfibers with nano-porous surface nanotopography for modulating the responses of vascular smooth muscle cells," *Journal of Materials Chemistry B*, vol. 3, no. 21, pp. 4439–4450, 2015.

[38] Q. Zhou, M. Bao, H. Yuan, S. Zhao, W. Dong, and Y. Zhang, "Implication of stable jet length in electrospinning for collecting well-aligned ultrafine PLLA fibers," *Polymer*, vol. 54, no. 25, pp. 6867–6876, 2013.

[39] Q. Zhou, H. Zhang, Y. Zhou et al., "Alkali-mediated miscibility of gelatin/polycaprolactone for electrospinning homogeneous composite nanofibers for tissue scaffolding," *Macromolecular Bioscience*, vol. 17, article 1700268, 2017.

[40] M. Bao, X. Lou, Q. Zhou, W. Dong, H. Yuan, and Y. Zhang, "Electrospun biomimetic fibrous scaffold from shape memory polymer of PDLLA-co-TMC for bone tissue engineering," *ACS Applied Materials & Interfaces*, vol. 6, no. 4, pp. 2611–2621, 2014.

[41] S. Zhao, Q. Zhou, Y.-Z. Long, G.-H. Sun, and Y. Zhang, "Nanofibrous patterns by direct electrospinning of nanofibers onto topographically structured non-conductive substrates," *Nanoscale*, vol. 5, no. 11, pp. 4993–5000, 2013.

[42] H. Yuan, Q. Zhou, and Y. Zhang, "6 - Improving fiber alignment during electrospinning," in *Electrospun Nanofibers*,

Series in Textiles, M. B. T.-E. N. Afshari, Ed., pp. 125–147, Woodhead Publishing, 2017.

[43] J. Doshi and D. H. Reneker, "Electrospinning process and applications of electrospun fibers," *Journal of Electrostatics*, vol. 35, no. 2-3, pp. 151–160, 1995.

[44] H. Fong and D. H. Reneker, "Electrospinning and the formation of nanofibers," in *Structure Formation in Polymeric Fibers*, pp. 225–246, Hanser, 1999.

[45] P. Ramesh Kumar, N. Khan, S. Vivekanandhan, N. Satyanarayana, A. K. Mohanty, and M. Misra, "Nanofibers: effective generation by electrospinning and their applications," *Journal of Nanoscience and Nanotechnology*, vol. 12, no. 1, pp. 1–25, 2012.

[46] K. Kalantari, A. M. Afifi, H. Jahangirian, and T. J. Webster, "Biomedical applications of chitosan electrospun nanofibers as a green polymer – review," *Carbohydrate Polymers*, vol. 207, pp. 588–600, 2019.

[47] Y. Lu, J. Huang, G. Yu et al., "Coaxial electrospun fibers: applications in drug delivery and tissue engineering," *Wiley Interdisciplinary Reviews: Nanomedicine and Nanobiotechnology*, vol. 8, no. 5, pp. 654–677, 2016.

[48] L. Zhou, J. Zhao, Y. Chen et al., "MoS2-ALG-Fe/GOx hydrogel with Fenton catalytic activity for combined cancer photothermal, starvation, and chemodynamic therapy," *Colloids Surfaces B Biointerfaces*, vol. 195, article 111243, 2020.

[49] K. Luo, J. Zhao, C. Jia et al., "Integration of $Fe_3O_4$ with $Bi_2S_3$ for multi-modality tumor theranostics," *ACS Applied Materials & Interfaces*, vol. 12, no. 20, pp. 22650–22660, 2020.

[50] A. Matsumoto, "Effect of strontium on the epiphyseal cartilage plate of rattibiae-histological and radiographic studies," *Θησαυρίσματα*, vol. 13, pp. 258–283, 1976.

[51] O. Z. Andersen, V. Offermanns, M. Sillassen et al., "Accelerated bone ingrowth by local delivery of strontium from surface functionalized titanium implants," *Biomaterials*, vol. 34, no. 24, pp. 5883–5890, 2013.

[52] C.-J. Chung and H.-Y. Long, "Systematic strontium substitution in hydroxyapatite coatings on titanium via micro-arc treatment and their osteoblast/osteoclast responses," *Acta Biomaterialia*, vol. 7, no. 11, pp. 4081–4087, 2011.

[53] C. B. Tovani, T. M. Oliveira, A. Gloter, and A. P. Ramos, "Sr2 +-substituted $CaCO_3$ nanorods: impact on the structure and bioactivity," *Crystal Growth & Design*, vol. 18, no. 5, pp. 2932–2940, 2018.

[54] R. J. Kavitha, K. Ravichandran, and T. S. N. Sankara Narayanan, "Deposition of strontium phosphate coatings on magnesium by hydrothermal treatment: characteristics, corrosion resistance and bioactivity," *Journal of Alloys and Compounds*, vol. 745, pp. 725–743, 2018.

[55] S. Peng, X. S. Liu, S. Huang et al., "The cross-talk between osteoclasts and osteoblasts in response to strontium treatment: involvement of osteoprotegerin," *Bone*, vol. 49, no. 6, pp. 1290–1298, 2011.

[56] H. Y. Lee, D. Lie, K. S. Lim, T. Thirumoorthy, and S. M. Pang, "Strontium ranelate-induced toxic epidermal necrolysis in a patient with post-menopausal osteoporosis," *Osteoporosis International*, vol. 20, no. 1, pp. 161-162, 2009.

[57] M. Pilmane, K. Salma-Ancane, D. Loca, J. Locs, and L. Berzina-Cimdina, "Strontium and strontium ranelate: historical review of some of their functions," *Materials Science and Engineering: C*, vol. 78, pp. 1222–1230, 2017.

[58] S. Bose, G. Fielding, S. Tarafder, and A. Bandyopadhyay, "Trace element doping in calcium phosphate ceramics to understand osteogenesis and angiogenesis," *Trends in Biotechnology*, vol. 18, pp. 1199–1216, 2013.

[59] S. Zhang, Y. Dong, M. Chen et al., "Recent developments in strontium-based biocomposites for bone regeneration," *Journal of Artificial Organs*, vol. 23, no. 3, pp. 191–202, 2020.

[60] P. J. Marie, "Strontium ranelate: a physiological approach for optimizing bone formation and resorption," *Bone*, vol. 38, no. 2, pp. 10–14, 2006.

[61] A. S. Hurtel-Lemaire, R. Mentaverri, A. Caudrillier et al., "The calcium-sensing receptor is involved in strontium ranelate-induced osteoclast apoptosis. New insights into the associated signaling pathways," *Journal of Biological Chemistry*, vol. 284, pp. 575–584, 2008.

[62] S. Takaoka, T. Yamaguchi, S. Yano, M. Yamauchi, and T. Sugimoto, "The calcium-sensing receptor (CaR) is involved in strontium ranelate-induced osteoblast differentiation and mineralization," *Hormone and Metabolic Research*, vol. 42, no. 9, pp. 627–631, 2010.

[63] F. Yang, D. Yang, J. Tu, Q. Zheng, L. Cai, and L. Wang, "Strontium enhances osteogenic differentiation of mesenchymal stem cells and in vivo bone formation by activating Wnt/catenin signaling," *Stem Cells*, vol. 29, no. 6, pp. 981–991, 2011.

[64] B. Ma, Q. Zhang, D. Wu et al., "Strontium fructose 1,6-diphosphate prevents bone loss in a rat model of postmenopausal osteoporosis via the OPG/RANKL/RANK pathway," *Acta Pharmacologica Sinica*, vol. 33, no. 4, pp. 479–489, 2012.

[65] L. Cianferotti, F. D'asta, and M. L. Brandi, "A review on strontium ranelate long-term antifracture efficacy in the treatment of postmenopausal osteoporosis," *Therapeutic Advances in Musculoskeletal Disease*, vol. 5, no. 3, pp. 127–139, 2013.

[66] L. Kyllönen, M. D'Este, M. Alini, and D. Eglin, "Local drug delivery for enhancing fracture healing in osteoporotic bone," *Acta Biomaterialia*, vol. 11, pp. 412–434, 2015.

[67] S. Pors Nielsen, "The biological role of strontium," *Bone*, vol. 35, no. 3, pp. 583–588, 2004.

[68] W. T. Su, P. S. Wu, and T. Y. Huang, "Osteogenic differentiation of stem cells from human exfoliated deciduous teeth on poly(ε-caprolactone) nanofibers containing strontium phosphate," *Materials Science and Engineering: C*, vol. 46, pp. 427–434, 2015.

[69] S. R. K. Meka, S. Jain, and K. Chatterjee, "Strontium eluting nanofibers augment stem cell osteogenesis for bone tissue regeneration," *Colloids Surfaces B Biointerfaces*, vol. 146, pp. 649–656, 2016.

[70] X. Han, X. Zhou, K. Qiu et al., "Strontium-incorporated mineralized PLLA nanofibrous membranes for promoting bone defect repair," *Colloids Surfaces B Biointerfaces*, vol. 179, pp. 363–373, 2019.

[71] G. Kumar, C. K. Tison, K. Chatterjee et al., "The determination of stem cell fate by 3D scaffold structures through the control of cell shape," *Biomaterials*, vol. 32, pp. 9188–9196, 2011.

[72] C. Xie, D. Reynolds, H. Awad et al., "Structural bone allograft combined with genetically engineered mesenchymal stem cells as a novel platform for bone tissue engineering," *Tissue Engineering*, vol. 13, no. 3, pp. 435–445, 2007.

[73] X. Wu, W. Shi, and X. Cao, "Multiplicity of BMP signaling in skeletal development," *Annals of the New York Academy of Sciences*, vol. 1116, no. 1, pp. 29–49, 2007.

[74] C. Maes, T. Kobayashi, M. K. Selig et al., "Osteoblast precursors, but not mature osteoblasts, move into developing and fractured bones along with invading blood vessels," *Developmental Cell*, vol. 19, no. 2, pp. 329–344, 2010.

[75] Y. Zhang, L. K. Yu, and N. Xia, "Evaluation of serum and pleural levels of endostatin and vascular epithelial growth factor in lung cancer patients with pleural effusion," *Asian Pacific Journal of Tropical Medicine*, vol. 5, no. 3, pp. 239–242, 2012.

[76] A. Javed, J. S. Bae, F. Afzal et al., "Structural coupling of Smad and Runx2 for execution of the BMP2 osteogenic signal," *The Journal of Biological Chemistry*, vol. 283, no. 13, pp. 8412–8422, 2008.

[77] P. Dy, W. Wang, P. Bhattaram et al., "Sox9 directs hypertrophic maturation and blocks osteoblast differentiation of growth plate chondrocytes," *Developmental Cell*, vol. 22, no. 3, pp. 597–609, 2012.

[78] M. Schumacher, A. Lode, A. Helth, and M. Gelinsky, "A novel strontium(II)-modified calcium phosphate bone cement stimulates human-bone-marrow-derived mesenchymal stem cell proliferation and osteogenic differentiation in vitro," *Acta Biomaterialia*, vol. 9, no. 12, pp. 9547–9557, 2013.

[79] J. Wang, X. Wang, Z. Sun et al., "Stem cells from human-exfoliated deciduous teeth can differentiate into dopaminergic neuron-like cells," *Stem Cells and Development*, vol. 19, no. 9, pp. 1375–1383, 2010.

[80] M. V. Jose, V. Thomas, K. T. Johnson, D. R. Dean, and E. Nyairo, "Aligned PLGA HA nanofibrous nanocomposite scaffolds for bone tissue engineering," *Acta Biomaterialia*, vol. 5, no. 1, pp. 305–315, 2009.

[81] S. Peng, X. S. Liu, T. Wang et al., "*In vivo* anabolic effect of strontium on trabecular bone was associated with increased osteoblastogenesis of bone marrow stromal cells," *Journal of Orthopaedic*, vol. 28, no. 9, pp. 1208–1214, 2010.

[82] K. Madhavan Nampoothiri, N. R. Nair, and R. P. John, "An overview of the recent developments in polylactide (PLA) research," *Bioresource Technology*, vol. 101, no. 22, pp. 8493–8501, 2010.

[83] A. Martins, A. R. C. Duarte, S. Faria, A. P. Marques, R. L. Reis, and N. M. Neves, "Osteogenic induction of hBMSCs by electrospun scaffolds with dexamethasone release functionality," *Biomaterials*, vol. 31, no. 22, pp. 5875–5885, 2010.

[84] B. Gupta, N. Revagade, and J. Hilborn, "Poly(lactic acid) fiber: an overview," *Progress in Polymer Science*, vol. 32, no. 4, pp. 455–482, 2007.

[85] G. Sui, X. Yang, F. Mei et al., "Poly-L-lactic acid/hydroxyapatite hybrid membrane for bone tissue regeneration," *Journal of Biomedical Materials Research Part A*, vol. 82A, pp. 445–454, 2007.

[86] L. E. Charles, E. R. Kramer, M. T. Shaw, J. R. Olson, and M. Wei, "Self-reinforced composites of hydroxyapatite-coated PLLA fibers: fabrication and mechanical characterization," *Journal of the Mechanical Behavior of Biomedical Materials*, vol. 17, pp. 269–277, 2013.

[87] S. Bhakta, P. E. Faira, L. A. Salata et al., "Determination of relative in vivo osteoconductivity of modified potassium fluorrichterite glass-ceramics compared with 45S5 bioglass," *Journal of Materials Science Materials in Medicine*, vol. 23, no. 10, pp. 2521–2529, 2012.

[88] J. S. Fernandes, P. Gentile, M. Martins et al., "Reinforcement of poly-L-lactic acid electrospun membranes with strontium borosilicate bioactive glasses for bone tissue engineering," *Acta Biomaterialia*, vol. 44, pp. 168–177, 2016.

[89] L. Chen, H. Mazeh, A. Guardia et al., "Sustained release of strontium ($Sr^{2+}$) from polycaprolactone/poly (D,L-lactide-co-glycolide)-polyvinyl alcohol coaxial nanofibers enhances osteoblastic differentiation," *Journal of Biomaterials Applications*, vol. 34, no. 4, pp. 533–545, 2019.

[90] A. B. Lino, A. D. McCarthy, and J. M. Fernández, "Evaluation of strontium-containing PCL-PDIPF scaffolds for bone tissue engineering: in vitro and in vivo studies," *Annals of Biomedical Engineering*, vol. 47, no. 3, pp. 902–912, 2019.

[91] S. W. Tsai, W. X. Yu, P. A. Hwang et al., "Fabrication and characterization of strontium-substituted hydroxyapatite-CaO-CaCO3 nanofibers with a mesoporous structure as drug delivery carriers," *Pharmaceutics*, vol. 10, no. 4, p. 179, 2018.

[92] S. W. Tsai, W. X. Yu, P. A. Hwang, Y. W. Hsu, and F. Y. Hsu, "Fabrication and characteristics of PCL membranes containing strontium-substituted hydroxyapatite nanofibers for guided bone regeneration," *Polymers*, vol. 11, no. 11, p. 1761, 2019.

[93] S. W. Tsai, F. Y. Hsu, and P. L. Chen, "Beads of collagen-nanohydroxyapatite composites prepared by a biomimetic process and the effects of their surface texture on cellular behavior in MG63 osteoblast-like cells," *Acta Biomaterialia*, vol. 4, no. 5, pp. 1332–1341, 2008.

[94] J. Caverzasio, "Strontium ranelate promotes osteoblastic cell replication through at least two different mechanisms," *Bone*, vol. 42, no. 6, pp. 1131–1136, 2008.

[95] P. F. Sharkey, P. M. Lichstein, C. Shen, A. T. Tokarski, and J. Parvizi, "Why are total knee arthroplasties failing today—-has anything changed after 10 years?," *The Journal of Arthroplasty*, vol. 29, pp. 1774–1778, 2013.

[96] W. Song, J. Seta, L. Chen et al., "Doxycycline-loaded coaxial nanofiber coating of titanium implants enhances osseointegration and inhibits *Staphylococcus aureus* infection," *Biomedical Materials*, vol. 12, article 045008, 2012.

[97] J. Wang, A. Shah, and X. Yu, "The influence of fiber thickness, wall thickness and gap distance on the spiral nanofibrous scaffolds for bone tissue engineering," *Materials Science and Engineering: C*, vol. 31, no. 1, pp. 50–56, 2011.

[98] T. Kohgo, Y. Yamada, K. Ito et al., "Bone regeneration with self-assembling peptide nanofiber scaffolds in tissue engineering for osseointegration of dental implants," *The International Journal of Periodontics & Restorative Dentistry*, vol. 31, no. 4, pp. e9–16, 2011.

[99] Z. Huang, R. H. Daniels, R. J. Enzerink, V. Hardev, V. Sahi, and S. B. Goodman, "Effect of nanofiber-coated surfaces on the proliferation and differentiation of osteoprogenitors in vitro," *Tissue Engineering Part A*, vol. 14, no. 11, pp. 1853–1859, 2008.

[100] J. M. Gluck, P. Rahgozar, N. P. Ingle et al., "Hybrid coaxial electrospun nanofibrous scaffolds with limited immunological response created for tissue engineering," *Journal of Biomedical Materials Research Part B: Applied Biomaterials*, vol. 99, no. B, pp. 180–190, 2011.

[101] L. Hench and J. Wilson, "Surface-active biomaterials," *Science*, vol. 226, no. 4675, pp. 630–636, 1984.

[102] Y. Li, B. Li, G. Xu et al., "A feasible approach toward bioactive glass nanofibers with tunable protein release kinetics for bone scaffolds," *Colloids Surfaces B Biointerfaces*, vol. 122, pp. 785–791, 2014.

[103] S. K. Boda, G. Thrivikraman, B. Panigrahy, D. D. Sarma, and B. Basu, "Competing roles of substrate composition, microstructure, and sustained strontium release in directing osteogenic differentiation of hMSCs," *ACS Applied Materials & Interfaces*, vol. 9, pp. 19389–19408, 2016.

[104] L. Weng, S. K. Boda, M. J. Teusink, F. D. Shuler, X. Li, and J. Xie, "Binary doping of strontium and copper enhancing osteogenesis and angiogenesis of bioactive glass nanofibers while suppressing osteoclast activity," *ACS Applied Materials & Interfaces*, vol. 9, no. 29, pp. 24484–24496, 2017.

[105] S. V. Fridrikh, J. H. Yu, M. P. Brenner, and G. C. Rutledge, "Controlling the fiber diameter during electrospinning," *Physical Review Letters*, vol. 90, 2003.

[106] S. Hesaraki, M. Alizadeh, H. Nazarian, and D. Sharifi, "Physico-chemical and in vitro biological evaluation of strontium/calcium silicophosphate glass," *Journal of Materials Science Materials in Medicine*, vol. 21, no. 2, pp. 695–705, 2010.

[107] S. Islam, F. Hassan, G. Tumurkhuu et al., "Bacterial lipopolysaccharide induces osteoclast formation in RAW 264.7 macrophage cells," *Biochemical and Biophysical Research Communications*, vol. 360, no. 2, pp. 346–351, 2007.

[108] M. Roy and S. Bose, "Osteoclastogenesis and osteoclastic resorption of tricalcium phosphate: effect of strontium and magnesium doping," *Journal of Biomedical Materials Research Part A*, vol. 100, no. A, pp. 2450–2461, 2012.

[109] M. M. Echezarreta-López and M. Landin, "Using machine learning for improving knowledge on antibacterial effect of bioactive glass," *International Journal of Pharmaceutics*, vol. 453, no. 2, pp. 641–647, 2013.

[110] L. L. Hench, "The story of Bioglass®," *Journal of Materials Science. Materials in Medicine*, vol. 17, no. 11, pp. 967–978, 2006.

[111] M. M. Echezarreta-López, T. De Miguel, F. Quintero, J. Pou, and M. Landín, "Fabrication of Zn-Sr–doped laser-spinning glass nanofibers with antibacterial properties," *Journal of Biomaterials Applications*, vol. 31, pp. 819–831, 2016.

[112] H. Doweidar, "Density-structure correlations in silicate glasses," *Journal of Non-Crystalline Solids*, vol. 249, no. 2-3, pp. 194–200, 1999.

[113] L. Gu, X. He, and Z. Wu, "Mesoporous hydroxyapatite: preparation, drug adsorption, and release properties," *Materials Chemistry and Physics*, vol. 148, no. 1-2, pp. 153–158, 2014.

[114] Y. J. Shyong, M. H. Wang, L. W. Kuo et al., "Mesoporous hydroxyapatite as a carrier of olanzapine for long-acting antidepression treatment in rats with induced depression," *Journal of Controlled Release*, vol. 255, pp. 62–72, 2017.

[115] T. A. Kuriakose, S. N. Kalkura, M. Palanichamy et al., "Synthesis of stoichiometric nano crystalline hydroxyapatite by ethanol-based sol-gel technique at low temperature," *Journal of Crystal Growth*, vol. 263, no. 1-4, pp. 517–523, 2004.

[116] M. H. Fathi, A. Hanifi, and V. Mortazavi, "Preparation and bioactivity evaluation of bone-like hydroxyapatite nanopowder," *Journal of Materials Processing Technology*, vol. 202, no. 1-3, pp. 536–542, 2008.

[117] P. Kanchana and C. Sekar, "Influence of strontium on the synthesis and surface properties of biphasic calcium phosphate (BCP) bioceramics," *Journal of Applied Biomaterials & Biomechanics*, vol. 8, no. 3, pp. 153–158, 2010.

Hindawi
Journal of Nanomaterials
Volume 2020, Article ID 8305871, 13 pages
https://doi.org/10.1155/2020/8305871

*Research Article*

# Synthesis and Characterization of Hierarchical Mesoporous-Macroporous $TiO_2$-$ZrO_2$ Nanocomposite Scaffolds for Cancellous Bone Tissue Engineering Applications

**Shima Mahtabian**,[1] **Zahra Yahay**,[1] **Seyed Mehdi Mirhadi**,[1] **and Fariborz Tavangarian**[2]

[1]*Department of Materials Engineering, Shahreza Branch, Islamic Azad University, 86145-311 Shahreza, Isfahan, Iran*
[2]*Mechanical Engineering Program, School of Science, Engineering and Technology, Pennsylvania State University, Harrisburg, Middletown, PA 17057, USA*

Correspondence should be addressed to Fariborz Tavangarian; fut16@psu.edu

Received 30 July 2020; Revised 31 August 2020; Accepted 17 September 2020; Published 6 October 2020

Academic Editor: Nicholas Dunne



Bone tissue engineering has been introduced several decades ago as a substitute for traditional grafting techniques to treat bone defects using engineered materials. The main goal in bone tissue engineering is to introduce materials and structures which can mimic the function of bone to restore the damaged tissue and promote cell restoration and proliferation. Titania and zirconia are well-known bioceramics which have been widely used in tissue engineering applications due to their unsurpassed characteristics. In this study, hierarchical meso/macroporous titania-zirconia ($TiO_2$-$ZrO_2$) nanocomposite scaffolds have been synthesized and evaluated for bone tissue engineering applications. The scaffolds were produced using the evaporation-induced self-assembly (EISA) technique along with the foamy method. To characterize the samples, X-ray diffraction (XRD), scanning electron microscopy (SEM), energy-dispersive X-ray spectroscopy (EDS), simultaneous thermal analysis (STA), and Brunauer-Emmett-Teller (BET) analysis were performed. The results showed that $TiO_2$-$ZrO_2$ scaffolds can be produced after sintering the samples at 550°C for 2 h. Among samples with different weight percentages of zirconia and titania, the sample containing 13 wt.% zirconia was considered as the optimum sample due to its structural integrity. This scaffold had pore size, pore wall size, and mesopores in the range of $185 \pm 66\,\mu$m, $15 \pm 4\,\mu$m, and 7-13 nm, respectively. The specific surface area obtained from the BET theory, total volume, and mean diameter of pores of this sample was 13.627 $m^2g^{1-}$, 0.03788 $cm^3g^{-1}$, and 11 nm, respectively. The results showed that the produced scaffolds can be considered as the promising candidates for cancellous bone regeneration.

## 1. Introduction

In recent decades, a great deal of effort and attention has been focused on designing scaffolds which are biologically, chemically, physically, mechanically, and structurally carefully matched to that of natural bone [1–23]. Although each type of bone tissue has specific requirements which must be met, there are some features in common that should be considered in designing bone scaffolds to present the exact function of host tissue [24, 25]. Generally, bone has a complex meso/macroporous hierarchical structure [24–29] with multisized interconnected pores [30, 31]. One of the main issues is to synthesize scaffolds with a hierarchical porous structure with pore interconnectivity to mimic the ECM of the host tissue. Different pore sizes play a remarkable role in enhancing cell viability and osteogenesis and finally in therapeutic effects for bone tissue engineering applications [32–36]. The macropore size of larger than 150 $\mu$m is required for cell accommodation and proliferation and also for vascularization [32, 37–42]. Mesopores with the size of 2-50 nm are also required to insert the nutrients and release the biological agents, to remove waste materials, and also to enhance the surface activity and bioactivity [37, 40–42].

Different techniques have been used to synthesize hierarchical structures including templating methods [43, 44], freeze-drying technique [45–47], and sol-gel method [48, 49]. In this study, the sol-gel method was utilized to synthesize the samples.

According to the literature, the sol-gel method is a facile way to synthesize metal oxide nanoparticles with high quality and purity at low temperatures. In this technique, precursors are dispersed in an aquatic or alcoholic environment at temperatures lower than 100°C. Through the hydrolysis and condensation, aggregation in the obtained colloidal solution which is called "sol" causes to make "gel" with a 3D network of M-O-M or M-OH-M units. Unlike other techniques such as the solid-state method, the sol-gel procedure requires low temperatures and very fine powders in which a homogeneous composition can be obtained. However, there are some disadvantages as well which should be considered such as a relatively high cost of initial precursors and the formation of cracks during the heat treatment cycles to remove the organic materials [50].

On the other hand, the evaporation-induced self-assembly technique (EISA) is a successful, simple, fast, and efficient method for the preparation of mesoporous metal oxides [51, 52]. The existence of hydrophobic and hydrophilic components in the surfactants causes the formation of micelle-like structures that are removed from the system by burning the hydrocarbon chains which leaves pores behind. This technique was first used to synthesize the silica mesoporous structure [53–55] and gradually was incorporated with the sol-gel method by using surfactants for other metal oxides [56]. Among many kinds of surfactants, the nonionic Pluronic F127 formed a well-organized mesopore structure [57].

$TiO_2$-$ZrO_2$ nanocomposite has been used in different applications. For example, Fu et al. [58] and Yu et al. [59] worked on its photocatalytic properties, individually. They reported that this nanocomposite shows better photocatalytic behavior compared to titania or zirconia, separately. The bioactivity of titania-zirconia nanocomposite has been studied by Marchi et al. [60]. The results showed an increase in apatite formation ability which indicates its good bioactivity in the biological environment. Also, this composite has been used as a 3D scaffold and coating. Tiainen et al. [61] investigated the mechanical properties of titania-zirconia nanocomposite scaffolds with different weight percentages of zirconia. The results showed that increasing the amount of zirconia in the composite decreased the mechanical strength of the scaffolds. Titania coating on its alloys is widely used in dental implants and hip prosthesis due to their excellent biocompatibility. According to the literature, $TiO_2$ has excellent biocompatibility, low toxicity, good corrosion resistance, and low density [62–64]. On the other hand, zirconia has several upsides over other bioceramics. Zirconia is bioinert in vivo and in vitro [65–67]. In vitro tests have shown that zirconia has lower toxicity than titanium oxide [68]. Additionally, cytotoxicity and carcinogenicity have not been reported [68]. Besides, it has good mechanical properties such as corrosion and abrasion resistance. Furthermore, it increases the crack self-healing potential of scaffolds by its transformation toughening mechanism [69, 70]. The strength of interfacial bonding between substrate and coating will be improved by the help of adding $ZrO_2$. Also, zirconia enhances apatite formation due to increasing the hydrophilicity of the substrate [71].


Figure 1: Schematic representation of the sol-gel method.

In the present study, for the first time, nanocomposite $ZrO_2$/$TiO_2$ scaffolds were produced using the EISA technique combined with the foamy method. Interconnected macropores were prepared by polyurethane (PU) (60 pores per inch (ppi)) sponge, and mesopores were made using Pluronic F127 surfactant by the help of a self-assembly technique in order to simulate the natural bone hierarchical porous structure. Structural features, chemical composition, and porosity features of the $ZrO_2$/$TiO_2$ nanocomposite scaffolds were evaluated. Furthermore, the formation mechanism of the produced scaffolds was evaluated as well.

## 2. Materials and Methods

*2.1. Sample Preparation.* In this study, the sol-gel technique was used to fabricate $TiO_2$-$ZrO_2$ nanocomposite scaffolds. A schematic representation of the sol-gel method is shown in Figure 1. To prepare the samples, titania and zirconia solutions were produced. Titania solution was prepared according to our previous study [72]. Briefly, 5 ml titanium (IV) butoxide ($C_{16}H_{36}O_4Ti$, 97%, Sigma-Aldrich) was added to 3.092 ml acetylacetone ($C_5H_8O_2$, 99.5%, Merck) and 125 ml absolute ethanol ($C_2H_6O$, 99.5%, Sigma-Aldrich). Next, a mixture of 2 gr Pluronic F127 (PF127, $C_3H_3O$ $[C_2H_4O]_x$ $[C_3H_6O]_y[C_2H_4O]_zC_3H_3O_2$, 99.5%, Sigma-Aldrich) that was dissolved in 125 ml absolute ethanol ($C_2H_6O$, 99.5%, Sigma-Aldrich) and 6.67 ml hydrochloric acid (HCL, 38 wt.%, to adjust the pH solution to 4 as the zeta potential of the solution in order to disperse the particles and avoid coagulation) was gently added to the previous solution, stirred for 24 h with the speed of 1000 rpm at room temperature, and then aged for 48 h at a location with 40% humidity.

Table 1: Designation and specification of different samples.

| Sample designation | $TiO_2$ content (wt.%) | $ZrO_2$ content (wt.%) | Solution type | Including foam | Including solution | Heat treatment |
|---|---|---|---|---|---|---|
| $S_{13Zr}$ | 87 | 13 | A | ✓ | ✓ | ✓ |
| $S_{26Zr}$ | 74 | 26 | B | ✓ | ✓ | ✓ |
| $S_{50Zr}$ | 50 | 50 | C | ✓ | ✓ | ✓ |
| $S_{76Zr}$ | 24 | 76 | D | ✓ | ✓ | ✓ |
| $S_{86Zr}$ | 14 | 86 | E | ✓ | ✓ | ✓ |
| SF | × | × | × | ✓ | × | × |
| SS | 87 | 13 | A | × | ✓ | × |
| SSF | 87 | 13 | A | ✓ | ✓ | × |

Based on the previous study [73], to prepare zirconia solution, 3.65 ml zirconium (IV) butoxide ($Zr(OC_4H_2)_4$, 80 wt.%, Sigma-Aldrich) and 0.63 gr citric acid ($C_6H_8O_7$, Merck) were dissolved in 125 ml absolute ethanol and stirred by a magnetic stirrer until a clear solution was obtained. Then, a combination of 2 gr PF127, 125 ml absolute ethanol, and 6.67 ml hydrochloric acid was gently added to the zirconia solution, stirred for 24 h with the speed of 1000 rpm at ambient temperature, and then aged for 48 h at a location with 40% humidity. Samples with different weight ratios of titania and zirconia solutions were prepared to investigate their effect on the sample integrity and microstructure. Table 1 shows the designation and specification of different samples.

PU sponge (60 PPI) with a mean pore size of 300-700 $\mu$m was used to make blocks with a dimension of 10 mm × 10 mm × 10 mm. The blocks were dipped in different solutions with various $ZrO_2$ to $TiO_2$ weight ratios for 1 h. The saturated PU blocks with the solution were squeezed by a hand roller. These blocks were then dried at room temperature for 72 h. The dried foams were sintered at 550°C for 2 h with the heating/cooling rate of 5°C min $^{-1}$. Figure 2 illustrates the preparation steps of different samples.

*2.2. Sample Characterization.* In order to assess the thermal decomposition temperature of PU foam and volatile materials and to optimize the calcination temperature of materials used to make the solutions, a simultaneous thermal analysis (STA) test was performed up to 550°C with the heating rate of 5°C/min, using the NETZSCH STA 449F3 machine.

To investigate the morphology and to measure the pore size of the scaffolds, scanning electron microscopy (SEM) was applied using SEM/EDS, Zeiss, Germany machine (FEI Quanta 200 SEM) with the working distance in the range of 9.5-13.8 $\mu$m and the voltage in the range of 15 to 25 kV. To evaluate the elemental compositions of samples, energy-dispersive spectroscopy (EDS) was utilized. Map scan analyses were performed to determine the elements formed in randomly selected locations of the scaffolds using the same machine. Small-angle X-ray scattering (SAXS) was performed using the Asenware AW-DX300 diffractometer to approve the formation of a mesoporous structure. SAXS traces were recorded with $2\theta$ in the range of 0.5-10 degrees with a Cu K$\alpha$ radiation source with $\lambda = 0.154184$ nm. Wide-angle X-ray diffraction (WAXRD) analysis with $2\theta$ in the range of 10-90 degrees was used to study the crystalline phase of samples using the same machine. The nitrogen adsorption-desorption isotherms were used at 77 K using the BELSORP-mini II analyzer to determine the pore structure and to assess the specific surface area.

## 3. Results and Discussions

*3.1. STA Evaluation.* To assess the weight loss and to determine the temperature of reactions that occurred during the sintering procedure of $TiO_2$-$ZrO_2$ scaffolds, simultaneous thermal analysis (STA) was utilized. Different samples (Table 1, SS which contains only solution, SF which contains only PU foam, and SSF which contains a solution with PU foam together), 3 samples for each, were used to accurately determine the effect of each component on the STA traces. Figure 3 shows the results of the thermogravimetry-differential scanning calorimeter (TG-DSC) curves of different samples. The TG curve of the SF sample (contains only PU foam) showed that foam is burned out at a temperature of around 310 ± 2°C (Figure 3(a)) [74]. The results proved that at the sintering temperature, no sponge was left in the structure.

Figure 3(b) shows the STA analysis of the SS sample which only contains solution A (see Table 1). The results showed that there is an exothermic peak at 301.6°C. The TGA result also showed that this exothermic process accounted for a substantial amount of the total weight loss on the whole decomposition process from about 50°C to around 300°C. The exothermic peak and the associated weight loss were due to the decomposition of organic materials and their removal from the system, as proved by the EDS analysis of the sintered scaffolds, at 550°C in which no organic material was detected (Figure 4).

The exothermic peak and subsequent mass change at around 300°C were in good agreement with the reported results of previous studies. In other words, the range of around 171.40-301.37°C has been considered as the decomposition temperature of Pluronic F127. The decomposition temperature of zirconium butoxide, acetylacetone, titanium butoxide, and citric acid was reported to be around 176.85°C, 280°C, 122°C, and 19.85-399.85°C, respectively [72, 75–80].

Also, Figure 3(c) pertains to the SSF sample, the one with both foam and solution. It can be seen that foam was removed from the system at 283.6 ± 2°C. The exothermic peak occurred at 434.9 ± 1°C could be ascribed to the oxidation of titanium and zirconium. Based on the results of Figure 3, the calcination temperature was adjusted to 550°C to ensure that at the end of the heat treatment cycle, no foam

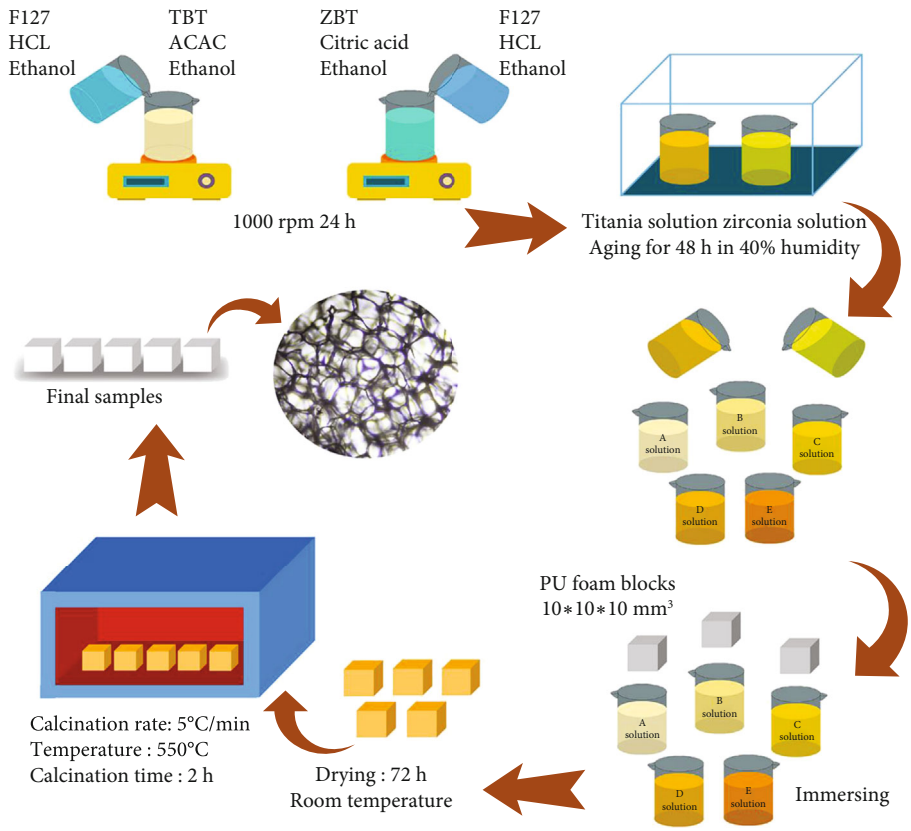


Figure 2: Schematic representation of the synthesis procedure of meso/macroporous $TiO_2$-$ZrO_2$ scaffolds.

and organic additives were left in the scaffolds and only titanium and zirconium oxides were present in the structure.

*3.2. SEM/EDS Evaluation.* The morphology and pore size of the scaffolds are extremely important to achieve desirable mechanical properties and to have effective cell adhesion, cell proliferation, and strong cell growth into the scaffolds. The optimized sample in this study was known as the one with structural integrity without any cracks. To investigate the morphology of pores that have been formed through the foamy method after heat treatment and their size, samples were studied with SEM. Figure 5 shows the structure, pore morphology, pore size, pore distribution, mesopores, and finally pore wall of a random macropore of $S_{13Zr}$ sample which was annealed at 550°C for 2 h. Figures 5(a) and 5(b) show the macropore structure, and Figures 5(c) and 5(d) show the mesopore structures in the scaffolds.

On the other hand, Figure 6 shows the structure of other samples with different amounts of zirconia that were annealed in the same condition. As can be seen in Figure 6, all samples have some structural defects such as cracks on the wall of pores (shown by arrows). The high amount of zirconia can be the reason for the existence of cracks in the scaffolds which makes them completely useless for bone tissue engineering applications [61]. However, as can be seen in Figure 5, $S_{13Zr}$ sample (containing 13 wt.% zirconia and 87 wt.% titania) exhibits an integrated structure with no crack, appropriate pore size for cell accommodation, cell growth, and cell proliferation. Therefore, $S_{13Zr}$ sample was considered as the optimized sample for further studies.

Figure 7 shows the histogram of the macropore size in the $S_{13Zr}$ sample. As it is obvious, the formation of appropriate macroporosity with a desirable size (more frequency in pore sizes measured greater than 150 $\mu$m that is beneficial for cell accommodation, penetration, and differentiation) in the produced scaffold can provide a suitable environment for the vascularization which plays a vital role in the success of the scaffold. EDS was utilized to reveal the average local chemical composition in the produced scaffold. Figure 4 shows the EDS results of the $S_{13Zr}$ sample. A homogeneous distribution of Ti and Zr elements was observed in the EDS results of the optimized scaffold.

Figure 8 shows the results of the EDS elemental mapping of the $S_{13Zr}$ sample. The results showed a homogeneous distribution of Ti and Zr in this sample which demonstrate the effectiveness of the fabrication technique to form a uniform structure.

*3.3. XRD Evaluation.* The phase transformation of the $S_{13Zr}$ sample was investigated by XRD. Figure 9(a) illustrates the wide-angle X-ray scattering (WAXRD) pattern. The presence of metal oxide formed at the low temperature was successfully proved by the XRD patterns. As can be seen in Figure 9(a), the sample has not been completely crystallized due to the low temperature used for heat treatment. The low annealing temperature was used to protect and retain the mesopores of the sample because the mesopores will collapse

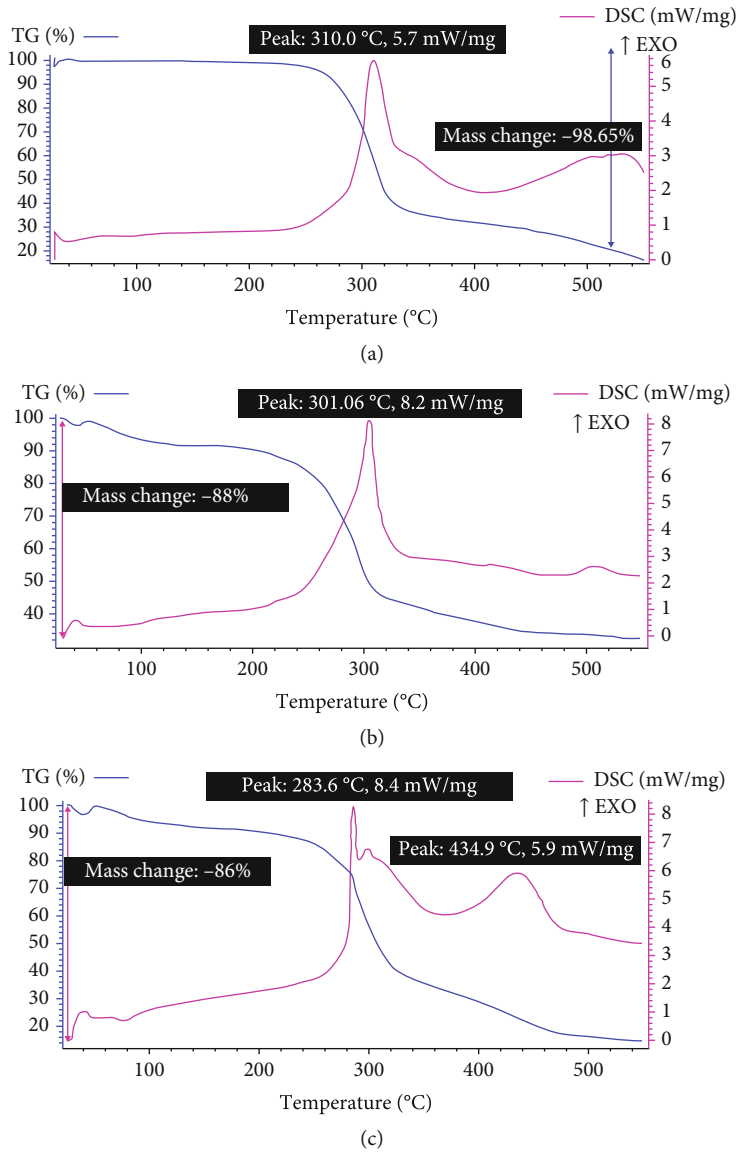


Figure 3: (a) Simultaneous thermal analysis of PU foam; (b) simultaneous thermal analysis of solution A (see Table 1); (c) simultaneous thermal analysis of SFF sample.

during a high temperature of sintering [81]. On the other hand, the mesoporous structure transforms the long-range order of crystals into the short-range order. So the XRD pattern of mesoporous structures is similar to semicrystalline structures [81]. An intensive peak can be seen in Figure 9(a) in $2\theta$ equals to 25 degrees that shows the formation of the anatase phase (XRD JCPDS data file No. 01-071-1169) in the structure.

Titania and zirconia can form different crystal polymorphs at different temperatures [82, 83]. According to their phase diagram and the calcination temperature, the anatase phase for titania and monoclinic phase for zirconia should be stable at room temperature [84].

Based on the literature, the monoclinic phase of zirconia is thermodynamically its most stable phase; however, the less stable phases of zirconia (cubic or tetragonal) could form at higher temperatures. In other words, according to the zirconia phase diagram, the monoclinic phase of zirconia is stable from ambient temperature to 1170°C. The tetragonal phase is stable from 1170°C to 2370°C, and from 2370°C to the melting point cubic phase of zirconia will be stable [83].

On the other hand, the most stable phase of titania is rutile; however, according to previous studies, the formation of short-range order $TiO_6$ in anatase is easier than the formation of long-range order $TiO_6$ in rutile [82]. Also, thermodynamically, the level of surface free energy of anatase is lower than that of the rutile phase which causes that $TiO_2$-based nanocomposites and nanofilms contain anatase phase at room temperature [82].

Some elements such as Ca, scandium, strontium, yttrium, niobium, barium, lanthanum, aurum (gold), boron, aluminum, silicon, phosphorus, sulfur, chlorine, cerium, neodymium, samarium, europium, gadolinium, terbium, dysprosium,

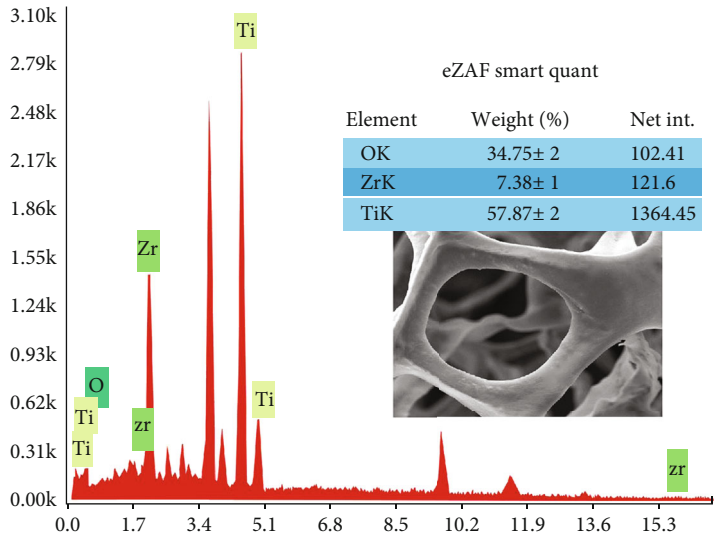


Figure 4: EDAX analysis of the $S_{13Zr}$ sample.

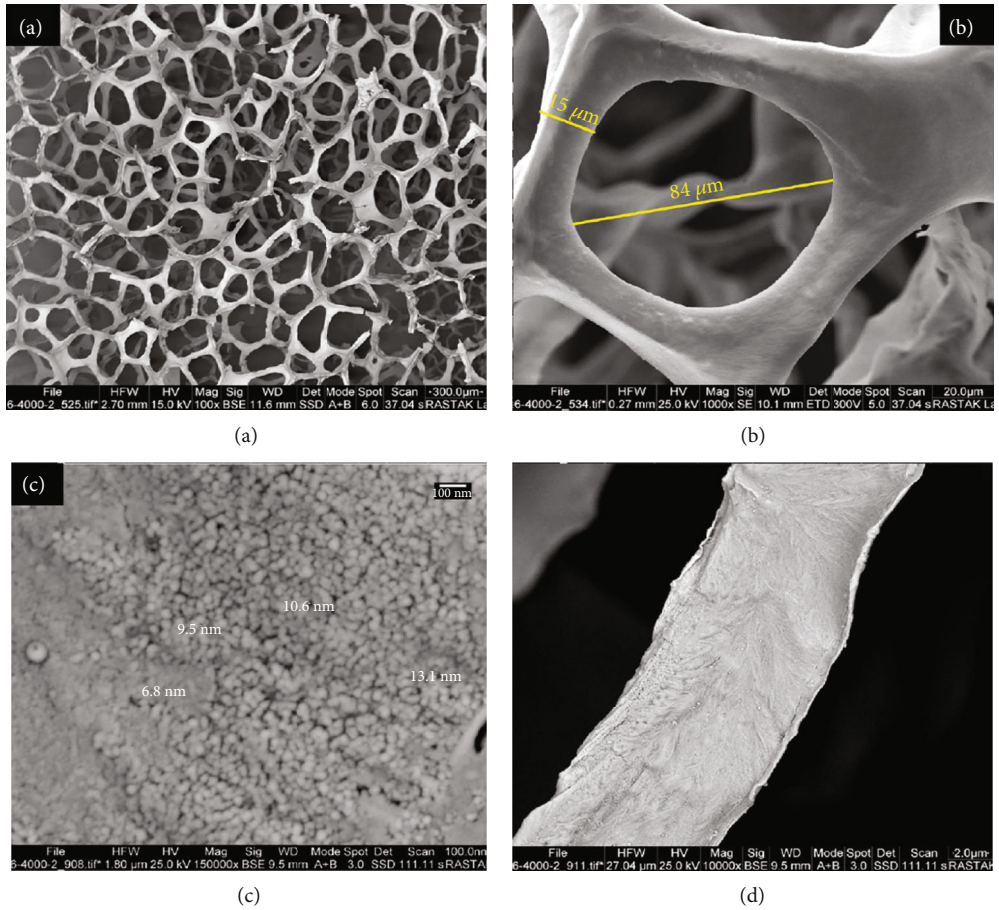


(a) (b) (c) (d)

Figure 5: Scanning electron microscopy (SEM) images of sample $S_{13Zr}$ as the optimized sample ($S_{13Zr}$) sintered at 550°C for 2 h: (a) the general shape of the scaffold which shows the favorable structural integrity, (b) acceptable pore morphology and pore size (no crack can be observed), (c) desirable size of mesopores which are the best space to insert nutrients to be used by cells in order to proliferate and grow into the scaffold, and (d) strong pore wall which exhibits nice interconnectivity and strong structure for each macropore to mimic the natural bone tissue structure.

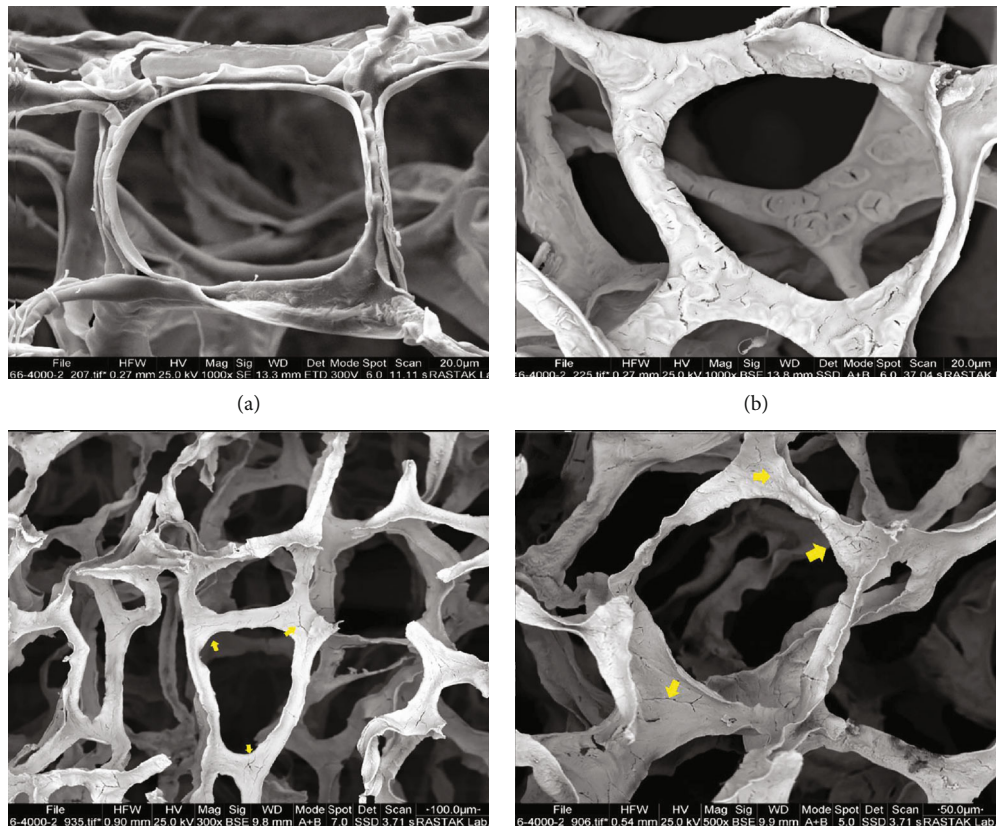


FIGURE 6: Scanning electron microscopy (SEM) images of (a) sample $S_{26Zr}$, (b) sample $S_{50Zr}$, (c) sample $S_{76Zr}$, and (d) sample $S_{86Zr}$ which are completely inappropriate for cells to attach and grow in. It seems that the different amount of zirconia and titania has made heterogeneity in their structure which results in forming cracks and weak pores and pore walls and also the high amount of zirconia in the samples has a detrimental role in structural integrity.

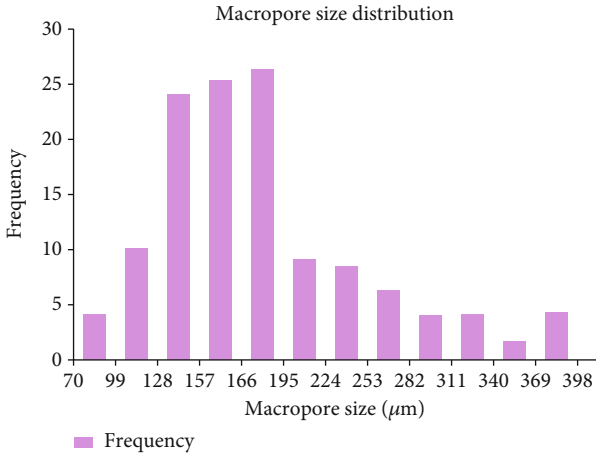


FIGURE 7: The histogram of the macropore size distribution in the $S_{13Zr}$ sample.

holmium, erbium, thulium, ytterbium, and specifically zirconia have an inhibitor role against phase transformation from anatase to rutile in titania [4, 82, 85]. In this study, Zr has been used as the second phase of the nanocomposite. In fact, the addition of zirconia to titania stabilizes the anatase phase of titania and inhibits its grain growth [86].

Figure 9(b) shows the small-angle X-ray spectroscopy (SAXS) pattern of sample $S_{13Zr}$ which was sintered at 550° for 2 h. In the SAXS analysis, the intensity and sharpness of the peak is a sign of the formation of a well-ordered mesoporous structure [87, 88]. SAXS was performed in the $2\theta$ range of 0.5-10 degrees. As can be seen in Figure 9(b), a sharp peak in $2\theta$ equals to 0.7 degrees can be observed which indicates the formation of well-ordered mesoporous structures in this sample. The results obtained from the SAXS analysis were in good agreement with those obtained from the SEM observation (Figure 5(c)).

In general, $TiO_2$ formation occurs in three different steps. As mentioned, the sol-gel method through the alkoxide route was used to prepare $TiO_2$ and $ZrO_2$ solutions. At the first step, the aqueous environment induces alkoxide hydrolysis and produces titanium hydroxide and zirconium hydroxide and alcohol (alkoxide group hydroxide). The second step can occur through the interaction between either two hydroxide metals or a hydroxide metal and an alkoxide metal that finally produce A-O-A, in which A refers to the metal (Zr or Ti) and O refers to the oxygen, and water or alcohol in an aqueous and alcoholic environment [89–91]. $TiO_2$ and $ZrO_2$ particles act as the nuclei to expand metal oxides formed during the synthesis procedure. The steps of the formation of $TiO_2$ can be expressed as follows [90]:

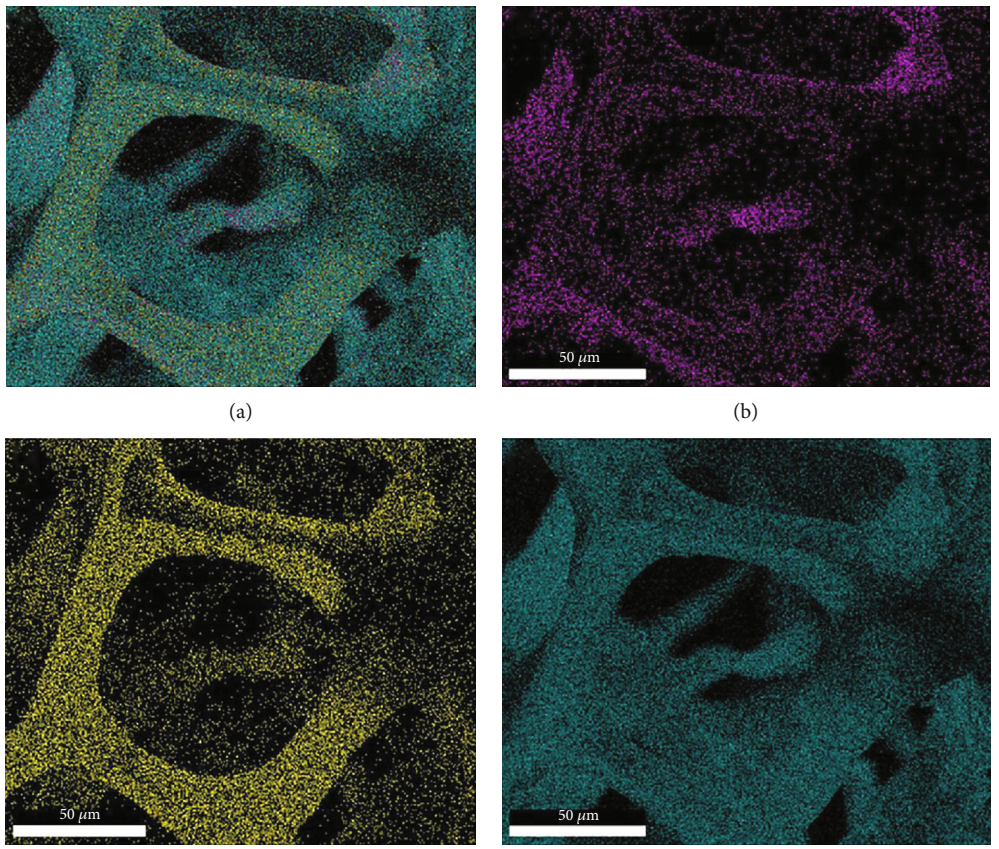


Figure 8: EDX elemental mapping of $S_{13Zr}$ sample: (a) oxygen (5 wt.%), zirconium (12 wt.%), and titanium (83 wt.%); (b) oxygen; (c) zirconium; (d) titanium.

(1) Hydrolysis of titanium alkoxide:

$$C_{16}H_{36}O_4Ti + 4H_2O \longrightarrow Ti(OH)_4 + 4C_4H_9OH \quad (1)$$

(2) Condensation of hydrolyzed species:

$$Ti(OH)_4 \longrightarrow TiO_2 + 2H_2O \quad (2)$$

Equation (2) can also be expressed as follows:

$$\begin{aligned}&\text{Water condensation}: Ti(OH)_4 + Ti(OH)_4 \longrightarrow Ti{-}O{-}Ti + HOH\\ &\text{Alcohol condensation}: Ti(OH)_4 + Ti(OC_4H_9)_4 \longrightarrow Ti{-}O{-}Ti\\ &\quad + C_4H_9OHTiO_2 \text{ sol particles}\end{aligned} \quad (3)$$

(3) Growth of $TiO_2$ sol particles

On the other hand, almost the same procedures happen during the formation of $ZrO_2$ [91]:

(1) Hydrolysis of zirconium alkoxide:

$$C_{16}H_8O_4Zr + H_2O \longrightarrow Zr(OH)_4 + C_{16}H_8O_4(OH) \quad (4)$$

(2) Condensation of hydrolyzed species:

$$Zr(OH)_4 + ZrO_4H_{36}C_{16} \longrightarrow Zr - O - Zr + C_{16}H_{36}O_4(OH) \quad (5)$$

In more details:

$$\begin{aligned}&\text{Water condensation}: Zr(OH)_4 + Zr(OH)_4 \longrightarrow Zr{-}O{-}Zr + HOH\\ &\text{Alcohol condensation}: Zr(OH)_4 + Zr(OR)_4 \longrightarrow Zr{-}O{-}Zr\\ &\quad + C_4H_9OHZrO_2 \text{ sol particles}\end{aligned} \quad (6)$$

(3) Growth of $ZrO_2$ sol particles

Figure 10 shows the schematic representation of the aforementioned steps clearly in detail.

The nuclei growth phenomenon stems from the incredible high surface area of particles and consequently their high

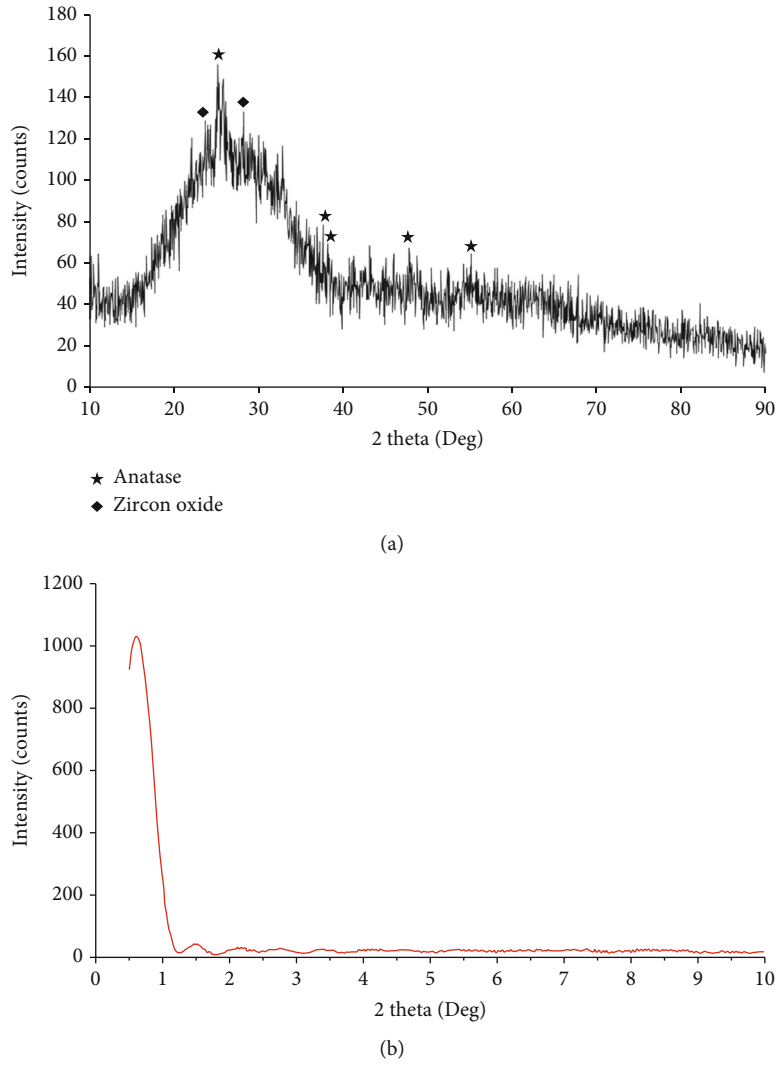


FIGURE 9: (a) Wide-angle XRD of the optimized sample contains 13 wt.% $ZrO_2$ and 87 wt.% $TiO_2$ heated at 550°C for 2 h with the heating/cooling rate of 5°C $min^{-1}$. (b) Small-angle XRD of optimized meso/macroporous titania-zirconia sample heated at 550°C for 2 h.

amount of energy which makes them thermodynamically unstable. For this purpose, metal oxide particles (as the nuclei) start to grow through Ostwald ripening or oriented attachment mechanism or even both, to decrease their energy level. According to Ostwald ripening phenomenon, small particles dissolve in the solution because of their high energy level and bigger particles get bigger and bigger in regular spherical shapes by attracting small particles. Based on the oriented attachment mechanism, small particles get together and aggregate at the first step; then, they will be considered as a specific place for other small particles to attach and consequently form crystals [92]. Linear F127 polymer that was used as the template for mesopores has hydrophilic and hydrophobic parts. After dissolving in ethanol, F127 forms special structures that usually transforms into regular spherical micelles in solution. Finally, drying and calcination cause the formation of mesostructure [93]. Figure 11 shows the mechanism of mesopore formation.

*3.4. BET Evaluation.* Figure 12 demonstrates the nitrogen adsorption-desorption isotherms of the $S_{13Zr}$ sample after sintering at 550°C for 2 h. The specific surface area of the $S_{13Zr}$ sample measured by the Brunauer-Emmett-Teller (BET) theory was 13.627 $m^2g^{-1}$; the total porosity volume obtained from the adsorption curve of the isotherm diagram and mean pore diameter were 0.03788 $cm^3g^{-1}$ and 11.119 nm, respectively.

## 4. Conclusions

In this study, hierarchical meso/macroporous hierarchical titania-zirconia nanocomposite was fabricated for tissue engineering applications. Different samples with different weight percentages of titania and zirconia were prepared by the help of the EISA technique coupled with the foamy method. The foamy method was applied to provide the macropore template, and the EISA method was utilized to

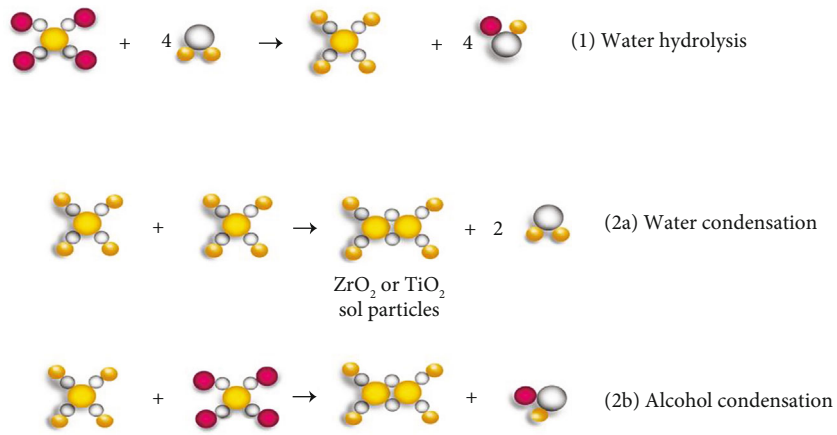


Figure 10: Schematic representation of chemical interactions involved in the sol-gel process.

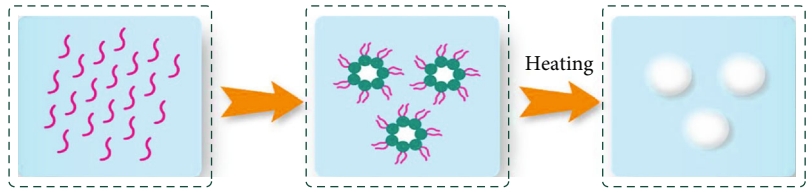


Figure 11: Schematic representation of mesopore formation mechanism and the behavior of F127 linear polymer in the solution.

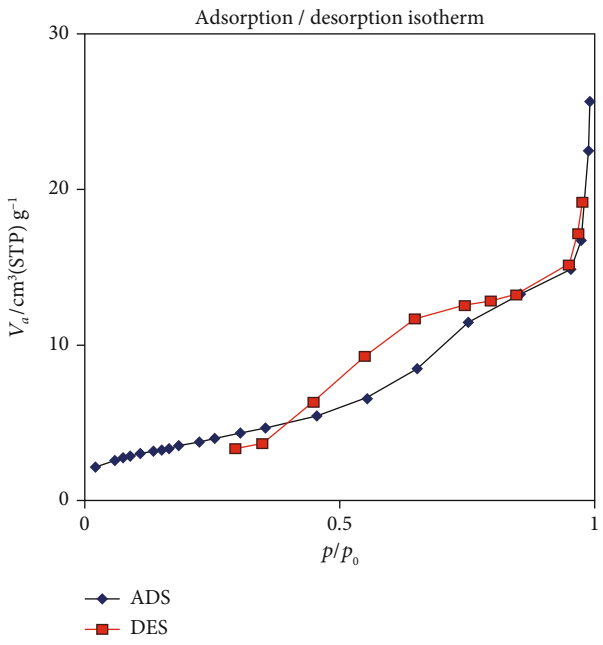


Figure 12: BET analysis of the $S_{13Zr}$ scaffold as the optimized sample.

provide a mesopore structure. The results showed that scaffolds with a lower amount of zirconia had less structural defects. This scaffold had pore size, pore wall size, and mesopores in the range of $185 \pm 66\,\mu$m, $15 \pm 4\,\mu$m, and 7-13 nm, respectively. The specific surface area obtained from the BET theory, total volume, and mean diameter of pores of this sample was 13.627 $m^2g^{-1}$, 0.03788 $cm^3g^{-1}$, and 11 nm, respectively.

## Data Availability

The raw/processed data required to reproduce these findings cannot be shared at this time as the data also forms part of an ongoing study. If you need to have access to some of the raw data, please contact the corresponding author.

## Additional Points

*Highlights*. (1) $ZrO_2/TiO_2$ nanocomposite scaffolds were synthesized using the EISA and foamy method. (2) The formation mechanism of the scaffolds was scrutinized. (3) The influence of the $ZrO_2$ on the integrity of the scaffolds was evaluated. (4) Nanocomposite scaffolds consisting of 13 wt.% $ZrO_2$ showed an integrated structure

## Conflicts of Interest

The authors declare that there is no conflict of interest regarding the publication of this article.

## References

[1] A. R. Amini, C. T. Laurencin, and S. P. Nukavarapu, "Bone tissue engineering: recent advances and challenges," *Critical Reviews in Biomedical Engineering*, vol. 40, no. 5, pp. 363–408, 2012.

[2] S. Bose, M. Roy, and A. Bandyopadhyay, "Recent advances in bone tissue engineering scaffolds," *Trends in Biotechnology*, vol. 30, no. 10, pp. 546–554, 2012.

[3] K. J. L. Burg, S. Porter, and J. F. Kellam, "Biomaterial developments for bone tissue engineering," *Biomaterials*, vol. 21, no. 23, pp. 2347–2359, 2000.

[4] C. Chen, E. Kelder, and J. Schoonman, "Electrostatic sol-spray deposition (ESSD) and characterisation of nanostructured $TiO_2$ thin films," *Thin Solid Films*, vol. 342, no. 1-2, pp. 35–41, 1999.

[5] C. J. Damien and J. R. Parsons, "Bone graft and bone graft substitutes: a review of current technology and applications," *Journal of Applied Biomaterials*, vol. 2, no. 3, pp. 187–208, 1991.

[6] P. V. Giannoudis, H. Dinopoulos, and E. Tsiridis, "Bone substitutes: an update," *Injury*, vol. 36, no. 3, pp. S20–S27, 2005.

[7] L. G. Griffith and G. Naughton, "Tissue engineering–current challenges and expanding opportunities," *Science*, vol. 295, no. 5557, pp. 1009–1014, 2002.

[8] L. L. Hench, "Bioceramics: from concept to clinic," *Journal of the American Ceramic Society*, vol. 74, no. 7, pp. 1487–1510, 1991.

[9] J. Henkel, M. A. Woodruff, D. R. Epari et al., "Bone regeneration based on tissue engineering conceptions — a 21st century perspective," *Bone Research*, vol. 1, no. 3, pp. 216–248, 2013.

[10] J. R. Jones and L. L. Hench, "Regeneration of trabecular bone using porous ceramics," *Current Opinion in Solid State and Materials Science*, vol. 7, no. 4-5, pp. 301–307, 2003.

[11] D. C. Lobb, B. R. DeGeorge Jr., and A. B. Chhabra, "Bone Graft Substitutes: current concepts and future expectations," *The Journal of Hand Surgery*, vol. 44, no. 6, pp. 497–505.e2, 2019.

[12] P. X. Ma, "Scaffolds for tissue fabrication," *Materials Today*, vol. 7, no. 5, pp. 30–40, 2004.

[13] A. G. Mikos, S. W. Herring, P. Ochareon et al., "Engineering complex tissues," *Tissue Engineering*, vol. 12, no. 12, pp. 3307–3339, 2006.

[14] R. G. Ribas, V. M. Schatkoski, T. L. d. A. Montanheiro et al., "Current advances in bone tissue engineering concerning ceramic and bioglass scaffolds: A review," *Ceramics International*, vol. 45, no. 17, pp. 21051–21061, 2019.

[15] F. R. A. J. Rose and R. O. C. Oreffo, "Bone tissue engineering: hope vs hype," *Biochemical and Biophysical Research Communications*, vol. 292, no. 1, pp. 1–7, 2002.

[16] A. J. Salinas, P. Esbrit, and M. Vallet-Regí, "A tissue engineering approach based on the use of bioceramics for bone repair," *Biomaterials Science*, vol. 1, no. 1, pp. 40–51, 2013.

[17] B. D. Smith and D. A. Grande, "The current state of scaffolds for musculoskeletal regenerative applications," *Nature Reviews Rheumatology*, vol. 11, no. 4, pp. 213–222, 2015.

[18] M. M. Stevens, "Biomaterials for bone tissue engineering," *Materials Today*, vol. 11, no. 5, pp. 18–25, 2008.

[19] J. Vacanti, "Tissue engineering and regenerative medicine: from first principles to state of the art," *Journal of Pediatric Surgery*, vol. 45, no. 2, pp. 291–294, 2010.

[20] W. Wang and K. W. K. Yeung, "Bone grafts and biomaterials substitutes for bone defect repair: a review," *Bioactive Materials*, vol. 2, no. 4, pp. 224–247, 2017.

[21] S. Yang, K.-F. Leong, Z. Du, and C.-K. Chua, "The design of scaffolds for use in tissue engineering. Part I. Traditional factors," *Tissue Engineering*, vol. 7, no. 6, pp. 679–689, 2001.

[22] X. Yu, X. Tang, S. V. Gohil, and C. T. Laurencin, "Biomaterials for bone regenerative engineering," *Advanced Healthcare Materials*, vol. 4, no. 9, pp. 1268–1285, 2015.

[23] K. Zhang, S. Wang, C. Zhou et al., "Advanced smart biomaterials and constructs for hard tissue engineering and regeneration," *Bone Research*, vol. 6, no. 1, pp. 1–15, 2018.

[24] M. J. Olszta, X. Cheng, S. S. Jee et al., "Bone structure and formation: A new perspective," *Materials Science and Engineering: R: Reports*, vol. 58, no. 3-5, pp. 77–116, 2007.

[25] S. H. Ralston, "Bone structure and metabolism," *Medicine*, vol. 41, no. 10, pp. 581–585, 2013.

[26] J. Buckwalter and R. Cooper, "Bone structure and function," *Instructional Course Lectures*, vol. 36, pp. 27–48, 1987.

[27] J. R. Jones, P. D. Lee, and L. L. Hench, "Hierarchical porous materials for tissue engineering," *Philosophical Transactions of the Royal Society A: Mathematical, Physical and Engineering Sciences*, vol. 364, no. 1838, pp. 263–281, 2006.

[28] J.-Y. Rho, L. Kuhn-Spearing, and P. Zioupos, "Mechanical properties and the hierarchical structure of bone," *Medical Engineering & Physics*, vol. 20, no. 2, pp. 92–102, 1998.

[29] S. Weiner and W. Traub, "Bone structure: from ångstroms to microns," *The FASEB Journal*, vol. 6, no. 3, pp. 879–885, 1992.

[30] J. X. Lu, B. Flautre, K. Anselme et al., "Role of interconnections in porous bioceramics on bone recolonization in vitro and in vivo," *Journal of Materials Science Materials in Medicine*, vol. 10, no. 2, pp. 111–120, 1999.

[31] M. Mastrogiacomo, S. Scaglione, R. Martinetti et al., "Role of scaffold internal structure on in vivo bone formation in macroporous calcium phosphate bioceramics," *Biomaterials*, vol. 27, no. 17, pp. 3230–3237, 2006.

[32] B. Feng, Z. Jinkang, W. Zhen et al., "The effect of pore size on tissue ingrowth and neovascularization in porous bioceramics of controlled architecturein vivo," *Biomedical Materials*, vol. 6, no. 1, article 015007, 2011.

[33] V. Karageorgiou and D. Kaplan, "Porosity of 3D biomaterial scaffolds and osteogenesis," *Biomaterials*, vol. 26, no. 27, pp. 5474–5491, 2005.

[34] C. M. Murphy, M. G. Haugh, and F. J. O'brien, "The effect of mean pore size on cell attachment, proliferation and migration in collagen–glycosaminoglycan scaffolds for bone tissue engineering," *Biomaterials*, vol. 31, no. 3, pp. 461–466, 2010.

[35] J. Zeltinger, J. K. Sherwood, D. A. Graham, R. Müeller, and L. G. Griffith, "Effect of pore size and void fraction on cellular adhesion, proliferation, and matrix deposition," *Tissue Engineering*, vol. 7, no. 5, pp. 557–572, 2001.

[36] W. Zhen, C. Jiang, B. Feng, S. Xiaojiang, L. Jianxi, and L. Li, "Role of the porous structure of the bioceramic scaffolds in bone tissue engineering," *Nature Precedings*, 2010.

[37] D. Lozano, M. Manzano, J. C. Doadrio et al., "Osteostatin-loaded bioceramics stimulate osteoblastic growth and differentiation," *Acta Biomaterialia*, vol. 6, no. 3, pp. 797–803, 2010.

[38] J. Rouwkema and A. Khademhosseini, "Vascularization and angiogenesis in tissue engineering: beyond creating static networks," *Trends in Biotechnology*, vol. 34, no. 9, pp. 733–745, 2016.

[39] J. Rouwkema, N. Rivron, and C. A. van Blitterswijk, "Vascularization in tissue engineering," *Trends in Biotechnology*, vol. 26, no. 8, pp. 434–441, 2008.

[40] W. Tang, D. Lin, Y. Yu et al., "Bioinspired trimodal macro/micro/nano-porous scaffolds loading rhBMP-2 for complete regeneration of critical size bone defect," *Acta Biomaterialia*, vol. 32, pp. 309–323, 2016.

[41] C. Wu and J. Chang, "Mesoporous bioactive glasses: structure characteristics, drug/growth factor delivery and bone regeneration application," *Review Interface Focus*, vol. 2, no. 3, pp. 292–306, 2012.

[42] S. Yang, K. Leong, Z. du, and C. K. Chua, "The design of scaffolds for use in tissue engineering. Part II. Rapid prototyping techniques," *Tissue Engineering*, vol. 8, no. 1, pp. 1–11, 2002.

[43] O. Sel, D. Kuang, M. Thommes, and B. Smarsly, "Principles of hierarchical meso- and macropore architectures by liquid crystalline and polymer colloid templating," *Langmuir*, vol. 22, no. 5, pp. 2311–2322, 2006.

[44] B. Smarsly and M. Antonietti, "Block copolymer assemblies as templates for the generation of mesoporous inorganic materials and crystalline films," *European Journal of Inorganic Chemistry*, vol. 2006, no. 6, pp. 1111–1119, 2006.

[45] S. Deville, "Freeze-casting of porous ceramics: a review of current achievements and issues," *Advanced Engineering Materials*, vol. 10, no. 3, pp. 155–169, 2008.

[46] M. C. Gutiérrez, M. L. Ferrer, and F. del Monte, "Ice-templated materials: sophisticated structures exhibiting enhanced functionalities obtained after unidirectional freezing and ice-segregation-induced self-assembly†," *Chemistry of Materials*, vol. 20, no. 3, pp. 634–648, 2008.

[47] L. Qian and H. Zhang, "Controlled freezing and freeze drying: a versatile route for porous and micro-/nano-structured materials," *Journal of Chemical Technology and Biotechnology*, vol. 86, no. 2, pp. 172–184, 2011.

[48] A. Feinle, M. S. Elsaesser, and N. Hüsing, "Sol–gel synthesis of monolithic materials with hierarchical porosity," *Chemical Society Reviews*, vol. 45, no. 12, pp. 3377–3399, 2016.

[49] A. Monnier, F. Schüth, Q. Huo et al., "Cooperative formation of inorganic-organic interfaces in the synthesis of silicate mesostructures," *Science*, vol. 261, no. 5126, pp. 1299–1303, 1993.

[50] L. W. Hench and J. K. West, "The sol-gel process," *Chemical Reviews*, vol. 90, no. 1, pp. 33–72, 1990.

[51] Y. Lu, H. Fan, A. Stump, T. L. Ward, T. Rieker, and C. J. Brinker, "Aerosol-assisted self-assembly of mesostructured spherical nanoparticles," *Nature*, vol. 398, no. 6724, pp. 223–226, 1999.

[52] H. Yang, N. Coombs, I. Sokolov, and G. A. Ozin, "Free-standing and oriented mesoporous silica films grown at the air–water interface," *Nature*, vol. 381, no. 6583, pp. 589–592, 1996.

[53] C. J. Brinker, "Evaporation-induced self-assembly: functional nanostructures made easy," *MRS Bulletin*, vol. 29, no. 9, pp. 631–640, 2004.

[54] G. J. Soler-Illia, P. C. Angelomé, M. C. Fuertes, D. Grosso, and C. Boissiere, "Critical aspects in the production of periodically ordered mesoporous titania thin films," *Nanoscale*, vol. 4, no. 8, pp. 2549–2566, 2012.

[55] G. Soler-Illia, C. Sanchez, B. Lebeau, and J. Patarin, "Chemical strategies to design textured materials: from microporous and mesoporous oxides to nanonetworks and hierarchical structures," *Chemical Reviews*, vol. 102, no. 11, pp. 4093–4138, 2002.

[56] P. Yang, D. Zhao, D. I. Margolese, B. F. Chmelka, and G. D. Stucky, "Generalized syntheses of large-pore mesoporous metal oxides with semicrystalline frameworks," *Nature*, vol. 396, no. 6707, pp. 152–155, 1998.

[57] H. Luo, C. Wang, and Y. Yan, "Synthesis of mesostructured titania with controlled crystalline framework," *Chemistry of Materials*, vol. 15, no. 20, pp. 3841–3846, 2003.

[58] X. Fu, L. A. Clark, Q. Yang, and M. A. Anderson, "Enhanced photocatalytic performance of titania-based binary metal oxides: TiO2/SiO2and TiO2/ZrO2," *Science and Technology*, vol. 30, no. 2, pp. 647–653, 1996.

[59] J. C. Yu, J. Lin, and R. W. M. Kwok, "Ti1-xZrxO2solid solutions for the photocatalytic degradation of acetone in air," *The Journal of Physical Chemistry. B*, vol. 102, no. 26, pp. 5094–5098, 1998.

[60] J. Marchi, E. M. Amorim, D. R. R. Lazar, V. Ussui, A. H. A. Bressiani, and P. F. Cesar, "Physico-chemical characterization of zirconia–titania composites coated with an apatite layer for dental implants," *Dental Materials*, vol. 29, no. 9, pp. 954–962, 2013.

[61] H. Tiainen, G. Eder, O. Nilsen, and H. J. Haugen, "Effect of $ZrO_2$ addition on the mechanical properties of porous $TiO_2$ bone scaffolds," *Materials Science and Engineering: C*, vol. 32, no. 6, pp. 1386–1393, 2012.

[62] V. Damodaran, D. Bhatnagar, V. Leszczak, and K. C. Popat, "Titania nanostructures: a biomedical perspective," *RSC Advances*, vol. 5, no. 47, pp. 37149–37171, 2015.

[63] M. Hamzeh and G. I. Sunahara, "*In vitro* cytotoxicity and genotoxicity studies of titanium dioxide ($TiO_2$) nanoparticles in Chinese hamster lung fibroblast cells," *Toxicology in Vitro*, vol. 27, no. 2, pp. 864–873, 2013.

[64] T. Kokubo, T. Matsushita, and H. Takadama, "Titania-based bioactive materials," *Journal of the European Ceramic Society*, vol. 27, no. 2-3, pp. 1553–1558, 2007.

[65] R. L. Hentrich, G. A. Graves, H. G. Stein, and P. K. Bajpai, "An evaluation of inert and resorbale ceramics for future clinical orthopedic applications," *Journal of Biomedical Materials Research*, vol. 5, no. 1, pp. 25–51, 1971.

[66] P. F. Manicone, P. Rossi Iommetti, and L. Raffaelli, "An overview of zirconia ceramics: basic properties and clinical applications," *Journal of Dentistry*, vol. 35, no. 11, pp. 819–826, 2007.

[67] C. Piconi and G. Maccauro, "Zirconia as a ceramic biomaterial," *Biomaterials*, vol. 20, no. 1, pp. 1–25, 1999.

[68] T. Thamaraiselvi and S. Rajeswari, "Trends Biomater," *Artificial Organs*, vol. 18, 2003.

[69] K. Houjou, K. Ando, and K. Takahashi, "Crack -Healing Behaviour of Zirconia/SiC Composite Ceramics," *Journal of the Society of Materials Science, Japan*, vol. 58, no. 6, pp. 510–515, 2009.

[70] K. Houjou, S. Sudo, and K. Takahashi, "Crack-Healing Behaviour of Zirconia /SiC Composite Ceramics and Strength Properties of Crack-Healing Specimens," *Journal of the Society of Materials Science, Japan*, vol. 60, no. 8, pp. 742–747, 2011.

[71] F. Samanipour, M. R. Bayati, F. Golestani-Fard, H. R. Zargar, T. Troczynski, and A. R. Mirhabibi, "An innovative technique to simply fabricate $ZrO_2$–HA–$TiO_2$ nanostructured layers," *Colloids and Surfaces B: Biointerfaces*, vol. 86, no. 1, pp. 14–20, 2011.

[72] S. M. Mirhadi, N. Hassanzadeh Nemati, F. Tavangarian, and M. Daliri Joupari, "Fabrication of hierarchical meso/macroporous TiO2 scaffolds by evaporation-induced self-assembly technique for bone tissue engineering applications," *Materials Characterization*, vol. 144, pp. 35–41, 2018.

[73] S. K. Das, M. K. Bhunia, A. K. Sinha, and A. Bhaumik, "Self-assembled mesoporous zirconia and sulfated zirconia nanoparticles synthesized by triblock copolymer as template," *Journal of Physical Chemistry C*, vol. 113, no. 20, pp. 8918–8923, 2009.

[74] J. Chambers and C. B. Reese, "The thermal decomposition of some polyurethane foams," *British Polymer Journal*, vol. 8, no. 2, pp. 48–53, 1976.

[75] J. Li, A. Kazakov, and F. L. Dryer, "Experimental and numerical studies of ethanol decomposition reactions," *The Journal of Physical Chemistry A*, vol. 108, no. 38, pp. 7671–7680, 2004.

[76] P. Moravec, J. Smolík, H. Keskinen, J. Mäkelä, and V. Levdansky, "Vapor Phase Synthesis of Zirconia Fine Particles from Zirconium Tetra-Tert-Butoxide," *Aerosol and Air Quality Research*, vol. 7, pp. 563–577, 2007.

[77] A. Radtke, P. Piszczek, T. Muziol, A. Wojtczak, and A. Grodzicki, "Synthesis, structural characterization, and thermal properties of zirconium(IV) $\beta$-ketodiester complexes," *Structural Chemistry*, vol. 21, pp. 367–375, 2009.

[78] L. Weng, X. Bao, and K. Sagoe-Crentsil, "Effect of acetylacetone on the preparation of PZT materials in sol–gel processing," *Materials Science and Engineering: B*, vol. 96, no. 3, pp. 307–312, 2002.

[79] D. Wyrzykowski, E. Hebanowska, G. Nowak-Wiczk, M. Makowski, and L. Chmurzyński, "Thermal behaviour of citric acid and isomeric aconitic acids," *Journal of Thermal Analysis and Calorimetry*, vol. 104, no. 2, pp. 731–735, 2011.

[80] H. Zhang, C. Tang, Y. Lv et al., "Synthesis, characterization, and catalytic performance of copper-containing SBA-15 in the phenol hydroxylation," *Journal of Colloid and Interface Science*, vol. 380, no. 1, pp. 16–24, 2012.

[81] J. A. Cecilia, R. Moreno Tost, and M. Retuerto Millán, "Mesoporous materials: from synthesis to applications," *International Journal of Molecular Sciences*, vol. 20, no. 13, p. 3213, 2019.

[82] D. Hanaor and C. Sorrell, "Review of the anatase to rutile phase transformation," *Journal of Materials Science*, vol. 46, no. 4, pp. 855–874, 2011.

[83] O. Kurapova and V. G. Konakov, "A Corriger Dans le Texte Aussi Oy Kurapova, and VG Konakov," *Reviews on Advanced Materials Science*, vol. 36, pp. 177–190, 2014.

[84] F. H. Brown Jr. and P. Duwez, "The zirconia-titania system," *Journal of the American Ceramic Society*, vol. 37, no. 3, pp. 129–132, 1954.

[85] J. Yang and J. M. F. Ferreira, "Inhibitory effect of the Al2O3–SiO2 mixed additives on the anatase–rutile phase transformation," *Materials Letters*, vol. 36, no. 5-6, pp. 320–324, 1998.

[86] A. Kubiak, K. Siwińska-Ciesielczyk, and T. Jesionowski, "Titania-based hybrid materials with ZnO, ZrO2 and MoS2: a review," *Materials*, vol. 11, no. 11, p. 2295, 2018.

[87] S. Mascotto, D. Wallacher, A. Brandt et al., "Analysis of microporosity in ordered mesoporous hierarchically structured silica by combining physisorption with in situ small-angle scattering (SAXS and SANS)," *Langmuir*, vol. 25, no. 21, pp. 12670–12681, 2009.

[88] M. Impéror-Clerc, P. Davidson, and A. Davidson, "Existence of a Microporous Corona around the Mesopores of Silica-Based SBA-15 Materials Templated by Triblock Copolymers," *Journal of the American Chemical Society*, vol. 122, pp. 11925–11933, 2000.

[89] S. Fessi, A.-S. Mamede, A. Ghorbel, and A. Rives, "Sol–gel synthesis combined with solid–solid exchange method, a new alternative process to prepare improved Pd/SiO2–Al2O3 catalysts for methane combustion," *Catalysis Communications*, vol. 27, pp. 109–113, 2012.

[90] T. Hirai, H. Sato, and I. Komasawa, "Mechanism of formation of titanium dioxide ultrafine particles in reverse micelles by hydrolysis of titanium tetrabutoxide," *Industrial and Engineering Chemistry Research*, vol. 32, no. 12, pp. 3014–3019, 1993.

[91] H. Kumazawa, Y. Hori, and E. Sada, "Synthesis of spherical zirconia fine particles by controlled hydrolysis of zirconium tetrabutoxide in 1-propanol," *The Chemical Engineering Journal*, vol. 51, no. 3, pp. 129–133, 1993.

[92] S. G. Kumar and K. S. R. K. Rao, "Polymorphic phase transition among the titania crystal structures using a solution-based approach: from precursor chemistry to nucleation process," *Nanoscale*, vol. 6, no. 20, pp. 11574–11632, 2014.

[93] D. R. Dunphy, P. H. Sheth, F. L. Garcia, and C. J. Brinker, "Enlarged Pore Size in Mesoporous Silica Films Templated by Pluronic F127: Use of Poloxamer Mixtures and Increased Template/$SiO_2$ Ratios in Materials Synthesized by Evaporation-Induced Self-Assembly," *Chemistry of Materials*, vol. 27, pp. 75–84, 2014.

Hindawi
Journal of Nanomaterials
Volume 2020, Article ID 2187169, 14 pages
https://doi.org/10.1155/2020/2187169

*Review Article*

# Exosome: A Novel Nanocarrier Delivering Noncoding RNA for Bone Tissue Engineering

**Keda Liu**,[1] **Nanjue Cao**,[2] **Yuhe Zhu**,[1] **and Wei Wang**[1]

[1]*School and Hospital of Stomatology, China Medical University, Liaoning Provincial Key Laboratory of Oral Diseases, Shenyang 110001, China*
[2]*The Fourth Affiliated Hospital, Zhejiang University School of Medicine, Yiwu 322000, China*

Correspondence should be addressed to Wei Wang; wwang75@cmu.edu.cn

Received 9 July 2020; Accepted 31 July 2020; Published 14 August 2020

Academic Editor: Hui-Qi Xie



Bone growth and metabolism are mainly regulated by a series of intracellular molecules and extracellular stimuli. Exosome, as a nanoscale substance secreted to the outside of the cells, plays an extensive role in intercellular communication. This review provides theoretical references and evidences for further exploration of exosomes as noncoding RNA carriers to regulate bone tissue recovery through the following aspects: (1) basic characteristics of exosomes, (2) research progress of exosomal noncoding RNA in bone tissue engineering, (3) current status and advantages of engineering exosomes as nanocarriers for noncoding RNA delivery, and (4) problems and application prospects of exosome therapy in the field of orthopedics.

## 1. Introduction

Destructive osteopathy is mainly due to the failure of the bone remodeling process, including enhanced osteoclast activity or reduced osteoblast generation [1, 2]. Osteoarthritis, osteoporosis, etc. will lead to a continuous decline in the quality of patients' life [3, 4], deemed to be an important global health problem [5, 6]. The process of bone remodeling is to repair bone damage and restore aging bone tissue [7]. This is the prerequisite for maintaining mass and mechanical strength of bone [8]. Mutual regulation of osteoblasts and osteoclasts is essential for bone remodeling [9], dominated by molecular signals [10, 11].

Extracellular vesicles are natural nanoscale particles secreted by cells. They are spherical bilayer membrane vesicles with diameters ranging from 30 nm to 1000 nm, including exosomes of uniform size (30-150 nm), microvesicles of varying sizes (50-1000 nm), and apoptotic bodies [12]. Recent studies reported that the key factor for bone reconstruction was exosome [13]. These organelles play a crucial role in intercellular messengers, transferring bioactive molecules to nearby or distant cells under physiological and pathological conditions [14, 15]. Noncoding RNAs in exosomes supply a method that cells can straightly regulate the expression of protein in target cells. As a kind of nanomaterial, exosome has been explored in the field of diagnostic [16], therapeutics [17], and drug delivery [18] (Figure 1).

Existing drug carriers, such as artificially manufactured liposomes, can cause accumulated toxicity and immunogenicity in the body, thus limiting the wide application of such drug carriers [20, 21]. As a natural drug delivery carrier, exosomes have significant advantages of biocompatibility, high stability, and targeting. In order to better understand the mechanism of exosomes as noncoding RNA vectors regulating bone remodeling, we reviewed the newest findings on the feature and role of exosomes in bone formation. In addition, we focused on elaborating the feasible clinical application of bone exosomes and the characteristics of exosomal noncoding RNAs in the regulation of bone reconstruction.

## 2. Biological Characteristics of Exosomes

Exosome was first discovered in 1981, considered cellular trash initially [22]. Subsequently, exosomes caught the interest of immunologists in the 1990s. Raposo et al. in 1996 reported that exosomes have the ability of antigen presentation, activating T cell immune response [23]. In addition,

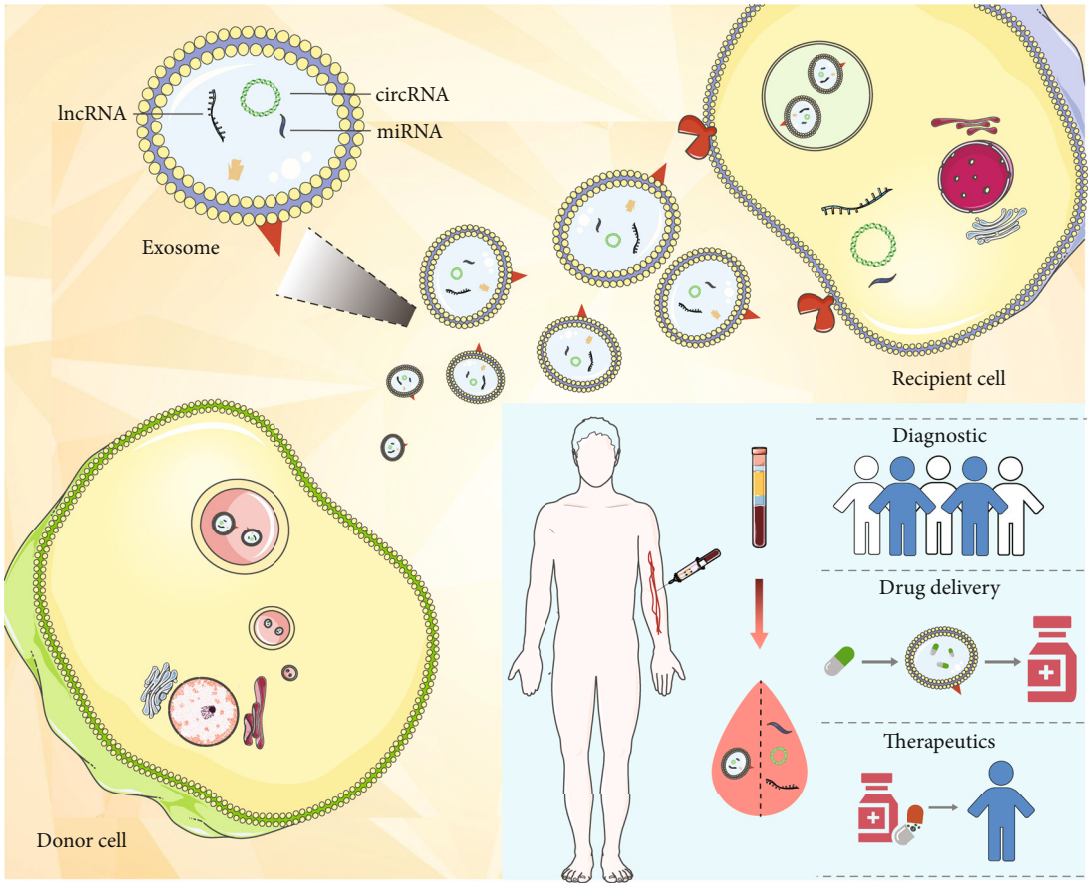


Figure 1: Exosome production, secretion, and cargo transfer from donor cells to recipient cells. The inset shows the clinical application of noncoding RNA exosomes [19].

exosomes were found to carry miRNAs and mRNAs for intercellular communication in 2007. Most importantly, the mechanism of exosomal transport was cracked by three independent groups [24–26]. The history, biomarkers, and functions of exosomes are shown in Figure 2.

Exosomes are membrane vesicles with diameters between 30 and 150 nm [27, 28] (Figure 3). They are derived from body cells including tumor cells [29, 30]. Studies revealed that exosomes are also secreted from bone-related cells (osteoclasts, osteoclast precursors, osteoblasts, and MSCs) [31–33]. Exosomes reflect the complex molecular processing that occurs inside the parent cells and are more appropriate as a potential replacement for parent cell in body fluids. Multiple studies have confirmed the loyalty of exosomal cargo to parental cells [34, 35]. Exosomes can encapsulate fragments of genomic and different kinds of RNA, such as miRNA, lncRNA, circRNA, and ribosomal RNA [36–39].

## 3. Exosomes from Osteoclasts and Osteoblasts

*3.1. Osteoclast Exosomes.* Exosomes secreted by osteoclasts may provide clues on how to coordinate bone absorption and construction. In calcitriol-stimulated mouse bone marrow (C-SMM), osteoclasts and osteoblasts differentiated synergistically within six days. Osteoclast precursor-derived exosomes stimulated the proliferation of osteoclasts in C-SMM, while exosomes of mature osteoclasts inhibited osteoclast formation [13, 40]. Osteoclast exosomes stimulate the osteoblasts and other nonosteoclasts in a paracrine manner and produce factors that regulate osteoclast differentiation.

miRNA-214, involved in bone remodeling, adjusts Osterix and activates transcription factor (ATF) 4, which is an essential transcription factor in osteogenesis process [41, 42]. Higher levels of miRNA-214 were noted in the plasma of fractured elderly women and ovariectomized mouse. In vitro, by using transwell membranes (that only permitted exosomes through), exosomal miRNA-214 was transmitted from osteoclasts to osteoblasts, inhibiting proliferation and mineralizing activity of osteoblast in vitro and vivo [43, 44].

*3.2. Osteoblast Exosomes.* Osteoblasts release exosomes containing receptor activator RANKL. These exosomes induce osteoclast precursors to differentiate to osteoclasts [31]. Osteoblasts release RANKL exosomes and osteoclasts release RANK exosomes. Studies have shown that the RANKL-RANK-osteoprotectin signal network is the essence of bone biology. RANKL exosome from osteoblasts may be capable of promoting osteoclast formation and activity without direct intercellular contact. RANK exosome may inhibit RANKL in a method the same as osteoprotectin. Both RANKL and

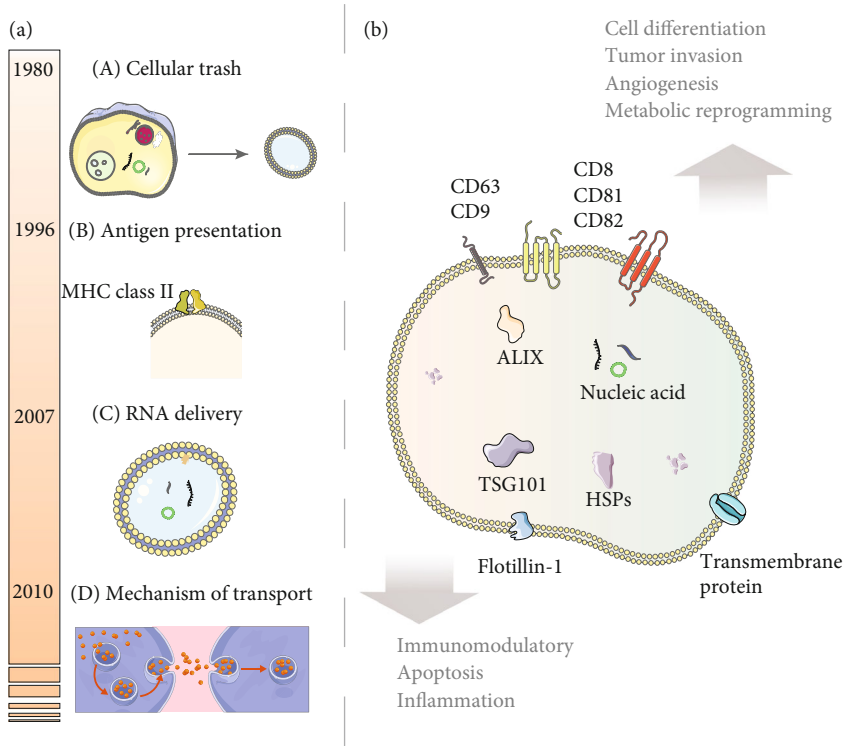


Figure 2: (a) Historical key developments in exosome research. (b) Biomarkers and functions of exosome.

RANK-containing exosome may be able to fuse in their target cells to release regulatory molecules, which could assist to reprogram target cells [45].

## 4. The Roles of Exosomal Noncoding RNAs in Bone Growth

Noncoding RNA refers to RNA that does not encode protein. They have biological functions at the RNA level. Noncoding RNAs are generally divided into 3 categories according to their size: less than 50 nt, including microRNA (miRNA), small interfering RNA (siRNA), and piwi-interacting RNA (piRNA); 50 nt to 500 nt, including nuclear small RNA (snRNA) and small nucleolar RNA (snoRNA); and greater than 500 nt, long noncoding RNA (lncRNA) and circular RNA (circRNA) [46, 47]. This article reviews current research hotspots of osteoarthritis: miRNA, lncRNA, and circRNA.

*4.1. miRNA.* The latest two years of exosome miRNA in the regulation of bone growth and development is listed in Table 1. Exosome miR-128-3p regulates osteogenesis and fracture healing by targeting Smad5 [48]. Decreasing miR-221-3p in exosomes can significantly reduce chondrocyte proliferation and migration in vitro [49]. Exosome miR-17 secreted by keratinocytes can induce osteoclast differentiation [30]. By freeze and thaw method, researchers combined exosomes and miR-140 to promote cartilage differentiation of bone marrow stem cells, thereby enhancing cartilage repair and regeneration [50]. Human umbilical cord mesenchymal stem cell exosomes can effectively inhibit bone marrow mesenchymal stem cell apoptosis and prevent osteoporosis in rats. The mechanism is mediated by the miR-1263/Mob1/Hippo signaling pathway [51]. Exosome miR-8485 promotes cartilage differentiation of bone marrow mesenchymal stem cells by regulating the Wnt/$\beta$-catenin pathway [52].

Studies on miRNAs have demonstrated that the regulation of the target genes affects the expression of regulators upstream and downstream of each signaling pathway, to regulate the osteogenic differentiation process [54]. Runx2 is a transcription factor that plays an important role in osteoblast differentiation [55], which is precisely or indirectly regulated by many miRNAs, including miR-221 [56, 57], miR-133a-5p [58], miR-467g [59], miR-218 [60, 61], and miR-210 [62]. The expression of Osx can be downregulated by some miRNAs, inhibiting osteogenic differentiation, such as miR-145 [63] and miR-143 [64, 65]. Some miRNAs that regulate the expression of bone-related gene have not been studied in exosomes, providing clues to the research of exosomes in the field of orthopedics (Table 2).

*4.2. lncRNA.* The lncRNA-miRNA-mRNA regulation model plays a critical role in osteogenic differentiation [66]. lncRNA can serve as a competitive endogenous RNA, competing for miRNA binding sites to reduce its direct impact on mRNA. lncRNA MALAT1 can competitively bind to miR-30, inhibiting the interaction between miR-30 and Runx2 to upregulate the transcription level of Runx2 and strengthen osteogenic differentiation of adipose mesenchymal stem cells [67]. Study revealed that lncRNA TUG1 [68], lncRNA PCAT1 [69], and lncRNA HIF1A-AS2 also indirectly regulate the activity of osteogenesis-related signaling molecules by adsorbing miRNA [70]. Downregulated lncRNA MEG3

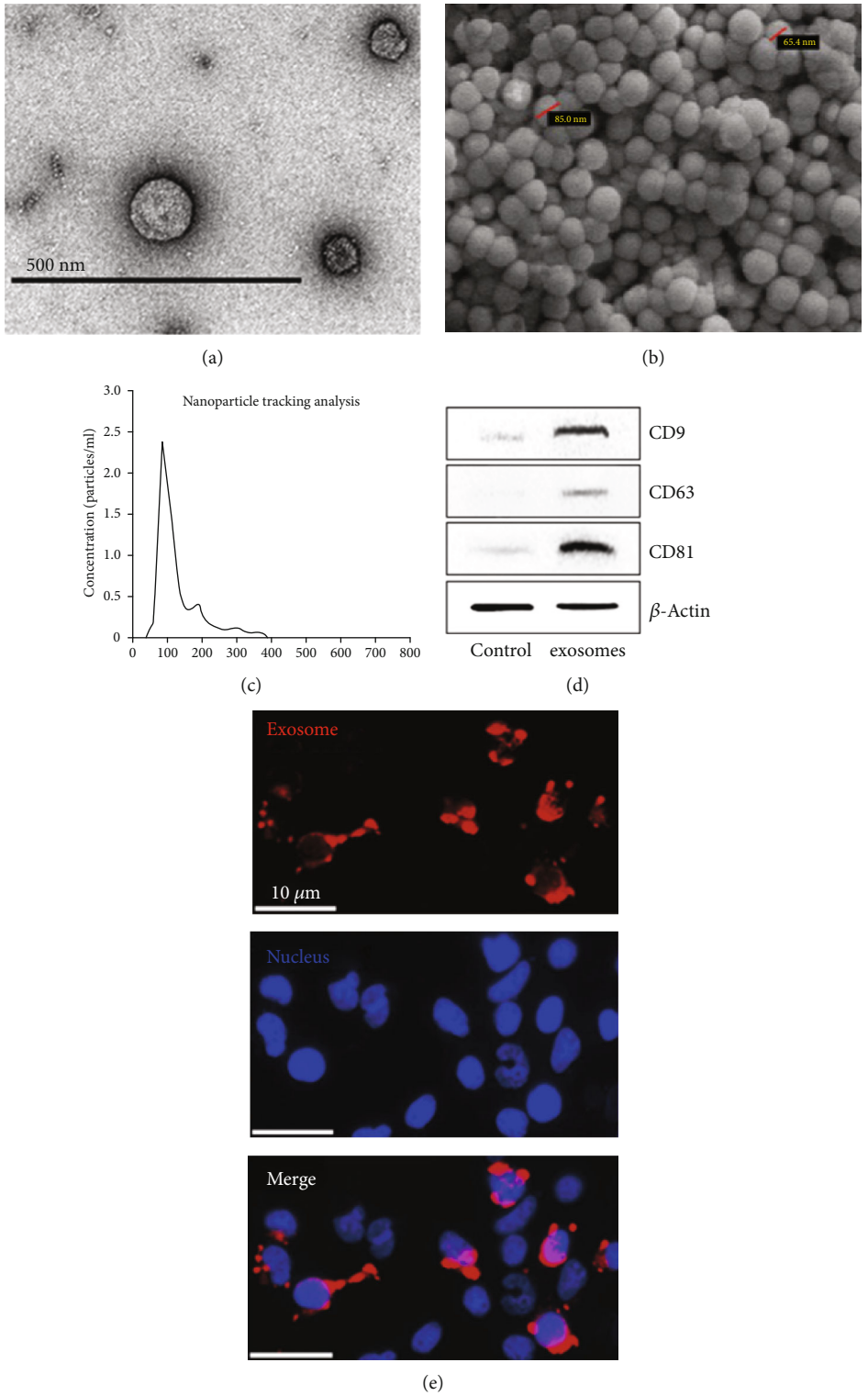


Figure 3: Characterization and cellular uptake of exosomes. As shown in (a) and (b), the morphology of exosomes was observed under TEM and SEM. In (c) and (d), exosome is a round membranous vesicle with a diameter of about 30-150 nm and the results of western blot showed that exosome was able to express marker proteins CD9, CD81, and CD63. In (e), to verify whether exosome interacts with cell, exosome labeled by Dil and receptor cell were cocultured in vitro for 6 h. Under a fluorescence microscope, over 85% of cell showed positive result of Dil, indicating that the Dil-labeled exosome has been efficiently transferred to receptor cells [30, 35, 53]. (a–d) Copyright 2020 BBRC published by Elsevier Ltd. (b) Copyright 2019 EXCLI J published by University of Mainz. (c) Copyright 2020 Int Immunopharmacology published by Elsevier Ltd.

Table 1: List of miRNA deliveries by exosome in both basic and clinical research of bone formation.

| miRNA | Target gene | Resource | Recipient cells | Mechanism and result | Ref. |
|---|---|---|---|---|---|
| miR-128-3P | Smad5 | MSCs | MSCs | miR-128-3p was highly expressed in aged exosome, inhibiting fracture healing by targeting Smad5. | [48] |
| miR-221-3p | | CPCs | Murine chondrocytes | In vivo experiments confirmed that miR-221-3p was highly enriched in CPCs-Exos, which can stimulate chondrocyte proliferation and migration. | [49] |
| miR-140 | | Freeze and thaw method | BMSCs | miR-140 was fused into exosomes by freezing and thawing, promoting the differentiation of BMSCs into chondrocytes.[ | [50] |
| miR-1263 | Mob1 | HUC-MSCs | BMSCs | Exosomes inhibit BMSC apoptosis through miR-1263/Mob1/Hippo signaling pathway. | [51] |
| miR-8485 | DACT1, GSK3B | Chondrocytes | BMSCs | Exosomal miR-8485 regulated the Wnt/$\beta$-catenin pathways to promote chondrogenic differentiation of BMSCs. | [52] |
| miR-192-5p | RAC2 | BMSCs | | The exosomal miR-192-5p of BMSCs can delay the inflammatory response of rheumatoid arthritis by regulating the expression of proinflammatory factors. | [53] |
| miR-375 | IGFBP3 | hASCs | BMSCs | Exosomes derived from hASCs overexpressing miR-375 promoted bone regeneration by binding to IGFBP3. | [84] |
| miR-26a-5p | PTGS2 | BMSC | Synovial fibroblasts | The hBMSC-derived exosome- miR-26a-5p inhibited the damage of synovial fibroblasts by targeting PTGS2. | [85] |
| miR-155 | | VECs | Macrophages | VEC-Exos was rich in miR-155, which indirectly inhibited osteoclast activity by interacting with macrophages to improve the symptoms of osteoporosis. | [86] |
| miR-129-5p | Sp1 | MMs | hMSCs | Multiple myeloma (MM) exosome miR-129-5p reduced alkaline phosphatase (ALPL) activity by inhibiting the expression of transcription factor Sp1 in hMSCs. | [87] |
| miR-17 | RANKL | Keratinocytes | Osteoclasts | The exosomal miR-17 secreted by keratinocytes with middle ear cholesteatoma can upregulate RANKL in fibroblasts and induce osteoclast differentiation. | [30] |

MSCs: mesenchymal stem cells; BMSCs: bone marrow mesenchymal stem cells; HUC-MSCs: human umbilical cord mesenchymal stem cells; hASCs: human adipose mesenchymal stem cells; VECs: vascular endothelial cells; CPCs: chondrogenic progenitor cells; MMs: multiple myelomas.

promotes osteogenic differentiation of human dental follicle stem cells by epigenetically regulating the Wnt pathway [71]. Researchers have indicated that exosome lncRNA-MALAT secreted by bone marrow mesenchymal stem cells enhanced osteoblast activity in osteoporotic mice [72]. Exosomal lncRNA-RUNX2-AS1 secreted by multiple myeloma cells can reduce osteogenic differentiation of MSC [73].

*4.3. circRNA.* Increasing evidence indicates the various functions of circRNA in bone marrow mesenchymal stem cell osteogenesis, which proves to be a valuable checkpoint for the treatment of bone diseases [74]. CircRNA_436 might be a part of the critical regulators of periodontal ligament stem cell differentiation by coordinating with miR-107 and miR-335 to affect the Wnt/$\beta$-catenin pathway [75]. CircRNA_0127781 may serve as one of the essential regulators in the inhibition of osteoblast differentiation by interacting with miR-210 and miR-335 [76–78]. CircRNA_33287 would block miR-214-3p to intensify the osteogenesis process and active the construction of ectopic bone [79]. Both circRNA_19142 and circRNA_5846 target miR-7067-5p to regulate osteoblast differentiation [80]. Lipopolysaccharide (LPS) is indicated to promote bone resorption by activating TLRs [81]. GO analysis showed that circRNA_3140 is related to the TLR signaling pathway [75]. The mechanism of exosomal circRNA in the regulation of osteogenic differentiation is seldom studied. However, the circular structure of circRNA makes it more stable than linear RNA and difficult to be degraded [82]. It has great research potential in exosome engineering. Studies have shown that during the osteogenic differentiation of periodontal ligament stem cells, differentially expressed circRNAs are rich in membrane-bound vesicles [83].

## 5. Engineering Exosomes as Nanocarrier for Noncoding RNA Delivery

*5.1. Methods of Exosome Extraction.* The separation and purification of exosomes have always been a concern of researchers. It is crucial to obtain high-purity exosomes for subsequent research. Researchers currently use ultracentrifugation [91], immunomagnetic beads [92], ultrafiltration [93], size-exclusion chromatography [94], or kits to achieve exosomes (Figure 4). In Table 3, we summarize several methods for extracting exosomes and list their characteristics.

*5.2. Merging Therapeutic RNA into Exosomes.* Exosome cargo with therapeutic activity is not restricted to naturally occurring cell-derived biomolecules. Instead, exosomes can also carry exogenous therapeutic molecules. Exosomes have been engineered to bind therapeutic molecules, including protein [95], small molecule drugs [96], peptide ligands [97], and therapeutic RNA [98, 99]. Researchers have used multiple methods to engineer exosomes for cargo delivery, including incubation with saponin, electrical stimulation, sonication

Table 2: List of miRNAs in bone formation.

| miRNA | Target genes | Cell type | Mechanism and result | Ref. |
|---|---|---|---|---|
| miR-221 | ZFPM2, Runx2 | Osteoblasts | miR-221 inhibited osteoblast differentiation by targeting ZFPM2 and Runx2 to reduce the expression levels of osteocalcin (OC), alkaline phosphatase (ALP), and collagen, type I, $\alpha$1 (COL1A1). | [56, 57] |
| miR-218 | Runx2 | Osteoclasts | miR-218 participated in the negative regulation of osteoclastogenesis and bone resorption by inhibiting the p38MAPK-c-Fos-NFATc1 signaling pathway. | [60, 61] |
| miR-210 | Runx2 | MSCs | Overexpression of miR-210 in MSC led to the differentiation of MSC into osteoblasts by upregulating Runx2, ALP, and osteocalcin. | [62] |
| miR-145 | Smad3, SEMA3A | BMSCs | MicroRNA-145 suppressed osteogenic differentiation of hBMSCs partially via targeting Smad3 and SEMA3A. | [63] |
| miR-143-3p | BMPR2 | BMSCs | miR-143-3p regulated the early chondrogenic differentiation of BMSCs and promoted cartilage damage repair by targeting BMPR2. | [64, 65] |
| miR-542-3p | SFRP1 | Osteoblasts | miR-542-3p prevented ovariectomy-induced osteoporosis in rats by targeting SFRP1. | [88] |
| miR-433-3p | DDK1 | Osteoblasts | MicroRNA-433-3p promoted osteoblast differentiation through targeting DKK1. | [89] |
| miR-133a-5p | Runx2 | Osteoblasts | miR-133a-5p inhibited the expression of osteoblast differentiation-associated markers by targeting the 3' UTR of RUNX2. | [58] |
| miR-467g | Ihh/Runx-2 | Osteoblasts | miR-467g inhibited new bone regeneration by targeting Ihh/Runx-2 signaling. | [59] |
| miR-208a-3p | ACVR1 | Osteoblasts | miR-208a-3p suppresses osteoblast differentiation and inhibits bone formation by targeting ACVR1. | [90] |

MSCs: mesenchymal stem cells; BMSCs: bone marrow mesenchymal stem cells.

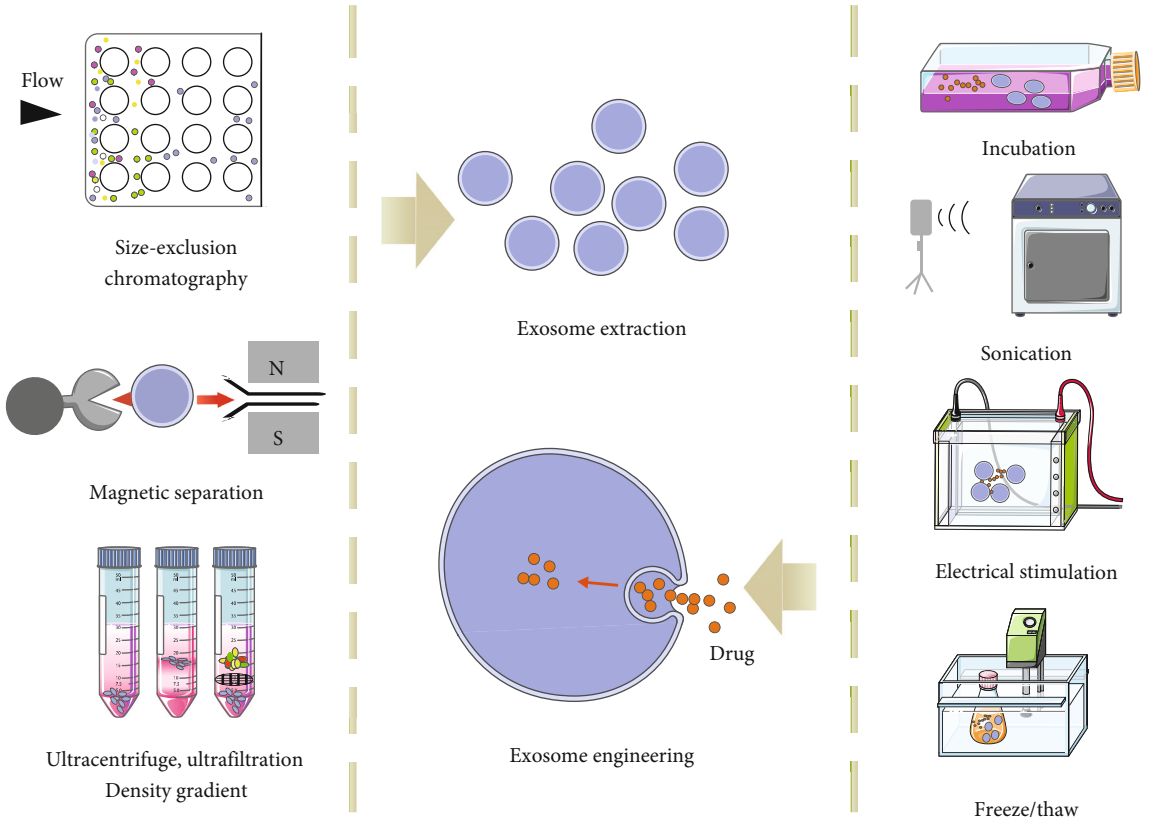


Figure 4: Methods of exosome extraction and engineering.

Table 3: Comparison of methods about exosome extraction.

| Name | Method | Advantage | Disadvantage | Ref. |
|---|---|---|---|---|
| Ultracentrifuge | (1) Low speed to remove cells and apoptotic debris<br>(2) High speed to eliminate larger vesicles<br>(3) Higher speed to precipitate exosomes | (1) The gold standard for exosome extraction<br>(2) Simple operation | (1) A lot of materials need to be prepared in the early stage<br>(2) The exosome yield is low<br>(3) Repeated centrifugation causes damage to exosome vesicles and reduces its quality<br>(4) Soluble proteins can form clumps with exosomes and cause pollution | [78] |
| Concentration gradient centrifugation | In different liquid density intervals, each particle will eventually stay at the same position as its own density | Compared with ultracentrifugation, the recovery rate and purity are higher | Same as above | [78, 82] |
| Ultrafiltration | Using ultrafiltration membranes with different molecular weight (MWCO) for separation, small molecular substances will be filtered to the other side of the membrane | Simple and efficient without affecting the biological activity of exosomes | (1) The adhesion of the filter membrane may lose exosomes<br>(2) The pressure and shearing force during filtration may cause of the damage of exosomes | [80] |
| Immunomagnetic bead | By incubating with magnetic beads coated with antimarker antibodies, exosomes can be adsorbed and separated | (1) High specificity<br>(2) Easy to operate<br>(3) Not affecting the exosomal morphological integrity | (1) Low efficiency<br>(2) Biological activity is easily affected by pH and salt concentration<br>(3) Not conducive to downstream experiments | [79] |
| Size-exclusion chromatography | With columns filled with porous polymer microspheres, molecules pass through the microspheres according to their diameter. Molecules with a small radius take longer to migrate through the pores of the column | Exosomes are not affected by shear forces | (1) Time-consuming<br>(2) Not suitable for large sample processing<br>(3) Special equipment required | [81] |

[100], extrusion, freeze/thaw [101], click chemistry [102, 103], and antibody binding [104] (Figure 4).

We concentrate on methods and applications of fusing exogenous RNA into exosomes. One mean is through electroporation of exosomes. Researchers electroplated siRNA into dendritic cell-derived exosomes. Up to 60% GAPDH RNA and protein were knocked down in the mouse cortex, midbrain, and striatum by intravenous injection of electroplated exosomes [98]. Electroplating of siRNA against MAPK-1 into exosomes derived from peripheral blood monocytes reduced the expression of MAPK-1 in donor lymphocytes and monocytes [105]. In a conclusion, these results indicated that electroporation is wildly used in various kinds of exosomes and recipient cells. However, this method is inappropriate for all types of RNA cargo. For instance, researchers reported that miRNA cannot be electroplated into HEK 293-derived exosomes, indicating that some dimension or structure of RNA may be less suitable for this method [106].

Another strategy for fusing RNA into exosomes is overexpressing the cargo RNA in the exosome donor cells. The specificity of this method is poor. This kind of cargo RNA includes chemically modified 3′benzopyridine miRNA [99], mRNA [107, 108], and shRNA [109]. Researchers incubated exosomes carrying these RNAs with recipient cells. These mRNAs were translated into protein. Target genes were knocked down by shRNA and miRNA. This strategy is applicable to various RNA cargos and recipient cells.

*5.3. Targeting Exosomes to Recipient Cells.* The safe application of exosome therapy requires the assessment of potential exosomes targeting cell and subcellular regions. Although the pharmacokinetics of exosomes used by IV has not been elaborated, the application of purified exosomes in mice can cause exosomes to accumulate in the kidney, liver, and spleen [98, 106]. This distribution is similar to most nanoparticle delivery vehicles, usually through bile excretion, kidney clearance, or macrophage clearance [110, 111]. Strategies for exosomes to target specific recipient cells have been reported.

One strategy is to utilize proteins and peptides from the virus with the ability of targeted delivery. For example, researchers used EBV glycoprotein 350 modifying exosomes to target CD19+ B cells, but not other peripheral blood mononuclear cells (PBMCs) [112, 113]. Ligands of viruses can also enhance exosome-mediated transport to target cells in vivo. RVG-labeled exosomes transferred siRNA to the mouse brain, while unlabeled exosomes convey siRNA to the liver, spleen, and kidney [98]. Viral ligands can not only enhance the targeting ability of exosomes but also enhance the ability of exosomes to be integrated into the recipient cells. Exosomes labeled with VSV-G and OVA peptides are

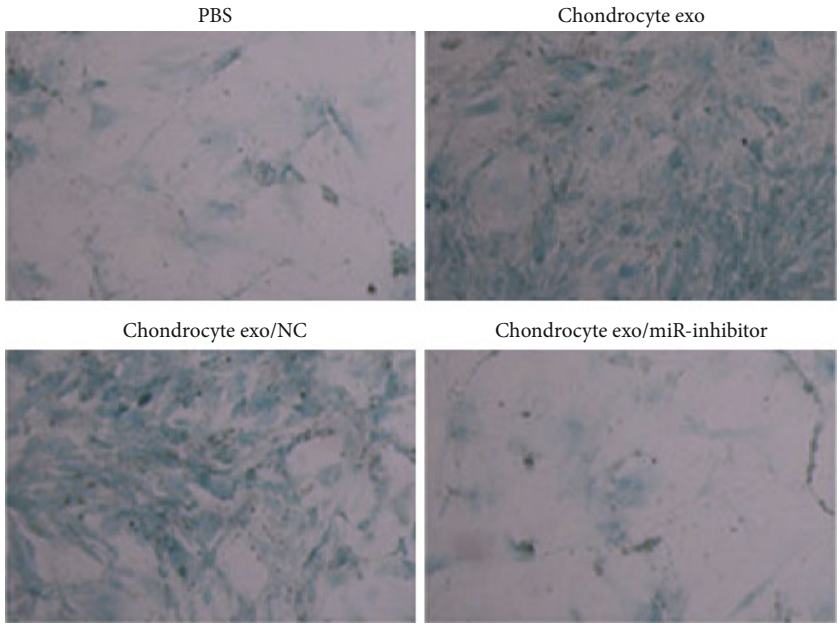


(a)

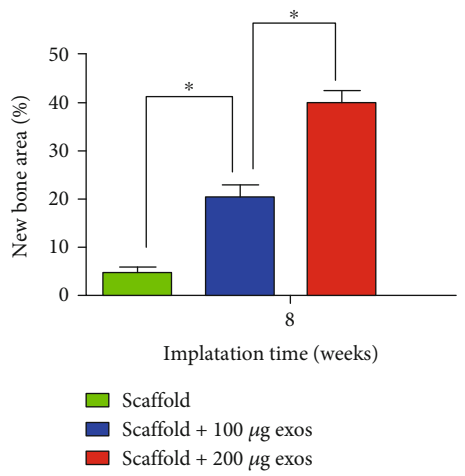


(b)

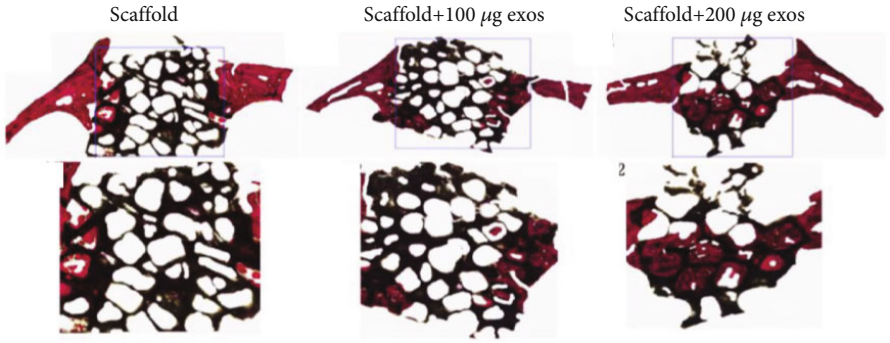


(c)

Figure 5: Effect of exosome on the differentiation of cells in vivo and vitro. In (a), the production of proteoglycan in BMSCs was induced by chondrocyte exosomes, but such effect was counteracted by chondrocyte exosomes with miR-8485 inhibitor. As is shown in (b) and (c), the results of Van Gieson staining of undecalcified specimens showed that bone regeneration was markedly increased in the scaffold+200 $\mu$g Exos group (40.11 ± 2.52%), and the percentage of new bone formation area was significantly greater than that in the scaffold group (4.52 ± 1.2%) or the scaffold+100 $\mu$g Exos group (20.45 ± 2.45%) ($P < 0.05$) [33, 52]. (a) Copyright 2020 BBRC published by Elsevier Ltd. (b, c) Copyright 2016 Int J Biol Sci published by Ivyspring International Publisher.

absorbed by DC at a higher rate than exosomes labeled with OVA alone [114, 115]. Although viruses can be used to improve the ability of exosome to target cells, the strategy is limited to the known interactions. The side effects of this strategy are still unknown.

## 6. Exosome-Based Strategies for Restoration of Bone Defect

Bone-derived exosome containing noncoding RNA is considered significant in regulating bone formation and absorption (Figure 5). Various key factors, regulating osteoclasts and osteoblasts (such as RUNX2, BMP, and sclerostin), are adjusted by specific bone-derived exosomes embodying noncoding RNA [116]. Studies showed that intravenously, exosomes tend to their original place [117].

However, the same noncoding exosomes may have opposite effect on the differentiation and proliferation of osteoclasts and osteoblasts. Therefore, during the process of bone remodeling, bone-derived exosomes may not have functions completely coherent with the parental cells. The abundance of noncoding RNA in recipient cells and exosomes does not

match, indicating that in addition to noncoding RNA, other components of exosomes also have regulatory effects [118]. Researchers have utilized exosomes from other tissues to enhance tissue healing efficacy [119] and to reduce joint injury and osteoarthritis by restoring matrix homeostasis and decreasing inflammation [120]. Efforts were being made to test the effects of engineered exosomes on orthodontic tooth movement models in mouse [121].

## 7. The Advantages of Exosomes as Noncoding RNA Delivery System

*7.1. Biocompatibility.* The advantage of exosomes as drug carriers over existing artificial liposomes lies in their good biocompatibility. Currently, liposomes are the main delivery for siRNA and other RNAs. Liposomes can cause accumulated toxicity and immune response in the human body, without good expected effects. Kamerkar et al. used exosomes to deliver siRNA to prevent the production of KRAS mutant proteins. Research results showed that compared with liposomes, intravenous injection of siRNA-loaded exosomes can better inhibit the expression of KRAS protein, without immunogenicity in vivo [122]. Usman et al. used electroporation technology to introduce nucleotides into red blood cell-derived exosomes. The results showed that the nucleotides loaded with exosomes have a significant inhibitory effect on breast cancer cells and there is no immunity in the body [123]. Compared with other RNA drug delivery vehicles (such as adenovirus, lentivirus, retrovirus, and liposome), exosomes are not immunogenic and cytotoxic, showing good biocompatibility.

*7.2. Biological Stability.* Exosomes derived from antigen-presenting cells can express membrane-bound complement regulators CD55 and CD59 to enhance the stability of circulation in the body [122]. Studies have shown that even if exposed to an inflammatory environment, exosomes still have a longer circulation time [124]. A large number of studies have proved that due to their small size (≤100 nm), nanoparticles can achieve targeted aggregation of tissues through enhanced penetration and retention effects [125]. In addition, the circulation time of polyethylene glycol-modified exosomes can reach more than 60 minutes in vivo [126]. Polyethylene glycol-modified exosomes can significantly improve the biological stability of exosomes in vivo by prolonging the clearance time, making the study of exosomes as drug carriers more promising.

*7.3. Targeting.* Multiple studies have confirmed the loyalty of exosomal cargo to parental cells. Exosomes derived from central nerve cells can pass through the blood-brain barrier and target specific neurons. Exosomes derived from hypoxic tumor cells tend to recruit into hypoxic tumor tissues [127, 128]. The results of biodistribution studies also showed that the accumulation of exosomes in tumor tissues depended on the type of embryonic cells. Therefore, when studying exosomes targeting specific tissues or cells, it is necessary to consider the targeting efficiency [129].

## 8. Conclusions and Perspective

Exosomes are increasingly being studied in the field of bone reconstruction. From the initial research on tumor diseases and related mechanisms to studies on drug delivery and engineering exosomes, there is still a lot of research space.

(1) How to select cells with strong ability to secrete exosomes? The scaffold used with MSCs provides an ideal environment for the osteogenic differentiation of MSCs [130][131]. However, there is no research on the inducing factors involved in this mechanism. Scaffold may enhance the paracrine function of MSCs, thereby secreting exosomes to induce the osteogenic differentiation. (2) The loading of exosomes on the scaffold to promote bone repair has been widely studied, but how to make the scaffold play a controlled or slow-release effect is another problem that needs to be solved. Maybe the solution is to control the pore size and degradation rate of the scaffold material. (3) Another direction is to improve their targeting ability by modifying the exosomal membrane molecules and preventing unwanted derivatives from entering the exosomes

Further research is needed to evaluate the biological efficacy of exosomes in treating bone defects in vivo and vitro. As therapeutic delivery vectors, exosomes have engineering potential, and they are easy to design and well tolerated in vivo. Overcoming each of these miseries will turn the surprise discovery of exosomes as a drug delivery system into a viable mature technology.

## Conflicts of Interest

All the authors declare no conflict of interest.

## Authors' Contributions

Keda Liu and Nanjue Cao contributed equally to this work.

## Acknowledgments

This study was supported by the National Natural Science Foundation of China (No. 81970980); Liaoning Province, Colleges and Universities Basic Research Project (No. LFWK201717); Liaoning Provincial Key Research Plan Guidance Project (No. 2018225078); Liaoning Provincial Natural Science Foundation Guidance Project (No. 2019-ZD-0749); Shenyang Major Scientific and Technological Innovation Research and Development Plan (No. 19-112-4-027); Shenyang Young and Middle-aged Technological Innovation Talent Plan (No. RC200060); and the Second Batch of Medical Education Scientific Research Projects of the 13th Five-Year Plan of China Medical University (No. YDJK2018017).

## References

[1] A. Šućur, V. Katavić, T. Kelava, Z. Jajić, N. Kovačić, and D. Grčević, "Induction of osteoclast progenitors in inflammatory conditions: key to bone destruction in arthritis," *International Orthopaedics*, vol. 38, no. 9, pp. 1893–1903, 2014.

[2] A. Sieberath, E. Della Bella, A. M. Ferreira, P. Gentile, D. Eglin, and K. Dalgarno, "A comparison of osteoblast and osteoclast in vitro co-culture models and their translation for preclinical drug testing applications," *International Journal of Molecular Sciences*, vol. 21, no. 3, p. 912, 2020.

[3] T. Kowada, J. Kikuta, A. Kubo et al., "In vivo fluorescence imaging of bone-resorbing osteoclasts," *Journal of the American Chemical Society*, vol. 133, no. 44, pp. 17772–17776, 2011.

[4] W. Liu, L. H. Yang, X. C. Kong, L. K. An, and R. Wang, "Meta-analysis of osteoporosis: fracture risks, medication and treatment," *Minerva Medica*, vol. 106, no. 4, pp. 203–214, 2015.

[5] S. C. Manolagas, "Steroids and osteoporosis: the quest for mechanisms," *Journal of Clinical Investigation*, vol. 123, no. 5, pp. 1919–1921, 2013.

[6] K. Zhang, Y. Fan, N. Dunne, and X. Li, "Effect of microporosity on scaffolds for bone tissue engineering," *Regenerative Biomaterials*, vol. 5, no. 2, pp. 115–124, 2018.

[7] K. Henriksen, M. A. Karsdal, and T. J. Martin, "Osteoclast-derived coupling factors in bone remodeling," *Calcified Tissue International*, vol. 94, no. 1, pp. 88–97, 2014.

[8] T. Miyazaki, F. Tokimura, and S. Tanaka, "A review of denosumab for the treatment of osteoporosis," *Patient Preference & Adherence*, vol. 8, pp. 463–471, 2014.

[9] G. Sánchez-Duffhues, C. Hiepen, P. Knaus, and P. ten Dijke, "Bone morphogenetic protein signaling in bone homeostasis," *Bone*, vol. 80, pp. 43–59, 2015.

[10] A. I. Alford, K. M. Kozloff, and K. D. Hankenson, "Extracellular matrix networks in bone remodeling," *The International Journal of Biochemistry & Cell Biology*, vol. 65, pp. 20–31, 2015.

[11] L. Wang, S. Wu, G. X. Cao, Y. B. Fan, N. Dunne, and X. M. Li, "Biomechanical studies on biomaterial degradation and co-cultured cells: mechanisms, potential applications, challenges and prospects," *Journal of Materials Chemistry B*, vol. 7, no. 47, pp. 7439–7459, 2019.

[12] S. E. Wang, "Extracellular vesicles and metastasis," *Cold Spring Harbor Perspectives in Medicine*, vol. 10, no. 7, article a037275, 2020.

[13] N. Huynh, L. VonMoss, D. Smith et al., "Characterization of regulatory extracellular vesicles from osteoclasts," *Journal of Dental Research*, vol. 95, no. 6, pp. 673–679, 2016.

[14] B. C. J. van der Eerden, "MicroRNAs in the skeleton: cell-restricted or potent intercellular communicators?," *Archives of Biochemistry and Biophysics*, vol. 561, pp. 46–55, 2014.

[15] H. X. Wang and O. Gires, "Tumor-derived extracellular vesicles in breast cancer: from bench to bedside," *Cancer Letters*, vol. 460, pp. 54–64, 2019.

[16] S. Lin, Z. Yu, D. Chen et al., "Progress in microfluidics-based exosome separation and detection technologies for diagnostic applications," *Small*, vol. 16, no. 9, article 1903916, 2019.

[17] C. K. Das, B. C. Jena, I. Banerjee et al., "Exosome as a novel shuttle for delivery of therapeutics across biological barriers," *Molecular Pharmaceutics*, vol. 16, no. 1, pp. 24–40, 2019.

[18] A. J. Vázquez-Ríos, Á. Molina-Crespo, B. L. Bouzo, R. López-López, G. Moreno-Bueno, and M. de la Fuente, "Exosome-mimetic nanoplatforms for targeted cancer drug delivery," *Journal of Nanobiotechnology*, vol. 17, no. 1, p. 85, 2019.

[19] Ó. Rapado-González, A. Álvarez-Castro, R. López-López, J. Iglesias-Canle, M. M. Suárez-Cunqueiro, and L. Muinelo-Romay, "Circulating microRNAs as promising biomarkers in colorectal cancer," *Cancers*, vol. 11, no. 7, p. 898, 2019.

[20] Y. Zheng, L. Tang, L. Mabardi, S. Kumari, and D. J. Irvine, "Enhancing adoptive cell therapy of cancer through targeted delivery of small-molecule immunomodulators to internalizing or noninternalizing receptors," *ACS Nano*, vol. 11, no. 3, pp. 3089–3100, 2017.

[21] N. Xu, J. Li, Y. Gao et al., "Apoptotic cell-mimicking gold nanocages loaded with LXR agonist for attenuating the progression of murine systemic lupus erythematosus," *Biomaterials*, vol. 197, pp. 380–392, 2019.

[22] E. G. Trams, C. J. Lauter, J. Norman Salem, and U. Heine, "Exfoliation of membrane ecto-enzymes in the form of micro-vesicles," *Biochimica et Biophysica Acta (BBA) - Biomembranes*, vol. 645, no. 1, pp. 63–70, 1981.

[23] G. Raposo, H. W. Nijman, W. Stoorvogel et al., "B lymphocytes secrete antigen-presenting vesicles," *The Journal of Experimental Medicine*, vol. 183, no. 3, pp. 1161–1172, 1996.

[24] D. M. Pegtel, K. Cosmopoulos, D. A. Thorley-Lawson et al., "Functional delivery of viral miRNAs via exosomes," *Proceedings of the National Academy of Sciences of the United States of America*, vol. 107, no. 14, pp. 6328–6333, 2010.

[25] N. Kosaka, H. Iguchi, Y. Yoshioka, F. Takeshita, Y. Matsuki, and T. Ochiya, "Secretory mechanisms and intercellular transfer of microRNAs in living cells," *The Journal of Biological Chemistry*, vol. 285, no. 23, pp. 17442–17452, 2010.

[26] Y. Zhang, D. Liu, X. Chen et al., "Secreted monocytic miR-150 enhances targeted endothelial cell migration," *Molecular Cell*, vol. 39, no. 1, pp. 133–144, 2010.

[27] T. L. Whiteside, "Tumor-derived exosomes and their role in cancer progression," *Advances in Clinical Chemistry*, vol. 74, pp. 103–141, 2016.

[28] L. Wang, C. Y. Wang, S. Wu, Y. B. Fan, and X. M. Li, "Influence of mechanical properties of biomaterials on degradability, cell behaviors and signaling pathways: current progress and challenges," *Biomaterials Science*, vol. 8, no. 10, pp. 2714–2733, 2020.

[29] A. Głuszko, M. J. Szczepański, N. Ludwig, S. M. Mirza, and W. Olejarz, "Exosomes in cancer: circulating immune-related biomarkers," *BioMed Research International*, vol. 2019, Article ID 1628029, 9 pages, 2019.

[30] N. Gong, W. Zhu, R. Xu et al., "Keratinocytes-derived exosomal miRNA regulates osteoclast differentiation in middle ear cholesteatoma," *Biochemical and Biophysical Research Communications*, vol. 525, no. 2, pp. 341–347, 2020.

[31] L. Deng, Y. Wang, Y. Peng et al., "Osteoblast-derived microvesicles: A novel mechanism for communication between osteoblasts and osteoclasts," *Bone*, vol. 79, pp. 37–42, 2015.

[32] L. Lieben, "Direct contact between mature osteoblasts and osteoclasts," *Nature Reviews Rheumatology*, vol. 14, no. 4, p. 183, 2018.

[33] X. Qi, J. Zhang, H. Yuan et al., "Exosomes secreted by human-induced pluripotent stem cell-derived mesenchymal stem cells repair critical-sized bone defects through enhanced angiogenesis and osteogenesis in osteoporotic rats," *International Journal of Biological Sciences*, vol. 12, no. 7, pp. 836–849, 2016.

[34] P. Kucharzewska, H. C. Christianson, J. E. Welch et al., "Exosomes reflect the hypoxic status of glioma cells and mediate

hypoxia-dependent activation of vascular cells during tumor development," *Proceedings of the National Academy of Sciences of the United States of America*, vol. 110, no. 18, pp. 7312–7317, 2013.

[35] M. Ghorbanian, S. Babashah, and F. Ataei, "The effects of ovarian cancer cell-derived exosomes on vascular endothelial growth factor expression in endothelial cells," *EXCLI Journal*, vol. 18, pp. 899–907, 2019.

[36] J. Ratajczak, K. Miekus, M. Kucia et al., "Embryonic stem cell-derived microvesicles reprogram hematopoietic progenitors: evidence for horizontal transfer of mRNA and protein delivery," *Leukemia*, vol. 20, no. 5, pp. 847–856, 2006.

[37] M. C. Deregibus, V. Cantaluppi, R. Calogero et al., "Endothelial progenitor cell derived microvesicles activate an angiogenic program in endothelial cells by a horizontal transfer of mRNA," *Blood*, vol. 110, no. 7, pp. 2440–2448, 2007.

[38] H. Valadi, K. Ekström, A. Bossios, M. Sjöstrand, J. J. Lee, and J. O. Lötvall, "Exosome-mediated transfer of mRNAs and microRNAs is a novel mechanism of genetic exchange between cells," *Nature Cell Biology*, vol. 9, no. 6, pp. 654–659, 2007.

[39] F. Fatima and M. Nawaz, "Vesiculated long non-coding RNAs: offshore packages deciphering trans-regulation between cells, cancer progression and resistance to therapies," *Non-Coding RNA*, vol. 3, no. 1, p. 10, 2017.

[40] L. S. Holliday, A. D. Dean, R. H. Lin, J. E. Greenwald, and S. L. Gluck, "Low NO concentrations inhibit osteoclast formation in mouse marrow cultures by cGMP-dependent mechanism," *The American Journal of Physiology*, vol. 272, no. 3, pp. F283–F291, 1997.

[41] X. Wang, B. Guo, Q. Li et al., "miR-214 targets _ATF4_ to inhibit bone formation," *Nature Medicine*, vol. 19, no. 1, pp. 93–100, 2013.

[42] T. Wang, C. H. Sun, H. B. Zhong et al., "N-(3-Methoxybenzyl) -(9Z,12Z,15Z)-octadecatrienamide promotes bone formation via the canonical Wnt/$\beta$-catenin signaling pathway," *Phytotherapy Research*, vol. 33, no. 4, pp. 1074–1083, 2019.

[43] D. Li, J. Liu, B. Guo et al., "Osteoclast-derived exosomal miR-214-3p inhibits osteoblastic bone formation," *Nature Communications*, vol. 7, no. 1, article 10872, 2016.

[44] W. Sun, C. Zhao, Y. Li et al., "Osteoclast-derived microRNA-containing exosomes selectively inhibit osteoblast activity," *Cell Discovery*, vol. 2, no. 1, article 16015, 2016.

[45] L. S. Holliday, K. P. McHugh, J. Zuo, J. I. Aguirre, J. K. Neubert, and W. J. Rody Jr., "Exosomes: novel regulators of bone remodelling and potential therapeutic agents for orthodontics," *Orthodontics & Craniofacial Research*, vol. 20, Supplement 1, pp. 95–99, 2017.

[46] M. Fu, G. Huang, Z. Zhang et al., "Expression profile of long noncoding RNAs in cartilage from knee osteoarthritis patients," *Osteoarthritis and Cartilage*, vol. 23, no. 3, pp. 423–432, 2015.

[47] Z. Zhang, Y. Kang, Z. Zhang et al., "Expression of microRNAs during chondrogenesis of human adipose-derived stem cells," *Osteoarthritis and Cartilage*, vol. 20, no. 12, pp. 1638–1646, 2012.

[48] T. Xu, Y. Luo, J. Wang et al., "Exosomal miRNA-128-3p from mesenchymal stem cells of aged rats regulates osteogenesis and bone fracture healing by targeting Smad5," *Journal of Nanobiotechnology*, vol. 18, no. 1, p. 47, 2020.

[49] R. Wang, W. Jiang, L. Zhang et al., "Intra-articular delivery of extracellular vesicles secreted by chondrogenic progenitor cells from MRL/MpJ superhealer mice enhances articular cartilage repair in a mouse injury model," *Stem Cell Research & Therapy*, vol. 11, no. 1, p. 93, 2020.

[50] G. W. Lee, M. Thangavelu, M. J. Choi et al., "Exosome mediated transfer of miRNA-140 promotes enhanced chondrogenic differentiation of bone marrow stem cells for enhanced cartilage repair and regeneration," *Journal of Cellular Biochemistry*, vol. 121, no. 7, pp. 3642–3652, 2020.

[51] B. C. Yang, M. J. Kuang, J. Y. Kang, J. Zhao, J. X. Ma, and X. L. Ma, "Human umbilical cord mesenchymal stem cell-derived exosomes act via the miR-1263/Mob1/Hippo signaling pathway to prevent apoptosis in disuse osteoporosis," *Biochemical and Biophysical Research Communications*, vol. 524, no. 4, pp. 883–889, 2020.

[52] Z. Li, Y. Wang, S. Xiang et al., "Chondrocytes-derived exosomal miR-8485 regulated the Wnt/$\beta$-catenin pathways to promote chondrogenic differentiation of BMSCs," *Biochemical and Biophysical Research Communications*, vol. 523, no. 2, pp. 506–513, 2020.

[53] J. Zheng, L. Zhu, I. Iok in, Y. Chen, N. Jia, and W. Zhu, "Bone marrow-derived mesenchymal stem cells-secreted exosomal microRNA-192-5p delays inflammatory response in rheumatoid arthritis," *International Immunopharmacology*, vol. 78, p. 105985, 2020.

[54] Q. Leng, L. Chen, and Y. Lv, "RNA-based scaffolds for bone regeneration: application and mechanisms of mRNA, miRNA and siRNA," *Theranostics*, vol. 10, no. 7, pp. 3190–3205, 2020.

[55] J. Zheng, X. Zhang, Y. Zhang, and F. Yuan, "Osteoblast differentiation of bone marrow stromal cells by femtosecond laser bone ablation," *Biomedical Optics Express*, vol. 11, no. 2, pp. 885–894, 2020.

[56] Y. Zhang, Y. Gao, L. Cai et al., "MicroRNA-221 is involved in the regulation of osteoporosis through regulates RUNX2 protein expression and osteoblast differentiation," *American Journal of Translational Research*, vol. 9, no. 1, pp. 126–135, 2017.

[57] X. Zheng, J. Dai, H. Zhang, and Z. Ge, "MicroRNA-221 promotes cell proliferation, migration, and differentiation by regulation of ZFPM2 in osteoblasts," *Brazilian Journal of Medical and Biological Research*, vol. 51, no. 12, article e7574, 2018.

[58] W. Zhang, Y. Wu, Y. Shiozaki et al., "miRNA-133a-5p inhibits the expression of osteoblast differentiation-associated markers by targeting the 3' UTR of RUNX2," *DNA and Cell Biology*, vol. 37, no. 3, pp. 199–209, 2018.

[59] J. Kureel, A. A. John, M. Dixit, and D. Singh, "MicroRNA-467g inhibits new bone regeneration by targeting Ihh/Runx-2 signaling," *The International Journal of Biochemistry & Cell Biology*, vol. 85, pp. 35–43, 2017.

[60] M. Han, L. Chen, and Y. Wang, "*miR-218* overexpression suppresses tumorigenesis of papillary thyroid cancer via inactivation of PTEN /PI3K/AKT pathway by targeting Runx2," *OncoTargets and therapy*, vol. 11, pp. 6305–6316, 2018.

[61] B. Qu, X. Xia, M. Yan et al., "miR-218 is involved in the negative regulation of osteoclastogenesis and bone resorption by partial suppression of p38MAPK-c-Fos-NFATc1 signaling: potential role for osteopenic diseases," *Experimental Cell Research*, vol. 338, no. 1, pp. 89–96, 2015.

[62] A. Asgharzadeh, S. Alizadeh, M. R. Keramati et al., "Upregulation of miR-210 promotes differentiation of mesenchymal

stem cells (MSCs) into osteoblasts," *Bosnian Journal of Basic Medical Sciences*, vol. 18, no. 4, pp. 328–335, 2018.

[63] Y. Jin, F. Hong, Q. Bao et al., "MicroRNA-145 suppresses osteogenic differentiation of human jaw bone marrow mesenchymal stem cells partially via targeting semaphorin 3A," *Connective Tissue Research*, pp. 1–9, 2019.

[64] S. Fang, Y. Deng, P. Gu, and X. Fan, "MicroRNAs regulate bone development and regeneration," *International Journal of Molecular Sciences*, vol. 16, no. 4, pp. 8227–8253, 2015.

[65] J. Tian, Y. J. Rui, Y. J. Xu, and S. A. Zhang, "MiR-143-3p regulates early cartilage differentiation of BMSCs and promotes cartilage damage repair through targeting BMPR2," *European Review for Medical and Pharmacological Sciences*, vol. 22, no. 24, pp. 8814–8821, 2018.

[66] J.-y. Wang, Y. Yang, Y. Ma et al., "Potential regulatory role of lncRNA-miRNA-mRNA axis in osteosarcoma," *Biomedicine & Pharmacotherapy*, vol. 121, p. 109627, 2020.

[67] L. Zhu and P. C. Xu, "Downregulated LncRNA-ANCR promotes osteoblast differentiation by targeting EZH2 and regulating Runx2 expression," *Biochemical and Biophysical Research Communications*, vol. 432, no. 4, pp. 612–617, 2013.

[68] C. Yu, L. Li, F. Xie et al., "LncRNA TUG1 sponges miR-204-5p to promote osteoblast differentiation through upregulating Runx2 in aortic valve calcification," *Cardiovascular Research*, vol. 114, no. 1, pp. 168–179, 2018.

[69] L. Yu, H. Qu, Y. Yu, W. Li, Y. Zhao, and G. Qiu, "LncRNA-PCAT1 targeting miR-145-5p promotes TLR4-associated osteogenic differentiation of adipose-derived stem cells," *Journal of Cellular and Molecular Medicine*, vol. 22, no. 12, pp. 6134–6147, 2018.

[70] R. Wu, J. Ruan, Y. Sun et al., "Long non-coding RNA HIF1A-AS2 facilitates adipose-derived stem cells (ASCs) osteogenic differentiation through miR-665/IL6 axis via PI3K/Akt signaling pathway," *Stem Cell Research & Therapy*, vol. 9, no. 1, p. 348, 2018.

[71] L. Deng, H. Hong, X. Zhang et al., "Down-regulated lncRNA MEG3 promotes osteogenic differentiation of human dental follicle stem cells by epigenetically regulating Wnt pathway," *Biochemical and Biophysical Research Communications*, vol. 503, no. 3, pp. 2061–2067, 2018.

[72] X. Yang, J. Yang, P. Lei, and T. Wen, "LncRNA MALAT1 shuttled by bone marrow-derived mesenchymal stem cells-secreted exosomes alleviates osteoporosis through mediating microRNA-34c/SATB2 axis," *Aging*, vol. 11, no. 20, pp. 8777–8791, 2019.

[73] B. Li, H. Xu, H. Han et al., "Exosome-mediated transfer of lncRUNX2-AS1 from multiple myeloma cells to MSCs contributes to osteogenesis," *Oncogene*, vol. 37, no. 41, pp. 5508–5519, 2018.

[74] X. Huang, X. Cen, B. Zhang et al., "Prospect of circular RNA in osteogenesis: a novel orchestrator of signaling pathways," *Journal of Cellular Physiology*, vol. 234, no. 12, pp. 21450–21459, 2019.

[75] H. Wang, C. Feng, Y. Jin, W. Tan, and F. Wei, "Identification and characterization of circular RNAs involved in mechanical force-induced periodontal ligament stem cells," *Journal of Cellular Physiology*, vol. 234, no. 7, pp. 10166–10177, 2019.

[76] M. Zhang, L. Jia, and Y. Zheng, "circRNA expression profiles in human bone marrow stem cells undergoing osteoblast differentiation," *Stem Cell Reviews and Reports*, vol. 15, no. 1, pp. 126–138, 2019.

[77] Y. Mizuno, Y. Tokuzawa, Y. Ninomiya et al., "miR-210 promotes osteoblastic differentiation through inhibition of AcvR1b," *FEBS Letters*, vol. 583, no. 13, pp. 2263–2268, 2009.

[78] J. Zhang, Q. Tu, L. F. Bonewald et al., "Effects of miR-335-5p in modulating osteogenic differentiation by specifically downregulating Wnt antagonist DKK1," *Journal of Bone and Mineral Research*, vol. 26, no. 8, pp. 1953–1963, 2011.

[79] W. Peng, S. Zhu, J. Chen, J. Wang, Q. Rong, and S. Chen, "Hsa_circRNA_33287 promotes the osteogenic differentiation of maxillary sinus membrane stem cells via miR-214-3p/Runx3," *Biomedicine & Pharmacotherapy*, vol. 109, pp. 1709–1717, 2019.

[80] D. Y. Qian, G. B. Yan, B. Bai et al., "Differential circRNA expression profiles during the BMP2-induced osteogenic differentiation of MC3T3-E1 cells," *Biomedicine & Pharmacotherap*, vol. 90, pp. 492–499, 2017.

[81] Q. Xing, P. de Vos, M. M. Faas, Q. Ye, and Y. Ren, "LPS promotes pre-osteoclast activity by up-regulating CXCR4 via TLR-4," *Journal of Dental Research*, vol. 90, no. 2, pp. 157–162, 2011.

[82] A. Huang, H. Zheng, Z. Wu, M. Chen, and Y. Huang, "Circular RNA-protein interactions: functions, mechanisms, and identification," *Theranostics*, vol. 10, no. 8, pp. 3503–3517, 2020.

[83] Y. Zheng, X. Li, Y. Huang, L. Jia, and W. Li, "The circular RNA landscape of periodontal ligament stem cells during osteogenesis," *Journal of Periodontology*, vol. 88, no. 9, pp. 906–914, 2017.

[84] S. Chen, Y. Tang, Y. Liu et al., "Exosomes derived from miR-375-overexpressing human adipose mesenchymal stem cells promote bone regeneration," *Cell Proliferation*, vol. 52, no. 5, article e12669, 2019.

[85] Z. Jin, J. Ren, and S. Qi, "Human bone mesenchymal stem cells-derived exosomes overexpressing microRNA-26a-5p alleviate osteoarthritis via down-regulation of PTGS2," *International Immunopharmacology*, vol. 78, article 105946, 2020.

[86] H. Song, X. Li, Z. Zhao et al., "Reversal of osteoporotic activity by endothelial cell-secreted bone targeting and biocompatible exosomes," *Nano Letters*, vol. 19, no. 5, pp. 3040–3048, 2019.

[87] S. Raimondo, O. Urzì, A. Conigliaro et al., "Extracellular vesicle microRNAs contribute to the osteogenic inhibition of mesenchymal stem cells in multiple myeloma," *Cancers*, vol. 12, no. 2, p. 449, 2020.

[88] X. Zhang, Y. Zhu, C. Zhang et al., "miR-542-3p prevents ovariectomy-induced osteoporosis in rats via targeting SFRP1," *Journal of Cellular Physiology*, vol. 233, no. 9, pp. 6798–6806, 2018.

[89] X. Tang, J. Lin, G. Wang, and J. Lu, "MicroRNA-433-3p promotes osteoblast differentiation through targeting DKK1 expression," *PLoS One*, vol. 12, no. 6, article e0179860, 2017.

[90] Y. Arfat, M. A. R. Basra, M. Shahzad, K. Majeed, N. Mahmood, and H. Munir, "miR-208a-3p Suppresses Osteoblast Differentiation and Inhibits Bone Formation by Targeting *ACVR1*," *Molecular Therapy - Nucleic Acids*, vol. 11, pp. 323–336, 2018.

[91] D. W. Greening, R. Xu, H. Ji, B. J. Tauro, and R. J. Simpson, "A protocol for exosome isolation and characterization: evaluation of ultracentrifugation, density-gradient separation, and immunoaffinity capture methods," *Methods in Molecular Biology*, vol. 1295, pp. 179–209, 2015.

[92] M. P. Oksvold, A. Neurauter, and K. W. Pedersen, "Magnetic bead-based isolation of exosomes," *Methods in Molecular Biology*, vol. 1218, pp. 465–481, 2015.

[93] R. J. Lobb, M. Becker, S. Wen Wen et al., "Optimized exosome isolation protocol for cell culture supernatant and human plasma," *Journal of Extracellular Vesicles*, vol. 4, no. 1, p. 27031, 2015.

[94] Y. Q. Koh, F. B. Almughlliq, K. Vaswani, H. N. Peiris, and M. D. Mitchell, "Exosome enrichment by ultracentrifugation and size exclusion chromatography," *Frontiers in Bioscience*, vol. 23, pp. 865–874, 2018.

[95] B. Shen, N. Wu, J.-M. Yang, and S. J. Gould, "Protein targeting to exosomes/microvesicles by plasma membrane anchors," *Journal of Biological Chemistry*, vol. 286, no. 16, pp. 14383–14395, 2011.

[96] D. Sun, X. Zhuang, X. Xiang et al., "A novel nanoparticle drug delivery system: the anti-inflammatory activity of curcumin is enhanced when encapsulated in exosomes," *Molecular Therapy*, vol. 18, no. 9, pp. 1606–1614, 2010.

[97] R. Chen, H. Huang, H. Liu et al., "Friend or foe? Evidence indicates endogenous exosomes can deliver functional gRNA and Cas9 protein," *Small*, vol. 15, no. 38, article e1902686, 2019.

[98] L. Alvarez-Erviti, Y. Seow, H. Yin, C. Betts, S. Lakhal, and M. J. Wood, "Delivery of siRNA to the mouse brain by systemic injection of targeted exosomes," *Nature Biotechnology*, vol. 29, no. 4, pp. 341–345, 2011.

[99] Y. Akao, A. Iio, T. Itoh et al., "Microvesicle-mediated RNA molecule delivery system using monocytes/macrophages," *Molecular Therapy*, vol. 19, no. 2, pp. 395–399, 2011.

[100] M. J. Haney, N. L. Klyachko, Y. Zhao et al., "Exosomes as drug delivery vehicles for Parkinson's disease therapy," *Journal of Controlled Release*, vol. 207, pp. 18–30, 2015.

[101] G. Fuhrmann, A. Serio, M. Mazo, R. Nair, and M. M. Stevens, "Active loading into extracellular vesicles significantly improves the cellular uptake and photodynamic effect of porphyrins," *Journal of Controlled Release*, vol. 205, pp. 35–44, 2015.

[102] T. Smyth, K. Petrova, N. M. Payton et al., "Surface functionalization of exosomes using click chemistry," *Bioconjugate Chemistry*, vol. 25, no. 10, pp. 1777–1784, 2014.

[103] X. M. Li, J. R. Wei, K. E. Aifantis et al., "Current investigations into magnetic nanoparticles for biomedical application," *Journal of Biomedical Materials Research Part A*, vol. 104, no. 5, pp. 1285–1296, 2016.

[104] J. N. Higginbotham, Q. Zhang, D. K. Jeppesen et al., "Identification and characterization of EGF receptor in individual exosomes by fluorescence-activated vesicle sorting," *Journal of Extracellular Vesicles*, vol. 5, no. 1, article 29254, 2016.

[105] J. Wahlgren, T. D. L. Karlson, M. Brisslert et al., "Plasma exosomes can deliver exogenous short interfering RNA to monocytes and lymphocytes," *Nucleic Acids Research*, vol. 40, no. 17, article e130, 2012.

[106] S. Ohno, M. Takanashi, K. Sudo et al., "Systemically injected exosomes targeted to EGFR deliver antitumor microRNA to breast cancer cells," *Molecular Therapy*, vol. 21, no. 1, pp. 185–191, 2013.

[107] E. Hergenreider, S. Heydt, K. Tréguer et al., "Atheroprotective communication between endothelial cells and smooth muscle cells through miRNAs," *Nature Cell Biology*, vol. 14, no. 3, pp. 249–256, 2012.

[108] A. Mizrak, M. F. Bolukbasi, G. B. Ozdener et al., "Genetically engineered microvesicles carrying suicide mRNA/protein inhibit schwannoma tumor growth," *Molecular Therapy*, vol. 21, no. 1, pp. 101–108, 2013.

[109] O. Rechavi, Y. Erlich, H. Amram et al., "Cell contact-dependent acquisition of cellular and viral nonautonomously encoded small RNAs," *Genes & Development*, vol. 23, no. 16, pp. 1971–1979, 2009.

[110] H. Iguchi, N. Kosaka, and T. Ochiya, "Secretory microRNAs as a versatile communication tool," *Communicative & Integrative Biology*, vol. 3, no. 5, pp. 478–481, 2014.

[111] Y. W. Yi, J. H. Lee, S. Y. Kim et al., "Advances in analysis of biodistribution of exosomes by molecular imaging," *International Journal of Molecular Sciences*, vol. 21, no. 2, p. 665, 2020.

[112] R. Ruiss, S. Jochum, R. Mocikat, W. Hammerschmidt, and R. Zeidler, "EBV-gp350 confers B-cell tropism to tailored exosomes and is a neo-antigen in normal and malignant B cells—a new option for the treatment of B-CLL," *PLoS One*, vol. 6, no. 10, article e25294, 2011.

[113] A. Farina, G. Peruzzi, V. Lacconi et al., "Epstein-Barr virus lytic infection promotes activation of Toll-like receptor 8 innate immune response in systemic sclerosis monocytes," *Arthritis Research & Therapy*, vol. 19, no. 1, p. 39, 2017.

[114] V. V. Temchura, M. Tenbusch, G. Nchinda et al., "Enhancement of immunostimulatory properties of exosomal vaccines by incorporation of fusion-competent G protein of vesicular stomatitis virus," *Vaccine*, vol. 26, no. 29-30, pp. 3662–3672, 2008.

[115] Y. Yang, Y. Hong, G. H. Nam, J. H. Chung, E. Koh, and I. S. Kim, "Virus-mimetic fusogenic exosomes for direct delivery of integral membrane proteins to target cell membranes," *Advanced Materials*, vol. 29, no. 13, article 1605604, 2017.

[116] Y. Qin, R. Sun, C. Wu, L. Wang, and C. Zhang, "Exosome: a novel approach to stimulate bone regeneration through regulation of osteogenesis and angiogenesis," *International Journal of Molecular Sciences*, vol. 17, no. 5, p. 712, 2016.

[117] O. P. B. Wiklander, J. Z. Nordin, A. O'Loughlin et al., "Extracellular vesicle in vivo biodistribution is determined by cell source, route of administration and targeting," *Journal of Extracellular Vesicles*, vol. 4, no. 1, article 26316, 2015.

[118] Y. Cui, J. Luan, H. Li, X. Zhou, and J. Han, "Exosomes derived from mineralizing osteoblasts promote ST2 cell osteogenic differentiation by alteration of microRNA expression," *FEBS Letters*, vol. 590, no. 1, pp. 185–192, 2016.

[119] Y. Nakamura, S. Miyaki, H. Ishitobi et al., "Mesenchymal-stem-cell-derived exosomes accelerate skeletal muscle regeneration," *FEBS Letters*, vol. 589, no. 11, pp. 1257–1265, 2015.

[120] J. Li, E. Hosseini-Beheshti, G. Grau, H. Zreiqat, and C. Little, "Stem cell-derived extracellular vesicles for treating joint injury and osteoarthritis," *Nanomaterials*, vol. 9, no. 2, p. 261, 2019.

[121] E. J. Toro, J. Zuo, A. Gutierrez et al., "Bis-enoxacin inhibits bone resorption and orthodontic tooth movement," *Journal of Dental Research*, vol. 92, no. 10, pp. 925–931, 2013.

[122] S. Kamerkar, V. S. LeBleu, H. Sugimoto et al., "Exosomes facilitate therapeutic targeting of oncogenic KRAS in pancreatic cancer," *Nature*, vol. 546, no. 7659, pp. 498–503, 2017.

[123] W. M. Usman, T. C. Pham, Y. Y. Kwok et al., "Efficient RNA drug delivery using red blood cell extracellular vesicles," *Nature Communications*, vol. 9, no. 1, p. 2359, 2018.

[124] J. P. Armstrong, M. N. Holme, and M. M. Stevens, "Re-engineering extracellular vesicles as smart nanoscale therapeutics," *ACS Nano*, vol. 11, no. 1, pp. 69–83, 2017.

[125] Y. Yang, X. Tai, K. Shi et al., "A new concept of enhancing immuno-chemotherapeutic effects against B16F10 tumor via systemic administration by taking advantages of the limitation of EPR effect," *Theranostics*, vol. 6, no. 12, pp. 2141–2160, 2016.

[126] S. A. A. Kooijmans, L. A. L. Fliervoet, R. van der Meel et al., "PEGylated and targeted extracellular vesicles display enhanced cell specificity and circulation time," *Journal of Controlled Release*, vol. 224, pp. 77–85, 2016.

[127] M. Shi, L. Sheng, T. Stewart, C. P. Zabetian, and J. Zhang, "New windows into the brain: central nervous system-derived extracellular vesicles in blood," *Progress in Neurobiology*, vol. 175, pp. 96–106, 2019.

[128] K. O. Jung, H. Jo, J. H. Yu, S. S. Gambhir, and G. Pratx, "Development and MPI tracking of novel hypoxia-targeted theranostic exosomes," *Biomaterials*, vol. 177, pp. 139–148, 2018.

[129] M. Mendt, S. Kamerkar, H. Sugimoto et al., "Generation and testing of clinical-grade exosomes for pancreatic cancer," *JCI Insight*, vol. 3, no. 8, 2018.

[130] M. Maqsood, M. Kang, X. Wu, J. Chen, L. Teng, and L. Qiu, "Adult mesenchymal stem cells and their exosomes: sources, characteristics, and application in regenerative medicine," *Life Sciences*, vol. 256, article 118002, 2020.

[131] K. Vaswani, Y. Q. Koh, F. B. Almughlliq, H. N. Peiris, and M. D. Mitchell, "A method for the isolation and enrichment of purified bovine milk exosomes," *Reproductive Biology*, vol. 17, no. 4, pp. 341–348, 2017.

Hindawi
Journal of Nanomaterials
Volume 2020, Article ID 4929151, 10 pages
https://doi.org/10.1155/2020/4929151

*Research Article*

# Sequential Delivery of BMP2-Derived Peptide P24 by Thiolated Chitosan/Calcium Carbonate Composite Microspheres Scaffolds for Bone Regeneration

**Zhaozhen Wang,[1] Xujie Liu,[2,3] Vidmi Taolam Martin,[1] Mohamed Abdullahi Abdi,[1] Lijun Chen,[4] Yong Gong,[1] Yiran Yan,[1] Liming Song,[1] Zhongxun Liu,[1] Xianliao Zhang,[1] Yan Chen,[4] and Bo Yu[1]**

[1]*Department of Orthopedics, Zhujiang Hospital of Southern Medical University, Guangzhou 510282, China*
[2]*Graduate School at Shenzhen, Tsinghua University, Shenzhen 518055, China*
[3]*State Key Laboratory of New Ceramics and Fine Processing, School of Materials Science and Engineering, Tsinghua University, Beijing 100084, China*
[4]*Department of Ultrasonic Diagnosis, Zhujiang Hospital, Southern Medical University, Guangzhou 510282, China*

Correspondence should be addressed to Yan Chen; smu_chen@163.com and Bo Yu; gzyubo@163.com

Zhaozhen Wang, Xujie Liu, and Vidmi Taolam Martin contributed equally to this work.

Received 4 April 2020; Accepted 19 May 2020; Published 13 July 2020

Academic Editor: Hui-Qi Xie



The combination of tissue-engineered bone scaffolds with osteogenic induction molecules is an important strategy for critical-sized bone defects repair. We synthesized a novel thiolated chitosan/calcium carbonate composite microsphere (TCS-P24/CA) scaffold as a carrier for bone morphogenetic protein 2- (BMP2-) derived peptide P24 and evaluated the release kinetics of P24. The effect of TCS-P24/CA scaffolds on the proliferation and differentiation of bone marrow mesenchymal stem cells (BMSCs) was evaluated by scanning electron microscope (SEM), CCK-8, ALP assay, alizarin red staining, and PCR. A 5 mm diameter calvarial defect was created, then new bone formation was evaluated by Micro-CT and histological examination at 4 and 8 weeks after operation. We found the sequential release of P24 could last for 29 days. Meanwhile, BMSCs revealed spindle-shaped surface morphology, indicating the TCS-P24/CA scaffolds could support cell adhesion and mRNA levels for ALP, Runx2, and COL1a1 were significantly upregulated on TCS-10%P24/CA scaffold compared with other groups in vitro ($p < 0.05$). Similarly, the BMSCs exhibited a higher ALP activity as well as calcium deposition level on TCS-10%P24/CA scaffolds compared with other groups ($p < 0.05$). Analysis of in vivo bone formation showed that the TCS-10%P24/CA scaffold induced more bone formation than TCS-5%P24/CA, TCS/CA, and control groups. This study demonstrates that the novel TCS-P24/CA scaffolds might contribute to the delivery of BMP2-derived Peptide P24 and is considered to be a potential candidate for repairing bone defects.

## 1. Introduction

Regeneration of critical-sized bone defects resulting from tumor resection and congenital malformation or trauma is still a challenging problem in orthopedic surgery [1–3]. Autograft is the "gold standard" and clinical approach for bone defect reconstruction; it has considerable limitations such as insufficient graft material, and unpredictable bone resorption [4, 5]. Hence, bone tissue engineering has been recommended as a promising approach for bone regeneration [6, 7]. However, most of the bone tissue engineering scaffolds were recorded for the significant lack of osteoinductivity. The combination of osteoinductive growth factors or peptides is of important significance [8].

BMP-2 has been proved previously in inducing bone formation owing to its better osteoinductive activity [9, 10]. BMP-2 is known as well too costly, and it usually needs to be applied in a high-dose for clinical therapy, followed by side effects such as promotion of tumor angiogenesis and excessive bone resorption [11, 12]. Alternatively, BMP-2 derived peptide P24 has been investigated and demonstrated as an enhanced effect of osteogenesis [13]. The P24 peptide is composed of small molecules and has chemical stability and structural alignment, which is beneficial to its biological effect [3]. Besides, the P24 peptide contained ample phosphorylated serine and aspartic acid, which can improve the acceleration of nucleation and mineralization [14]. Also, P24 peptide has a low production cost and is suitable for preparation [3]. According to these characteristics, BMP-2-derived peptide p24 seems to have application space.

Over the past few decades, scaffolds used to release peptides or proteins have received considerable attention. Chitosan has attracted remarkable attention for bone tissue engineering owing to its promising nontoxicity, biodegradability, and biocompatibility [15]. The addition of the thiol group on the amino group of chitosan can ameliorate some properties of chitosan [16]. Chitosan is not soluble in neutral medium, however, the thiolated chitosan showed good solubility under the condition of neutral pH [17]. Therefore, thiolated chitosan-based scaffolds suitable for delivering peptides or proteins sensitive to pH changes were prepared [18]. This thiol group on thiolated chitosan might be more conducive to the delivery of cysteine-rich peptides or proteins in the thiolated chitosan-based scaffolds.

However, the structure of the pure thiolated chitosan scaffold has the drawback of quick degradation and weak mechanical properties [19]. Therefore, thiolated chitosan scaffolds may be compounded with calcium carbonate, which is bioabsorbable and has good bone conductivity and biocompatibility. Synthetic calcium carbonate composite scaffolds have been considered as a promising material for bone defect repair [20]. In this research, carboxymethyl chitosan known as a derivative of chitosan, with better water solubility, has been used to prepare and incorporate at the same time an intermediate formula for calcium carbonate. The calcium carbonate hybrid microspheres have excellent biocompatibility, bone conductivity, and biodegradability [21]. According to these findings, we believe that when calcium carbonate microsphere, being synthesized by in-situ precipitation method and combined with thiolated chitosan, can be used as an effective carrier of P24 peptide [22–25]. However, thiolated chitosan/calcium carbonate composite scaffolds for P24 peptide sustained release have not been reported yet. Thus, it is highly significant to analyze the P24 sustained release characteristics for the potential application of TCS-P24/CA scaffolds in bone tissue engineering.

In this study, we synthesized a novel TCS-P24/CA scaffolds for the continuous delivery of P24 peptide. First of all, we tested the physical properties of TCS-P24/CA scaffolds in vitro. Secondly, we performed the proliferation and shape of BMSCs on the TCS-P24/CA scaffolds. Thirdly, the ALP activity, osteogenic-specific genes, and calcium deposition of BMSCs cultured on the TCS-P24/CA scaffolds were evaluated. Finally, calvarial bone defect models were created to evaluate the effect of TCS-P24/CA scaffolds for bone regeneration.

## 2. Materials and Methods

Calcium chloride, chitosan (degree of deacetylation: 80%–95%), ammonia carbonate, and sodium tripolyphosphate were purchased from Sinopharm Chemical Reagent Co. Ltd., China. Chondroitin sulfate C and carboxymethyl chitosan (Molecular weight: ~150 kDa, deacetylation degree: ≥90%) were purchased from Rubio Co. Ltd, Germany. 2-iminothiolane hydrochloride was purchased from Sigma, USA. P24 Peptide (N → C: KIPKA SSVPT ELSAI STLYL SGGC) was synthesized by Shanghai ZiYu Biotech Co. China.

*2.1. Thiolated Chitosan Fabrication.* Thiolated chitosan (TCS) was fabricated by a previously described method [26]. Briefly, 400 mg of chitosan was dissolved in 200 mL 1% acetic acid for 5 h to obtain a 0.2% (*w*/*v*) chitosan solution. 80 mg of 2-iminothiolane hydrochloride was added into the solution, and the pH was adjusted to 6. Furthermore, the mixed solution was dialyzed against 5 mM HCl once, 5 mM HCl (containing 1% NaCl) twice, 5 mM HCl once, and 1 mM HCl once, 1 day for each time. The TCS samples were obtained by lyophilizing the mixed solution at −80°C and 20 Pa.

*2.2. Calcium Carbonate Microspheres (CA) Fabrication.* 10 mg/mL of carboxymethyl chitosan and 0.4 mol/L of calcium chloride solution were mixed and stirred for 10minutes, recorded as solution A. Concerning solution B, 20 mg/mL of chondroitin sulfate and 0.8 mol/L of ammonium carbonate solution were mixed and stirred for 10 minutes. Solution B was added drop by drop into solution A and then stirred for half an hour. Finally, the solution was mixed and washed 4 times, and then the calcium carbonate microspheres were obtained by drying the sediment for 48 hours.

*2.3. TCS-P24/CA Scaffold Fabrication.* 100 mg calcium carbonate microspheres (CA) were added to 5 mL 2% thiolated chitosan (TCS) solution and mixed by ultrasonic crusher. The different amounts of P24 were used to fabricate TCS/CA, TCS-5%P24/CA, or TCS-10%P24/CA mixed solution. Therefore, a 96-well plate was used as a mold and the mixed solution was lyophilized at −80°C and 20 Pa to obtain the TCS/CA, TCS-5%P24/CA, or TCS-10%P24/CA scaffolds.

*2.4. In Vitro P24 Release Study from TCS-P24/CA Scaffold.* TCS-P24/CA scaffold was prepared as previously described. TCS/CA scaffolds loaded with P24 were placed in Eppendorf tube. After that, 3 mL PBS was added to the Eppendorf tube. All samples were continuous shaking at 60 rpm and incubated under 37°C. During the designed time interval, the amount of 0.5 mL release medium was tested and replaced by the PBS. The concentration of P24 is determined by the BCA detection kit (Nanjing Jiancheng, China) according to the company's guidelines.

*2.5. Cell Preparation.* BMSCs were isolated as described elsewhere [27]. The primary BMSCs were cultured in DMEM-F12 with 10% fetal bovine serum in a mixed environment at 37°C and 5% CO2. Cell passage numbers P3 and P6 were identified and utilized for all experiments.

*2.6. Characterization of Scaffold and Observation of Cell Morphology.* The interior morphology of the TCS-P24/CA composite scaffolds was observed by scanning electron microscopy (SEM) as described [28]. And then, BMSCs were seeded onto TCS-P24/CA scaffolds and cultured in DMEM-F12 with 10% fetal bovine serum. After 5 days of coculture, samples were fixed with 0.25% glutaraldehyde solution for 24 h and immersed in OsO4 for 1 h and then rinsed 5 times in 1x PBS. The samples were dehydrated with increasing concentrations of acetone (30–100%). Therefore, the samples were fixed on aluminum stubs and then observed under scanning electron microscopy (Hitachi S-3000 N, Japan).

*2.7. Cell Proliferation Assay.* BMSCs were seeded on TCS-P24/CA scaffolds. At present time points, the Cell Counting Kit-8 (CCK-8, Dojindo) was used to assess cell activity according to the user manual, and OD values were measured at 450 nm by a microplate reader.

*2.8. In Vitro Osteogenesis Study.* BMSCs were cultured for 1, 3, and 7 days. Alkaline phosphatase (ALP) activity of the BMSCs in the different groups was determined by the ALP assay kit (Nanjing Jiancheng, China) according to the user manual. The calcium mineral deposition formed by BMSCs was evaluated by alizarin red staining (AR-S). BMSCs were cultured in osteogenic induction medium for 21 days, cells were fixed in 4% paraformaldehyde, rinsed three times with PBS and treated with alizarin red (Beyotime) for 10 min, and washed with ultrapure water. Three randomly selected fields were analyzed by Image-J for calcium mineral deposition area under a microscope.

*2.9. Real-Time Polymerase Chain Reaction (PCR).* The total RNA was isolated by Trizol reagent, and the synthesized cDNA was used to perform PCR. Specific primers (Table 1) were used for PCR amplification to analyze the expression of type I collagen a1 (COL1a1), alkaline phosphatase (ALP), and runt-related transcription factor 2 (Runx2). Transcriptor cDNA Synth Kit and Fast Start Universal SYBR Green Master were used for PCR. All of the reactions were normalized to GAPDH.

*2.10. In Vivo Study.* All in vivo experiments were conducted according to the protocols approved by the Southern Medical University Institutional Animal Care and Use Committee. Twenty-four female SD rats (180-250 g) were used in this study, and rats were randomly assigned to the control group (no scaffold), TCS/CA group, TCS-5%P24/CA group, and TCS-10%P24/CA group. General anesthesia was induced by 1.0 ml 2% pentobarbital sodium. Under general anesthesia, a dental bur was used to create a circular calvarial bone defect of 5 mm. Then, the scaffolds were implanted into the calvarial bone defect, and the skin was closed. After 4 and 8 weeks, all calvarial samples were harvested and soaked in 4% paraformaldehyde.

*2.11. Micro-CT Analysis.* The harvested calvarial samples for weeks 4 and 8 were examined using an advanced micro-computed tomography instrument (Micro-CT, ZKKS-MC-Sharp-IV, Zhongke Kaisheng Bio, Inc.) with scanning parameters of a 0.5 mm aluminum filter, 200 mA, and 50 kV. Morphometric parameters such as the bone mineral density (BMD) were analyzed.

*2.12. Histological Examination.* After Micro-CT imaging, all calvarial samples were fixed and decalcified, and the specimens were dehydrated through an alcohol gradient and embedded in paraffin blocks. 5 $\mu$m thick serial slices was prepared and subsequently stained with hematoxylin and eosin (HE) and Masson's trichrome staining.

*2.13. Statistical Analysis.* All data are expressed as mean ± SD ; the student's $t$-test was used to examine whether the differences between groups were statistically significant. The probability level of significant difference is $p < 0.05$.

## 3. Results

*3.1. Characterization of Scaffold, Morphology, and Proliferation of BMSCs on Scaffold.* The inner structure and morphology of the scaffold were examined by Scanning Electron Microscope (SEM). As shown in Figure 1(a), the majority of the pores have a diameter from 90-120 $\mu$m. To evaluate whether the scaffolds affected cell growth, BMSCs were seeded onto TCS/CA, TCS-5%P24/CA, and TCS-10%P24/CA scaffolds. The SEM results indicated that most of the BMSCs showed a spindle morphology on TCS/CA, TCS-5%P24/CA, and TCS-10%P24/CA (Figure 1(b): B1, B2, and B3), which have been shown to promote the differentiation and maintain the multipotency efficiency of BMSCs. Cell viability and proliferation were measured by the CCK-8 assay (Figure 2(a)). CCK-8 results showed that the proliferation of BMSCs on TCS-P24/CA scaffolds (Figure 2(a)) was similar to control groups after 1, 3, 7, 10 days. These results demonstrated that the TCS-P24/CA scaffolds were noncytotoxic to BMSCs and might support a good proliferation pattern of BMSCs.

*3.2. Release Behaviors of the BMP2-Derived Peptide P24.* The cumulative release amounts of P24 from TCS-P24/CA scaffolds are shown in Figure 1(c). The TCS-P24/CA scaffolds could release P24 peptide continuously for 29 days. The cumulative release curve of P24 peptide showed that during the 29-day release cycle, the release rate of P24 peptide was faster in the first 7 days, then slowed down and the release curve tended to be stable. 80% of P24 was released from the TCS-P24/CA scaffold within 29 days. In summary, the TCS-P24/CA scaffold can release P24 peptide continuously and effectively.

*3.3. In Vitro Osteogenesis.* Osteogenic differentiation by BMSCs within the TCS-P24/CA scaffolds was evaluated by the ALP activity, the expression of osteogenic genes, and the level of calcium deposition. As shown in Figure 2(b), on

Table 1: Primer sequences of osteogenic markers.

| mRNA | Forward (5′-3′) | Reverse (5′-3′) |
|---|---|---|
| COL1a1 | GCAACAGTCGCTTCACCTACA | CAATGTCCAAGGGAGCCACAT |
| GAPDH | TGTGTCCGTCGTGGATCTGA | TTGCTGTTGAAGTCGCAGGAG |
| ALP | GGCTGGAGATGGACAAATTCC | CCGAGTGGTAGTCACAATGCC |
| Runx2 | CCAACCCACGAATGCACTATC | TAGTGAGTGGTGGCGGACATAC |

COL1a1: collagen type I alpha 1; GADPH: glyceraldehyde-3-phosphate dehydrogenase; ALP: alkaline phosphatase; Runx2: runt-related transcription factor 2.

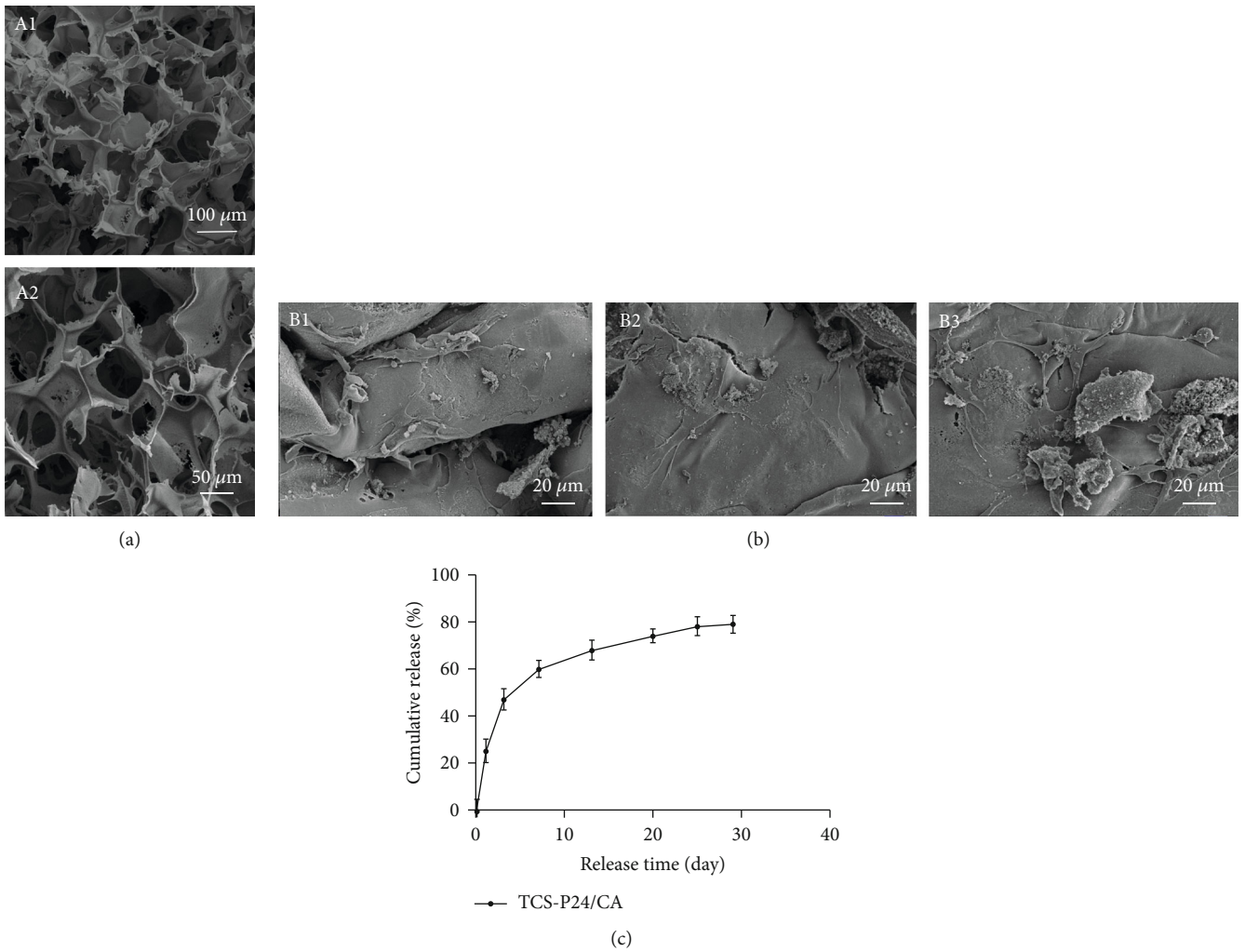


Figure 1: (a) SEM image of TCS-P24/CA scaffold (A1:100X; A2:200X). (b) SEM view of BMSCs cultured on (B1) TCS/CA, (B2) TCS-5%P24/CA, and (B3) TCS-10%P24/CA scaffolds at a magnification of 5000X. (c) Cumulative in vitro release curves of the TCS-P24/CA scaffold. Error bars represent mean ± SD ($n = 3$).

day 3, the ALP activity of BMSCs in the TCS-5%P24/CA and TCS-10%P24/CA groups was significantly higher than control and TCS/CA groups ($p < 0.01$). On day 7, the ALP activity of BMSCs of TCS-10%P24/CA group was significantly higher than other groups ($p < 0.05$). The level of calcium nodule deposition after 21 days in culture was investigated by alizarin red staining. The results revealed that the control group showed almost no positive staining; TCS/CA and TCS-5%P24/CA groups showed positive staining, while TCS-10%P24/CA group presented the most significantly positive staining ($p < 0.05$ Figure 2(c)). Moreover, as shown in Figure 2(d), PCR showed that ALP, Runx2, and COL1a1 gene expression increased in the TCS-10%P24/CA group compared to the other groups ($p < 0.05$).

*3.4. TCS-P24/CA Scaffolds Promote Bone Regeneration.* We next investigated the effect of TCS-P24/CA scaffold on rat calvarial defect repair at 4 and 8 weeks after operation. The Micro-CT results revealed that there was no bone repair in the control group (Figure 3(a)), whereas the TCS/CA and TCS-5%P24/CA groups demonstrated a small amount of new bone formation into the defect. Additionally, bone

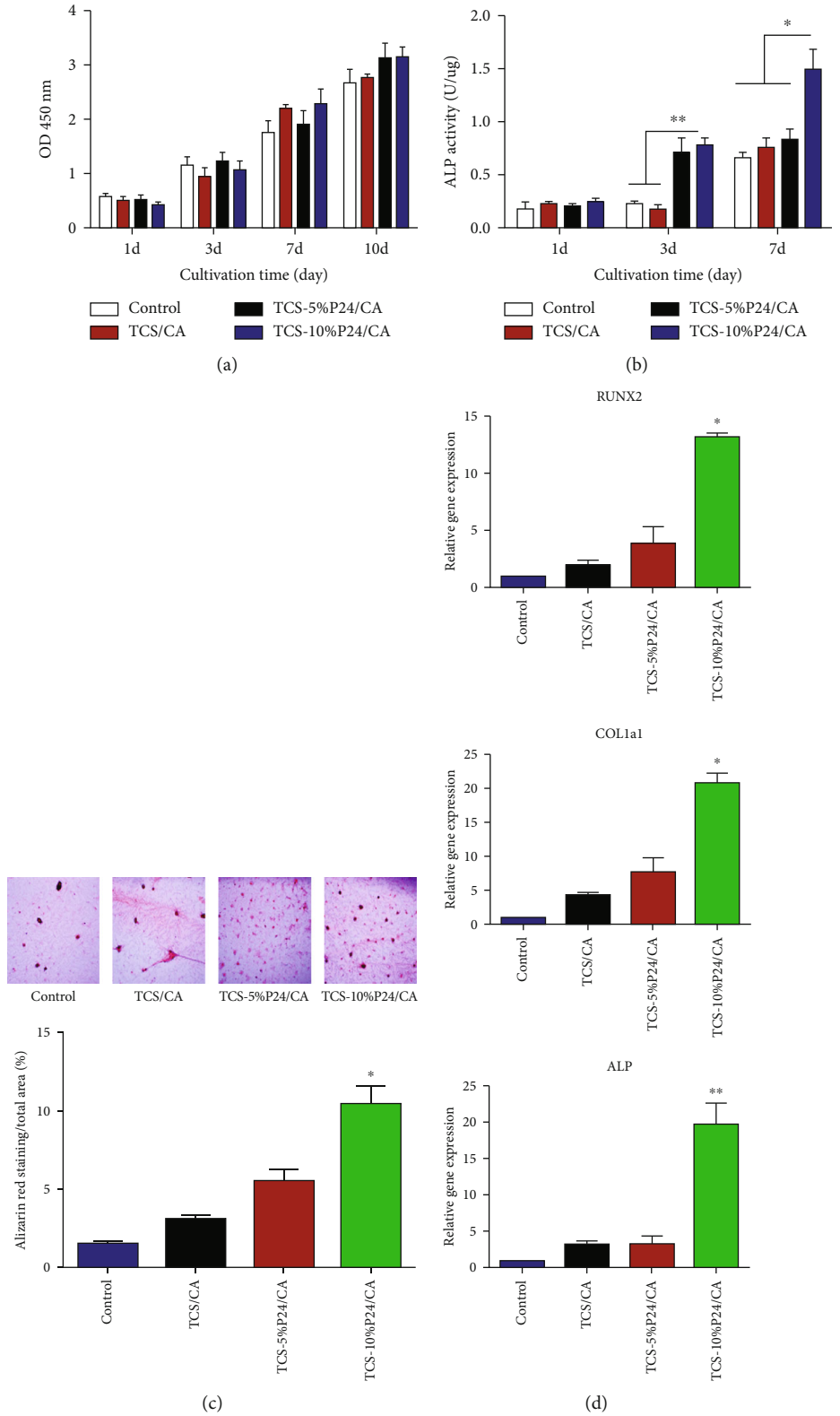


Figure 2: (a) CCK-8 test of BMSCs viability after coculture with TCS/CA, TCS-5%P24/CA, and TCS-10%P24/CA scaffolds at days 1, 3, 7, and 10. (b) The relative ALP activity of BMSCs cultured in a scaffold-stimulated medium. (c) Alizarin red S staining of BMSCs cultured with TCS/CA, TCS-5%P24/CA, and TCS-10%P24/CA scaffolds for 21 days. (d) The level of the mRNA for osteogenic-specific genes (Runx2 and ALP) and related matrix genes (COL1a1) of rat BMSCs cultured on TCS-P24/CA scaffolds for 7 days. Levels, quantified using real-time RT-PCR, are normalized to the reference gene GAPDH. ($^{*}p < 0.05$; $^{**}p < 0.01$); Error bars represent mean ± SD ($n = 3$).

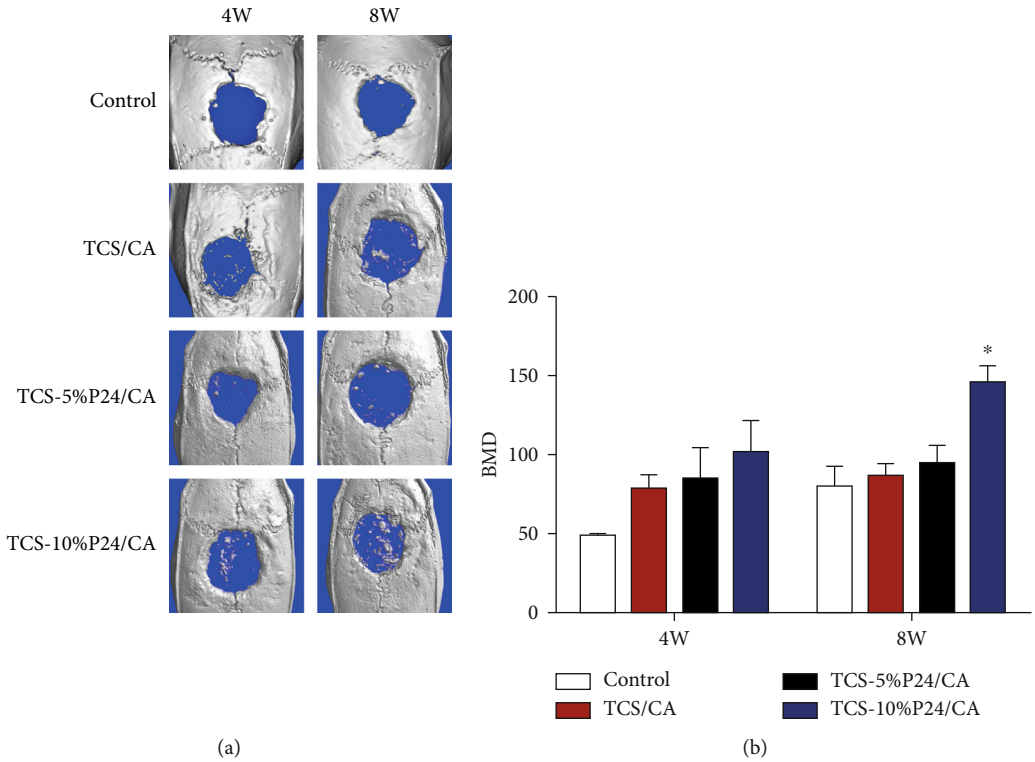


Figure 3: Evaluation of calvarial bone defect repair in vivo. (a) Micro-CT analysis of skulls 4 and 8 weeks post-surgery. (b) Quantitative analysis of BMD 4 and 8 weeks postsurgery. $^{*}p < 0.05$.

formation was significantly increased in the TCS-10%P24/CA group compared to other groups at 8 weeks. After 8 weeks, according to Micro-CT analysis, the BMD was significantly higher in the TCS-10%P24/CA group.

We performed HE and Masson staining to further verify the repair effect after 4 and 8 weeks (Figure 4). At 4 weeks, although there was no new bone formation in the control group, which had fibrous tissue formation, a small amount of new bone formation was found in the TCS/CA, TCS-5%P24/CA, and TCS-10%P24/CA groups. 8 weeks after implantation, different from the lack of obvious bone formation in the defect area of the control, TCS/CA, and TCS-5%P24/CA groups, the repaired area of TCS-10%P24/CA group had stronger osteogenic ability, and more osteoblasts were observed around the new bone, and vascularization could be seen at the edge of the bone defect. In summary, our results demonstrated that TCS-10%P24/CA significantly enhances bone regeneration in vivo.

## 4. Discussion

Excellent bone tissue engineering scaffold should not only support cell attachment, cell proliferation, and migration but also could to carry and release osteogenic induction molecules [29, 30]. In the present study, the TCS-P24/CA scaffold was used to accomplish the controlled delivery of P24 peptide to enhance osteogenesis. Our findings demonstrated the safety and efficiency of the TCS-P24/CA scaffold in bone regeneration and affirmed the potential application value of this material in bone regeneration.

The efficiency of BMP-2 depends on the form of delivery. It has been proved that long-term delivery of BMP-2 is more effective in promoting bone formation in a certain dose range [31]. At present, one of the pivotal issues of BMP-2 is to select a suitable drug delivery system to ensure its controlled release and maintain biological activity. In many cases, the BMP-2 deposited in the material is released with an early eruption. Therefore, a more reliable carrier for sequential delivery of growth factors to the target has received widespread attention. As a carrier for localization and delivery of BMP-2, the system includes polylactic-glycolic acid, absorbable collagen [32]. Chitosan is also a well-tested vehicle. The effectiveness of thiolated chitosan as a drug controlled release scaffold has been confirmed by drugs such as insulin [33]. However, most studies have focused on systematic drug delivery [28]. At the same time, although thiolated chitosan has many advantages in tissue engineering, however, the structure of the pure thiolated chitosan scaffold has the drawback of quick degradation and weak mechanical properties. Therefore, thiolated chitosan scaffolds may be compounded with inorganic minerals to improve the mechanical properties. At present, there are many kinds of bone scaffold materials in tissue engineering technology. Calcium carbonate used in this experiment is a kind of artificial bone, which also includes nanohydroxyapatite, tricalcium phosphate, calcium sulfate, and calcium phosphate cement [34]. As a bone substitute material, nanohydroxyapatite has been used in the clinic for a long time and shows good biocompatibility, bioactivity, and bone conductivity, but it has low bending strength, high brittleness, easy to fracture, and difficult to

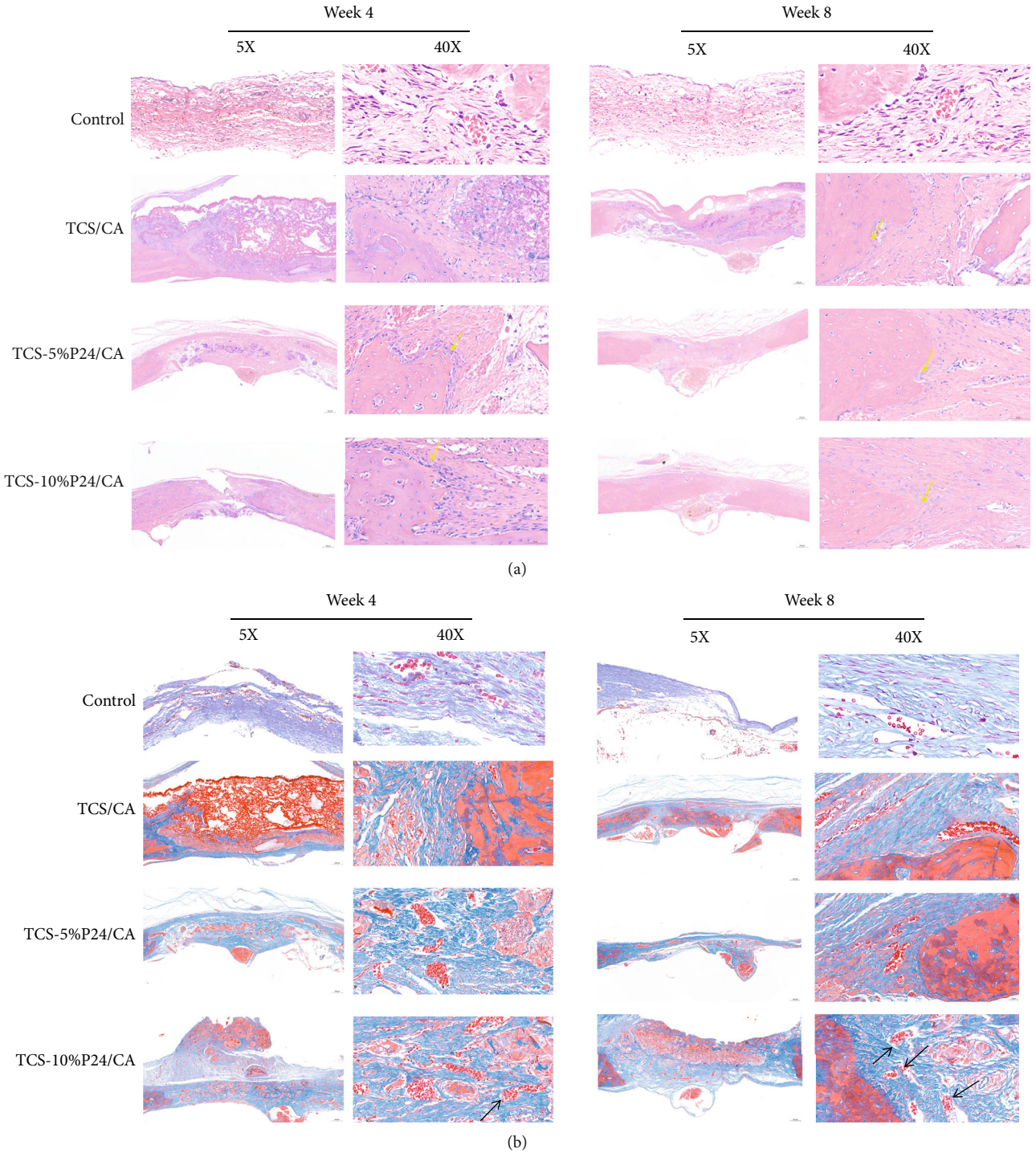


Figure 4: Histology of the cranial specimens at 4 and 8 weeks after implantation in vivo. (a) Hematoxylin and eosin staining of harvested tissues in Control, TCS/CA, TCS-5%P24/CA, and TCS-10%P24/CA groups. Yellow arrow represents new bone. (b) Masson's trichrome staining of harvested tissues in Control, TCS/CA, TCS-5%P24/CA, and TCS-10%P24/CA groups. Black arrow represents new vessel.

shape [28]. Tricalcium phosphate is similar to bone in chemical composition and crystal structure [35]. Due to its fine particle size and micropore structure, tricalcium phosphate has good bone conductivity and biodegradability. However, its application is limited by its brittleness, intolerance to pressure, and easy decomposition. Calcium sulfate is one of the earliest bone substitute materials; as a bone conduction material, it can be completely absorbed with the formation of bone tissue and bone structure remodeling, but it often reduces its mechanical strength because it is absorbed too fast, which is not conducive to the repair of bone defects at the weight-bearing site [36]. Calcium phosphate cement is a kind of injectable biological bone substitute material, which has attracted many scholars in recent years because of its good

biocompatibility and easy shaping. However, the material must be closely attached to the bone bed when filling the defect, and even so, its bone conductivity is still limited, which limits its clinical application [37].

Calcium carbonate is the main component of coral and widely used in the repair of bone defects in the clinic [22]. Calcium carbonate is bioabsorbable and has excellent biocompatibility and osteoconductivity. However, coral bone transplantation is confronting limitations, such as changes in physical marine, ecological environment, and chemical properties [38]. Synthetic calcium carbonate-based biomaterials are considered to be effective materials to replace corals to repair bone defects. The addition of carboxymethyl chitosan makes calcium carbonate hybrid microspheres have good biocompatibility, osteoconductivity, and biodegradability. The addition of carboxymethyl chitosan makes calcium carbonate hybrid microspheres have more excellent biocompatibility and biodegradability. Meanwhile, the potential application of this novel thiolated chitosan/calcium carbonate composite microsphere scaffold in bone tissue has not been studied.

Bone tissue engineering scaffolds usually require extremely porous and interconnected pore structures. More extensive pore size and porosity usually indicate a large surface area ratio, which is favorable toward cell adhesion to the scaffold and improves bone tissue reconstruction [39, 40]. A previous study has shown that the growth quality of bones in porous systems depends on their pore size [41, 42]. The optimal pore size for mineralized bone growth is still a controversial topic. The previous study has shown that the pore size of regenerated mineralized bone should be greater than 100 $\mu$m [43]. A study [19] revealed pores greater than 20-100 $\mu$m were beneficial to cell infiltration, and the neovascularization was improved significantly after exceeding 100 $\mu$m. The porous structure of our scaffold was obtained by a freeze-drying technique. The results of SEM demonstrated that the majority of the pores have a diameter from 90-120 $\mu$m. Our studies further revealed that TCS-P24/CA scaffolds can effectively promote cell proliferation and bone growth, indicating that TCS-P24/CA scaffolds with a pore diameter of 90-120 $\mu$m are suitable for bone growth.

In addition to the favorable controlled delivery performance of the TCS-P24/CA scaffolds, its biological effects are also desirable. It is well justified for their osteoconductivity and osteoinductivity of P24 peptides, P24 peptides play a significant role in osteogenic differentiation [44], they are indispensable in different stages of bone healing. A study [45] has revealed that adenovirus-mediated BMP therapy can cause harmful side effects, such as immunogenicity and tumorigenesis. However, biomaterials as carriers, which can provide controllable and continuous transmission of growth factors at the defect site and simulate its time distribution during bone healing in vivo [46]. The results showed that the TCS-P24/CA group maintains the prolonged release of P24 continued for 29 days, suggesting that the release velocity from the TCS-P24/CA scaffold manifests a sustained release of P24 and leads to osteogenic differentiation of the BMSCs and promoting bone regeneration.

The biological properties of the TCS-P24/CA scaffolds in vitro were investigated. CCK-8 analysis showed that the number of BMSCs in the TCS-P24/CA composite scaffolds group was similar to that in the control group, indicating that the composite stent provided a suitable microenvironment for cell proliferation. Furthermore, the important markers to assess the differentiation of osteoblasts are the activity of ALP and the level of calcium deposition and the expression of osteogenic genes. These results showed that ALP activity of TCS-10%P24/CA group significantly increased on day 7 compared to the other groups. Similarly, the level of calcium mineral deposition increased as well in the TCS-10%P24/CA group after 3 weeks. Furthermore, PCR results showed that Runx2, Alp, and COL1a1 mRNA expression increased significantly in the TCS-10%P24/CA group. These results indicate that P24, when delivered in TCS-P24/CA scaffolds, still retains its biological ability. TCS-P24/CA scaffolds provide an effective approach to P24 delivery and have stimulatory effects on the matrix mineralization and differentiation of osteoblastic cells.

In vivo osteoinductive studies, to further evaluate the ability of TCS-P24/CA scaffolds and promote bone formation. We created calvarial bone defects in SD rats. These results demonstrated that BMD in the TCS-10%P24/CA group was much higher than in the other groups and exhibited robust osteogenic activity. Histological analysis was similar to the BMD result (Figure 4). These data revealed that TCS-10%P24/CA scaffolds enhanced the repair and mineralization of defects compared to other groups, indicating TCS-P24/CA that scaffolds are osteoconductive, while TCS-10%P24/CA scaffold can provide an even more effective approach to the repair of a critical-sized bone defect. These results may be due to the role of TCS-P24/CA in promoting osteogenic differentiation in BMSCs and supporting BMSC adhesion and proliferation. These data confirmed the effectiveness and feasibility of developing functional TCS-P24/CA scaffolds as a biological factor delivery platform for bone repair.

There are still some limitations in this experiment, such as the failure to establish more concentration gradients to explore the most appropriate concentration of P24 polypeptide to promote osteogenesis and further explore the signal transduction mechanism of materials in the process of osteogenesis. Thus, further experiments are needed to improve.

## 5. Conclusions

In this study, a novel thiolated chitosan-P24/calcium carbonate composite microspheres scaffold (TCS-P24/CA), synthesized by the in-situ coprecipitation and the freeze-drying methods, can steadily release P24 for 29 days. In vitro investigation regarding SEM showed that the majority of the pores have a diameter from 90-120 $\mu$m. Moreover, it was demonstrated to promote BMSCs adhesion, viability, and proliferation. Additionally, TCS-P24/CA induced osteogenic differentiation of BMSCs in vitro. Finally, the promoting effect of TCS-10%P24/CA scaffold on bone regeneration was significantly higher than that of other groups in vivo. The novel TCS-P24/CA scaffold is expected to become a

novel bone substitute material with clinical application prospects.

## Data Availability

The data used to support the findings of this study are included within the article.

## Conflicts of Interest

The authors declare that they have no conflicts of interest.

## Authors' Contributions

Zhaozhen Wang, Xujie Liu, and Vidmi Taolam Martin contributed equally to this work.

## Acknowledgments

Financial support from the Basic Research on Scientific creation Committee of Shenzhen City, China (JCYJ20160 531195524566) is gratefully acknowledged.

## References

[1] L. Li, G. Zhou, Y. Wang, G. Yang, S. Ding, and S. Zhou, "Controlled dual delivery of BMP-2 and dexamethasone by nanoparticle-embedded electrospun nanofibers for the efficient repair of critical-sized rat calvarial defect," *Biomaterials*, vol. 37, pp. 218–229, 2015.

[2] Y. Li, Z. Zhang, and Z. Zhang, "Porous chitosan/nano-hydroxyapatite composite scaffolds incorporating simvastatin-loaded PLGA microspheres for bone repair," *Cells, Tissues, Organs*, vol. 205, no. 1, pp. 20–31, 2018.

[3] Y. Chen, X. Liu, R. Liu et al., "Zero-order controlled release of BMP2-derived peptide P24 from the chitosan scaffold by chemical grafting modification technique for promotion of osteogenesisinvitro and enhancement of bone repairin vivo," *Theranostics*, vol. 7, no. 5, pp. 1072–1087, 2017.

[4] L. Ning, H. Malmström, and Y. F. Ren, "Porous collagen-hydroxyapatite scaffolds with mesenchymal stem cells for bone regeneration," *The Journal of Oral Implantology*, vol. 41, no. 1, pp. 45–49, 2015.

[5] R. Hou, F. Chen, Y. Yang et al., "Comparative study between coral-mesenchymal stem cells-rhBMP-2 composite and auto-bone-graft in rabbit critical-sized cranial defect model," *Journal of Biomedical Materials Research Part A*, vol. 80, no. 1, pp. 85–93, 2007.

[6] Y. Gong, S. Li, W. Zeng, J. Yu, Y. Chen, and B. Yu, "Controlled *In vivo* bone formation and vascularization using ultrasound-triggered release of recombinant vascular endothelial growth factor from Poly(D,L-lactic-co-glycolicacid) microbubbles," *Frontiers in Pharmacology*, vol. 10, p. 413, 2019.

[7] X. Liu, Q. Feng, A. Bachhuka, and K. Vasilev, "Surface modification by allylamine plasma polymerization promotes osteogenic differentiation of human adipose-derived stem cells," *ACS Applied Materials & Interfaces*, vol. 6, no. 12, pp. 9733–9741, 2014.

[8] I. H. Bae, B. C. Jeong, M. S. Kook, S. H. Kim, and J. T. Koh, "Evaluation of a thiolated chitosan scaffold for local delivery of BMP-2 for osteogenic differentiation and ectopic bone formation," *BioMed Research International*, vol. 2013, Article ID 878930, 10 pages, 2013.

[9] S. D. Nath, C. Abueva, B. Kim, and B. T. Lee, "Chitosan-hyaluronic acid polyelectrolyte complex scaffold crosslinked with genipin for immobilization and controlled release of BMP-2," *Carbohydrate Polymers*, vol. 115, pp. 160–169, 2015.

[10] S. E. Kim, Y. P. Yun, Y. K. Han et al., "Osteogenesis induction of periodontal ligament cells onto bone morphogenic protein-2 immobilized PCL fibers," *Carbohydrate Polymers*, vol. 99, pp. 700–709, 2014.

[11] M. Raida, A. C. Heymann, C. Günther, and D. Niederwieser, "Role of bone morphogenetic protein 2 in the crosstalk between endothelial progenitor cells and mesenchymal stem cells," *International Journal of Molecular Medicine*, vol. 18, no. 4, pp. 735–739, 2006.

[12] H. Kaneko, T. Arakawa, H. Mano et al., "Direct stimulation of osteoclastic bone resorption by bone morphogenetic protein (BMP)-2 and expression of BMP receptors in mature osteoclasts," *Bone*, vol. 27, no. 4, pp. 479–486, 2000.

[13] A. Saito, Y. Suzuki, S. I. Ogata, C. Ohtsuki, and M. Tanihara, "Activation of osteo-progenitor cells by a novel synthetic peptide derived from the bone morphogenetic protein-2 knuckle epitope," *Biochim Biophys Acta*, vol. 1651, no. 1-2, pp. 60–67, 2003.

[14] B. Wu, Q. Zheng, X. Guo, Y. Wu, Y. Wang, and F. Cui, "Preparation and ectopic osteogenesis in vivo of scaffold based on mineralized recombinant human-like collagen loaded with synthetic BMP-2-derived peptide," *Biomedical Materials (Bristol, England)*, vol. 3, no. 4, article 044111, 2008.

[15] Y. Boukari, O. Qutachi, D. J. Scurr, A. P. Morris, S. W. Doughty, and N. Billa, "A dual-application poly (dl-lactic-co-glycolic) acid (PLGA)-chitosan composite scaffold for potential use in bone tissue engineering," *Journal of Biomaterials Science Polymer Edition*, vol. 28, no. 16, pp. 1966–1983, 2017.

[16] K. Kafedjiiski, A. H. Krauland, M. H. Hoffer, and A. Bernkop-Schnürch, "Synthesis and in vitro evaluation of a novel thiolated chitosan," *Biomaterials*, vol. 26, no. 7, pp. 819–826, 2005.

[17] A. Matsuda, H. Kobayashi, S. Itoh, K. Kataoka, and J. Tanaka, "Immobilization of laminin peptide in molecularly aligned chitosan by covalent bonding," *Biomaterials*, vol. 26, no. 15, pp. 2273–2279, 2005.

[18] X. Liu, B. Yu, Q. Huang et al., "*In vitro* BMP-2 peptide release from thiolated chitosan based hydrogel," *International Journal of Biological Macromolecules*, vol. 93, Part A, pp. 314–321, 2016.

[19] X. He, Y. Liu, X. Yuan, and L. Lu, "Enhanced healing of rat calvarial defects with MSCs loaded on BMP-2 releasing chitosan/alginate/hydroxyapatite scaffolds," *PLoS One*, vol. 9, no. 8, article e104061, 2014.

[20] H. D. Yu, Z. Y. Zhang, K. Y. Win, J. Chan, S. H. Teoh, and M. Y. Han, "Bioinspired fabrication of 3D hierarchical porous nanomicrostructures of calcium carbonate for bone regeneration," *Chemical Communications (Cambridge, England)*, vol. 46, no. 35, pp. 6578–6580, 2010.

[21] H.-C. Ge and D.-K. Luo, "Preparation of carboxymethyl chitosan in aqueous solution under microwave irradiation," *Carbohydrate Research*, vol. 340, no. 7, pp. 1351–1356, 2005.

[22] F. He, J. Zhang, X. Tian, S. Wu, and X. Chen, "A facile magnesium-containing calcium carbonate biomaterial as

potential bone graft," *Colloids and Surfaces B: Biointerfaces*, vol. 136, pp. 845–852, 2015.

[23] J. Wang, J. S. Chen, J. Y. Zong et al., "Calcium carbonate/carboxymethyl chitosan hybrid microspheres and nanospheres for drug delivery," *The Journal of Physical Chemistry C*, vol. 114, no. 44, pp. 18940–18945, 2010.

[24] F. He, J. Zhang, F. Yang, J. Zhu, X. Tian, and X. Chen, "In vitro degradation and cell response of calcium carbonate composite ceramic in comparison with other synthetic bone substitute materials," *Materials Science & Engineering C: Materials for Biological Applications*, vol. 50, pp. 257–265, 2015.

[25] X. Liu, T. A. Elkhooly, Q. Huang et al., "A facile way to prepare mesoporous spherical calcites controlled by chondroitin sulfate for shape and carboxymethyl chitosan for size," *CrystEngComm*, vol. 18, no. 44, pp. 8582–8586, 2016.

[26] X. Liu, Y. Chen, Q. Huang, W. He, Q. Feng, and B. Yu, "A novel thermo-sensitive hydrogel based on thiolated chitosan/-hydroxyapatite/beta-glycerophosphate," *Carbohydrate Polymers*, vol. 110, pp. 62–69, 2014.

[27] B. Yu, Y. Zhang, X. Li et al., "The use of injectable chitosan/-nanohydroxyapatite/collagen composites with bone marrow mesenchymal stem cells to promote ectopic bone formation in vivo," *Journal of Nanomaterials*, vol. 2013, Article ID 506593, 8 pages, 2013.

[28] Y. Chen, X. Liu, R. Liu et al., "Zero-order controlled release of BMP2-derived peptide P24 from the chitosan scaffold by chemical grafting modification technique for promotion of osteogenesis *in vitro* and enhancement of bone repair *in vivo*," *Theranostics*, vol. 7, no. 5, pp. 1072–1087, 2017.

[29] T. Garg, O. Singh, S. Arora, and R. S. R. Murthy, "Scaffold: a novel carrier for cell and drug delivery," *Critical Reviews in Therapeutic Drug Carrier Systems*, vol. 29, no. 1, pp. 1–63, 2012.

[30] X. Li, J. Wei, K. E. Aifantis et al., "Current investigations into magnetic nanoparticles for biomedical applications," *Journal of Biomedical Materials Research Part A*, vol. 104, no. 5, pp. 1285–1296, 2016.

[31] W.-G. La, S.-W. Kang, H. S. Yang et al., "The efficacy of bone morphogenetic protein-2 depends on its mode of delivery," *Artificial Organs*, vol. 34, no. 12, pp. 1150–1153, 2010.

[32] K. J. Rambhia and P. X. Ma, "Controlled drug release for tissue engineering," *Journal of Controlled Release: Official Journal of the Controlled Release Society*, vol. 219, pp. 119–128, 2015.

[33] L. Yin, J. Ding, C. He, L. Cui, C. Tang, and C. Yin, "Drug permeability and mucoadhesion properties of thiolated trimethyl chitosan nanoparticles in oral insulin delivery," *Biomaterials*, vol. 30, no. 29, pp. 5691–5700, 2009.

[34] S. K. Nandi, S. Roy, P. Mukherjee, B. Kundu, D. K. de, and D. Basu, "Orthopaedic applications of bone graft & graft substitutes: a review," *The Indian Journal of Medical Research*, vol. 132, pp. 15–30, 2010.

[35] S. K. Ghosh, S. K. Nandi, B. Kundu et al., "In vivo response of porous hydroxyapatite and $\beta$-tricalcium phosphate prepared by aqueous solution combustion method and comparison with bioglass scaffolds," *Journal of Biomedical Materials Research Part B: Applied Biomaterials*, vol. 86B, no. 1, pp. 217–227, 2008.

[36] K. A. Hing, L. F. Wilson, and T. Buckland, "Comparative performance of three ceramic bone graft substitutes," *The Spine Journal*, vol. 7, no. 4, pp. 475–490, 2007.

[37] C. Knabe, G. Berger, R. Gildenhaar et al., "Effect of rapidly resorbable calcium phosphates and a calcium phosphate bone cement on the expression of bone-related genes and proteinsin vitro," *Journal of Biomedical Materials Research*, vol. 69A, no. 1, pp. 145–154, 2004.

[38] S. A. Clarke, P. Walsh, C. A. Maggs, and F. Buchanan, "Designs from the deep: marine organisms for bone tissue engineering," *Biotechnology Advances*, vol. 29, no. 6, pp. 610–617, 2011.

[39] A. Cipitria, C. Lange, H. Schell et al., "Porous scaffold architecture guides tissue formation," *Journal of Bone and Mineral Research: The Official Journal of the American Society for Bone and Mineral Research*, vol. 27, no. 6, pp. 1275–1288, 2012.

[40] K. Zhang, Y. Fan, N. Dunne, and X. Li, "Effect of microporosity on scaffolds for bone tissue engineering," *Regenerative Biomaterials*, vol. 5, no. 2, pp. 115–124, 2018.

[41] A. I. Itälä, H. O. Ylänen, C. Ekholm, K. H. Karlsson, and H. T. Aro, "Pore diameter of more than 100 microm is not requisite for bone ingrowth in rabbits," *Journal of Biomedical Materials Research*, vol. 58, no. 6, pp. 679–683, 2001.

[42] A. Aarvold, J. O. Smith, E. R. Tayton et al., "The effect of porosity of a biphasic ceramic scaffold on human skeletal stem cell growth and differentiation in vivo," *Journal of Biomedical Materials Research Part A*, vol. 101, no. 12, pp. 3431–3437, 2013.

[43] S. F. Hulbert, F. A. Young, R. S. Mathews, J. J. Klawitter, C. D. Talbert, and F. H. Stelling, "Potential of ceramic materials as permanently implantable skeletal prostheses," *Journal of Biomedical Materials Research*, vol. 4, no. 3, pp. 433–456, 1970.

[44] H. Liu, H. Peng, Y. Wu et al., "The promotion of bone regeneration by nanofibrous hydroxyapatite/chitosan scaffolds by effects on integrin-BMP/Smad signaling pathway in BMSCs," *Biomaterials*, vol. 34, no. 18, pp. 4404–4417, 2013.

[45] Y. Liu, S. Zhang, G. Ma, F. Zhang, and R. Hu, "Efficacy and safety of a live canine adenovirus-vectored rabies virus vaccine in swine," *Vaccine*, vol. 26, no. 42, pp. 5368–5372, 2008.

[46] M. Yamamoto, Y. Takahashi, and Y. Tabata, "Controlled release by biodegradable hydrogels enhances the ectopic bone formation of bone morphogenetic protein," *Biomaterials*, vol. 24, no. 24, pp. 4375–4383, 2003.

Hindawi
Journal of Nanomaterials
Volume 2020, Article ID 6014816, 12 pages
https://doi.org/10.1155/2020/6014816

*Research Article*

# Enhanced Crystallinity and Antibacterial of PHBV Scaffolds Incorporated with Zinc Oxide

**Cijun Shuai**,[1,2,3] **Chen Wang**,[1] **Fangwei Qi**,[1] **Shuping Peng**,[4,5] **Wenjing Yang**,[1] **Chongxian He**,[1] **Guoyong Wang**,[1] **and Guowen Qian**[1]

[1]*Institute of Bioadditive Manufacturing, Jiangxi University of Science and Technology, Nanchang 330013, China*
[2]*State Key Laboratory of High Performance Complex Manufacturing, Central South University, Changsha 410083, China*
[3]*Shenzhen Institute of Information Technology, Shenzhen 518172, China*
[4]*NHC Key Laboratory of Carcinogenesis, School of basic Medical Science, Central South University, Changsha, Hunan 410013, China*
[5]*School of Energy and Machinery Engineering, Jiangxi University of Science and Technology, Nanchang 330013, China*

Correspondence should be addressed to Fangwei Qi; qfw@jxust.edu.cn and Shuping Peng; shuping@csu.edu.cn

Received 29 May 2020; Accepted 29 June 2020; Published 8 July 2020

Academic Editor: Xiaoming Li



Poly(3-hydroxybutyrate-co-3-hydroxyvalerate) (PHBV) has a great potential in bone repair, but unfortunately, the poor mechanical properties limit its further application. In this work, zinc oxide (ZnO) nanoparticles were incorporated into PHBV porous scaffold fabricated by selective laser sintering technique. It was because ZnO nanoparticles could provide nucleating sites for the orderly stacking of polymer chains, thereby enhancing the crystallinity of PHBV. It was well known that the mechanical properties of PHBV scaffold could be enhanced with the increase of crystallinity. More significantly, the released $Zn^{2+}$ would combine negatively charged cell membranes of bacterial through electrostatic interaction and consequently destructed the protein structure and resulted in the death of bacterial, which was highly desired in reducing the risk of implant infection. Results indicated that the relative crystallinity of scaffold with 3 wt.% ZnO increased remarkably from 38% to 64% compared to pure PHBV scaffold, which effectively enhanced the compression strength and modulus by 56% and 51.5%, respectively. Moreover, the scaffold had a favorable antibacterial activity. Cell culture experiments proved that the scaffold could promote the cell behaviors. The positive results demonstrated the scaffold may serve as a potential replacement in bone repair.

## 1. Introduction

The large bone defects resulted from trauma, infection, and tumor are commonly difficult to heal by their own ability, which seriously affects the patients' living quality and health level [1]. Artificial bone scaffolds, which enable to provide a mechanical and physiological support to cells for *in vitro* tissue regeneration and/or *in vivo* implantation, are considered to be a promising alternative in the treatment of large bone defects [2, 3]. Among various biomaterials, poly(3-hydroxybutyrate-co-3-hydroxyvalerate) (PHBV) has received considerable attention because of its favorable biocompatibility and biodegradability. It can degrade *in vivo* to hydroxybutyric, which is a normal component of human blood [4]. However, insufficient mechanical performance has limited its further application in bone repair.

It is well established that the mechanical property of PHBV is positively related to its crystallinity [5]. Introducing nanofillers is considered to be an effective countermeasure to improve the crystallinity [6]. For example, Jun et al. [7] have found that the crystallinity of PHBV was greatly improved with the incorporation of carbon nanotubes. Kouhi et al. [8] fabricated PHBV/hydroxyapatite/bredigite scaffolds and found that the incorporation of nanoparticles increased the crystallinity of PHBV matrix and subsequently enhanced the Young's modulus and ultimate strength. Zhang et al. [9] prepared PHBV/cellulose nanocrystals/silver nanocomposites by using solution casting. It was found that the composites showed higher

crystallinity and smaller average crystallite size compared to PHBV. Meanwhile, the tensile strength and modulus of the composites were greatly increased by 97.6% and 231%, respectively.

Among various nanofillers, zinc oxide (ZnO) nanoparticles possess good biocompatibility, which has been approved as a biomedical material by Food and Drug Administration (FDA) [10]. More interestingly, ZnO has a favorable antibacterial ability against a wide a range of bacteria. It can release zinc ions ($Zn^{2+}$) to combine with the negatively charged cell membranes of bacterial through electrostatic interaction and consequently destructed the protein structure and resulted in the death of bacterial, which was highly desired in reducing the risk of implant infection [11]. Furthermore, it can also generate reactive oxygen species (ROS) under the irradiation of ultraviolet light to damage the cell membranes of bacterial [12, 13]. Moreover, Zn is an important trace element in the human body and participates in various metabolic processes [14]. It has been reported that an appropriate amount of Zn can promote bone formation while inhibiting bone resorption.

Although different fabrication methods including solvent casting, particle-leaching, and foam replication have been developed to manufacture bone scaffolds with desirable properties, these techniques have great difficulty in fabricating bone scaffolds with controllable porous structure and personalized shape [15]. It is well established that the porous structure of the scaffold is conducive to the growth of cells, the transmission of nutrients, and the discharge of metabolites, whereas the personalized shape design can meet the requirements of various patients [16, 17]. As an emerging additive manufacturing technique, selective laser sintering (SLS) can precisely construct bone scaffold with complicated structure and customized shape from 3D digital data by sequentially fusing region in a powder bed, layer-by-layer, *via* a computer-controlled scanning laser beam. More particularly, any powdered biomaterial that will fuse but not decompose under the irradiation of laser beam can be used to fabricate scaffold [18].

In this work, PHBV/ZnO scaffolds were manufactured by selective laser sintering. The crystallization behaviors, mechanical performances, and antibacterial activities were systematically investigated. The relationship between the crystallization behavior and mechanical properties was discussed in depth. Moreover, *in vitro* cell behaviors were also explored. This work attempts to provide an effective countermeasure to simultaneously improve the mechanical property and antibacterial activity of PHBV scaffold and also supplies a strategy to overcome challenges in rapidly fabricating scaffolds with controllable pore structure.

## 2. Experiment

*2.1. Materials.* PHBV powders (molecular weight: 280 kDa, density: 1.25 g/cm$^3$) were provided by TianAn Biological Materials Co., Ltd. (Ningbo, China). ZnO nanoparticles with average size of 50 nm and specific surface area of 15-25 m$^2$/g were supplied by Aladdin Reagent Co., Ltd. (Shanghai, China).

*2.2. Preparation of PHBV/ZnO Scaffold.* The fabrication process of three-dimensional porous PHBV/ZnO composite scaffolds is illustrated in Figure 1. In detail, a certain amount of PHBV and ZnO powders was weighted according to the designed mass ratio and then poured into a beaker containing ethanol solution. Subsequently, the mixed suspensions were subjected to mechanical agitation and ultrasonic dispersion simultaneously for 2 h. Afterwards, the well-mixed suspensions were filtered and dried in the vacuum drying oven. Ultimately, the mixed powders could be obtained by using ball milling.

The scaffolds were manufactured by a laser 3D molding system with independent intellectual property rights. It mainly consisted of a continuous wave $CO_2$ laser with the wavelength of 10.6 $\mu$m. The whole processing parameters in this study were set as follows: laser power 5 W, scanning speed 100 mm/s, and scanning space 0.15 mm. The three-dimensional porous scaffolds could be obtained through layer-by-layer construction. For the convenience of description, PHBV scaffold with various ZnO contents of 1, 3, and 5 wt.%, which were named as PHBV/1nZnO, PHBV/3nZnO, and PHBV/5nZnO, respectively.

*2.3. Microstructure and Mechanical Property.* The morphologies of the samples were characterized by scanning electron microscopy (SEM, Zeiss, Germany). The functional groups of the scaffolds were analyzed by the Fourier transform infrared spectroscopy (FTIR, Tianjin Gang Dong Technology Co. Ltd., China). The phase structures of the scaffolds were measured by utilizing X-ray diffractometer (XRD, Karlsruhe, Germany). The melting and crystallization performance of the scaffolds under a constant heating and cooling rate of 10°C/min was measured by differential scanning calorimeter (DSC, TA, USA). The samples were firstly heated from 30 to 210°C to remove the thermal story of the PHBV and then cooled to 30°C. Afterwards, the samples were heated to 210°C again. The thermal stabilities of the samples were investigated by thermogravimetric analyzer (TG, PerkinElmer, USA). The $Zn^{2+}$ concentration released by scaffold in the deionized water was quantitative analyzed *via* inductively coupled plasma optical emission spectrometer (ICP-OES, SPECTROBLUE SOP, Germany). The compression properties of the scaffolds were measured by mechanical testing machine (CMTS5205, MTS, USA) under a deformation rate of 0.5 mm/s.

*2.4. Antibacterial Activity.* Before the experiment, all experimental apparatus and the samples were washed with ethyl alcohol under the ultrasound bath and subsequently sterilized with ultraviolet (UV) for 1 h. The phosphate buffer solution (PBS) was used to dilute the bacterial suspensions and then seeded to lysogeny broth (LB) culture medium.

The *Escherichia coli* (*E. coli*, ATCC 25922) were selected to explore the antibacterial properties of the scaffolds. The antibacterial properties of the scaffolds against *E. coli* were quantitatively evaluated by the bacterial inhibition rate. In detail, the scaffolds with various ZnO contents were immersed in the Petri dish containing bacterial suspensions with a density of $1 \times 10^6$ CFU/mL and cultured for 1, 4, and

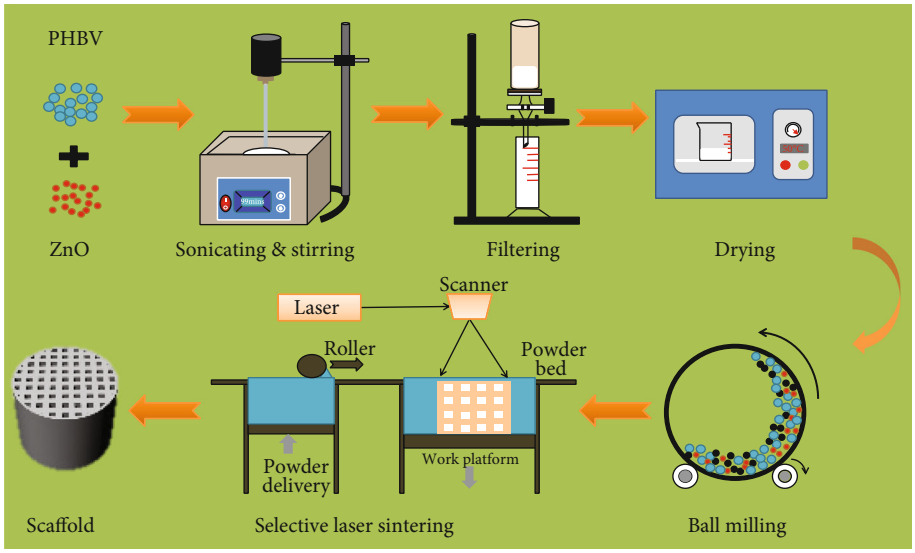


Figure 1: The manufacturing process of the scaffolds.

7 days at 37°C. Then, the optical density of bacterial was also measured by a microplate reader (Beckman, USA) at 600 nm. The antibacterial rate was calculated as the following equation:

$$\text{Antibacterial rate}\,(\%) = \frac{A_2 - A_1}{A_1} \times 100\% \qquad (1)$$

where $A_2$ and $A_1$ were the optical density of the bacterial suspensions contained with and without scaffolds, respectively. Each sample was tested for three times.

The morphologies of bacterial on the scaffolds were observed by SEM. In detail, the bacterial-scaffold complexes were taken out from the Petri dish and cleaned with PBS. Afterwards, the bacterial-scaffold complexes were fixed with glutaraldehyde and dehydrated with a series of alcohol. Subsequently, the complex was dried in vacuum drying oven and finally observed by SEM.

*2.5. Cell Response.* The cell response of the scaffolds was evaluated by using human osteoblast-like MG-63 cells. Prior to testing, the cells were cultured in glucose DMEM containing 10% fetal bovine serum at 37°C under a humidified environment with 5% $CO_2$, and the culture medium was refreshed every two days. Before cell seeding, the scaffolds were washed with PBS and sterilized with UV for 30 min followed by transferring them into a 12-well dish. Subsequently, the cells were seeded on scaffolds with a density of $1 \times 10^4$ cell/mL.

The cell adhesion on scaffold cultured for various periods was observed by SEM. After 1, 3, and 5 days of cultivation, the cell-scaffold complex was taken out and then washed with PBS. Hereafter, the cells on scaffolds were fixed with glutaraldehyde and dehydrated with gradient ethanol. Ultimately, the morphologies of the cells on the scaffolds were observed.

Fluorescence microscope (Olympus Co. Ltd., Tokyo, Japan) was adopted to observe the cell proliferation. The cell-scaffold complex was taken out from medium and washed with PBS for three times after culturing for 1, 3, and 5 days. Then, the cell-scaffold complex was stained with live/dead staining agent (PBS solution with 2 $\mu$M calcein AM and 4 $\mu$M EthD-1) and continuously incubated for another 30 min. Finally, fluorescence microscope was selected to observe the living/dead cell morphologies.

The proliferation of MG-63 cell on scaffolds was quantitatively analyzed by the Cell Counting Kit-8 (CCK-8) assay. The cell-scaffold complex was gently washed with PBS and transferred into a new medium containing CCK-8 reagent (Dojindo Laboratory, Kumamoto, Japan) after 1, 3, and 5 days of cultivation. 100 $\mu$L of medium was moved to a 96-well plate after culture for another 2 hours, and the optical density was measured *via* a microplate reader (Beckman, USA) at 450 nm.

Alkaline phosphatase (ALP), as a specific marker for early osteoblast differentiation, was observed by ALP staining. After 1, 3, and 5 days of cultivation, the cell-scaffold complex was gently rinsed with PBS and fixed with 4% paraformaldehyde for 20 min. Subsequently, ALP staining was carried out using the ALP staining kit (Wako, Osaka, Japan), and images were photographed *via* a microscopy.

*2.6. Statistical Analysis.* One-way analysis of variance (ANOVA) was selected to evaluate the statistical significance. All data were presented as mean ± standard deviations. The difference with $*p < 0.05$ was recognized to be significant.

## 3. Results and Discussion

*3.1. Microstructure.* The digital photos and the microstructures of the represent scaffold with height of 10 mm and diameter of 10 mm are shown in Figure 2(a). Obviously, the scaffold displayed a well porous structure, which was consistent with the as-designed models. The pore size of the scaffold was approximately 500 $\mu$m. It had been reported that the minimum pore size of the bone scaffold should not be less than 100 $\mu$m to ensure the nutrients transport and cells

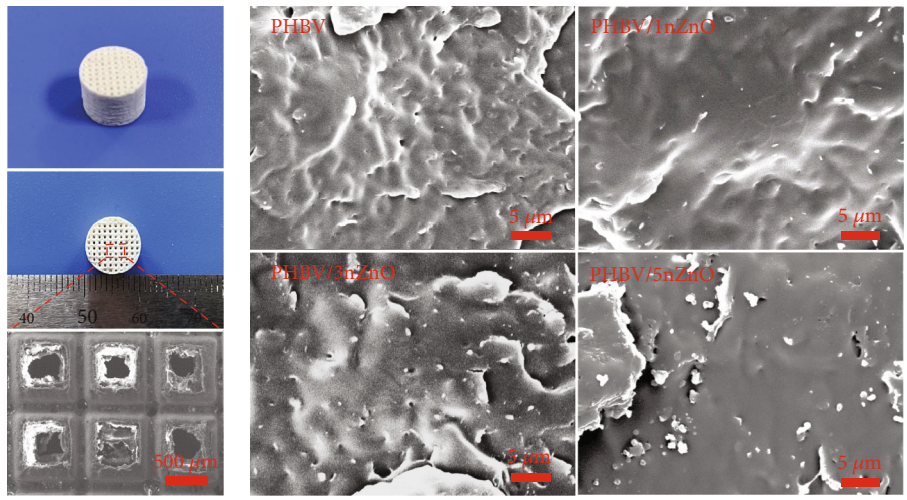


(a) (b)

Figure 2: (a) The digital photos and the microstructures of the represent scaffold; (b) the cryofractured morphologies of PHBV and PHBV/nZnO scaffolds.

growth [19]. Meanwhile, the mechanical performance of the scaffold would be deteriorated with the continuous ascent of the pore size, and the maximum pore size should not be higher than 1000 $\mu$m [20]. It could be concluded that the pore size of the as-prepared scaffold was in the range of 100~1000 $\mu$m and fulfilled the requirement of the bone scaffold. As reported in the literature, the dispersion state of the nanofillers in the polymer matrix had a significant influence on their comprehensive properties [21].

The cryofracture morphologies of the scaffolds are displayed in Figure 2(b). It could be obviously found that the composite scaffold presented a random and uniform nanofiller distribution with the content of ZnO lower than 3 wt.%. However, the composite scaffold with 5 wt.% ZnO presented poor nanofiller distribution, with small agglomeration composed of a few particles.

*3.2. Thermal Behaviors.* The thermal stabilities of the scaffold were measured by TG, and the results are shown in Figure 3(a). It could be seen from TG curves that all scaffolds exhibited a single decomposition stage. The initial decomposition temperature of PHBV scaffolds remarkably increased with the increase of ZnO. For instance, the initial decomposition temperature of PHBV/5nZnO scaffold increased from 261.2°C to 288.7°C in comparison with that of the PHBV scaffold. This improvement might be attributed to the interaction between the hydroxyl group of ZnO and the carbonyl of PHBV, which could form a barrier effect [22]. This barrier effect could prevent the transmission of the decomposition products. Furthermore, ZnO with excellent thermal conductivity could accelerate the heat dissipation in the composite and thereby enhance the thermal stability of the composite [23, 24]. It could also be found that the char residue of PHBV scaffold was gradually increased with increasing ZnO content, which was attributed to the relatively higher decomposition temperature of ZnO nanoparticles [25].

The melting and crystallization behaviors of the scaffolds are displayed in Figures 3(b) and 3(c). It could be seen from the melting curves that pure PHBV scaffold presented two obvious endothermic peaks located at 160.9°C and 170.6°C, which were due to the melting of the initial crystals and the recrystallized crystals during the DSC heating process, respectively [26]. The endothermic peaks of the composite scaffolds decreased with the increase of ZnO. The crystallization peak temperature of PHBV scaffolds gradually shifted to a higher temperature, which demonstrated that the nanofillers could efficiently promote the crystallization rate of the polymer (Figure 3(c)) [27]. In addition, the crystallization peak became more sharpened in the composite scaffolds, indicating that the nanofillers could efficiently accelerate the crystallization process of the polymer [28]. The relative crystallinity of the scaffolds could be calculated by the following equation:

$$X_c = \frac{\Delta H_m}{\Delta H_{\circ m} \times w} \times 100\% X_c = \frac{\Delta H_m}{\Delta H_{100} \times w} \times 100\%. \quad (2)$$

where $\Delta H_m$ is the melting enthalpy of PHBV, $w$ is the mass fraction of PHBV in the composites, and $\Delta H_m^o$ is the theoretical enthalpy of PHBV (109 J/g) [29]. It could be found that there was a remarkable increase in the relative crystallinity of PHBV/3nZnO composite scaffold from 38% to 64% in comparison with that of PHBV scaffolds, which might be attributed to the accelerated nucleation effect of ZnO nanoparticles. However, relative crystallinity of the composite scaffolds was decreased with the further increase of nanofillers. This might be due to the aggregation of the nanofillers, which hindered the mobility of the polymer chains during the crystallization process.

The XRD patterns of the scaffolds are shown in Figure 3(d). There was two obvious peaks located at $2\theta$ of 13.4° and 16.9°, being ascribed to the (020) and (110) crystalline planes of PHBV, respectively [30]. The characteristic

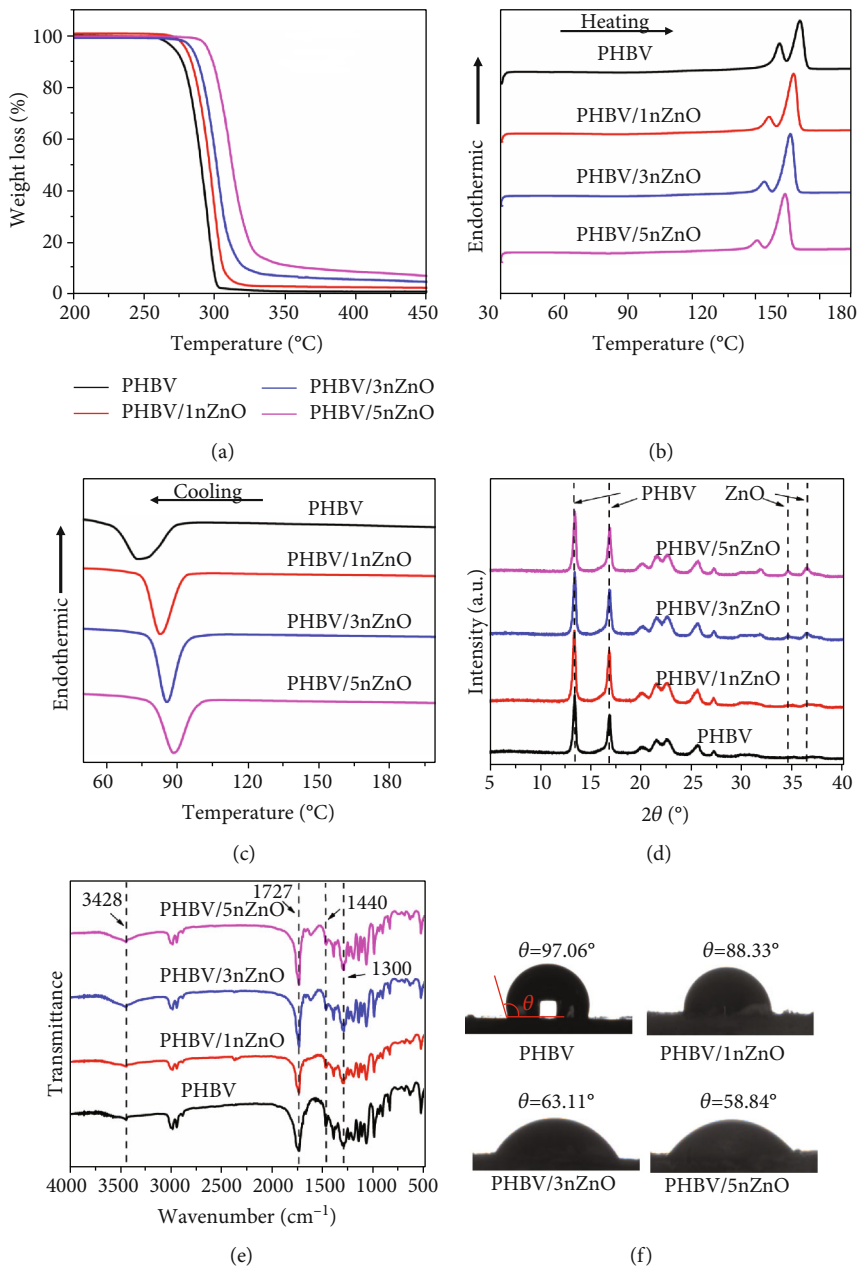


FIGURE 3: (a) TG curves, (b) DSC heating curves, (c) DSC cooling curves, (d) XRD patterns, (e) FTIR spectra, and (f) water contact angles of the scaffolds.

peaks located at 34.5° and 36.1° were ascribed to the (002) and (101) crystalline planes of ZnO, respectively [31]. Compared with PHBV, the peak in the composite scaffold became narrower and more intense, which indicated that the nanofiller could efficiently promote the crystallization of PHBV, thereby resulting in the formation of smaller crystals. Moreover, there was no peak shift in the XRD patterns, which revealed that the SLS process did not destroy the crystal structures of the materials.

The functional groups of the scaffolds were characterized by FTIR, and the results are shown in Figure 3(e). Pure PHBV presented a strong peak situated at 1727 $cm^{-1}$, which was assigned to the telescopic vibration of carbonyl group [32]. The peaks situated at 1445 and 1300 $cm^{-1}$, which were ascribed to the asymmetric bending vibration of $CH_3$ and the in-plane bending vibration of H-C-O [33]. Once ZnO nanoparticles were incorporated, a broad band appeared at 3428 $cm^{-1}$, being attributed to the stretching vibration of hydroxyl group on the nanoparticle surface [34]. It should be noted that the carbonyl band in the composite scaffolds became more intense and slightly shifted to lower wavenumber in comparison with that of pure PHBV, implying that there was a hydrogen bond interactions between the carbonyl group of PHBV and hydroxyl group of the nanoparticles [35].

The wettability of the scaffold had a significant influence on cell behaviors. It was established that the PHBV presented

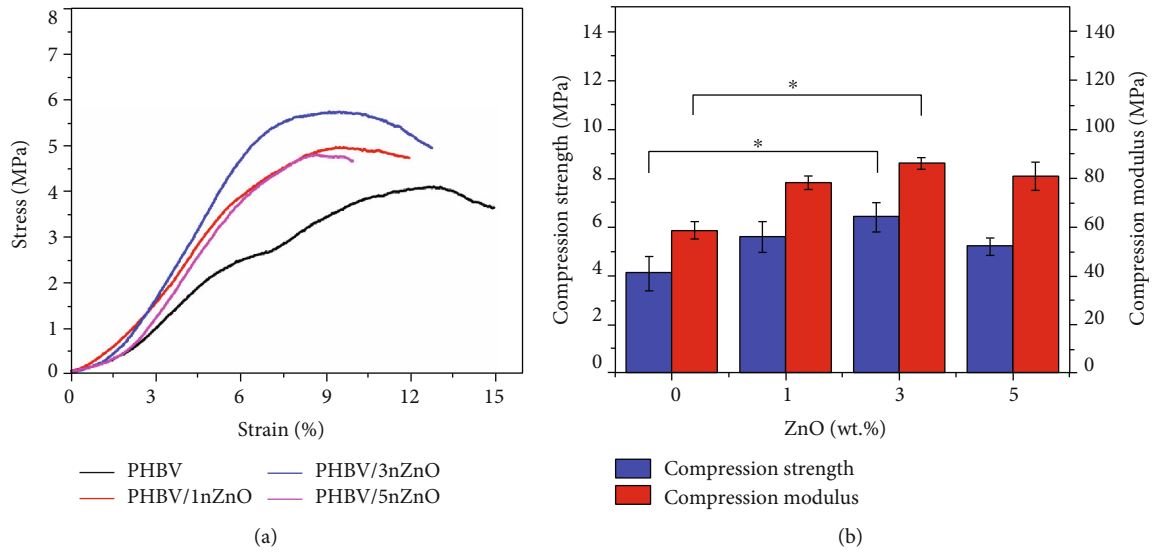


Figure 4: (a) The compression stress-strain curves, (b) compression strength and compression modulus of composite scaffold. $n = 3$, $*p < 0.05$.

inherent hydrophobic characteristic, which had limited its further application in bone defects treatment [36]. The water contact angles of the scaffold are shown in Figure 3(f). As expected, PHBV scaffold displayed a water contact angle of $97.06 \pm 1.33^{\circ}$. It was excited to found that the water contact angles of the composite scaffolds significantly decreased with the increase of ZnO content. For instance, the water contact angle of PHBV/5nZnO composite scaffold sharply decreased to $58.84 \pm 1.29^{\circ}$, which implied that the incorporation of ZnO could achieve a conversion of PHBV scaffold from hydrophobicity to hydrophilicity. This transformation might be attributed to a fact that the ZnO with hydroxyl groups was facilitated to the absorption of water molecules and thereby enhancing the hydrophilicity of the composite scaffolds [37].

*3.3. Compressive Performance.* The compressive performance of the scaffold plays a critical role in bearing different stresses and offering structural support to the bone tissues [38]. The compressive stress-strain curves were measured by mechanical testing equipment and are displayed in Figure 4(a). The compressive strength and compressive modulus of the composite scaffolds calculated from their stress-strain curves are presented in Figure 4(b). The compressive strength of the composite scaffolds firstly raised and then reduced with the increase of ZnO content. For instance, the compressive strength of PHBV/3nZnO scaffold increased from $4.1 \pm 0.7$ to $6.4 \pm 0.6$ MPa, which increased by 56% as compared with pure PHBV scaffold. This might mainly be ascribed to the combination of the increase in the crystallinity of PHBV and a uniform nanoparticle distribution. In detail, the uniformly distributed nanoparticles in the polymer could accelerate the orderly stacking of polymer chains, thus enhancing the crystallinity of the composites. The enhanced crystallinity could efficiently reduce the deformable space inside the composites, thereby enhancing their compressive strength. Meanwhile, the rigid nanoparticles could hinder the proliferation and development of cracks [39]. Moreover, the hydrogen bonding interaction between PHBV and ZnO might absorb a part of energy during the compressive process [40]. However, the compressive strength of the composite scaffold reduced with ZnO content further increasing to 5 wt.%, which might be ascribed to the aggregation of ZnO. Even so, the scaffold fabricated in this work still fulfilled the requirements for compressive strength of natural cancellous bone, which commonly exhibited a compressive strength of 1~10 MPa [41]. Furthermore, it could be found that the compressive modulus of the composite scaffolds improved with the continuously increasing of ZnO content. For example, the compressive modulus of PHBV/3nZnO scaffold increased from $58.6 \pm 3.36$ to $88.8 \pm 5.56$ MPa, which increased by 51.5% in comparison with that of pure PHBV scaffold. This might be attributed to the relatively high modulus of ZnO nanoparticles, which was in agreement with the results as reported in the literature [42].

*3.4. Antibacterial Properties.* Trauma infection was still a big challenge in bone repair, which required bone implants to have antibacterial activity [43, 44]. The bacterial inhibition rates of the scaffolds with various ZnO contents for 1, 4, and 7 days are shown in Figure 5(a). Obviously, the bacterial inhibition rates of the scaffolds increased with the extension of days. The bacterial morphologies on the various scaffolds for 7 days are shown in Figures 5(b). Obviously, several rod-like bacteria were adhered and connected to each other on the surface of PHBV scaffold. On the contrary, the number of adhered bacteria was greatly decreased with the introduction of ZnO. More interestingly, the shapes of bacteria became distorted and shriveled, which implied that the cellular structure was damaged. It has been reported that the concentration of $Zn^{2+}$ within 3 mg/L shows no cytotoxicity to normal cells [45]. In this work, the $Zn^{2+}$ releases concentrations of scaffold in the deionized water for 1, 4, and 7 days were measured by ICP-OES, and the corresponding results is displayed in Figure 5(c). All scaffolds showed a slow

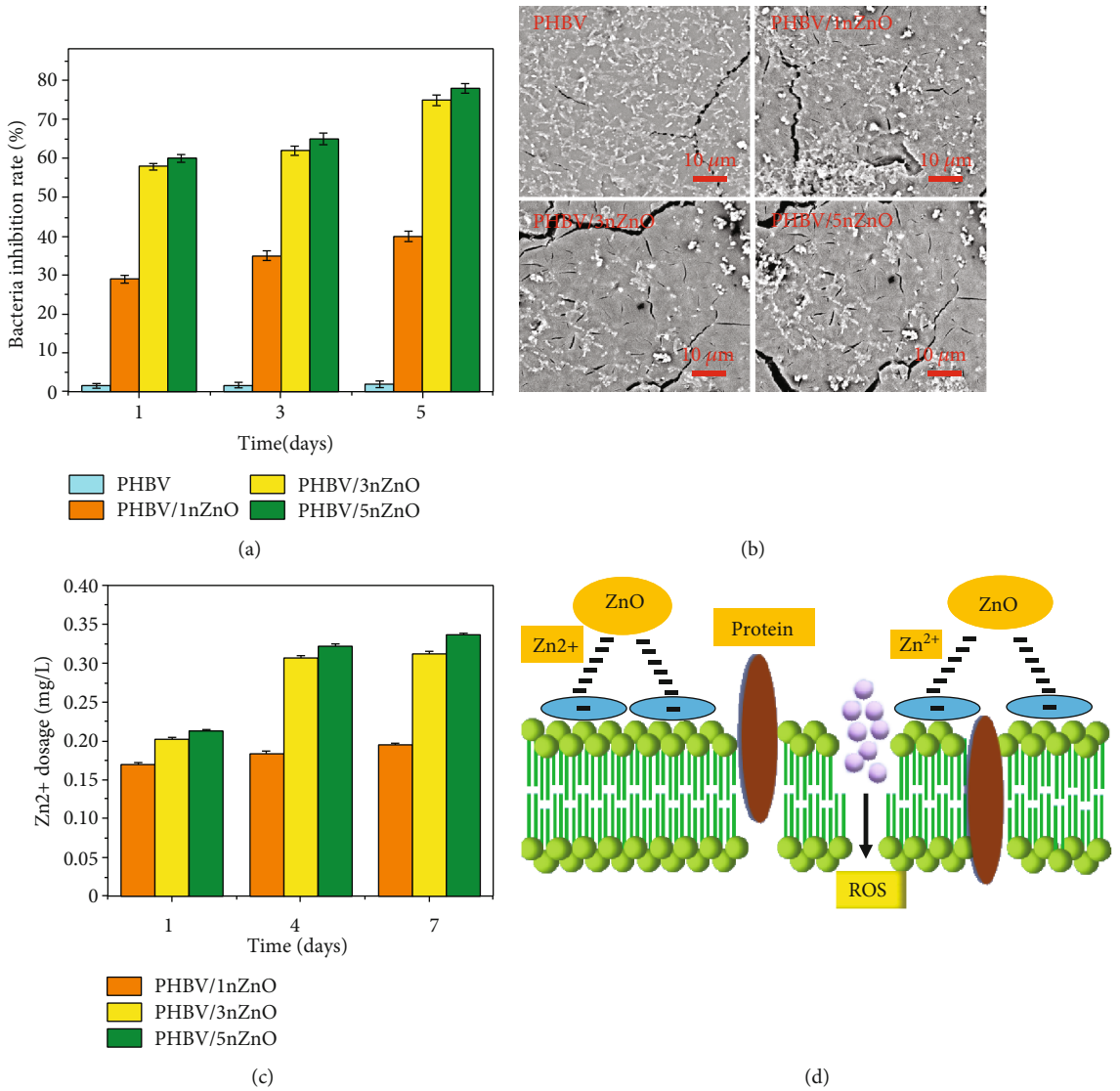


Figure 5: (a) Bacterial inhibition rate of *E. coli* cultured in medium containing various scaffolds for 1, 4, and 7 days; (b) bacterial morphology on the scaffolds; (c) $Zn^{2+}$ release of the scaffolds after immersion in deionized water for different time; (d) a schematic for the antibacterial mechanism.

and sustained $Zn^{2+}$ release throughout the whole process. The maximum released $Zn^{2+}$ concentration of the scaffold was $0.3364 \pm 0.0024$ mg/L, which was much lower than 3 mg/L. Therefore, the scaffolds have no negative effect on the normal function of cell.

Several antibacterial mechanisms had been proposed to interpret the antibacterial activity of ZnO nanoparticles, as shown in Figure 5(d). Briefly, it mainly consisted of the release of $Zn^{2+}$; the mechanical damage of the cell membranes resulted from penetration of the nanoparticles, and the generation of reactive oxygen species [46]. In this work, the average size of ZnO was 50 nm, which was unlikely to penetrate into the cell wall to destroy the bacteria [47]. Moreover, the production of reactive oxygen species by ZnO should be in the irradiation of ultraviolet light [48]. Therefore, the release of $Zn^{2+}$ might be a potential reason for the antibacterial activity of the scaffolds. Pasquet et al. [49] demonstrated that $Zn^{2+}$ could absorb on the negatively charged bacterial wall by electrostatic interactions and thereby destroying the normal structure and function of the bacterial membrane, as well as interfering with protein metabolism and genetic expression of bacteria.

*3.5. Cell Response.* The cell response of the scaffolds plays a vital in bone repair [50, 51]. Considering the mechanical and antibacterial properties of the scaffolds, the PHBV/3nZnO scaffold was selected to further explore its cell behaviors. Cell adhesion was a prerequisite for a series of reactions such as migration, proliferation, and differentiation [52]. The SEM images of MG63 cells on PHBV and PHBV/3nZnO scaffolds for 1, 3, and 5 days are displayed in Figure 6. Apparently, the spread area of the cell on the scaffolds increased with the prolongation of time. It could be found that the cell on PHBV scaffold presented an ellipse shape in the whole culture

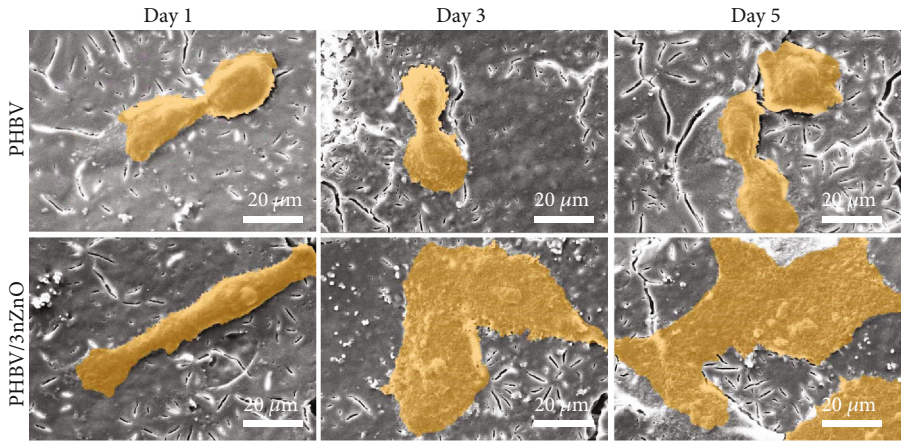


Figure 6: SEM images regarding the cell adhesion behavior on PHBV and PHBV/3nZnO scaffolds for 1, 3, and 5 days of culture.

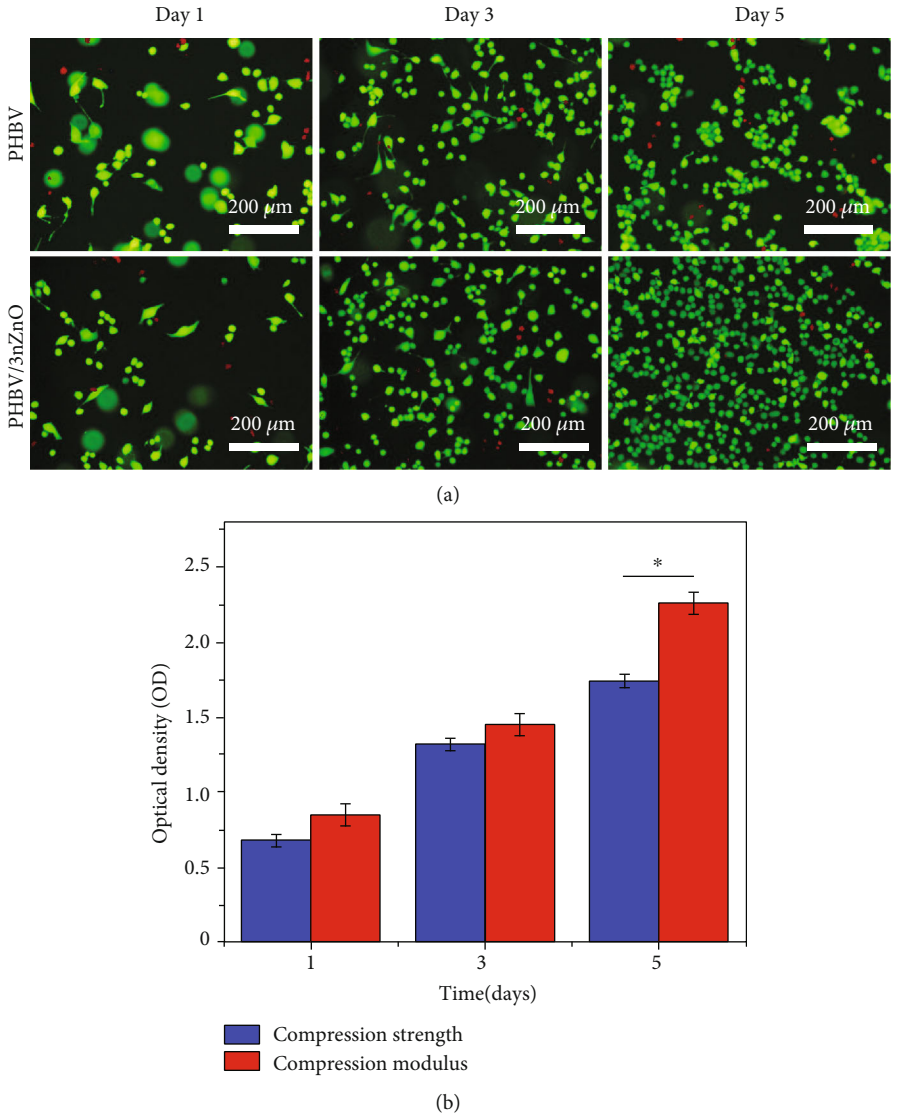


Figure 7: (a) Fluorescence images and (b) optical density of cells on PHBV and PHBV/3nZnO scaffolds after 1, 3, and 5 days of culture. $n = 3$, $*p < 0.05$.

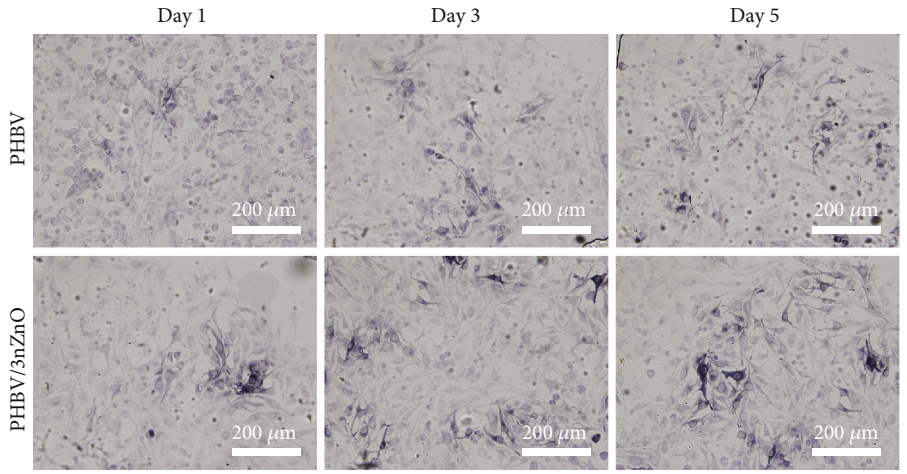


Figure 8: ALP staining images of MG-63 cells on PHBV and PHBV/3nZnO scaffolds after 1, 3, and 5 days of culture.

periods, which was attributed to the hydrophobic properties of the scaffolds [53]. Compared with the PHBV scaffold, the cells on PHBV/3nZnO displayed a flat and stretched shape after 1 day of culture. With the increase of culturing time, more adhered cells with longer filopodia attachment were observed on the PHBV/3nZnO scaffold, indicating its positive effect on cell adhesion and spreading.

Fluorescence test was performed to further explored the proliferation of cells on PHBV and PHBV/3nZnO scaffolds and the corresponding fluorescence images for 1, 3, and 5 days of cultures are shown in Figure 7(a). Live cells are stained in green, whereas dead cells are stained in red. Clearly, after 1-day culture, the cells on scaffold presented a healthy and normal polygonal shape, without obvious dead cells, which indicated that these scaffolds provided favorable survival environment. Meanwhile, the cell numbers increased significantly after 3 and 5 days of culture. The cell proliferation was quantitatively described by CCK-8 measurements, and the results are displayed in Figure 7(b). The optical density of PHBV and PHBV/3nZnO scaffolds displayed a significant difference after 5-day culture, implying that the ZnO could promote the cell proliferation.

Alkaline phosphatase (ALP) activity, as a typical marker, was widely accepted to reflect the early differentiation of osteoblasts [54, 55]. The staining images of MG-63 cell on PHBV and PHBV/3nZnO scaffolds after 1, 3, and 5 days of culture are presented in Figure 8. The ALP-positive areas of the cells increased with the increase of culture time. Moreover, the MG-63 cells seeded on PHBV/3nZnO scaffolds displayed a more significant ALP staining than that of PHBV scaffolds at the same culture time, which indicated that the PHBV/3nZnO scaffolds could promote the cell differentiation. Combining with CCK-8 and live/dead staining assays, it was indicated that PHBV/3nZnO scaffold was more conducive to cell adhesion, growth, and differentiation. The released $Zn^{2+}$ could participate in the modulation of cellular signaling transduction [56]. Meanwhile, the $Zn^{2+}$ could regulate the interaction between signal peptides and extramembrane receptors, thereby improving the cell behaviors [57]. In addition, Zn is an important trace element, which widely involves in synthesis of several nucleic acid and protein [58].

## 4. Conclusion

In this study, ZnO nanoparticles were incorporated into PHBV scaffolds fabricated by the SLS technique, aiming at improving their mechanical properties and antibacterial activities. The results indicated that a scaffold with 3 wt.% ZnO exhibited a uniform dispersion and simultaneously could provide a nucleating site for the orderly stacking of PHBV chains. The relative crystallinity of PHBV/3nZnO scaffold remarkably increased from 38% to 64% in comparison with that of pure PHBV scaffold. The improved crystallinity could effectively enhance the compression strength and modulus of the scaffold by 56% and 51.5%, respectively. Moreover, $Zn^{2+}$ released by the scaffolds could efficiently inhibit the growth of *E. coli* and promote the cell behaviors in terms of cell proliferation and differentiation. All these positive results confirmed that the scaffold was one potential bone scaffold material.

## Data Availability

The case data used to support the findings of this study are included within the article.

## Conflicts of Interest

The authors declare that they have no conflicts of interest.

## Acknowledgments

This study was supported by the following funds: (1) The Natural Science Foundation of China (51935014, 51905553, 81871494, 81871498, and 51705540); (2) Hunan Provincial Natural Science Foundation of China (2019JJ50774, 2018 JJ3671, and 2019JJ50588); (3) The Provincial Key R&D Projects of Jiangxi (20201BBE51012); (4) JiangXi Provincial Natural Science Foundation of China (20192ACB20005); (5) Guangdong Province Higher Vocational Colleges & Schools Pearl River Scholar Funded Scheme (2018); (6) The Project of Hunan Provincial Science and Technology Plan (2017 RS3008), (7) Shenzhen Science and Technology Plan Project (JCYJ20170817112445033), (8) Innovation Team Project on

University of Guangdong Province (2018GKCXTD001), and (9) Technology Innovation Platform Project of Shenzhen Institute of Information Technology 2020 (PT2020E002).

## References


[1] X. Ye, L. Li, Z. Lin et al., "Integrating 3D-printed PHBV/calcium sulfate hemihydrate scaffold and chitosan hydrogel for enhanced osteogenic property," *Carbohydrate Polymers*, vol. 202, pp. 106–114, 2018.

[2] C. Shuai, G. Liu, Y. Yang et al., "A strawberry-like Ag-decorated barium titanate enhances piezoelectric and antibacterial activities of polymer scaffold," *Nano Energy*, vol. 74, p. 104825, 2020.

[3] L. Zhang, G. Yang, B. N. Johnson, and X. Jia, "Three-dimensional (3D) printed scaffold and material selection for bone repair," *Acta Biomaterialia*, vol. 84, pp. 16–33, 2019.

[4] M. Kouhi, M. Fathi, M. P. Prabhakaran, M. Shamanian, and S. Ramakrishna, "Poly L lysine-modified PHBV based nanofibrous scaffolds for bone cell mineralization and osteogenic differentiation," *Applied Surface Science*, vol. 457, pp. 616–625, 2018.

[5] V. Jost and H.-C. Langowski, "Effect of different plasticisers on the mechanical and barrier properties of extruded cast PHBV films," *European Polymer Journal*, vol. 68, pp. 302–312, 2015.

[6] Z. Gu, R. Yang, J. Yang et al., "Dynamic Monte Carlo simulations of effects of nanoparticle on polymer crystallization in polymer solutions," *Computational Materials Science*, vol. 147, pp. 217–226, 2018.

[7] D. Jun, Z. Guomin, P. Mingzhu, Z. Leilei, L. Dagang, and Z. Rui, "Crystallization and mechanical properties of reinforced PHBV composites using melt compounding: effect of CNCs and CNFs," *Carbohydrate Polymers*, vol. 168, pp. 255–262, 2017.

[8] M. Kouhi, M. P. Prabhakaran, M. Shamanian, M. Fathi, M. Morshed, and S. Ramakrishna, "Electrospun PHBV nanofibers containing HA and bredigite nanoparticles: fabrication, characterization and evaluation of mechanical properties and bioactivity," *Composites Science and Technology*, vol. 121, pp. 115–122, 2015.

[9] H. Zhang, H.-Y. Yu, C. Wang, and J. Yao, "Effect of silver contents in cellulose nanocrystal/silver nanohybrids on PHBV crystallization and property improvements," *Carbohydrate Polymers*, vol. 173, pp. 7–16, 2017.

[10] P. K. Mishra, H. Mishra, A. Ekielski, S. Talegaonkar, and B. Vaidya, "Zinc oxide nanoparticles: a promising nanomaterial for biomedical applications," *Drug Discovery Today*, vol. 22, no. 12, pp. 1825–1834, 2017.

[11] Y.-W. Wang, A. Cao, Y. Jiang et al., "Superior antibacterial activity of zinc oxide/graphene oxide composites originating from high zinc concentration localized around bacteria," *ACS Applied Materials & Interfaces*, vol. 6, no. 4, pp. 2791–2798, 2014.

[12] Y. Li, W. Zhang, J. Niu, and Y. Chen, "Mechanism of photogenerated reactive oxygen species and correlation with the antibacterial properties of engineered metal-oxide nanoparticles," *ACS Nano*, vol. 6, no. 6, pp. 5164–5173, 2012.

[13] N. Padmavathy and R. Vijayaraghavan, "Enhanced bioactivity of ZnO nanoparticles—an antimicrobial study," *Science and Technology of Advanced Materials*, vol. 9, no. 3, article 035004, 2016.

[14] D. Bian, W. Zhou, J. Deng et al., "Development of magnesium-based biodegradable metals with dietary trace element germanium as orthopaedic implant applications," *Acta Biomaterialia*, vol. 64, pp. 421–436, 2017.

[15] P. Deb, A. B. Deoghare, A. Borah, E. Barua, and S. Das Lala, "Scaffold development using biomaterials: a review," *Materials Today: Proceedings*, vol. 5, no. 5, pp. 12909–12919, 2018.

[16] C. Shuai, S. Li, W. Yang, Y. Yang, Y. Deng, and C. Gao, "$MnO_2$ catalysis of oxygen reduction to accelerate the degradation of Fe-C composites for biomedical applications," *Corrosion Science*, vol. 170, article 108679, 2020.

[17] Y. Yang, C. Lu, S. Peng et al., "Laser additive manufacturing of Mg-based composite with improved degradation behaviour," *Virtual and Physical Prototyping*, vol. 15, pp. 278–293, 2020.

[18] G. Wang, C. He, W. Yang et al., "Surface-modified graphene oxide with compatible interface enhances Poly-L-Lactic acid bone scaffold," *Journal of Nanomaterials*, vol. 2020, Article ID 5634096, 11 pages, 2020.

[19] K. Zhang, Y. Fan, N. Dunne, and X. Li, "Effect of microporosity on scaffolds for bone tissue engineering," *Regenerative Biomaterials*, vol. 5, no. 2, pp. 115–124, 2018.

[20] S. Tarafder, V. K. Balla, N. M. Davies, A. Bandyopadhyay, and S. Bose, "Microwave-sintered 3D printed tricalcium phosphate scaffolds for bone tissue engineering," *Journal of Tissue Engineering and Regenerative Medicine*, vol. 7, no. 8, pp. 631–641, 2013.

[21] W. Noohom, K. S. Jack, D. Martin, and M. Trau, "Understanding the roles of nanoparticle dispersion and polymer crystallinity in controlling the mechanical properties of HA/PHBV nanocomposites," *Biomedical Materials*, vol. 4, no. 1, article 015003, 2008.

[22] P. Li, Y. Zheng, M. Li et al., "Enhanced flame-retardant property of epoxy composites filled with solvent-free and liquid-like graphene organic hybrid material decorated by zinc hydroxystannate boxes," *Composites Part A: Applied Science and Manufacturing*, vol. 81, pp. 172–181, 2016.

[23] F.-Y. Yuan, H.-B. Zhang, X. Li, X.-Z. Li, and Z.-Z. Yu, "Synergistic effect of boron nitride flakes and tetrapod-shaped ZnO whiskers on the thermal conductivity of electrically insulating phenol formaldehyde composites," *Composites Part A: Applied Science and Manufacturing*, vol. 53, pp. 137–144, 2013.

[24] L. Fang, W. Wu, X. Huang, J. He, and P. Jiang, "Hydrangea-like zinc oxide superstructures for ferroelectric polymer composites with high thermal conductivity and high dielectric constant," *Composites Science and Technology*, vol. 107, pp. 67–74, 2015.

[25] H. Wang, Z. Lu, D. Lu, C. Li, P. Fang, and X. Wang, "The synthesis of Cu/plate-like ZnO nanostructures and their self-assembly mechanism," *Solid State Sciences*, vol. 55, pp. 69–76, 2016.

[26] E. B. C. Santos, J. J. P. Barros, D. A. de Moura, C. G. Moreno, F. de Carvalho Fim, and L. B. da Silva, "Rheological and thermal behavior of PHB/piassava fiber residue-based green composites modified with warm water," *Journal of Materials Research and Technology*, vol. 8, no. 1, pp. 531–540, 2019.

[27] I. Kaygusuz and C. Kaynak, "Influences of halloysite nanotubes on crystallisation behaviour of polylactide," *Plastics, Rubber and Composites*, vol. 44, no. 2, pp. 41–49, 2015.

[28] Q. Xing, R. Li, X. Dong et al., "Enhanced crystallization rate of poly (l-lactide) mediated by a hydrazide compound:

nucleating mechanism study," *Macromolecular Chemistry and Physics*, vol. 216, no. 10, pp. 1134–1145, 2015.

[29] J. Castro-Mayorga, M. Fabra, and J. Lagaron, "Stabilized nanosilver based antimicrobial poly(3-hydroxybutyrate-co-3-hydroxyvalerate) nanocomposites of interest in active food packaging," *Innovative Food Science & Emerging Technologies*, vol. 33, pp. 524–533, 2016.

[30] L. Wei, N. M. Stark, and A. G. McDonald, "Interfacial improvements in biocomposites based on poly (3-hydroxybutyrate) and poly (3-hydroxybutyrate-co-3-hydroxyvalerate) bioplastics reinforced and grafted with $\alpha$-cellulose fibers," *Green Chemistry*, vol. 17, no. 10, pp. 4800–4814, 2015.

[31] M. Shaban, M. Zayed, and H. Hamdy, "Nanostructured ZnO thin films for self-cleaning applications," *RSC Advances*, vol. 7, no. 2, pp. 617–631, 2017.

[32] H.-Y. Yu and J.-M. Yao, "Reinforcing properties of bacterial polyester with different cellulose nanocrystals via modulating hydrogen bonds," *Composites Science and Technology*, vol. 136, pp. 53–60, 2016.

[33] A. Aramvash, S. Hajizadeh-Turchi, F. Moazzeni-zavareh, N. Gholami-Banadkuki, N. Malek-sabet, and Z. Akbari-Shahabi, "Effective enhancement of hydroxyvalerate content of PHBV in Cupriavidus necator and its characterization," *International Journal of Biological Macromolecules*, vol. 87, pp. 397–404, 2016.

[34] R. Saravanan, V. Gupta, T. Prakash, V. Narayanan, and A. Stephen, "Synthesis, characterization and photocatalytic activity of novel Hg doped ZnO nanorods prepared by thermal decomposition method," *Journal of Molecular Liquids*, vol. 178, pp. 88–93, 2013.

[35] Z. Yu, M. R. Kumar, D. Sun, L. Wang, and R. Hong, "Large scale production of hexagonal ZnO nanoparticles using PVP as a surfactant," *Materials Letters*, vol. 166, pp. 284–287, 2016.

[36] I. Unalan, O. Colpankan, A. Z. Albayrak, C. Gorgun, and A. S. Urkmez, "Biocompatibility of plasma-treated poly (3-hydroxybutyrate-co-3-hydroxyvalerate) nanofiber mats modified by silk fibroin for bone tissue regeneration," *Materials Science and Engineering: C*, vol. 68, pp. 842–850, 2016.

[37] Y. Qing, C. Yang, C. Hu, Y. Zheng, and C. Liu, "A facile method to prepare superhydrophobic fluorinated polysiloxane/ZnO nanocomposite coatings with corrosion resistance," *Applied Surface Science*, vol. 326, pp. 48–54, 2015.

[38] C. Shuai, L. Yu, P. Feng, C. Gao, and S. Peng, "Interfacial reinforcement in bioceramic/biopolymer composite bone scaffold: the role of coupling agent," *Colloids and Surfaces B: Biointerfaces*, vol. 193, article 111083, 2020.

[39] A. Ashori, M. Jonoobi, N. Ayrilmis, A. Shahreki, and M. A. Fashapoyeh, "Preparation and characterization of polyhydroxybutyrate-co-valerate (PHBV) as green composites using nano reinforcements," *International Journal of Biological Macromolecules*, vol. 136, pp. 1119–1124, 2019.

[40] W. Mook Choi, T. Wan Kim, O. Ok Park, Y. Keun Chang, and J. Woo Lee, "Preparation and characterization of poly (hydroxybutyrate-co-hydroxyvalerate)–organoclay nanocomposites," *Journal of Applied Polymer Science*, vol. 90, no. 2, pp. 525–529, 2003.

[41] S.-I. Roohani-Esfahani, P. Newman, and H. Zreiqat, "Design and fabrication of 3D printed scaffolds with a mechanical strength comparable to cortical bone to repair large bone defects," *Scientific Reports*, vol. 6, no. 1, article 19468, 2016.

[42] C. Shuai, B. Wang, S. Bin, S. Peng, and C. Gao, "Interfacial strengthening by reduced graphene oxide coated with MgO in biodegradable Mg composites," *Materials & Design*, vol. 191, p. 108612, 2020.

[43] A. Bari, N. Bloise, S. Fiorilli et al., "Copper-containing mesoporous bioactive glass nanoparticles as multifunctional agent for bone regeneration," *Acta Biomaterialia*, vol. 55, pp. 493–504, 2017.

[44] E. Barua, A. B. Deoghare, S. Chatterjee, and P. Sapkal, "Effect of ZnO reinforcement on the compressive properties, in vitro bioactivity, biodegradability and cytocompatibility of bone scaffold developed from bovine bone-derived HAp and PMMA," *Ceramics International*, vol. 45, no. 16, pp. 20331–20345, 2019.

[45] G. Jin, H. Cao, Y. Qiao, F. Meng, H. Zhu, and X. Liu, "Osteogenic activity and antibacterial effect of zinc ion implanted titanium," *Colloids and Surfaces B: Biointerfaces*, vol. 117, pp. 158–165, 2014.

[46] J. Li, L. Tan, X. Liu et al., "Balancing bacteria–osteoblast competition through selective physical puncture and biofunctionalization of ZnO/polydopamine/arginine-glycine-aspartic acid-cysteine nanorods," *ACS Nano*, vol. 11, no. 11, pp. 11250–11263, 2017.

[47] R. Javed, M. Usman, S. Tabassum, and M. Zia, "Effect of capping agents: structural, optical and biological properties of ZnO nanoparticles," *Applied Surface Science*, vol. 386, pp. 319–326, 2016.

[48] J. Podporska-Carroll, A. Myles, B. Quilty et al., "Antibacterial properties of F-doped ZnO visible light photocatalyst," *Journal of Hazardous Materials*, vol. 324, pp. 39–47, 2017.

[49] J. Pasquet, Y. Chevalier, E. Couval, D. Bouvier, and M.-A. Bolzinger, "Zinc oxide as a new antimicrobial preservative of topical products: interactions with common formulation ingredients," *International Journal of Pharmaceutics*, vol. 479, no. 1, pp. 88–95, 2015.

[50] C. Shuai, B. Wang, S. Bin, S. Peng, and C. Gao, "TiO2 induced in situ reaction in graphene oxide reinforced AZ61 biocomposites to enhance the interfacial bonding," *ACS Applied Materials & Interfaces*, vol. 12, no. 20, pp. 23464–23473, 2020.

[51] C. Shuai, Y. Cheng, W. Yang et al., "Magnetically actuated bone scaffold: microstructure, cell response and osteogenesis," *Composites Part B: Engineering*, vol. 192, p. 107986, 2020.

[52] L. Cao, W. Liu, Y. Zhong et al., "Linc02349 promotes osteogenesis of human umbilical cord-derived stem cells by acting as a competing endogenous RNA for miR-25-3p and miR-33b-5p," *Cell Proliferation*, vol. 53, no. 5, article e12814, 2020.

[53] X. Li, J. Wei, K. E. Aifantis et al., "Current investigations into magnetic nanoparticles for biomedical applications," *Journal of Biomedical Materials Research Part A*, vol. 104, no. 5, pp. 1285–1296, 2016.

[54] S. He, S. Yang, Y. Zhang et al., "LncRNA ODIR1 inhibits osteogenic differentiation of hUC-MSCs through the FBXO25/H2BK120ub/H3K4me3/OSX axis," *Cell Death & Disease*, vol. 10, no. 12, article 947, 2019.

[55] W. Yang, Y. Zhong, C. He et al., "Electrostatic self-assembly of pFe3O4 nanoparticles on graphene oxide: a co-dispersed nanosystem reinforces PLLA scaffolds," *Journal of Advanced Research*, vol. 24, pp. 191–203, 2020.

[56] G. Zhang, Y. Zhao, B. Peng et al., "A fluorogenic probe based on chelation–hydrolysis-enhancement mechanism for

visualizing Zn 2+ in Parkinson's disease models," *Journal of Materials Chemistry B*, vol. 7, no. 14, pp. 2252–2260, 2019.

[57] Z. Zhang, H. Hao, Z. Tang et al., "Identification and characterization of a new alkaline thermolysin-like protease, BtsTLP1, from Bacillus thuringiensis Serovar Sichuansis strain MC28," *Journal of Microbiology and Biotechnology*, vol. 25, no. 8, pp. 1281–1290, 2015.

[58] A. Fallah, A. Mohammad-Hasani, and A. H. Colagar, "Zinc is an essential element for male fertility: a review of Zn roles in men's health, germination, sperm quality, and fertilization," *Journal of Reproduction & Infertility*, vol. 19, no. 2, p. 69, 2018.

Hindawi
Journal of Nanomaterials
Volume 2020, Article ID 9480537, 11 pages
https://doi.org/10.1155/2020/9480537

*Research Article*

# Effect of Gradient Nanostructured Ti on Behaviours of MG63 Cells *In Vitro*

**Xue Luo,[1] Chen Liang,[2] Ning Li,[3] Yuhe Zhu,[1] Nanjue Cao,[4] Jin Wang,[1] Keda Liu,[1] Hongwei Zhao,[3] Zhenbo Wang,[2] and Wei Wang[1]**

[1]*School and Hospital of Stomatology, China Medical University, Liaoning Provincial Key Laboratory of Oral Diseases, Shenyang 110001, China*
[2]*Shenyang National Laboratory for Materials Science, Institute of Metal Research, Chinese Academy Sciences, Shenyang 110016, China*
[3]*Department of Orthopedics, The Fourth Central Hospital of Baoding City, Baoding 072350, China*
[4]*The Fourth Affiliated Hospital, Zhejiang University School of Medicine, Yiwu 322000, China*

Correspondence should be addressed to Hongwei Zhao; 13931386052@163.com, Zhenbo Wang; zbwang@imr.ac.cn, and Wei Wang; wwang75@cmu.edu.cn

Received 6 April 2020; Accepted 24 April 2020; Published 5 June 2020

Academic Editor: Hui-Qi Xie



Titanium (Ti) is widely used in oral implants. However, there is still a challenge to promote the osseointegration of bone tissue on the surface of Ti. To solve this problem, we prepared novel gradient nanostructured (GNS) Ti and studied the effect of GNS on the adhesion, proliferation, and apoptosis of MG63 cells *in vitro*. The results demonstrated that the GNS Ti promoted the adhesion effect and proliferation of MG63 cells better than the annealed Ti, while the ability of GNS Ti to inhibit cell apoptosis was better than that of the annealed Ti, the preliminary mechanism of which indicated by this study might be the enhanced mineralization capacity, protein adsorption ability, and hydrophilicity of the GNS Ti due to its specific nanostructure which improved the cell behaviours. The results in this study provide the theoretical and experimental foundations for the applications of GNS Ti in dental implants and joint replacements.

## 1. Introduction

Titanium (Ti) is widely used in oral implants due to its nontoxicity, lightweight, high specific strength, corrosion resistance, and fatigue resistance [1–3]. However, Ti is a biologically inert material [4–6], which tends to form fibrous bonds with bone tissue instead of osseointegration [7–11].

To improve the combination between Ti to bone tissue, a large number of researchers have used surface modification methods to enhance the bonding strength between Ti and bone tissue [12]. Especially, nanostructured surface could hopefully bring desired effects on behaviours of surrounding cells, thereby promoting bone formation [13]. Chen et al. reported that nano-scale Ti materials demonstrated better biocompatibility than micron-scale and millimeter-scale counterparts, and that the ability of the nano-scale Ti materials to improve osteogenic differentiation of bone marrow mesenchymal stem cells was significantly better than that of the control groups [14]. Yang et al. cultured MC-3T3 cells on micro-scale and nano-scale silicon structures with different surface modifications and found that the silicon scaffolds with nanostructure had better ability to promote MC-3T3 cells proliferation and adhesion than those with coarse structure [15]. The study of Huang et al. demonstrated that their prepared nanostructured Ti-25Nb-3Mo-3Zr-2Sn (TLM) could support the adhesion and proliferation of hFOB1.19 cells better than their prepared microstructured TLM [16]. Moreover, Li et al. found that the compacts made of carbon nanotubes could promote osteogenic differentiation of human adipose-derived MSCs *in vitro* and bone formation

*in vivo*, while graphite compacts with the same component and dimension could not [17]. Therefore, the construction of nanostructures on Ti surface may be one of the effective methods to improve its osseointegration.

Surface mechanical attrition treatment (SMAT) is a potential physical modification method to obtain novel gradient nanostructured surface (GNS) Ti materials. The principle involves the use of steel balls to impact metal-based materials at high speed with indefinite impact direction under the action of ultrasonic waves, by which the surface of the material undergoes strong plastic deformation, gradually refined to nano-scale [18–25]. The surface of GNS is nano-scale and gradually increased to the micron levels as the distance from the surface increases.

In this study, the GNS Ti samples were prepared by SMAT, and annealed Ti samples were obtained by recrystallization annealing, making sure that the two kinds of specimens had similar roughness. Then, MG63 cells were cocultured with the two kinds of different structured Ti to investigate the material structure effects on the cellular behaviours. The effects of material structure changes on surface properties including mineralization capacity, protein adsorption capacity, and hydrophilicity were also comparatively investigated. This study aimed at elucidating the effects of GNS Ti on adhesion, proliferation, and apoptosis of the cells and clarifying the preliminary mechanism, providing a theoretical basis for the application of GNS Ti as a new dental implant or joint replacement material.

## 2. Materials and Methods

*2.1. Preparation of Materials.* The Ti plates were put into ultrasonic-assisted SMAT to produce GNS Ti, as described in previous work. Briefly, repeated plastic deformation under high strains and strain rates was produced within the surface layer of samples using a large number of hardened steel (AISI 52100) balls, which were vibrated in a chamber driven by an ultrasonic generator. Consequently, grains in the surface layer were effectively refined on the nano-scale, and a depth-dependent microstructure was generated. In this study, the SMAT process was performed for 20 min at a driving frequency of 20 kHz.

The controlled group was prepared by the SMAT procedure and followed by a recrystallization annealing process at 680°C for 2 h, so that the grain size was grown. The surface roughness values of the experimental group and controlled group were similar.

The GNS Ti and the annealed Ti were cut into cylindrical Ti pieces with a diameter of 11 mm and a thickness of 2.5 mm by using the electrospark discharge method. After being pickled in a 2 M HCl aqueous solution to remove any possible contamination, the samples were subsequently cleaned in acetone, absolute alcohol, and distilled water under ambient conditions and finally dried in air before testing.

*2.2. Surface Structures and Roughness.* The longitudinal sectional morphology was observed using an FEI Nova Nano SEM 430 scanning electronic microscope (SEM) operated at a voltage of 15 kV. Meanwhile, the samples were mechanically ground and polished and then etched in an electrolyte of perchloric acid, butyl alcohol, and methanol with the ratio 1 : 6 : 10 (in volume). Detailed microstructural characterization of the SMAT surface was conducted using transmission electron microscopy (TEM) with a JEOL-2010 unit operated at 200 kV. TEM thin foils were cut using the electrospark discharge technique, mechanically polished, dimpled, and finally ion milled from the untreated side. The surface roughness values of the different samples were observed using an Olympus LEXT OLS4000 confocal laser scanning microscope.

*2.3. Culture of MG63 Cells.* MG63 cells were provided by the Stem Cell and Regenerative Medicine Laboratory of China Medical University. MG63 cells were cultured in a high-glucose medium containing 10% fetal bovine serum and 0.2% gentamicin at 37°C with a humidified incubator containing 5% $CO_2$.

*2.4. SEM Observation.* After 1 day of culture, the two groups of materials were transferred to a new 24-well plate and washed three times with PBS for 5 min each. Then, the samples were fixed by 2.5% ($W/W$) buffered glutaraldehyde in 4°C refrigerator for more than 4 h and washed three times with PBS for 5 min each. Finally, the samples were dehydrated by gradient concentrations (15%, 30%, 45%, 60%, 75%, 90%, and 100%) of ethanol for 10 minutes each time and dried overnight. The adhesion and morphology of the cells were observed with a Hitachi S-3- 400 SEM operated at a voltage of 15 kV.

*2.5. MTS Analysis of Cell Proliferation.* The proliferation behaviour of MG63 cells was analyzed using optical density (OD) absorbance measurements. MG63 cells were seeded at $2 \times 10^4$ cells/cm$^2$ into two groups of materials and blank plates, and each well was made up with 2 ml of culture medium. Each group of materials was paved with 3 holes. After 1, 3, 5, and 7 days of culture, each group of materials was transferred to a new 24-well plate and rinsed twice with PBS. The samples were further cultured for 2 h in culture medium added with MTS. The optical density (OD) value of each well was measured by using an Infinite M200 microplate reader (Tecan Company, Switzerland) at a wavelength of 450 nm.

*2.6. Flow Cytometric Analysis of Cell Apoptosis.* The two groups of materials were immersed in DMEM culture medium at a ratio of 1 ml DMEM culture medium per 3 cm$^2$ and placed them in a 37°C incubator for 72 h. Effect of materials on cell apoptosis was studied using an Annexin V-FITC cell apoptosis detection kit from Solarbio (Beijing, China). The cells were seeded in new 24-well plates at a density of $1 \times 10^6$ cells/well. After 24 h of culture, the culture medium was replaced by the GNS Ti and annealed Ti extraction medium and incubated in 5% $CO_2$ at 37°C for 48 h. Cells cultured in the absence of samples were used as the negative control. The cells were collected by centrifugation and washed twice with PBS. Cell pellets were resuspended in 195 ml of Annexin V-FITC binding buffer. After the addition of 5 ml of Annexin V-FITC and 10 ml of propidium

iodide (PI), cells were incubated at room temperature for 15 minutes and subjected to analysis on a flow cytometer (Beckman Coulter, USA).

*2.7. Biomimetic Mineralization Experiment.* The GNS Ti and annealed Ti were placed vertically into six-well plates and immersed in simulated body fluid (SBF). The SBF was changed every two days. The samples were cultured in a constant temperature incubator (37°C) for 28 days. SEM was used to observe the change of surface morphology. Energy-dispersive X-ray spectroscopy (EDX, Hitachi, Japan) was used to detect the composition of surface deposits.

*2.8. Protein Adsorption Experiment.* The two groups of samples after sterilization were placed in 24-well plates with the treatment surface facing up. Each sample was added culture medium containing 10% fetal bovine serum and incubated at a 37°C incubator for 1, 4, and 24 hours. Then, the samples were transferred to new 24-well plates and gently rinsed 3 times with 1 ml phosphate buffer solution (PBS). One percent ($W/V$) of sodium dodecyl sulfate (SDS) was added to each well. The samples were shaken on a shaker at 70 r/min for 30 min to elute the protein adsorbed on the surface of the samples. The total protein concentration collected in the SDS solution was measured by a microplate reader at a wavelength of 562 nm.

*2.9. Hydrophilic Experiment.* The hydrophilicity of GNS Ti and annealed Ti was studied by measuring the contact angles with deionized water and materials by using a contact angle measuring instrument (German DataPhysics Company). Three parallel samples were set in the experiment. Different areas of each sample was tested three times with deionized water. The average value was used as the corresponding index test value to ensure the reliability of the experimental results.

*2.10. Statistical Analysis.* All results were generated in three independent experiments with three repeats. The results were processed by the SPSS17.0 software and expressed as mean ± standard deviation (standard error). One-way ANOVA was used to compare the OD value and protein adsorption between the groups. The comparison between groups was performed by the LSD $t$ test. The difference was statistically significant at $P < 0.05$.

## 3. Results

*3.1. Surface Structure and Roughness of the GNS Ti and the Annealed Ti.* In this study, the samples were characterized by SEM, TEM, and confocal laser scanning microscopy, respectively. Evidence of plastic deformation, microstructure refinement, and the differences in surface roughness between the materials were clearly observed in Figure 1. As shown in Figures 1(a) and 1(b), the longitudinal section image of GNS Ti samples displayed a gradient change that the grain size gradually decreased from the sample interior to the treated surface, accompanied by gradually intensifying plastic deformation. The microstructure in the top surface layer could not be clearly observed in the SEM image due to the extremely small grain size and intensive deformation. In comparison, no gradient microstructural characterization could be found in annealed Ti samples. As shown in Figure 1(c), TEM observation revealed that the grains in the top surface layer of the GNS Ti samples were refined into nanometer scale with random crystallographic orientations. The difference of surface morphology was further demonstrated by the 3D isoheight images captured by the confocal laser scanning microscopy and quantified with surface roughness parameters, as shown in Figures 1(d) and 1(e). The surface roughness ($R_a$) values of the GNS Ti and annealed Ti samples were $1.76 \pm 0.13\,\mu$m and $1.84 \pm 0.09\,\mu$m, respectively. After statistical analysis, there was no statistical difference in surface roughness between two groups of materials ($P > 0.05$). The effect of material surface roughness on the cellular behaviours was ruled out.

*3.2. Behaviours of MG63 Cells on the GNS Ti Samples and the Annealed Ti Samples.* As shown in Figures 2(a)–2(f), the morphology of MG63 cells cultured on the two kinds of materials for 1 day was presented. The MG63 cells were observed to spread homogenously and fully on the surface of GNS Ti samples. Meanwhile, the MG63 cells were predominantly in the shape of polygon, reaching out plentiful filopodia to touch the surface of samples or connecting neighboring cells. In contrast, the number of MG63 cells that adhered to the annealed Ti was less than that on the GNS Ti. MG63 cells were usually isolated on the surface of annealed Ti, having fewer pseudopods protruding.

Typically, OD absorbance values of samples cultured for different times were measured to evaluate the proliferation kinetics of MG63 cells. MG63 cells were cocultured with GNS Ti and annealed Ti for 1, 3, 5, and 7 days. As shown in Figure 2(g), MG63 cells proliferated well on the GNS Ti surface within the entire culturing time, suggesting good biocompatibility of the GNS Ti group. There was no difference in the number of MG63 cells at 1 day between the two groups, while the GNS Ti group showed significantly higher OD values at 3, 5, and 7 days ($P < 0.05$), implying MG63 cells displayed better proliferation capacity on the GNS Ti. Slopes of the two group of samples are as follows: from day 1 to day 3: $0.13185 \pm 0.03035$ vs. $0.08835 \pm 0.03515$, $P < 0.05$; from day 3 to day 5: $0.05995 \pm 0.0018$ vs. $0.0338 \pm 0.00885$, $P < 0.05$; and from day 5 to day 7: $0.0657 \pm 0.01395$ vs. $0.04915 \pm 0.00335$, $P < 0.05$. After statistical analysis, the slopes of samples were statistically different on the 3rd, 5th, and 7th days ($P < 0.05$).

The scatter plot of cell suspensions was observed to reveal the results of cell apoptosis, as shown in Figures 2(h)–2(j). The blank control group and the GNS Ti group were concentrated a large number of live cells in the lower left quadrant, and the late apoptotic cells of the GNS Ti group were significantly more than the blank control group. Numerous advanced apoptotic and necrotic cells were identified in the right upper quadrant of the annealed Ti group. Table 1 showed that no significant differences among the contents of the early apoptotic cells, late apoptotic cells, and necrotic cells were found between the blank control group and the GNS Ti group. However, these three types of cells in the

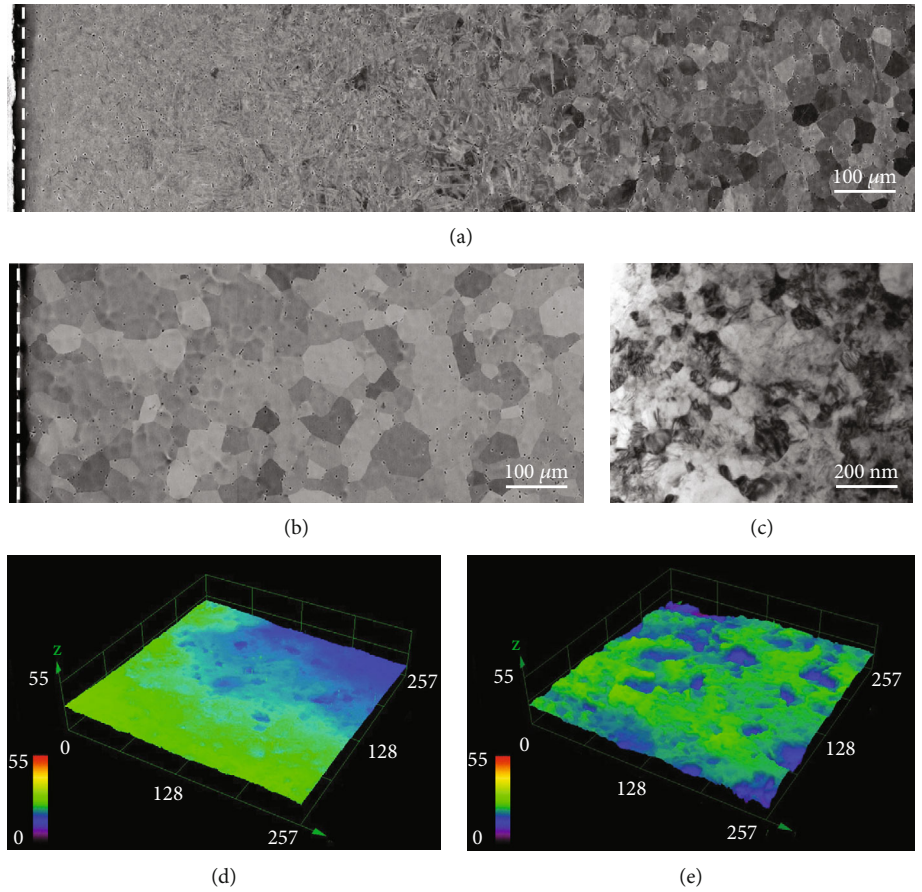


Figure 1: (a, b) Longitudinal section SEM images of the GNS Ti samples and the annealed Ti samples. The dashed lines mark the treated surfaces before and after annealing. (c) Typical bright-field TEM images of the top surface layer of the GNS Ti samples. (d, e) 3D isoheight images show the surface roughness values of the GNS Ti samples and the annealed Ti samples.

annealed Ti group were larger in number than those in the blank control group ($P < 0.05$). The early apoptotic cells, late apoptotic cells, and necrotic cells in the group were higher than those in the GNS Ti group ($P < 0.05$).

*3.3. Surface Properties of the GNS Ti Samples and the Annealed Ti Samples.* To compare the biomineralization ability, the samples were immersed in SBF for 28 days. From Figures 3(a)–3(d), it could be seen that the surface of GNS Ti induced the formation of new compounds and formed a spherical coating after 28 days of SBF incubation. The surface of annealed Ti was snow-like coating that did not induce the formation of new compounds. Furthermore, the EDX analysis showed that these new compounds on the GNS Ti surface (Figures 3(e) and 3(f)) mainly contained calcium and phosphorus.

The difference in surface properties of the GNS Ti and annealed Ti was reflected by measuring the total protein adsorption of the two groups of samples. The total protein adsorbed on the GNS Ti and annealed Ti surfaces from cell culture medium containing fetal bovine serum after 1, 4, and 24 h of incubation are displayed in Table 2 and Figure 3(g). At each incubation time, the GNS Ti significantly promoted the adsorption amounts of total protein compared to annealed Ti. After statistical analysis, the protein adsorption results between the two groups were statistically different on the 1st, 4th, and 24th hours ($P < 0.05$). Especially, the amount of protein adsorption of the GNS Ti increased rapidly during 4 hours compared with that of the annealed Ti. Overall, the GNS Ti completed the protein adsorption on the surface in a comparatively short time.

Water droplet contact angle measurements were used to test the surface hydrophilicity of the GNS Ti and the annealed Ti (Figures 3(h) and 3(i)). The contact angle of the GNS Ti surface was significantly smaller than that of the control surface ($53.7^\circ \pm 2.4^\circ$ vs. $96.9^\circ \pm 3.8^\circ$, $P < 0.05$), suggesting relatively better hydrophilicity of GNS Ti surfaces, which might come from the specific nanostructure of GNS Ti.

## 4. Discussion

In this study, to improve the osseointegration ability of Ti, we prepared GNS Ti samples by SMAT. The annealed Ti samples were used as control. It was shown by SEM that the average grain size of GNS Ti was nano-scale on the uppermost surface and gradually increased to submicron and micron levels as the distance from the surface increases. In comparison, no such nanostructural characterization could be found

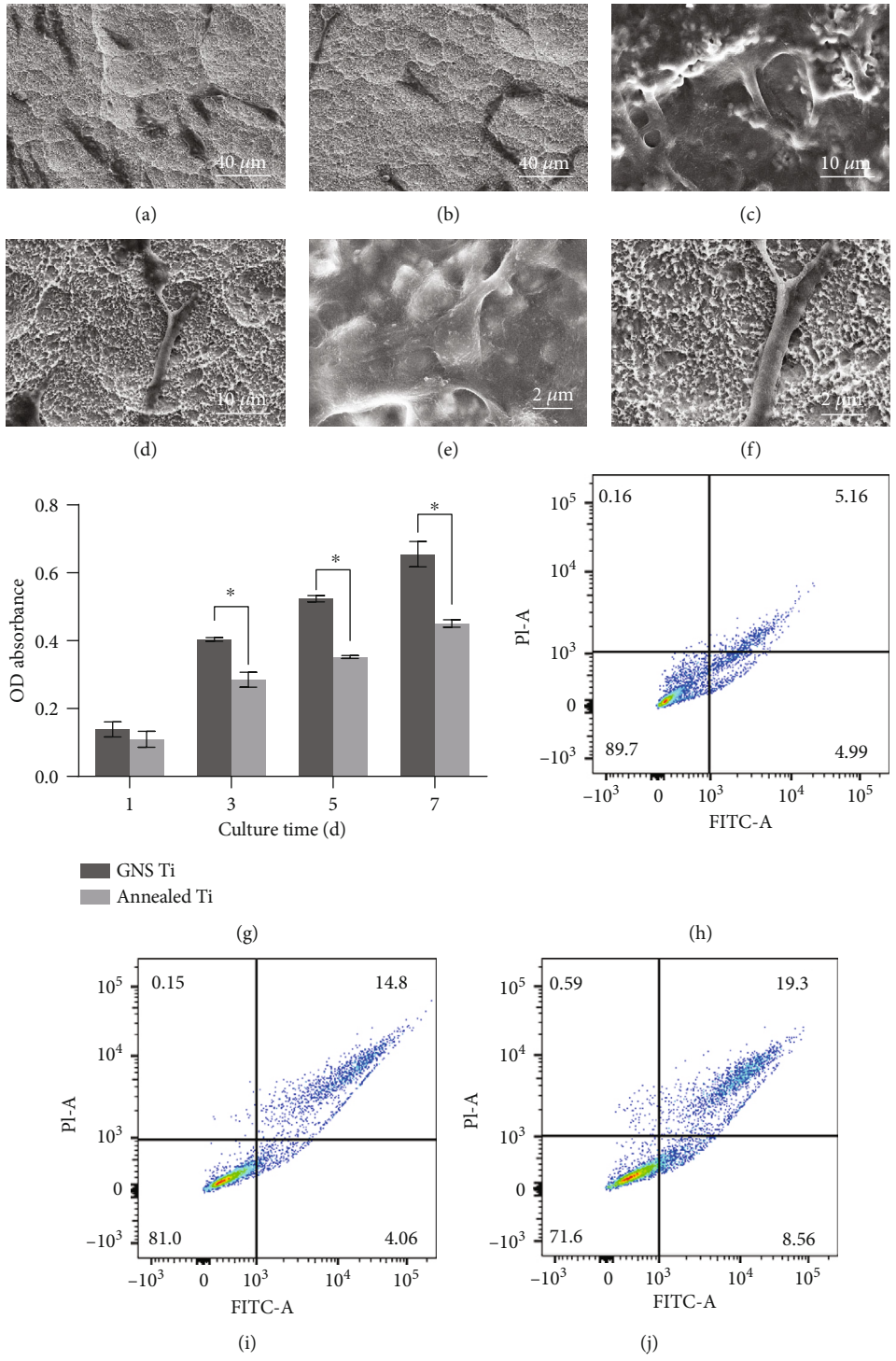


FIGURE 2: (a–f) SEM morphologies of MG63 cells cultured the surfaces of (a, c, e) the GNS Ti samples and (b, d, f) the annealed Ti samples after culturing for 1 day. (g) Proliferation curves of MG63 cells on the GNS Ti and the annealed Ti samples, reflected by measuring OD absorbance values after cultured for 1, 3, 5, and 7 days (mean ± SD, $n = 3$, * indicates $P < 0.05$). (h–j) Flow cytometry results show the MG63 cells apoptosis rate of the blank control group, the GNS Ti group, and the annealed Ti group.

in the annealed Ti samples, and the average grain size of annealed Ti was micron-scale in the top surface layer. To evaluate the effectiveness of the nanostructure *in vitro*, we cultured MG63 cells on the two kinds of Ti samples and subsequently compared cellular behaviours. MG63 cells had the ability of rapid proliferation, strong activity, and unlimited channels. In recent years, they had been widely used in the research of coculture of metal materials and osteoblast-like cells [26]. After 1 day of culture, samples were observed by SEM operated at voltage of 15 kV, which showed the

Table 1: Flow cytometry results showing the MG63 cells apoptosis rate of the blank control group, the GNS Ti group, and the annealed Ti group.

| Cell | Blank control (%) | GNS Ti (%) | Annealed Ti (%) |
|---|---|---|---|
| Late apoptotic cells and necrotic cells | $6.76 \pm 2.07$ | $10.38 \pm 3.52^{\Delta}$ | $15.82 \pm 3.30^{*}$ |
| Early apoptotic cells | $3.93 \pm 1.11$ | $4.31 \pm 0.97^{\Delta}$ | $9.83 \pm 3.74^{*}$ |
| Normal cells | $88.03 \pm 2.43$ | $84.54 \pm 3.77^{\Delta}$ | $73.42 \pm 2.49$ |

Data are presented as mean ± SD, $n = 3$, and $^{*}$ indicates $P < 0.05$, compared with the blank control group. Data are presented as mean ± SD, $n = 3$, $^{\Delta}$ indicates $P < 0.05$, compared with the annealed Ti group.

adhesion and morphology of the MG63 cells. The proliferation behaviour of MG63 cells was analyzed by optical density (OD) absorbance measurements after 1, 3, 5, and 7 days of culture. After 6 days of culture, we analyzed the cell suspensions of each group by flow cytometry to study the effect of materials on cell apoptosis. Cell adhesion, proliferation, and apoptosis have been always important indicators for evaluating osteointegration of implants. Adhesion is usually the initial event after cells come into contact with materials [27]. Bahl et al. reported that the cellular ability to resist the impact of body fluids or blood flow increased with the improving cell adhesion effect in a physiological environment [28]. On the other hand, Logan et al. found that the enhanced adhesion effect of mesenchymal stem cells could promote subsequent cell proliferation and osteogenic differentiation [29]. Therefore, cell adhesion effect was crucial for regulating subsequent cellular behaviours. Wang et al. reported that the main functions of osteoblasts which induced from stem cells were to synthesize bone matrix and promote mineralization of the matrix to form bone tissue [30]. The excellent osteoblast proliferation ability could accelerate the occurrence of osteointegration on the surface of the materials [31]. Yuan et al. reported that osteoblast apoptosis was related to bone reconstruction in multiple parts of the body. Inhibition of osteoblast apoptosis could prolong the survival time of cells and affect osseointegration around orthopedic implants [32]. It was found in this study that the MG63 cells on the GNS Ti spread better and the cells were polygonal with more pseudopods after 1 day of culture. The result suggested that GNS Ti could promote the cell adhesion effect better than the annealed Ti. The OD values of the two groups of materials were statistically different on the 3rd, 5th, and 7th days ($P < 0.05$). Moreover, the slope of the GNS Ti group was larger than that of the control group, indicating that GNS Ti could promote the cell proliferation better than the control group. The results of flow cytometry demonstrated that the number of viable cells in the GNS Ti group was more than that in the annealed Ti group, while the number of late apoptotic cells in the annealed Ti group were significantly more than that in the GNS Ti group, which showed that the ability of GNS Ti to inhibit cell apoptosis was higher than that of annealed Ti. The above results demonstrated that the nanostructure on the Ti surface might be one of the effective methods to improve cellular behaviours of the osteoblast-like cells.

In order to explore the related mechanism of GNS Ti promoting cellular behaviours, we tested the mineralization ability, protein adsorption, and hydrophilicity of two sets of materials because it has been shown that cellular behaviours might be affected by those properties [33–40]. Lee et al. found that the compound formed by calcium and phosphorus deposition could significantly improve the adhesion and proliferation of bone marrow mesenchymal stem cells [41]. Moreover, Sharkov et al. reported that the osteoblasts were cocoltured with compound formed by calcium and phosphorus deposition, the results of which showed that the compound could obviously upregulate the expression level of osteogenesis-related genes of the cells [42]. So, the increased calcium and phosphorus deposition could promote osteogenic behaviours of cells. The results of biomimetic mineralization experiment in this study demonstrated that the surface of GNS Ti induced the formation of new compounds and formed a spherical coating. The surface of annealed Ti was snow-like coating and did not induce the formation of new compounds. Furthermore, the EDX analysis showed that those new compounds on the GNS Ti surface mainly contained calcium and phosphorus. Durmus et al. reported that the SMAT metal materials showed excellent hydrogen storage reversibility and promoted surface activation. As the surface activation energy was increasing, the adsorption capacity for calcium and phosphorus ions increased [26]. Venkatsurya et al. found that the surface energy of materials was increased after SMAT, so that the mineralization was promoted [43]. Therefore, the gradient nanostructure obtained after SMAT treatment in this study might improve the surface mineralization ability of materials.

On the other hand, it was well known that the first step for biomaterial after implantation is protein adsorption, and the composition and structure of the material surface determine the amount and type of protein adsorption [44]. The greater the amount of protein adsorbed, the better the adhesion of subsequent cells [45–50]. In this study, it was shown that as the incubation time increased, the amount of protein adsorption of the GNS Ti was always more than that of the annealed Ti. The amount of protein adsorption was statistically different on 1st, 4th, and 24th hours ($P < 0.05$). Especially, the amount of protein adsorption of the GNS Ti materials increased rapidly during 4 hours compared with that of the annealed Ti. So it was indicated that the GNS Ti had better protein adsorption capacity than the annealed Ti and completed the protein adsorption on the surface in a comparatively short time.

Moreover, the cellular behaviours were closely related to the hydrophilicity of the materials [51]. It was reported that the surface of untreated Ti implants were generally weakly hydrophilic or even hydrophobic [52]. However, in this

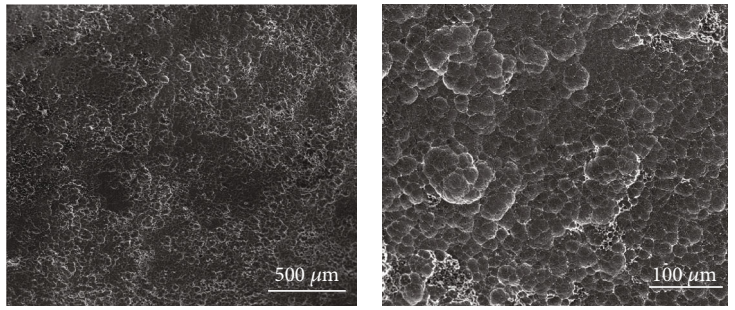


(a) (b)

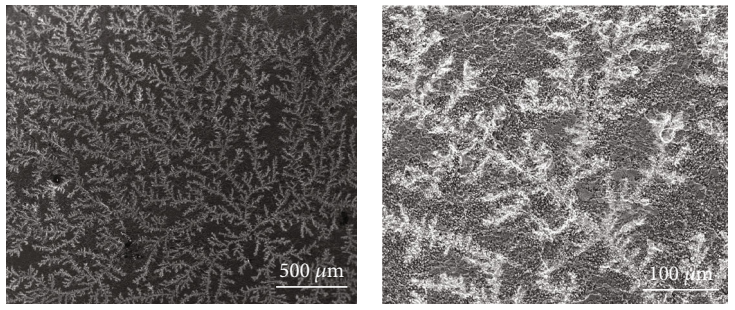


(c) (d)

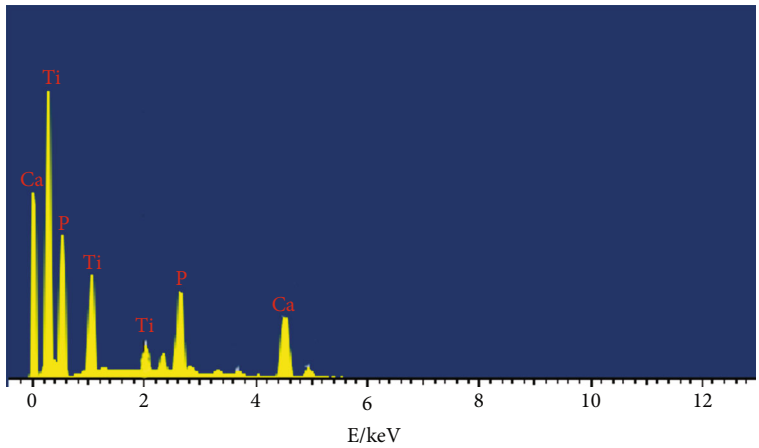


(e)

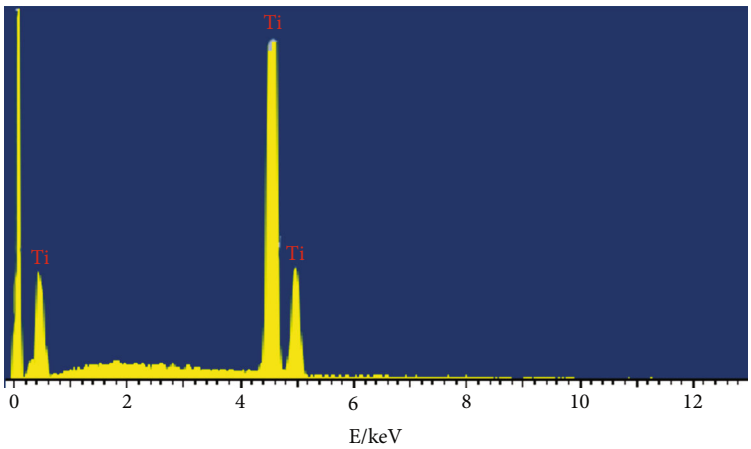


(f)

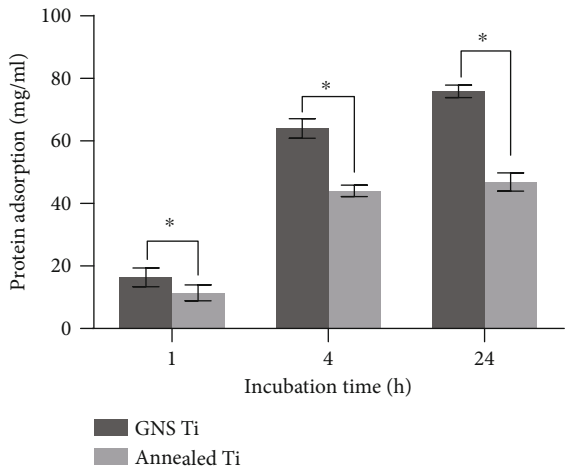


(g)

Figure 3: Continued.

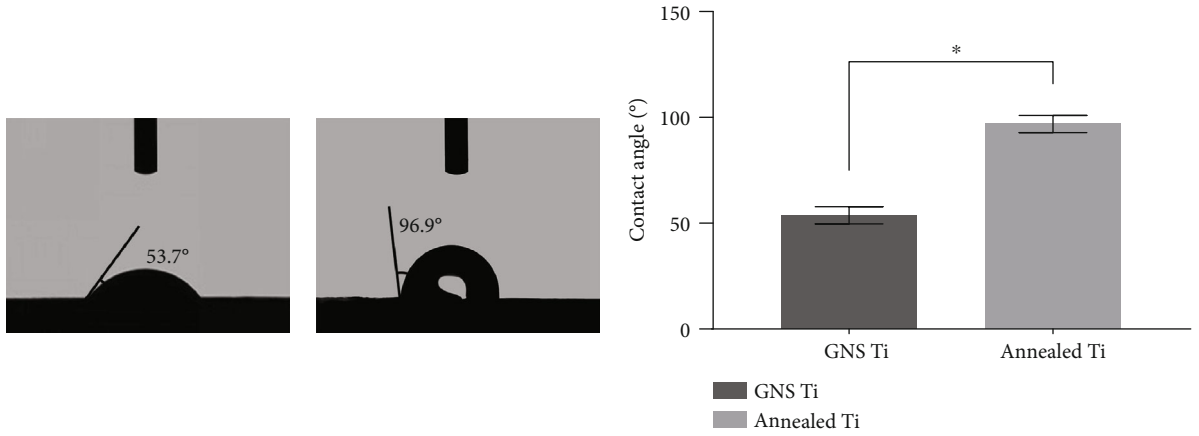


Figure 3: (a–d) SEM images show the results of biomimetic mineralization on the surface of (a, b) the GNS Ti samples and (c, d) the annealed Ti samples after immersion in SBF for 28 days. (e, f) EDX analysis performed on the GNS Ti samples and the annealed Ti samples immersed in SBF for 28 days. (g) Protein adsorption results on the GNS Ti samples and the annealed Ti samples immersed in medium containing 10% fetal bovine serum for 1, 4, and 24 h. (mean ± SD, $n = 3$, * indicates $P < 0.05$). (h–j) Water droplet contact angles of the GNS Ti samples and the annealed Ti samples (mean ± SD, $n = 3$, * indicates $P < 0.05$).

Table 2: The protein adsorption results of the GNS Ti and annealed Ti samples at different time points.

| Time/h | 1 | 4 | 24 |
|---|---|---|---|
| GNS Ti ($\mu$g/ml) | 16.3861 ± 3.0270* | 64.0108 ± 3.1453* | 75.8873 ± 2.0287* |
| Annealed Ti ($\mu$g/ml) | 11.4245 ± 2.5289 | 54.0222 ± 1.8226 | 56.8764 ± 2.9268 |

Data are presented as mean ± SD, $n = 3$, * indicates $P < 0.05$, compared with the annealed Ti group.

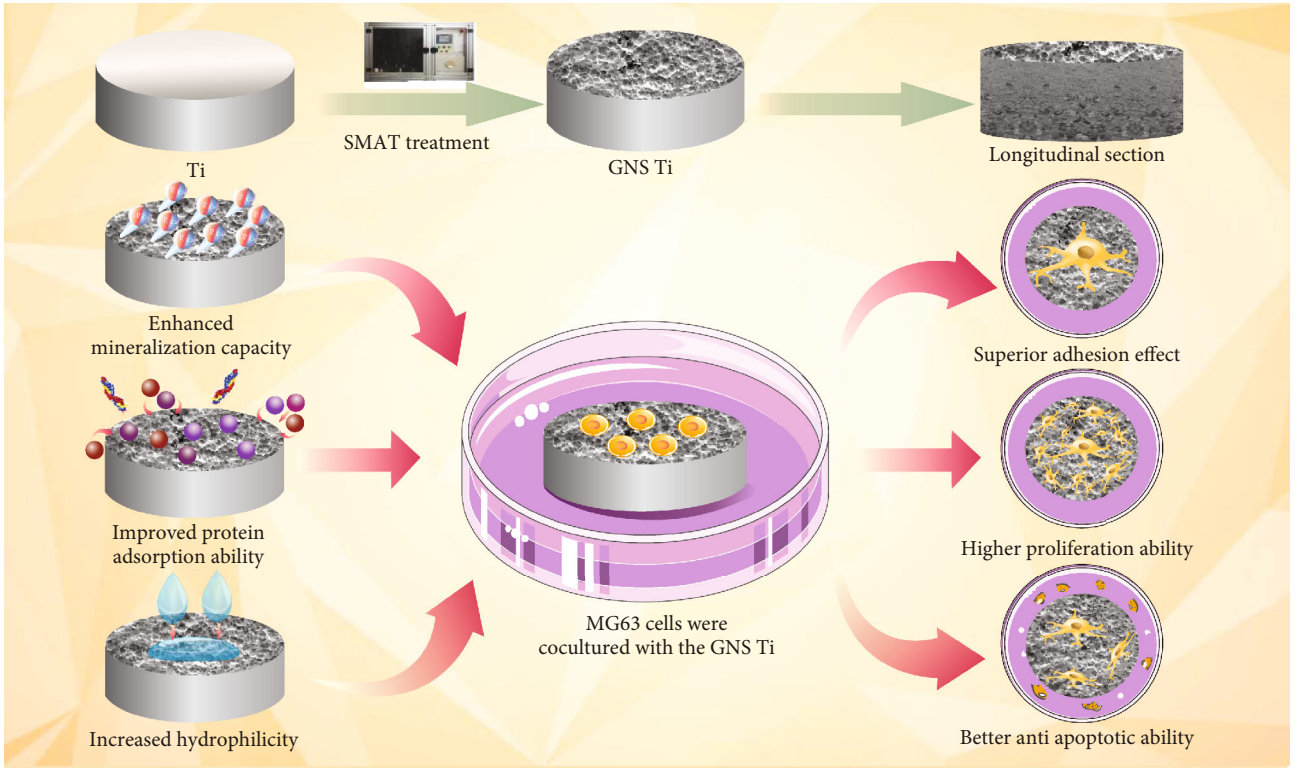


Figure 4: The pattern diagram for the effect of GNS Ti on behaviours of MG63 cells *in vitro* and its preliminary mechanism.

study, the results showed that GNS Ti was significantly more hydrophilic than the annealed Ti. Ji et al. reported that the surface of the hydrophilic material could increase the amount of adsorbed protein, thereby promoting the adhesion of osteoblasts and inhibiting cell apoptosis [53]. Li et al. found that the excellent surface hydrophilicity could obtain larger surface energy, promoting the behaviours of human periodontal ligament stem cells [54]. Edalati et al. reported that the surface of the hydrophilic material had a more active biological conformation, which promoted adhesion of MC-3T3 cells [55].

In this study, the enhanced hydrophilicity might be another main reason why the GNS Ti promoted cellular behaviours better.

Above all, this study has demonstrated the effects of GNS Ti on behaviours of MG63 cells *in vitro* and elucidated its preliminary mechanism, as shown in Figure 4. It provides the theoretical and experimental foundations for the applications of GNS Ti in dental implants. However, the related molecular biology mechanism of GNS Ti remains unclear, and *in vivo* study is still blank. Before a new material can be used in clinic, it must undergo a lot of comprehensive *in vivo* and *in vitro* studies [56, 57]. In the near future, we will focus on whether GNS Ti can promote osteogenic differentiation of bone-related cells to further examine the osteogenic functions of the GNS Ti. Simultaneously, we will conduct a series of animal experiments to detect whether the material has the problems of metal ion release in the body and evaluate the biocompatibility of the GNS Ti. Furthermore, we will implant GNS Ti into the mandibular defect of animals to examine the formation of the new bone around the material. Hopefully, we can come up with more meaningful and constructive research results soon.

## 5. Conclusion

In this study, GNS Ti was successfully prepared by means of SMAT. *In vitro* studies into behaviours of the cultured MG63 cells demonstrated that the GNS Ti promoted adhesion effect and proliferation of the cells better than the annealed Ti, while the ability of GNS Ti to inhibit cell apoptosis was better than that of annealed Ti, the preliminary mechanism of which indicated by this study might be the enhanced mineralization capacity, protein adsorption ability, and hydrophilicity of the GNS Ti due to its specific nanostructure that improved the cell behaviours. Although further investigations into the *in vivo* responses are needed, we believe that the GNS Ti will find broad applications in dental implants and joint replacements.

## Data Availability

The data used to support the findings of this study are available from the corresponding author upon request.

## Conflicts of Interest

The authors declare that there are no conflicts of interest regarding the publication of this paper.

## Authors' Contributions

Xue Luo, Chen Liang, and Ning Li contributed equally to this work.

## Acknowledgments

This study was supported by the National Natural Science Foundation of China (No. 81970980), Liaoning Provincial Key Research Plan Guidance Project (No. 2018225078), Liaoning Provincial Natural Science Foundation Guidance Project (No. 2019-ZD-0749), Liaoning Province, Colleges and Universities Basic Research Project (No. LFWK201717), Central Government of Liaoning Province to Guide Local Science and Technology Development Project (No. 2017108001), Shenyang Major Scientific and Technological Innovation Research and Development Plan (No. 19-112-4-027), and the Second Batch of Medical Education Scientific Research Projects of the 13th Five-Year Plan of China Medical University (No. YDJK2018017).

## References

[1] N. Aparna and S. Rajesh, "Tooth-implant connection: a critical review," *Journal of Dental Implants*, vol. 3, no. 2, pp. 142–147, 2013.

[2] G. E. Abrosimova and A. S. Aronin, "Surface morphology of deformed amorphous-nanocrystalline materials and the formation of nanocrystals," *Journal of Surface Investigation: X-Ray, Synchrotron and Neutron Techniques*, vol. 12, no. 3, pp. 492–498, 2018.

[3] A. Muthuchamy, M. Rajadurai, A. R. Annamalai, and D. K. Agrawal, "Effect of nickel addition on microstructure and mechanical properties of the spark plasma sintered Ti–6Al–4V alloy," *Transactions of the Indian Institute of Metals*, vol. 72, no. 8, pp. 2127–2134, 2019.

[4] H. Xing, X. Wang, S. Xiao et al., "Osseointegration of layer-by-layer polyelectrolyte multilayers loaded with IGF1 and coated on titanium implant under osteoporotic condition," *International Journal of Nanomedicine*, vol. 12, no. 3, pp. 7709–7720, 2017.

[5] C. C. Novak, A. R. Hsu, C. J. Della Valle et al., "Metal ion levels in maternal and placental blood after metal-on-metal total hip arthroplasty," *American Journal of Orthopedics*, vol. 43, no. 12, pp. E304–E308, 2014.

[6] A. Deing, T. Ebel, R. Willumeit-Römer, and B. J. C. Luthringer, "Comparison of the influence of phospholipid-coated porous Ti-6Al-4V material on the osteosarcoma cell line Saos-2 and primary human bone derived cells," *Metals*, vol. 6, no. 3, p. 66, 2016.

[7] A. Hatem, J. Lin, R. Wei et al., "Tribocorrosion behavior of low friction TiSiCN nanocomposite coatings deposited on titanium alloy for biomedical applications," *Surface & Coatings Technology*, vol. 347, no. 7, pp. 1–12, 2018.

[8] Q. Yao, J. Sun, G. Zhang, W. Tong, and H. Zhang, "Enhanced toughness of nitrided layers formed on Ti-6Al-4V alloy via surface mechanical attrition pre-treatment," *Vacuum*, vol. 142, no. 3, pp. 45–51, 2017.

[9] F. Veronesi, G. Giavaresi, M. Fini et al., "Osseointegration is improved by coating titanium implants with a nanostructured thin film with titanium carbide and titanium oxides clustered

around graphitic carbon," *Materials Science and Engineering C*, vol. 70, Part 1, pp. 264–271, 2017.

[10] T. J. Webster and J. U. Ejiofor, "Increased osteoblast adhesion on nanophase metals: Ti, Ti6Al4V, and CoCrMo," *Biomaterials*, vol. 25, no. 19, pp. 4731–4739, 2004.

[11] G. K. Thakral, R. Thakral, N. Sharma, J. Seth, and P. Vashisht, "Nanosurface – the future of implants," *Journal of Clinical and Diagnostic Research*, vol. 8, no. 5, pp. ZE07–ZE10, 2014.

[12] K. Zhang, Y. Fan, N. Dunne, and X. Li, "Effect of microporosity on scaffolds for bone tissue engineering," *Regenerative Biomaterials*, vol. 5, no. 2, pp. 115–124, 2018.

[13] L. Bacakova, E. Filova, J. Liskova, I. Kopova, M. Vandrovcova, and J. Havlikova, "Chapter 4 - Nanostructured materials as substrates for the adhesion, growth, and osteogenic differentiation of bone cells," *Nanobiomaterials in Hard Tissue Engineering*, vol. 4, pp. 103–153, 2016.

[14] Y. Chen, H. Zhao, R. Wang, B. Lan, and L. Deng, "Characterization and evaluation of titanium substrates coated with gelatin/hydroxyapatite composite for culturing rat bone marrow derived mesenchymal stromal cells," *Biomedical Engineering: Applications, Basis and Communications*, vol. 24, no. 3, pp. 197–206, 2012.

[15] S. P. Yang, H. S. Wen, T. M. Lee, and T. S. Lui, "Cell response on the biomimetic scaffold of silicon nano- and microtopography," *Journal of Materials Chemistry B*, vol. 4, no. 10, pp. 1891–1897, 2016.

[16] R. Huang, H. Zhuang, and Y. Han, "Second-phase-dependent grain refinement in Ti–25Nb–3Mo–3Zr–2Sn alloy and its enhanced osteoblast response," *Materials Science and Engineering: C*, vol. 35, no. 7, pp. 144–152, 2014.

[17] X. Li, H. Liu, X. Niu et al., "The use of carbon nanotubes to induce osteogenic differentiation of human adipose-derived MSCs *in vitro* and ectopic bone formation *in vivo*," *Biomaterials*, vol. 33, no. 19, pp. 4818–4827, 2012.

[18] W. Wang, S. Liao, Y. Zhu, M. Liu, Q. Zhao, and Y. Fu, "Recent applications of nanomaterials in prosthodontics," *Journal of Nanomaterials*, vol. 2015, Article ID 408643, 11 pages, 2015.

[19] X. Wu, N. Tao, Y. Hong et al., "Strain-induced grain refinement of cobalt during surface mechanical attrition treatment," *Acta Materialia*, vol. 53, no. 3, pp. 681–691, 2005.

[20] W. Wang, Q. Zhao, S. Liao, and Y. Zhu, "Application of stem cells and nanomaterials in prosthodontics," *Journal of Nanoscience and Nanotechnology*, vol. 16, no. 9, pp. 8935–8947, 2016.

[21] C. Y. Guo, A. T. H. Tang, and J. P. Matinlinna, "Insights into surface treatment methods of titanium dental implants," *Journal of Adhesion Science and Technology*, vol. 26, no. 1-3, pp. 189–205, 2012.

[22] X. Li, L. Wang, Y. Fan, Q. Feng, F. Z. Cui, and F. Watari, "Nanostructured scaffolds for bone tissue engineering," *Journal of Biomedical Materials Research Part A*, vol. 101A, no. 8, pp. 2424–2435, 2013.

[23] X. Li, J. Wei, K. E. Aifantis et al., "Current investigations into magnetic nanoparticles for biomedical applications," *Journal of Biomedical Materials Research Part A*, vol. 104, no. 5, pp. 1285–1296, 2016.

[24] G. Wang, X. Liu, H. Zreiqat, and C. Ding, "Enhanced effects of nano-scale topography on the bioactivity and osteoblast behaviors of micron rough $ZrO_2$ coatings," *Colloids and Surfaces B: Biointerfaces*, vol. 86, no. 2, pp. 267–274, 2011.

[25] F. F. Borghi, P. A. Bean, M. D. M. Evans, T. van der Laan, S. Kumar, and K. Ostrikov, "Nanostructured graphene surfaces promote different stages of bone cell differentiation," *Nano-Micro Letters*, vol. 10, no. 3, p. 47, 2018.

[26] N. G. Durmus and T. J. Webster, "Nanostructured titanium: the ideal material for improving orthopedic implant efficacy?," *Nanomedicine*, vol. 7, no. 6, pp. 791–793, 2012.

[27] B. B. Shotorbani, E. Alizadeh, R. Salehi, and A. Barzegar, "Adhesion of mesenchymal stem cells to biomimetic polymers: a review," *Materials Science and Engineering*, vol. 71, no. 4, pp. 1192–1200, 2017.

[28] S. Bahl, B. T. Aleti, S. Suwas, and K. Chatterjee, "Surface nanostructuring of titanium imparts multifunctional properties for orthopedic and cardiovascular applications," *Materials & Design*, vol. 144, no. 7, pp. 169–181, 2018.

[29] N. Logan, A. Sherif, A. J. Cross et al., "$TiO_2$-coated CoCrMo: improving the osteogenic differentiation and adhesion of mesenchymal stem cells *in vitro*," *Journal of Biomedical Materials Research Part A*, vol. 103, no. 3, pp. 1208–1217, 2015.

[30] P. Wang, L. Zhao, J. Liu, M. D. Weir, X. Zhou, and H. H. K. Xu, "Bone tissue engineering via nanostructured calcium phosphate biomaterials and stem cells," *Bone Research*, vol. 2, no. 1, article 14017, 2014.

[31] X. Liu, B. Wang, Y. Sun, Y. Jia, and Z. Xu, "Astragalus root extract inhibits retinal cell apoptosis and repairs damaged retinal neovascularization in retinopathy of prematurity," *Cell Cycle*, vol. 18, no. 22, pp. 3147–3159, 2019.

[32] Y. Yuan, S. Jin, X. Qi et al., "Osteogenesis stimulation by copper-containing 316L stainless steel via activation of akt cell signaling pathway and Runx2 upregulation," *Journal of Materials Science & Technology*, vol. 35, no. 11, pp. 2727–2733, 2019.

[33] F. Variola, J. B. Brunski, G. Orsini, P. Tambasco de Oliveira, R. Wazen, and A. Nanci, "Nanoscale surface modifications of medically relevant metals: state-of-the art and perspectives," *Nanoscale*, vol. 3, no. 2, pp. 335–353, 2011.

[34] K. Zhang, X. F. Xiao, X. M. Wang, Y. B. Fan, and X. M. Li, "Topographical patterning: characteristics of current processing techniques, controllable effects on material properties and co-cultured cell fate, updated applications in tissue engineering, and improvement strategies," *Journal of Materials Chemistry B*, vol. 7, no. 45, pp. 7090–7109, 2019.

[35] L. Wang, S. Wu, G. Cao, Y. Fan, N. Dunne, and X. Li, "Biomechanical studies on biomaterial degradation and co-cultured cells: mechanisms, potential applications, challenges and prospects," *Journal of Materials Chemistry B*, vol. 7, no. 47, pp. 7439–7459, 2019.

[36] S. Faghihi, D. Li, and J. A. Szpunar, "Tribocorrosion behaviour of nanostructured titanium substrates processed by high-pressure torsion," *Nanotechnology*, vol. 21, no. 48, article 485703, 2010.

[37] B. C. Ward and T. J. Webster, "The effect of nanotopography on calcium and phosphorus deposition on metallic materials *in vitro*," *Biomaterials*, vol. 27, no. 16, pp. 3064–3074, 2006.

[38] C. Wang, G. Cao, T. Zhao et al., "Terminal group modification of carbon nanotubes determines covalently bound osteogenic peptide performance," *ACS Biomaterials Science & Engineering*, vol. 6, no. 2, pp. 865–878, 2020.

[39] R. Huang, S. Lu, and Y. Han, "Role of grain size in the regulation of osteoblast response to Ti–25Nb–3Mo–3Zr–2Sn alloy,"

*Colloids and Surfaces B: Biointerfaces*, vol. 111, no. 1, pp. 232–241, 2013.

[40] M. Jamesh, T. S. N. Sankara Narayanan, P. K. Chu, I. S. Park, and M. H. Lee, "Effect of surface mechanical attrition treatment of titanium using alumina balls: surface roughness, contact angle and apatite forming ability," *Frontiers of Materials Science*, vol. 7, no. 3, pp. 285–294, 2013.

[41] J. H. Lee, S. M. Lee, Y. C. Shin et al., "Spontaneous osteodifferentiation of bone marrow-derived mesenchymal stem cells by hydroxyapatite covered with graphene nanosheets," *Journal of Biomaterials and Tissue Engineering*, vol. 6, no. 10, pp. 818–825, 2016.

[42] E. V. Sharkov, A. V. Chistyakov, V. V. Shchiptsov, M. M. Bogina, and P. V. Frolov, "Origin of Fe-Ti oxide mineralization in the middle Paleoproterozoic Elet'ozero Syenite-Gabbro intrusive complex (Northern Karelia, Russia)," *Geology of Ore Deposits*, vol. 60, no. 2, pp. 172–200, 2018.

[43] P. K. C. Venkatsurya, W. W. Thein-Han, R. D. K. Misra, M. C. Somani, and L. P. Karjalainen, "Advancing nanograined/-ultrafine-grained structures for metal implant technology: interplay between grooving of nano/ultrafine grains and cellular response," *Materials Science and Engineering: C*, vol. 30, no. 7, pp. 1050–1059, 2010.

[44] S. A. Chamgordani, R. Miresmaeili, and M. Aliofkhazraei, "Improvement in tribological behavior of commercial pure titanium (CP-Ti) by surface mechanical attrition treatment (SMAT)," *Tribology International*, vol. 119, no. 2, pp. 744–752, 2018.

[45] A. Przekora, A. Benko, M. Blazewicz, and G. Ginalska, "Hybrid chitosan/$\beta$-1,3-glucan matrix of bone scaffold enhances osteoblast adhesion, spreading and proliferation via promotion of serum protein adsorption," *Biomedical Materials*, vol. 11, no. 4, article 045001, 2016.

[46] S. Khan, A. A. Ansari, C. Rolfo et al., "Evaluation of *in vitro* cytotoxicity, biocompatibility, and changes in the expression of apoptosis regulatory proteins induced by cerium oxide nanocrystals," *Science and Technology of Advanced Materials*, vol. 18, no. 1, pp. 364–373, 2017.

[47] G. O. Alrabeah, P. Brett, J. C. Knowles, and H. Petridis, "The effect of metal ions released from different dental implant-abutment couples on osteoblast function and secretion of bone resorbing mediators," *Journal of Dentistry*, vol. 66, pp. 91–101, 2017.

[48] D. De Santis, P. Pancera, U. Luciano et al., "Short-term in vivo evaluation of cellular DNA damage induced by fixed orthodontic appliances," *Journal of Biological Regulators and Homeostatic Agents*, vol. 32, 2 Supplement 2, pp. 75–80, 2018.

[49] T. A. Bhat, A. K. Chaudhary, S. Kumar et al., "Endoplasmic reticulum-mediated unfolded protein response and mitochondrial apoptosis in cancer," *Biochimica et Biophysica Acta - Reviews on Cancer*, vol. 1867, no. 1, pp. 58–66, 2017.

[50] C. Zhao, W. Ji, P. Han, J. Zhang, Y. Jiang, and X. Zhang, "In vitro and in vivo mineralization and osseointegration of nanostructured Ti6$Al_4$V," *Journal of Nanoparticle Research*, vol. 13, no. 2, pp. 645–654, 2011.

[51] K. M. Hotchkiss, G. B. Reddy, S. L. Hyzy, Z. Schwartz, B. D. Boyan, and R. Olivares-Navarrete, "Titanium surface characteristics, including topography and wettability, alter macrophage activation," *Acta Biomaterialia*, vol. 31, no. 3, pp. 425–434, 2016.

[52] I. G. Siller, A. Enders, T. Steinwedel et al., "Real-time live-cell imaging technology enables high-throughput screening to verify in vitro biocompatibility of 3D printed materials," *Materials*, vol. 12, no. 13, p. 2125, 2019.

[53] W. P. Ji, P. Han, C. L. Zhao, Y. Jiang, and X. N. Zhang, "Increased osteoblast adhesion on nanophase Ti6$Al_4$V," *Science Bulletin*, vol. 53, no. 11, pp. 1757–1762, 2008.

[54] Z. Li, J. Qiu, L. Q. du, L. Jia, H. Liu, and S. Ge, "$TiO_2$ nanorod arrays modified Ti substrates promote the adhesion, proliferation and osteogenic differentiation of human periodontal ligament stem cells," *Materials Science and Engineering: C*, vol. 76, pp. 684–691, 2017.

[55] K. Edalati, M. Novelli, S. Itano et al., "Effect of gradient-structure versus uniform nanostructure on hydrogen storage of Ti-V-Cr alloys: Investigation using ultrasonic SMAT and HPT processes," *Journal of Alloys and Compounds*, vol. 737, no. 4, pp. 337–346, 2018.

[56] X. Li, L. Wang, Y. Fan, Q. Feng, and F. Z. Cui, "Biocompatibility and toxicity of nanoparticles and nanotubes," *Journal of Nanomaterials*, vol. 2012, Article ID 548389, 19 pages, 2012.

[57] Z. Lin, Y. Zhao, P. K. Chu et al., "A functionalized $TiO_2$/$Mg_2$-$TiO_4$ nano-layer on biodegradable magnesium implant enables superior bone-implant integration and bacterial disinfection," *Biomaterials*, vol. 219, article 119372, 2019.

Hindawi
Journal of Nanomaterials
Volume 2020, Article ID 3863428, 13 pages
https://doi.org/10.1155/2020/3863428

*Research Article*

# Printability Optimization of Gelatin-Alginate Bioinks by Cellulose Nanofiber Modification for Potential Meniscus Bioprinting

**Wenbin Luo**,[1] **Zhengyi Song**,[2] **Zhonghan Wang**,[1] **Zhenguo Wang**,[2] **Zuhao Li**,[1] **Chenyu Wang**,[1,3] **He Liu**,[1] **Qingping Liu**,[2] **and Jincheng Wang**[1]

[1]*Department of Orthopedics, The Second Hospital of Jilin University, Changchun 130041, China*
[2]*Key Laboratory of Bionic Engineering (Ministry of Education), Jilin University, Changchun 130022, China*
[3]*Department of Plastic and Cosmetic Surgery, The First Hospital of Jilin University, Changchun 130021, China*

Correspondence should be addressed to He Liu; heliu@jlu.edu.cn, Qingping Liu; liuqp@jlu.edu.cn, and Jincheng Wang; jinchengwang2015@gmail.com

Received 21 March 2020; Accepted 7 April 2020; Published 5 May 2020

Academic Editor: Hui-Qi Xie



Meniscal injury is more likely to cause a permanent alteration of the biomechanical and biological environment of the knee joint, mainly due to the morphological mismatch and substantial loss of meniscal tissues. Herein, to overcome this challenge, we developed an improved bioink with enhanced printability, while maintaining the biocompatibility of major cellular component of the meniscus, namely fibrochondrocytes. Firstly, cellulose nanofiber (CNF) was mixed with gelatin-alginate thermal-responsive bioinks to improve the printability. Afterward, individual-specific meniscal prototypes based on the 3D reconstruction of MRI data were bioprinted using our bioink. The rheological and printability properties of the bioinks were characterized to select proper bioink content and bioprinting parameters. And then, a series of biological characterizations of the bioprinted samples, such as cell viability, metabolic activity, and extracellular matrix accumulation, were carried out in vitro. The results indicated that superior rheological performance and printability of CNF-modified bioink were achieved, ensuring high-precision bioprinting of specific-designed meniscal prototype when compared with the non-CNF-containing counterparts. Meanwhile, biological tests indicated that fibrochondrocytes encapsulated within the CNF-modified bioink maintained long-term cellular viability as well as acceptable extracellular matrix accumulation. This study demonstrates that the CNF-modified bioink is in favor of the printing fidelity of specific meniscus by improved rheological properties, minimizing the mismatch between artificial meniscal implants and native knee joint tissues, thereby permitting the evolution of clinical therapeutic methods of meniscal reconstruction.

## 1. Introduction

The menisci are two semilunar fibrocartilage structures located at the medial and lateral surface of the tibial plateau, which play a vital role in stabilization, nourishment, and force distribution of the knee joint [1]. Unfortunately, menisci are commonly involved in acute knee injury and osteoarthritis, resulting in substantial loss of meniscal tissue and permanent alteration of the biomechanical and biological environment of the knee joint [2]. Generally, meniscal allografts are applied in clinical with acceptable long-term follow-up results [3]. However, like all other allograft transplantation treatments, meniscal allografts are limited to tissue resources and the potential risk of mismatch, immunoreactivity, and disease transmission [4].

Several tissue engineering scaffolds have been developed with encouraging progress in avoiding meniscal allografting-relevant complications [5]. However, the mismatch of meniscal defect size and baseline articular cartilage still exists, leading to worsening articular cartilage status and greater displacement during long-term follow-up [6]. It has been reported that 1/3 mismatch of the meniscus could result in a 65% increase in peak local contact stresses, significantly deteriorating the degenerative changes of the articular cartilage [7]. Thus, the patient-specific design meeting individuals' joint requirements has been a vital element to

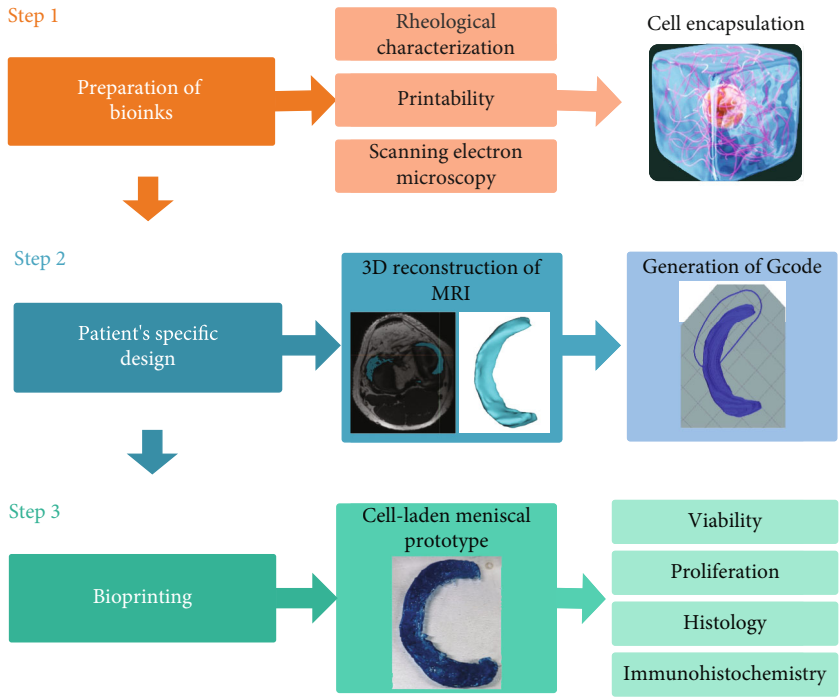


Scheme 1: Schematic representation of the study process.

improve the biological and biomechanical performances of tissue engineering meniscal scaffolds.

Bioprinting technology as a group of additive, bottom-up, nature-like technologies has made it possible to spatially pattern cells, bioactive factors, and biomaterials in the 3D microenvironment [8–11]. Bioprinting meniscal-shaped structures with stem cells or chondrocytes via microextrusion bioprinting technology as proof-of-concept tests have been reported [12, 13]. However, there are few meniscal bioprinting studies involving patient-specific design using major cellular components of the native meniscus with proper mechanically featured bioink until now.

Gelatin-alginate-based hydrogel has been widely applied as a bioink source in microextrusion approaches [14, 15]. As a hydrolytic product of collagen, gelatin can provide a favorite microenvironment enhancing cell attachment and proliferation, while alginate presents the feature of instant gelation via cross-linking by calcium ions ($Ca^{2+}$), enabling acceptable mechanical performance for bioprinted products [16]. Gelatin-alginate-based bioink systems present various advantages including widely available and economical material source, relatively simple producing process, and verified cytocompatibility [17]. Moreover, the thermal reversible feature of the gelatin-alginate-based bioink system enables a relatively simplified bioprinting process and device design [18]. However, during the microextrusion bioprinting process, the gelatin-alginate based hydrogels are fragile and changeable before further cross-linking, causing unstable mechanical condition especially in fabricating complex structures like the meniscus [19, 20].

Originating from the most abundant bioresource, wood biomass, cellulose nanofiber (CNF) is representative in building components in nature and has attracted significant interest as a potential biomaterial candidate [21]. In addition, CNF provides acceptable mechanical properties, relatively good rheological properties, and most importantly, cytocompatibility [22, 23]. However, to our knowledge, there has been no report of adapting CNF to improve the printability of alginate-gelatin-based bioink systems via hydrophobic interactions and hydrogen bonding for individual-specific meniscus biofabrication.

In this study, CNF was mixed with gelatin-alginate thermal-responsive bioinks to improve the printability. The rheological and morphological properties of the bioinks were characterized. While cell-laden meniscal prototype basing on MRI data was bioprinted using our CNF-modified bioinks, subsequently, the bioprinted prototypes underwent histological and immunohistochemical assessments to verify biological potentials as presented in Scheme 1. The current work aims at carrying out the preliminary practice on bioprinting implant prototype of patients' specific-designed, cell-laden products for potential meniscus transplantation.

## 2. Materials and Methods

*2.1. Materials.* The bioprinter (BioPrinter-1, BP-1) used in the current study was developed by our research group. Gelatin type B from bovine skin (G8061) and Na-alginate (A9640) were purchased from Solarbio Inc. (China). Wood-based cellulose nanofiber powder was purchased from Guilin Qihong Technology Co. (China). High-glucose Dulbecco's modified Eagle's medium (DMEM), fetal bovine serum (FBS, HyClone), penicillin/streptomycin, and other reagents for cell preparation were all purchased from GE Inc. (China). A live/dead staining kit (BB-4126) was purchased from BestBio Inc. (China). An alamar blue assay kit

Table 1: Proportion of ingredients in the tested hydrogels.

| Group | Abbreviation | Gelatin | Alginate | CNF |
|---|---|---|---|---|
| 1 | HGA-CNF | 20% (*w*/*v*) | 1.25% (*w*/*v*) | 0.25% (*w*/*v*) |
| 2 | HGA | 20% (*w*/*v*) | 1.25% (*w*/*v*) | — |
| 3 | LGA-CNF | 10% (*w*/*v*) | 1.25% (*w*/*v*) | 0.25% (*w*/*v*) |
| 4 | LGA | 10% (*w*/*v*) | 1.25% (*w*/*v*) | — |

(A7631) was purchased from Solarbio Inc. An immunohistochemistry tool kit (SP-0023), rabbit monoclonal primary antibodies for collagen type I (BS-10423R 1 : 400, 1 mg mL$^{-1}$), collagen type II (BS-10589R, 1 : 100, 1 mL mL$^{-1}$), and collagen type X (BS-0554R, 1 : 200, 1.4 mg mL$^{-1}$) were purchased from Bioss Inc. (China).

*2.2. Preparation of Bioinks.* CNF powder was diluted in deionized water to a final concentration of 0.25 wt% through stirring at 1000 rpm for 30 min at room temperature to acquire a homogenous solution. The solution was then heated to 70°C, and the Na-alginate powder was added under magnetic stirring for 30 min. Gelatin powder was added and dissolved when the solution was cooled to approximately 50°C under magnetic stirring for another 30 min. NaOH was used to adjust the pH of the solution to approximately 7.5. The hydrogel solution was then placed in a constant temperature oscillator at 200 rpm and 37°C overnight to eliminate bubbles and maintain a homogenous mixture. The bioink was prepared on a clean bench, and all the components and equipment were autoclaved and/or sterilized using UV light. After the preparation was finished, the final hydrogel was heated to 100°C for 1 h and then sealed to keep it sterile. The bioink was stored at 4°C and heated to 37°C for 30 min in a water bath before the bioprinting process. To verify the printability and biocompatibility of the bioinks, six groups of hydrogels were prepared with varying concentrations of gelatin and CNF. To simplify the narration, hydrogels containing higher and lower content of gelatin were recorded as high-gelatin-containing alginate group (HGA) and low-gelatin-containing alginate group (LGA), respectively. The CNF-modified hydrogels were named as HGA-CNF and LGA-CNF, respectively (Table 1).

*2.3. Rheological Characterization.* The rheological analysis was performed using an MCR 702 rheometer (AtonParr, Austria) using a 25 mm parallel plate. All 4 groups of cell-free bioink samples were tested before and after cross-linking. 0.1% (*w*/*v*) $CaCl_2$ solution was used as a cross-linker. The cross-linking time was 1 min. The samples were store at 37°C before the test and heated to the experimental temperature for 5 min before the rheological measurements. Non-cross-linked hydrogels were characterized through flow and temperature sweeps. The flow sweeps were conducted to evaluate viscosity at a shear rate ranging from 0.1 to 100 s$^{-1}$ at 25°C. To evaluate the thermal responsivity of the hydrogels, the viscosity was measured at temperatures ranging from 1°C to 40°C, at a fixed shear rate of 1 s$^{-1}$. The cross-linked hydrogels were characterized through oscillatory frequency sweeps between 0.1 and 10 Hz in the linear viscoelastic region of the hydrogels at 37°C.

*2.4. Cell Preparation.* Primary rabbit fibrochondrocytes (rFCs) were used in bioprinting the cell-laden meniscal prototypes. The isolation and culture of rFCs have been described by previous studies [24]. Briefly, sequential treatment of finely diced meniscus (from 6-month-old rabbits) using 0.5% hyaluronidase, 0.2% trypsin, and 0.2% collagenase was applied to obtain the cells. Then, the cells were filtered through a fine nylon mesh to separate them from undigested tissue and debris. The filtrate was washed several times through gentle suspension in D-Hank's solution and underwent centrifugation at low speed ($1000 \times g$) to form a cell pellet. The cells were then cultured under conventional conditions at 37°C in a humidified atmosphere of 5% $CO_2$. Once a sufficient cell quantity was achieved, usually after the third or fourth passage, the cells were used for further bioprinting process.

*2.5. Design of Microextrusion Bioprinter.* In the current study, a microextrusion-based bioprinter (BP-1) was developed by our group. The minimum mechanical travel distance is ±0.05 mm for the *XY*-axes and ±0.01 mm for the *Z*-axis. The extrusion module was consisting of a precision piston for extruding materials, a syringe heater for thinning printing materials, and a standard medical syringe (10 mL) as a cartridge with 22G metal nozzles for depositing bioinks. The whole printing system is enclosed by a clean bench with a temperature-humidity control system. A UV light source was also integrated for sterilization. In a typical print procedure, the *XY* stage will translate the extruder at speeds ranging from 1 mm/s to 10 mm/s to pattern the predetermined 2D cross-section on the printing substrate, and then the *Z* stage elevates to repeat the process for the next layer. Special methods were applied to ensure the sterilization of the whole bioprinting system. Firstly, the whole bioprinter was installed in a modified super clean bench which was divided into two separate cabins by a plate. The mechanical structures of the bioprinter were in the upper cabin where the bioprinting process was carried out and the control system was installed in the cabin below. All cables in the upper cabin were waterproof. Secondly, before the bioprinting process, thorough disinfection by alcohol spray and UV irradiation was carried out in the upper cabin for 40 min. At last, the super clean bench was kept closed the positive pressure during the bioprinting process.

*2.6. Printability Verification Process.* The bioinks were heated in a water bath at 37°C for 30 min and extracted into a standard sterile syringe with 22G (0.42 mm inner diameter) metal needles. The samples were printed directly onto sterile Petri dishes on the printing platform, which was cooled down to 4°C by the printing platform during the process. Square blocks (15 mm × 15 mm × 2 mm) consisting of four perpendicular layers with a 40% filling rate were 3D printed. Considering the nonlinear rheological performance of living cells, the samples used for printability tests were cell-free to reduce disturbance. The printing temperature range was

Table 2: MRI parameters for knee scanning.

| FOV, mm | Matrices | TR, ms | TE, ms | Slice thickness, mm |
|---|---|---|---|---|
| 180 × 180 | 320 × 320 | 1500 | 32 | 0.8 |
| Bandwidth, kHz | Echo train length | NEX | Scan time, mins | |
| 83.33 | 60 | 1 | 6.29 | |

FOV: field of view; TR: repetition; TE: echo time; NEX: number of excitations.

20°C–25°C. The best printing temperature was decided on the base of the actual filamentation of each group under a certain temperature. The platform temperature for all groups was set to 4°C. The moving speed of the nozzle in $XY$-axes was 3 mm/s. All samples were cross-linked immediately using 0.1% $w/v$ $CaCl_2$ for 1 min and then washed twice using Dulbecco's phosphate-buffered saline (DPBS).

*2.7. Patient's Specific Design of Meniscal Prototype.* To mimic the native shape of the meniscus, a 3D model of the medial meniscus was achieved based on MRI scans from one healthy volunteer of the authors. MRI images were acquired through the 3Tesla Discovery MR750 GEM Magnetic Resonance Imaging System (GE Healthcare, United Kingdom) with a 16-element phased-array flexible coil. A general supine position with a relaxed limb was used when performing the scan. Sagittal 3D fast-spin-echo (FSE) with high spatial, contrast resolution and no chem SAT was applied for image achievement. MRI scan parameters for the knee imaging are listed in Table 2.

The MRI data were saved as a sequence of Digital Imaging and Communications in Medicine (DICOM) files and processed via the Mimics software (Materialise 21, Belgium). The threshold was set to 50-200 GV to identify meniscal tissues from surrounding tissues. The model was then carefully trimmed artificially by an experienced orthopedic surgeon to reconstruct the morphology of the medial meniscus. After that, an automatic adjustment was applied to fill the cavities caused by signal noise and exported as an STL file. The STL model was then converted to a motion program (G-code) using an open-source software (Repetier-Host, Germany), which describes the operation of the dispensing nozzles, printing speed, nozzle heat, and other relative information. A different open-source software (Printrun, by Kliment Yanev) was applied to transfer the G-code files into the operating computer for bioprinting.

*2.8. Bioprinting Process.* After the printability verification process, HGA-CNF was selected as the bioink used for further bioprinting tests. Centrifuged rFCs were resuspended with 5 mL liquefied HGA-CNF directly. The cell number of the resuspension solution was $5 \times 10^6$. Slight oscillation of the mixed bioink was performed for 10 min at 37°C to homogenize the solution. The cell-laden bioinks were extracted into syringes with 22G (0.42 mm inner diameter) metal needles. To eliminate the bubbles in the bioinks, all syringes were settled in the incubator at 37°C for 20 min. The bioprinting process was conducted with BP-1, and the structures were printed directly onto sterile Petri dishes on the printing platform, which was cooled down to 4°C during the process.Since it has been reported that cellular activities would be compromised when encapsulated into solidly structured hydrogel scaffolds [25, 26]. To improve the nutrition exchange inside the hydrogel-based scaffolds, all structures were designed based on the lattice structure. The printing temperature was 25°C. The platform temperature was set to 4°C. The 3D-reconstructed meniscus model with a 40% filling rate and rectilinear filling patterned was bioprinted. The printing speed was 3 mm/s. All samples were cross-linked immediately after bioprinting using 0.1% $w/v$ $CaCl_2$ for 1 min. To simplify the process, cell-laden, square block samples were bioprinted for metabolic activity test. The bioprinted samples were cultured in a petri dish ($\varphi = 55$ mm) and incubated for 14 days. The medium was changed every 3 d.

*2.9. Printability Evaluation and Characterization.* The printing quality was evaluated by imaging the cross-linked cell-free samples using a ×4 air objective with an SZX16 stereoscopic microscope (OLYMPUS, Japan), and bioinks from all groups were used in this test. Briefly, cross-linked cell-free structures with four layers were imaged to measure the strand width and pore size using the ImageJ software. The spreading ratio was calculated by dividing the strand width by the inter diameter (22G, ~420 $\mu$m) of the nozzle. The printed structures were stained using trypan blue after printing for better visualization. Scanning electron microscopy (SEM, Zeiss EVO 18, Cambridge, England) was applied to further characterize the porosity and interconnectivity of the bioprinted samples. The samples were lyophilized and sputter-coated with gold to observe the topography. Images (×25 and ×1500) were taken using SEM at an accelerating voltage of 3 kV to evaluate the morphology and microarchitectures. Three random images were taken from each sample from every region. To better visualize the rFCs encapsulated inside the structures, three samples were first graded ethanol dehydrated and then went through the same processes as other samples.

*2.10. Cell Viability and Metabolic Activity.* The cell viability of cells in the bioprinted structures was qualitatively analyzed at day 1, as well as 4, 7, and 14 d of culture using a live/dead staining kit in accordance with the manufacturer's instructions. Briefly, the bioprinted structures were rinsed using DPBS twice and incubated in 5 mL of live/dead solution (calcein-AM and ethidium homodimer) at 4°C for 20 min. The samples were examined using a fluorescence microscope (Zeiss, Axio Imager 2, Germany). Five randomly selected images obtained at ×4 magnification were used to evaluate the percentage of cell viability via ImageJ. The viability was calculated as the average ratio of live cells to total cells. An alamar blue assay kit was used to measure cell proliferation. The metabolic activity of the encapsulated cells was analyzed at 1, 4, 7, and 14 d after bioprinting. The square block bioprinted structures were incubated in 6-well plates for 7 h with 0.3 mL of alamar blue solution for each 3 mL of culture media. Fluorescence intensity was measured at an excitation

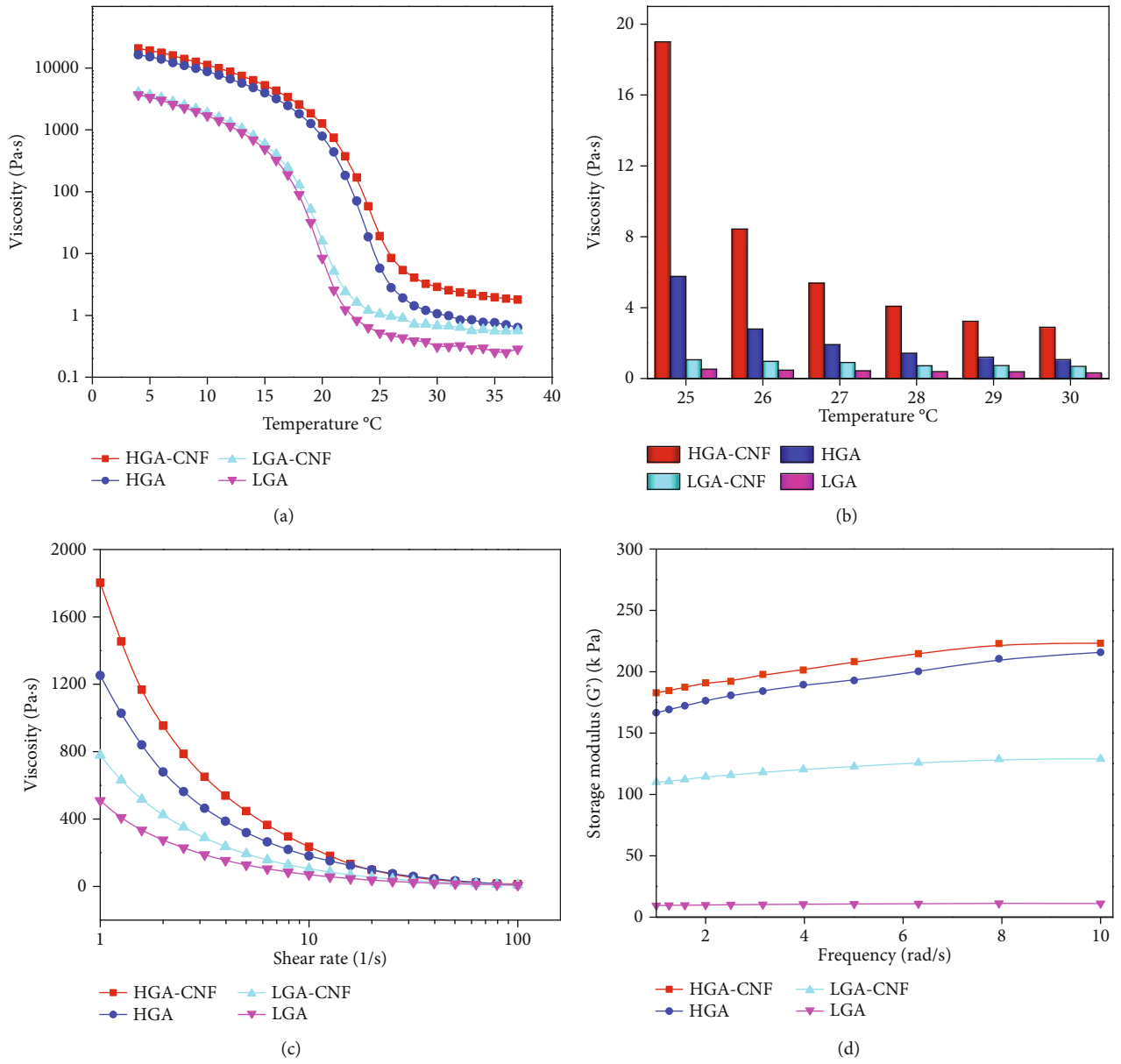


Figure 1: Rheological characterization of the cell-free hydrogels. (a) Viscosity at temperatures ranging from 5°C to 37°C at a shear rate of 1 $s^{-1}$. (b) Non-cross-linked viscosity at bioprinting temperature from 20°C to 25°C at a shear rate of 1 $s^{-1}$. (c) Non-cross-linked viscosity at various shear rates at 25°C. (d) Storage modulus after cross-linking at 37°C.

wavelength of 530 nm and an emission wavelength of 590 nm (Varioskan Flash, Thermo Fisher, USA).

*2.11. Histology and Immunohistochemistry.* The prototypes incubated for 14 d in the culture medium were fixed in paraformaldehyde/barium chloride overnight. The fixed samples were then cryosectioned, embedded in paraffin wax, sectioned at 5 $\mu$m, and affixed to microscope slides. Hematoxylin-eosin, picrosirius red, and alcian blue staining were applied to assess calcium, collagen, and glycosaminoglycan accumulation, respectively. Immunohistochemistry techniques were applied to evaluate and identify collagen types I, II, and X, as previously described [27]. Briefly, samples were treated using peroxidase and chondroitinase ABC and then incubated with fetal calf serum to reduce nonspecific binding. Collagen type I, collagen type II, and collagen type X rabbit monoclonal primary antibodies were applied for 1 h at room temperature. The secondary antibody (anti-rabbit IgG biotin conjugate) was added for 1 h, followed by incubation with an ABC reagent for 45 min. Finally, sections were developed using DAB peroxidase for 5 min.

*2.12. Statistical Analysis.* Results are expressed as mean ± standard deviation. Statistical analyses were performed using the SPSS v22.0 software (SPSS Inc., Chicago, IL, USA).

## 3. Results

The rheological behavior is considered as the major concern to select the bioink candidate for further bioprinting tests. All

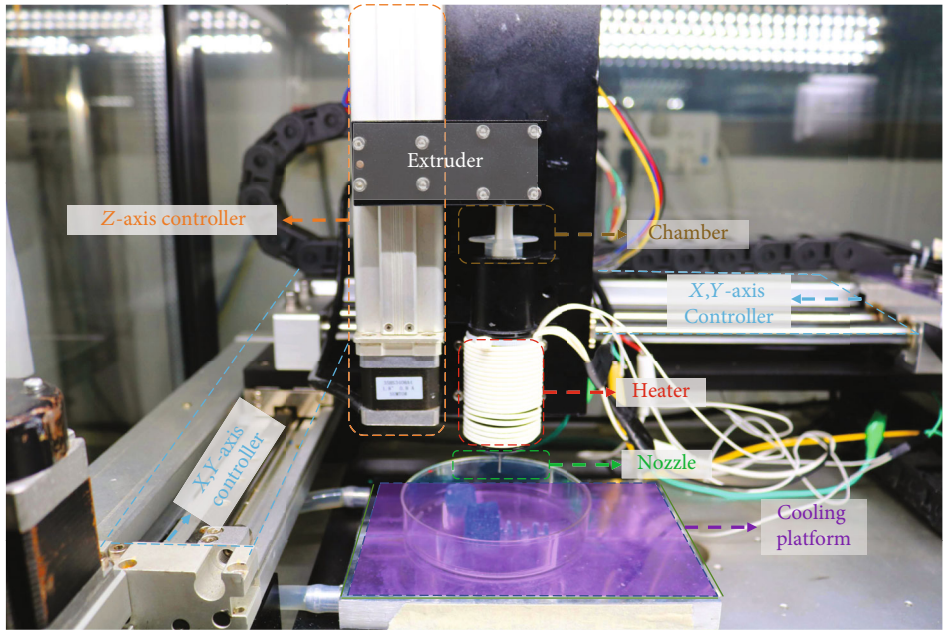


Figure 2: Microextrusion-based bioprinter developed by our group.

four groups of prepared hydrogels with varying gelatin and CNF content were tested (Figure 1). The samples showed a significant decrease in viscosity as the temperature increased during a temperature sweep (Figure 1(a)). Hydrogels containing a higher concentration of gelatin (20% *w*/*v*) maintained higher viscosity among all the groups when the temperature raised to 25°C, which is the minimum acceptable printing temperature for the bioprinter. CNF-modified hydrogels exhibit prior viscosities and lower decreasing rates than their non-CNF-containing counterparts. At the designated bioprinting temperature window of 25°C to 30°C, HGA-CNF exhibited more than a threefold increase in viscosity compared with HGA (Figure 1(b)), indicating prominent superiority in printability potential. A shear-thinning behavior was observed among all the bioink candidates. As CNF strengthened the viscosity, hydrogels modified with CNF tended to maintain more solid-like behaviors than non-CNF-containing hydrogels at the same shear rate (Figure 1(c)). The frequency sweep also showed a similar tendency, and hydrogels modified with CNF showed higher storage modulus than pure gelatin with alginate when being cross-linked by $Ca^{2+}$, indicating priority in the mechanical performance of CNF-modified samples (Figure 1(d)).

Printability is the vital access to maintain the fidelity of the meniscal prototype. Cell-free square block samples and rFCs cell-laden meniscal prototypes were printed using our microextrusion-based bioprinter (Figure 2). The quality assessments and characterization of the printed structures are presented in Figure 3. To acquire better printing filamentation, all the hydrogels were tested under a printing temperature range from 20°C to 25°C, which was decided based on the rheological results of the hydrogels (Figure 3(a)). HGA-CNF and HGA showed the best filamentation under 25°C while the highest acceptable printing temperature for LGA-CNF and LGA was 20°C. The other printing parameters remained the same for all hydrogels. Top-view images are presented in Figure 3(b). The results showed that only HGA-CNF and HGA formed 3D lattice structures with relatively acceptable fidelity and integrity. Samples bioprinted with LGA showed completely fused constructs during the test. Thus, the measurement of the filament was not performed for LGA. To analyze the bioprinted samples in more detail, stereomicroscope images of the top layers were taken. The strand width and pore size were measured (Figures 3(c) and 3(d)). The spreading ratios of HGA-CNF, HGA, and LGA-CNF were $0.88 \pm 0.08$, $1.07 \pm 0.03$, and $1.03 \pm 0.07$, respectively. The strands of the CNF-modified hydrogels (HGA-CNF and LGA-CNF) were stretched at different levels during the printing process, which led to a thinner strand width than their non-CNF-containing counterparts. The pore size measurement further confirmed this feature. The presence of CNF resulted in a thinner strand width and better lattice formation in the printed structures. Structural investigations of the printed structures of cell-laden HGA-CNF via scanning electron microscopy (SEM) are presented in Figure 3(e). Hierarchical porous structures of micron order were observed, presenting a similar microenvironment to the morphological features of the extracellular matrix (ECM). The sign of cellular component in the bioink was more distinct after treating the samples with graded ethanol dehydration. The bioink scaffold and rFCs encapsulated inside were colored as green and fuchsia, respectively, for better visualization. Homogeneous distribution of rFCs within the hydrogel-based scaffolds was observed, indicating the biocompatibility of our bioprinting process. In summary, good printability of HGA-CNF was demonstrated, and this was then selected as a bioink for further bioprinting tests.

The anatomical features of the meniscus extracted from the 2D MRI images were preserved and reshaped as 3D

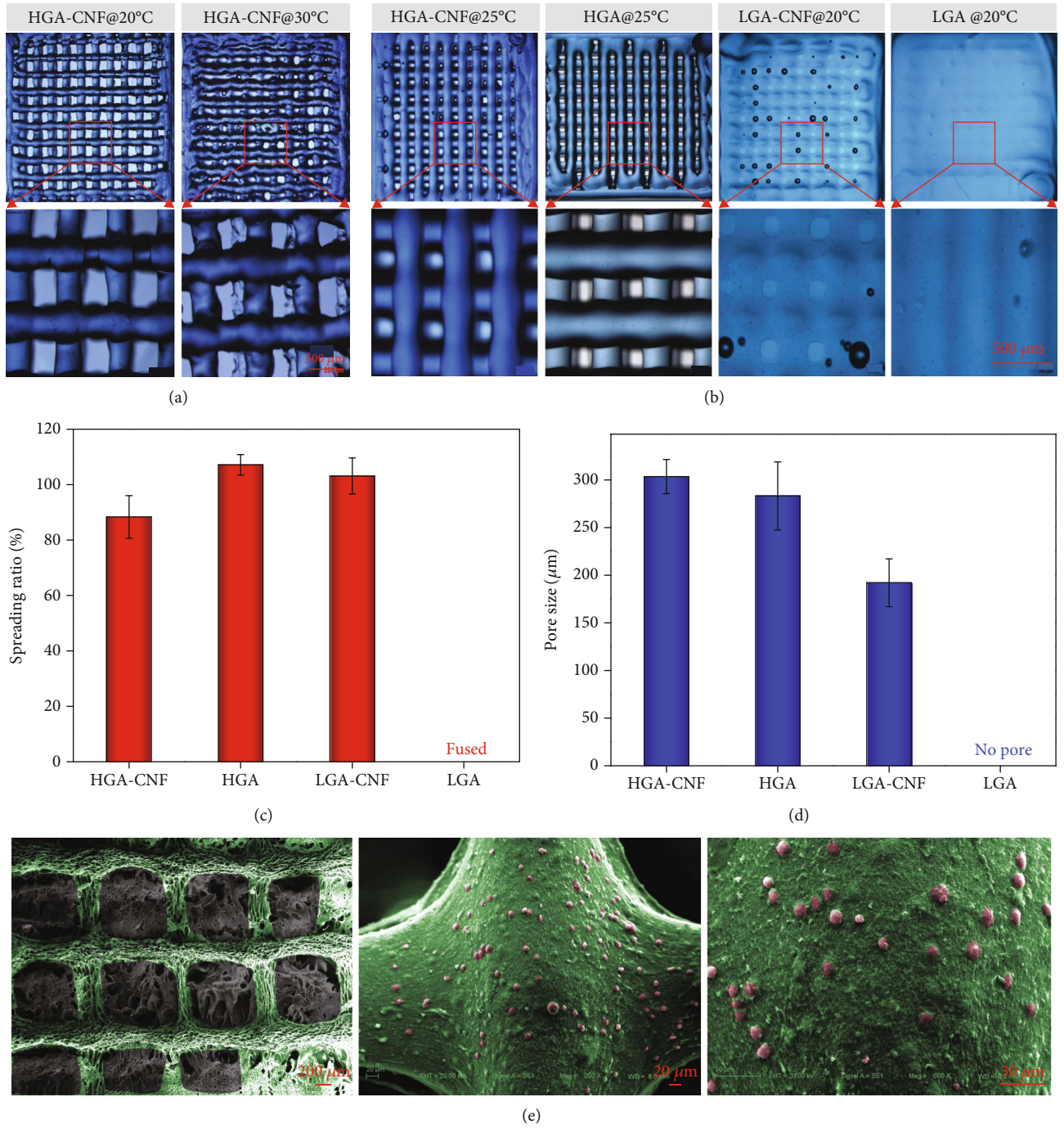


FIGURE 3: Bioprinting quality assessment. (a) As the printing temperature raise, gelling properties from over extrusion (30°C) and poor gelling (20°C) of the bioinks were observed. (b) Upper row: top-view images of the printed four-layer structures (trypan blue stained, cross-linked) obtained using a stereoscopic microscope. (c) The spreading ratios of the non-cross-linked fourth layer strands were measured. (d) The pore sizes of the non-cross-linked four-layer structures were measured. (e) SEM analysis of the printed structures. The bioink and rFCs are colored green and fuchsia, respectively.

volumetric information and then bioprinted into a hydrogel-based, cell-laden meniscal prototype (Figure 4). The selected bioink (HGA-CNF) presented good printability and shape fidelity during the printing process. The 3D-printed meniscus prototype was consisting of 19 layers, consuming approximately 991.85 $mm^3$ volume of bioink. The actual size of the printed meniscus prototype was approximately 48.3 × 40.5 × 8.28 mm before cross-linking, while the designed shape of the 3D model reconstructed from MRI date was 45.42 × 41.13 × 8.81 mm, indicating highly consistency.

The viability and metabolic activity of rFCs in the printed samples are presented in Figure 5. The results showed very high viability after the bioprinting process in a live/dead staining assay (Figure 5(a)). In detail, the average cell viability

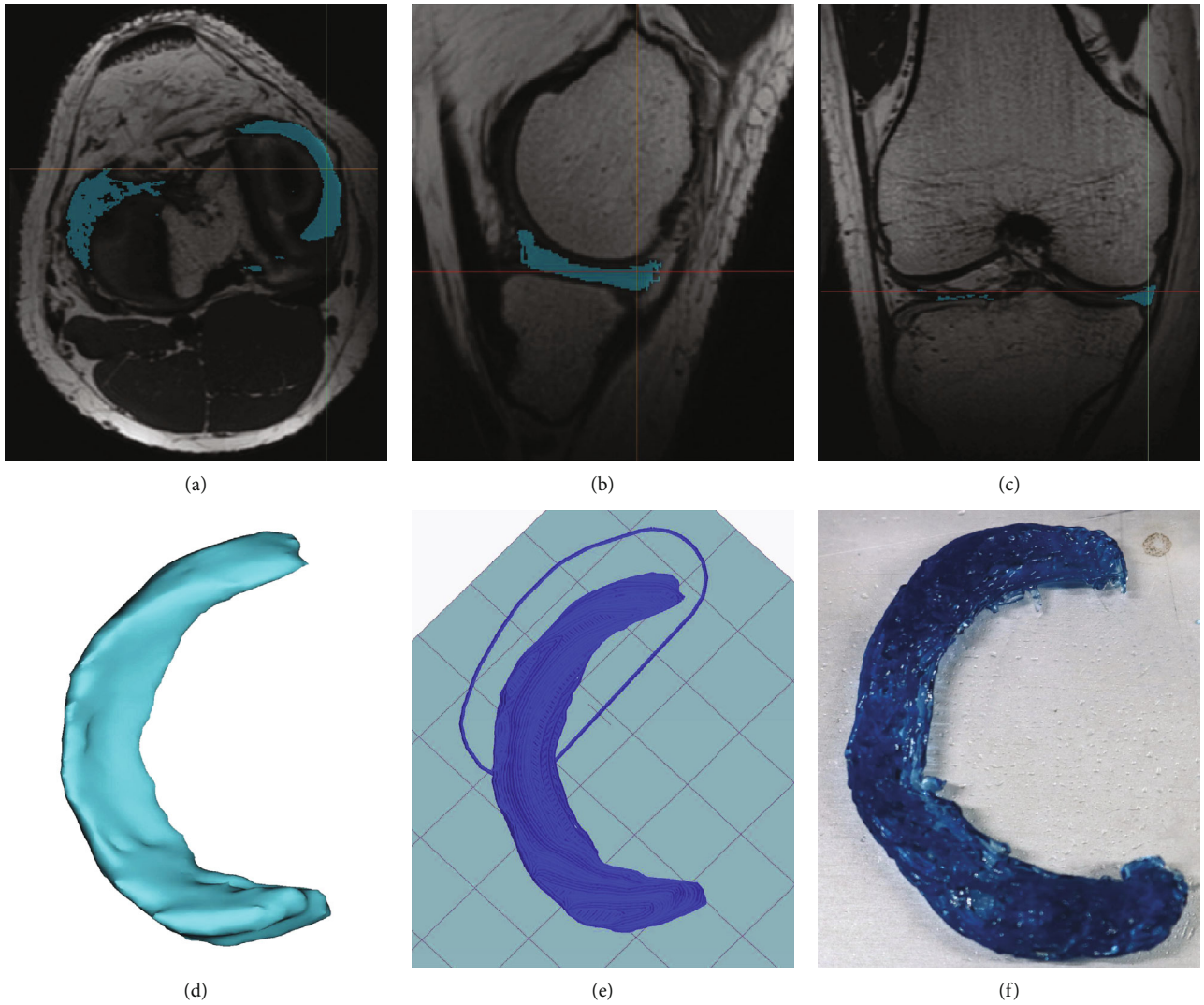


Figure 4: 3D reconstruction from MRI images and 3D printing process of a patient's specific medial meniscus. (a–c) MRI data gathered from a healthy volunteer were processed to identify the structure of medial meniscus. (d) A 3D model was then reconstructed and converted to STL file. (e) The STL model was imported into the slicing software to calculate the printing route and a G-code file was generated. (f) Bioink-based, cell-free meniscal prototype was then 3D printed basing on the G-code file.

of the rFCs on day 1 was $94 \pm 0.03\%$. However, the bioprinted cells recovered from the printing shock within 4 d of culture ($95 \pm 0.05\%$) and retained high performance throughout the culture period. When it came to day 7, the viability of the rFCs reached a peak of nearly 99% and then dropped to $96 \pm 0.02\%$ for the following 7 d of culture, demonstrating the excellent biocompatibility of HGA-CNF (Figure 5(b)). The alamar blue assay of the bioprinted rFCs (Figure 5(c)) was in line with the viability results. The metabolic activity of the printed cells was initially hampered by the bioprinting process and then recovered to a significantly high level at 4 d after bioprinting, indicating high cell proliferation activity during the first few days. The metabolic activity decreased gradually between 4 and 7 d of culture and stabilized at day 14.

To ascertain the deposition of collagen and sGAG in vitro, bioprinted samples encapsulating rFCs were histologically stained after 14 d of incubation (Figure 6(a)). Picrosirius red and alcian blue staining was positive in the intercellular space of rFCs encapsulated in the bioprinted samples, indicating collagen and glycosaminoglycans accumulation. HE staining of the bioprinted structures revealed rFCs were homogeneously distributed in the bioink. Immunohistochemical staining showed barely signs of collagen type I and abundant accumulation of collagen types II and X (Figure 6(b)).

## 4. Discussion

To meet the growing demand for meniscus tissue engineering, both synthetically and naturally derived biomaterials have been reported [28]. However, although it has been reported that shape mismatch can lead to a negative influence on the biomechanical performance of implanted meniscus [29, 30], the morphological design of the meniscus and development of relative fabrication approaches were unvalued to some

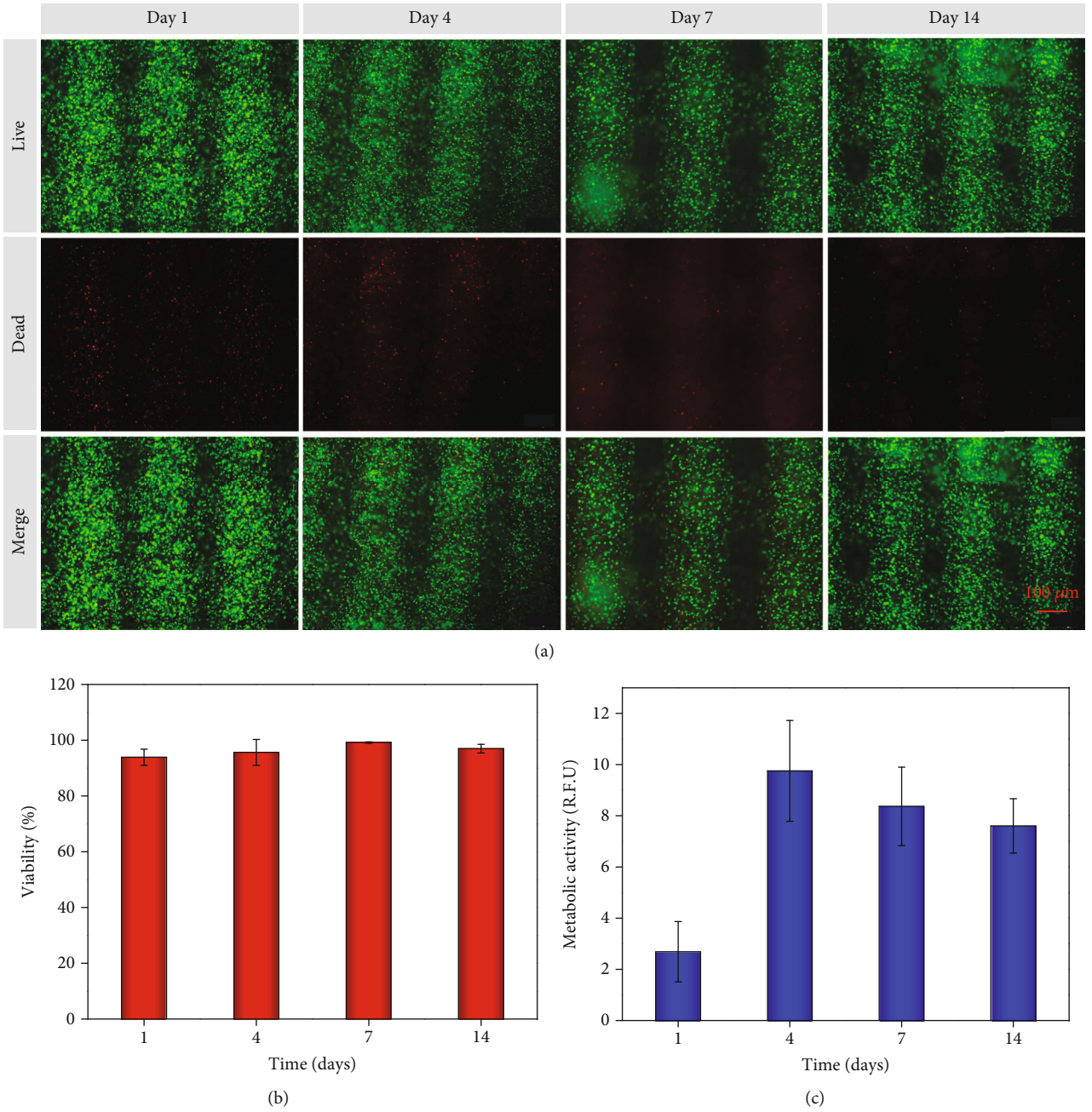


Figure 5: Viability and metabolic activity of bioprinted samples. (a) Live/dead staining of rFCs immediately at 1, 4, 7, and 14 d of culturing in vitro. Living cells are stained green and dead cells red. Scale bar 100 $\mu$m. (b) Quantitative statistics of the bioprinted samples at different time points using ImageJ. (c) Metabolic activity values of bioprinted rFCs using an alamar blue assay at different time points.

extent. To address this situation, the precise morphological design was stressed in this study. A 3D-reconstructed model was achieved from the patient's MRI images, aiming at accurately revealing the native shape parameters of the meniscus. During the MRI scanning, modified parameters were applied to acquire better accuracy. Generally, OAx fs PD, OSag fs PD, and OCor fs PD models were used for a meniscal scan while our scan was a combination of these three models with a thinner slice thickness. The time consuming for a general meniscal MRI scan was approximately 5.23 min while our modified model was 6.29 min. The modified parameters were prestored in the MRI device and could be readily switched as needed. Neither additional equipment nor extra economic cost was needed for the modified scan. Moreover, with the assistance of the 3D reconstruction software like Mimics, the meniscal model could also be achieved via mirroring the healthy side MRI data of the patient when the major substance of injured meniscus has been damaged. As for partial meniscal injure cases, a mirroring of the healthy side MRI data could be used as a reference. The injured area could be underlined via a matching between the healthy and injured meniscus.

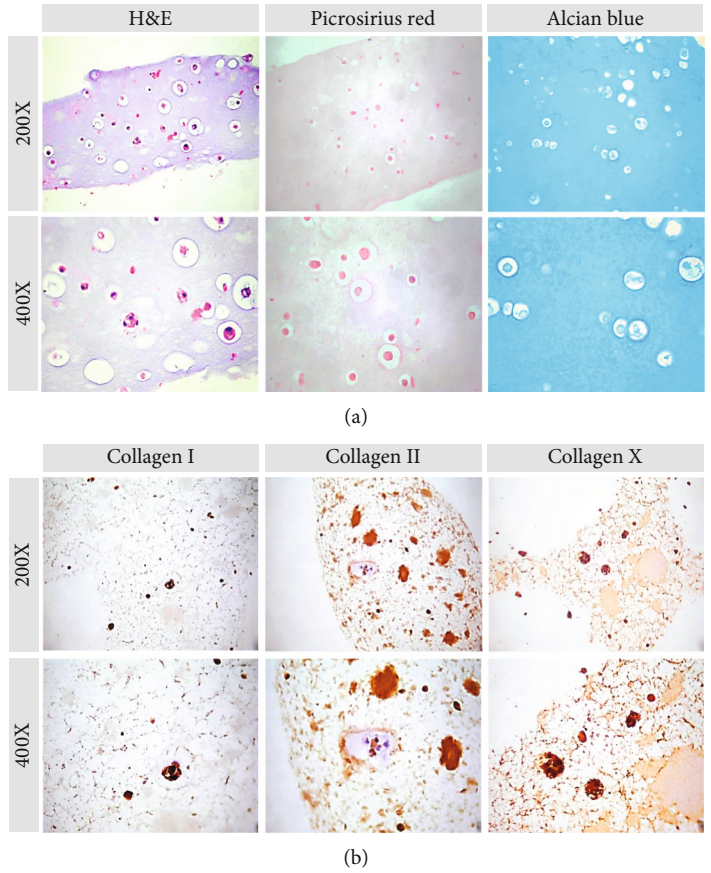


FIGURE 6: Histological and immunohistochemical results of bioprinted structures. (a) Histological staining of bioprinted rFCs structures with HE, picrosirius red, and alcian blue. (b) Immunohistochemical for collagen I, II, and X accumulation in the bioprinted rFCs samples.

Benefitting from a bottom-up style of manufacturing and precise cell patterning, bioprinting is naturally suitable for biofabricating tissue engineering scaffolds with complex structures. In this process, the balance between printability and biocompatibility has been a major challenge since the early development of bioinks. In this context, a microextrusion-based bioprinting system was built by the current research group to explore its potential of personalized-designed meniscal reconstruction. Gelatin-alginate-based bioink was adapted to achieve thermoresponsive and calcium ions cross-linking gelling features [31]. However, the thermal curing of gelatin is unstable and reversible during bioprinting, which commonly leads to inferior printability and fidelity when fabricating complex structures. Thus, maintaining a self-supporting hydrogel before ionic cross-linking is also an attractive feature that would improve printability.

The rheological characterization of the prepared hydrogels further confirmed the influence of CNF. Hydrogels containing CNF showed prior viscosity performance than their non-CNF-containing counterparts at a wide range of temperatures. This phenomenon could be attributed to the physicochemical interaction between CNF, alginate, and gelatin. It has been reported that hydroxyl surface groups exist in CNF and alginate can interact through hydrogen formation with carbonyl and amine groups in gelatin [32], improving the gelling strengthen of the hydrogel. Moreover, the existence of CNF also significantly improved the shear-thin behaviors of the hydrogels via the breakage of fiber networks under shear force [33]. In addition, nanofibers of CNF underwent shear-induced alignment from the nozzle, which further enhanced the bioink flow [34], resulting in better printability. The role of CNF in the bioink is a "booster" for both the extrusion and curing process through enhancing the shear-thinning behavior. During the extrusion process, the extrusion flow through the nozzle was enhanced by CNF via shear-induced fibril alignment, which results in a smoother and more continuous flow out of the nozzle. When the gelatin had undergone gelation, the CNF material present resulted in relatively high stiffness and self-supporting features through the formation of a self-aligned fibrous network scaffold which served as a stiff filler with favorable shear-thinning properties [35]. To enhance the printability of gelatin-alginate bioink, 0.25% *w*/*v* CNF was added in the current study. The bioprinted meniscus prototype can maintain shape fidelity without being instantly cross-linked.

Origin from natural resources, the biocompatibility of gelation and alginate has been verified [36]. As for CNF, although it is not degradable inside the human body, it has been reported that owing to the small size and inertness of CNF, the newly formed matrix simply surrounds the fibers and integrates them into the tissue without any adverse side effects [37]. The density value of CNF in this study is

therefore decided based on the reported studies [32]. The cytocompatibility of CNF-modified bioink, with a concentration of 0.25 mg/mL of CNF, was confirmed after the bioprinting process and additional incubation for 14 d. Our results showed that the bioprinted structures encapsulating rFCs allowed acceptable cell viability. Moreover, a structural investigation through SEM confirmed a multiscale interconnected porous morphology in the bioprinted structures, which could provide a suitable 3D environment for cell attachment, proliferation, and metabolism [38]. The metabolic activity that showed the bioactivities of rFCs were tiny compromised and quickly recovered after 4 days of incubation.

In this research, we used fibrochondrocytes to verify the ability bioprinting meniscal relevant cellular components of our system. Although applying stem cells in meniscal reconstruction has been reported by some groups. However, complex-staged-inducing methods were required for stem cells in fibrocartilaginous differentiation, consuming a relatively long period of cell culture which compromised the clinical potential [39]. Thus, mature cells were preferred by our group. Nevertheless, as the progress of coculturing stem cells with other meniscal relevant cells such as fibrochondrocytes and chondrocytes in 3D environments are reported recently [40, 41], further experiments on bioprinting mixed cell groups to enhance the proliferation and differentiation will be carried out by our group.

To further assess the ECM accumulation of fibrochondrocytes, sGAG and collagen types II and X were confirmed by histological and immunohistochemical tests simultaneously. The results showed the ECM components were similar to the native meniscus. This progress will pave the way towards the reconstruction of the patient's specific-designed, bioactive meniscal substitution. Moreover, to the best of our knowledge, this is the first time that primary fibrochondrocytes have survived through the bioprinting process and maintained viability and biofunction during further in vitro incubation. The bioprinted meniscal prototype would bring more flexible, adaptable, and easily accessible methods in meniscal repairment and reconstruction.

However, the current study still has some limitations. Firstly, further biomechanical tests of cell-laden meniscal prototypes are still needed to evaluate the in vitro mechanical performance. Considering the inferior mechanical properties of hydrogel-based bioinks, to further improve the mechanical performance of the meniscal prototype, coprinting of thermoplastic polymer and bioink would be our further direction [11]. Benefiting from the highly scalable of our bioprinter, the modification would be easily accessed. Moreover, in vivo implantation on animal models should be carried out further to verify the tissue formation abilities of our bioprinted prototypes. We predict that biofabrication of cell-laden meniscus prototype with proper biomechanical features meeting the clinical implantation demands would not be a barrier as the advance of bioprinting and biomaterial approaches.

## 5. Conclusions

The CNF-modified gelatin-alginate bioink has achieved encouraging results in mechanical performance and printability. Combining with MRI 3D reconstruction, the preliminary attempt of applying modified bioink in bioprinting individual-specific meniscus prototype is achieved with favorable biofunction. The application of bioprinting approaches might minimize the mismatch between artificial meniscal implants and native knee joint tissues, thereby permitting the evolution of clinical therapeutic methods of meniscal reconstruction.

## Data Availability

The data used to support the findings of this study are available from the corresponding author upon request.

## Conflicts of Interest

The funders had no role in the design of the study; in the collection, analyses, or interpretation of data; in the writing of the manuscript; or in the decision to publish the results.

## Authors' Contributions

Conceptualization was done by Wenbin Luo and Zhengyi Song; methodology by Wenbin Luo; formal analysis by Wenbin Luo and Zhenguo Wang; investigation by Zuhao Li and Chenyu Wang; resources by He Liu; data curation by Jincheng Wang and Qingping Liu; writing original draft preparation by Wenbin Luo; visualization by He Liu and Qingping Liu; supervision by Jincheng Wang and Qingping Liu; project administration by Jincheng Wang and Qingping Liu. All authors have read and agreed to the published version of the manuscript.

## Acknowledgments

This study was supported by the National Natural Science Foundation of China (grant no. 81671804 and 81772456), Scientific Development Program of Jilin Province (grant no. 20190304123YY, 20180623050TC, and 20180201041SF), Program of Jilin Provincial Health Department (grant no. 2019SCZT001 and 2019SRCJ001), Cultivation Program from the Second Hospital of Jilin University for National Natural Science Foundation (grant no. KYPY2018-01), and Youth Talents Promotion Project of Jilin Province (grant no. 192004), and Jilin Province Key Scientific and Technological Project (no. 20170204061GX).

## Supplementary Materials

*Supplementary 1*. Video S1: bioprinting process of the meniscal prototypes.

*Supplementary 2*. Video S2: bioprinting process of the square block samples.

## References

[1] A. Heijink, A. H. Gomoll, H. Madry et al., "Biomechanical considerations in the pathogenesis of osteoarthritis of the knee," *Knee Surgery, Sports Traumatology, Arthroscopy*, vol. 20, no. 3, article 1818, pp. 423–435, 2012.

[2] S. J. Lee, K. J. Aadalen, P. Malaviya et al., "Tibiofemoral contact mechanics after serial medial meniscectomies in the human cadaveric knee," *The American Journal of Sports Medicine*, vol. 34, no. 8, pp. 1334–1344, 2006.

[3] N. A. Smith, N. Parsons, D. Wright et al., "A pilot randomized trial of meniscal allograft transplantation versus personalized physiotherapy for patients with a symptomatic meniscal deficient knee compartment," *The Bone & Joint Journal*, vol. 100-B, no. 1, pp. 56–63, 2018.

[4] P. Mickiewicz, M. Binkowski, H. Bursig, and Z. Wróbel, "Preservation and sterilization methods of the meniscal allografts: literature review," *Cell and Tissue Banking*, vol. 15, no. 3, pp. 307–317, 2014.

[5] K. R. Myers, N. A. Sgaglione, and A. D. Goodwillie, "Meniscal scaffolds," *The Journal of Knee Surgery*, vol. 27, no. 6, pp. 435–442, 2014.

[6] Y. S. Shin, H. N. Lee, H. B. Sim, H. J. Kim, and D. H. Lee, "Polyurethane meniscal scaffolds lead to better clinical outcomes but worse articular cartilage status and greater absolute meniscal extrusion," *Knee Surgery, Sports Traumatology, Arthroscopy*, vol. 26, no. 8, pp. 2227–2238, 2018.

[7] M. E. Baratz, F. H. Fu, and R. Mengato, "Meniscal tears: the effect of meniscectomy and of repair on intraarticular contact areas and stress in the human knee. A preliminary report," *The American Journal of Sports Medicine*, vol. 14, no. 4, pp. 270–275, 1986.

[8] Y. S. Zhang, K. Yue, J. Aleman et al., "3D bioprinting for tissue and organ fabrication," *Annals of Biomedical Engineering*, vol. 45, no. 1, pp. 148–163, 2017.

[9] G. Gao, Y. Huang, A. F. Schilling, K. Hubbell, and X. Cui, "Organ bioprinting: are we there yet," *Advanced Healthcare Materials*, vol. 7, no. 1, article 1701018, 2018.

[10] M. Touri, F. Kabirian, M. Saadati, S. Ramakrishna, and M. Mozafari, "Additive manufacturing of biomaterials– the evolution of rapid prototyping," *Advanced Engineering Materials*, vol. 21, no. 2, p. 1800511, 2019.

[11] W. Luo, H. Liu, C. Wang, Y. Qin, Q. Liu, and J. Wang, "Bioprinting of human musculoskeletal interface," *Advanced Engineering Materials*, vol. 21, no. 7, article 1900019, 2019.

[12] S. Romanazzo, S. Vedicherla, C. Moran, and D. J. Kelly, "Meniscus ECM-functionalised hydrogels containing infrapatellar fat pad-derived stem cells for bioprinting of regionally defined meniscal tissue," *Journal of Tissue Engineering and Regenerative Medicine*, vol. 12, no. 3, pp. e1826–e1835, 2018.

[13] K. Markstedt, A. Mantas, I. Tournier, H. Martínez Ávila, D. Hägg, and P. Gatenholm, "3D bioprinting human chondrocytes with nanocellulose-alginate bioink for cartilage tissue engineering applications," *Biomacromolecules*, vol. 16, no. 5, pp. 1489–1496, 2015.

[14] S. Bose, D. Ke, H. Sahasrabudhe, and A. Bandyopadhyay, "Additive manufacturing of biomaterials," *Progress in Materials Science*, vol. 93, pp. 45–111, 2017.

[15] C. Mandrycky, Z. Wang, K. Kim, and D. H. Kim, "3D bioprinting for engineering complex tissues," *Biotechnology Advances*, vol. 34, no. 4, pp. 422–434, 2016.

[16] H. A. Awad, M. Q. Wickham, H. A. Leddy, J. M. Gimble, and F. Guilak, "Chondrogenic differentiation of adipose-derived adult stem cells in agarose, alginate, and gelatin scaffolds," *Biomaterials*, vol. 25, no. 16, pp. 3211–3222, 2004.

[17] M. Hospodiuk, M. Dey, D. Sosnoski, and I. T. Ozbolat, "The bioink: a comprehensive review on bioprintable materials," *Biotechnology Advances*, vol. 35, no. 2, pp. 217–239, 2017.

[18] S. Wüst, M. E. Godla, R. Müller, and S. Hofmann, "Tunable hydrogel composite with two-step processing in combination with innovative hardware upgrade for cell-based three-dimensional bioprinting," *Acta Biomaterialia*, vol. 10, no. 2, pp. 630–640, 2014.

[19] M. Neufurth, X. Wang, H. C. Schröder et al., "Engineering a morphogenetically active hydrogel for bioprinting of bioartificial tissue derived from human osteoblast-like SaOS-2 cells," *Biomaterials*, vol. 35, no. 31, pp. 8810–8819, 2014.

[20] L. G. Bracaglia, B. T. Smith, E. Watson, N. Arumugasaamy, A. G. Mikos, and J. P. Fisher, "3D printing for the design and fabrication of polymer-based gradient scaffolds," *Acta Biomaterialia*, vol. 56, pp. 3–13, 2017.

[21] T. Saito, T. Uematsu, S. Kimura, T. Enomae, and A. Isogai, "Self-aligned integration of native cellulose nanofibrils towards producing diverse bulk materials," *Soft Matter*, vol. 7, no. 19, pp. 8804–8809, 2011.

[22] A. Rashad, K. Mustafa, E. B. Heggset, and K. Syverud, "Cytocompatibility of wood-derived cellulose nanofibril hydrogels with different surface chemistry," *Biomacromolecules*, vol. 18, no. 4, pp. 1238–1248, 2017.

[23] X. Li, J. Wei, K. E. Aifantis et al., "Current investigations into magnetic nanoparticles for biomedical applications," *Journal of Biomedical Materials Research Part A*, vol. 104, no. 5, pp. 1285–1296, 2016.

[24] M. S. Son and M. E. Levenston, "Quantitative tracking of passage and 3D culture effects on chondrocyte and fibrochondrocyte gene expression," *Journal of Tissue Engineering and Regenerative Medicine*, vol. 11, no. 4, pp. 1185–1194, 2017.

[25] K. Zhang, Y. Fan, N. Dunne, and X. Li, "Effect of microporosity on scaffolds for bone tissue engineering," *Regenerative Biomaterials*, vol. 5, no. 2, pp. 115–124, 2018.

[26] C. R. Pimentel, S. K. Ko, C. Caviglia et al., "Three-dimensional fabrication of thick and densely populated soft constructs with complex and actively perfused channel network," *Acta Biomaterialia*, vol. 65, pp. 174–184, 2018.

[27] E. Harris, Y. Liu, G. Cunniffe et al., "Biofabrication of soft tissue templates for engineering the bone-ligament interface," *Biotechnology and Bioengineering*, vol. 114, no. 10, pp. 2400–2411, 2017.

[28] L. Roseti, C. Cavallo, G. Desando et al., "Three-dimensional bioprinting of cartilage by the use of stem cells: a strategy to improve regeneration," *Materials*, vol. 11, no. 9, p. 1749, 2018.

[29] S. V. Sekaran, M. L. Hull, and S. M. Howell, "Nonanatomic location of the posterior horn of a medial meniscal autograft implanted in a cadaveric knee adversely affects the pressure distribution on the tibial plateau," *The American Journal of Sports Medicine*, vol. 30, no. 1, pp. 74–82, 2002.

[30] M. Dienst, P. E. Greis, B. J. Ellis, K. N. Bachus, and R. T. Burks, "Effect of lateral meniscal allograft sizing on contact mechanics of the lateral tibial plateau: an experimental study in human cadaveric knee joints," *The American Journal of Sports Medicine*, vol. 35, no. 1, pp. 34–42, 2007.

[31] Q. Gao, Y. He, J. Z. Fu, A. Liu, and L. Ma, "Coaxial nozzle-assisted 3D bioprinting with built-in microchannels for nutrients delivery," *Biomaterials*, vol. 61, pp. 203–215, 2015.

[32] K. Wang, K. C. Nune, and R. D. Misra, "The functional response of alginate-gelatin-nanocrystalline cellulose injectable hydrogels toward delivery of cells and bioactive molecules," *Acta Biomaterialia*, vol. 36, pp. 143–151, 2016.

[33] M. Ojansivu, A. Rashad, A. Ahlinder et al., "Wood-based nanocellulose and bioactive glass modified gelatin-alginate bioinks for 3D bioprinting of bone cells," *Biofabrication*, vol. 11, no. 3, article 035010, 2019.

[34] S. S. Athukoralalage, R. Balu, N. K. Dutta, and C. N. Roy, "3D bioprinted nanocellulose-based hydrogels for tissue engineering applications: a brief review," *Polymers*, vol. 11, no. 5, p. 898, 2019.

[35] A. S. Gladman, E. A. Matsumoto, R. G. Nuzzo, L. Mahadevan, and J. A. Lewis, "Biomimetic 4D printing," *Nature Materials*, vol. 15, no. 4, pp. 413–418, 2016.

[36] L. Benning, L. Gutzweiler, K. Tröndle et al., "Cytocompatibility testing of hydrogels toward bioprinting of mesenchymal stem cells," *Journal of Biomedical Materials Research Part A*, vol. 105, no. 12, pp. 3231–3241, 2017.

[37] M. Müller, E. Öztürk, Ø. Arlov, P. Gatenholm, and M. Zenobi-Wong, "Alginate sulfate-nanocellulose bioinks for cartilage bioprinting applications," *Annals of Biomedical Engineering*, vol. 45, no. 1, pp. 210–223, 2017.

[38] A. G. Tabriz, M. A. Hermida, N. R. Leslie, and W. Shu, "Three-dimensional bioprinting of complex cell laden alginate hydrogel structures," *Biofabrication*, vol. 7, no. 4, article 045012, 2015.

[39] C. H. Lee, S. A. Rodeo, L. A. Fortier, C. Lu, C. Erisken, and J. J. Mao, "Protein-releasing polymeric scaffolds induce fibrochondrocytic differentiation of endogenous cells for knee meniscus regeneration in sheep," *Science Translational Medicine*, vol. 6, no. 266, p. 266ra171, 2014.

[40] L. Moradi, M. Vasei, M. M. Dehghan, M. Majidi, S. Farzad Mohajeri, and S. Bonakdar, "Regeneration of meniscus tissue using adipose mesenchymal stem cells-chondrocytes co-culture on a hybrid scaffold: in vivo study," *Biomaterials*, vol. 126, pp. 18–30, 2017.

[41] M. C. McCorry, J. L. Puetzer, and L. J. Bonassar, "Characterization of mesenchymal stem cells and fibrochondrocytes in three-dimensional co-culture: analysis of cell shape, matrix production, and mechanical performance," *Stem Cell Research & Therapy*, vol. 7, no. 1, p. 39, 2016.

Hindawi
Journal of Nanomaterials
Volume 2020, Article ID 5634096, 11 pages
https://doi.org/10.1155/2020/5634096

*Research Article*

# Surface-Modified Graphene Oxide with Compatible Interface Enhances Poly-L-Lactic Acid Bone Scaffold

**Guoyong Wang,[1] Chongxian He,[1] Wengjing Yang,[1] Fangwei Qi,[1] Guowen Qian,[1] Shuping Peng,[1,2] and Cijun Shuai[1,3,4]**

[1]*Institute of Bioadditive Manufacturing, Jiangxi University of Science and Technology, Nanchang 330013, China*
[2]*School of Basic Medical Science, Central South University, Changsha 410083, China*
[3]*State Key Laboratory of High Performance Complex Manufacturing, Central South University, Changsha 410083, China*
[4]*Shenzhen Institute of Information Technology, Shenzhen 518172, China*

Correspondence should be addressed to Cijun Shuai; shuai@csu.edu.cn

Received 7 February 2020; Accepted 21 February 2020; Published 7 March 2020

Academic Editor: Xiaoming Li



Graphene oxide (GO) usually serves as a reinforce phase in polymer because of its superior mechanical strength and high specific surface area. In this work, GO was grafted with L-lactic acid monomer (denoted as GO@PLLA) to overcome the aggregation in matrix and then incorporated into the poly-L-lactic acid (PLLA) scaffold fabricated by selective laser sintering. In hybrid scaffold, GO@PLLA exhibited uniform dispersion in the matrix. Furthermore, mechanical interlock between GO@PLLA and PLLA matrix formed and reinforced the interface bonding. On the other hand, the heterogeneous distributed GO acted as effective nucleating agent and resultantly enhanced the crystallization. Results showed that the tensile and compressive strength of scaffolds increased by 143.3% and 127.6%, respectively. Meanwhile, the scaffold exhibited an increased degradation rate of 37.9%, which could be attributed to the abundant hydrophilic functional groups on GO. Moreover, the scaffold exhibited favorable bioactivity and biocompatibility. Herein, the developed hybrid scaffold showed potential capacity for bone tissue engineering.

## 1. Introduction

Poly-L-lactic acid (PLLA) has been receiving intensive attention in tissue engineering due to its especially favorable biocompatibility and degradability [1, 2]. However, its insufficient mechanical properties handicap its profound application in bone tissue engineering [3–5]. Incorporating reinforcement phases to obtain a composite material is a feasible method to overcome this issue [6–8]. Nanofillers such as graphene oxide [9, 10], carbon nanotubes [11, 12], diamond nanoparticles [13, 14], and magnesium oxide nanoparticles [15–17] have been introduced into PLLA matrix to improve the mechanical performance. Amongst them, GO as a reinforcement phase was used to enhance the polymer due to its unique mechanical strength, including a strength of approximately 130 GPa and modulus of approximately 1 TPa [18]. In addition, the large specific surface area of GO is also conducive to its mechanical reinforcing effect [19]. What is more, GO exhibits suitable biological properties due to its abundant functional groups on the surface [20]. Nevertheless, the nanoreinforced effect of GO in polymer matrix was severely weakened because of its easy agglomeration in matrix [21, 22].

Surface modification is an effective strategy to promote the dispersion of reinforcement phase in polymer [23–25]. Lactic acid monomer possesses carboxyl and hydroxyl double functional groups, which could bond with the active functional groups of GO. Thus, lactic acid monomer could be grafted on GO, which then polymerized into PLLA chain through liner condensation [26]. GO grafted with PLLA (denoted as GO@PLLA) was expected to mix well with PLLA matrix [27, 28]. More significantly, GO@PLLA can intertwine with polymer matrix, which may form the mechanical interlock between matrix and GO@PLLA, thus effectively

enhancing the interfacial bonding strength. For instance, Sun and He [29] reported that GO grafted with poly (D-lactide) (GO-*g*-PDLA) by the polymerization method. Subsequently, PLLA/GO-*g*-PLDA nanocomposites were prepared and enhanced the interfacial compatibility between GO-*g*-PLDA and PLLA. Zhang et al. [30] proposed an approach to graft GO with poly (ethylene glycol) and then fabricated the composites nanofibrous scaffold via electrospinning technique, which exhibited enhanced the tensile strength and wettability.

Herein, GO@PLLA was prepared via in situ polycondensation method. GO@PLLA was then incorporated into PLLA to prepared hybrid scaffolds by selective laser sintering (SLS) [31]. Comparing with traditional methods, such as fused deposition modeling [32], electrospinning technique [33], and foaming technique [34], SLS exhibits great advantages including precise control of porous structure and personalized customization of bone scaffold. Then, the microstructure, mechanical properties, and degradation properties were evaluated. The enhancement mechanism was discussed and clarified. Furthermore, cell adhesion and proliferation were performed to verify the hybrid scaffolds as a potential candidate for bone regeneration.

## 2. Materials and Methods

*2.1. Materials.* GO was purchased from Chinese Academy of Sciences Chengdu organic chemistry Co. Ltd., China. PLLA powder (2.0 dL/g, $M_w$: 150 kDa) was provided by Shandong Academy of Pharmaceutical Sciences Pilot Plant, China. The L-lactic acid aqueous solution (90%, $M_w$: 90.08 kDa) was procured from Shanghai Aladdin Biochemical Technology Co. Ltd.

*2.2. Preparation of GO@PLLA.* GO@PLLA was prepared by in situ melt polycondensation in vacuum autoclave. The process to prepare GO@PLLA was demonstrated in Figure 1. A certain amount of GO (0.5 g) was added into the L-lactic acid aqueous solution (100 mL). The mixed solution was magnetically stirred 30 min under room temperature and then sonicated for 60 min to ensure GO homogeneously dispersed in the solution, followed by the adding of zinc oxide (5 mg) into the solution as the initiator. The polycondensation process was executed in vacuum autoclave accompanied by magnetic stirring and the reaction at 120°C for 12 h. After the polycondensation was completed, the condensation product was dissolved in excessive ethyl alcohol and centrifuged under the speed of 3000 r/min. Abovementioned process was repeated until the unreacted substances were removed. The final production was dried at 55°C under vacuum until weight unchanged.

*2.3. GO@PLLA Characterization.* The variation of chemical structure of GO@PLLA was obtained by X-ray photoelectron spectrometer (XPS; Thermo ESCALAB 250XI, USA). The thermal stability was evaluated by a thermal gravimetric analyzer (TGA, 209 F3 Tarsus Netzsch). Each sample was heated from room temperature to 800°C at a rate of 10°C/min in nitrogen environment. After keeping for 3 min to eliminate heat history, the samples were cooled to room temperature. The weight loss was recorded. Fourier-transform infrared (FTIR; Bruker Vertex 70 spectrometer) spectrometer was employed to measure the functional groups of composites within the range of 4000 to 400 $cm^{-1}$. Raman spectra of the composites were acquired by a Raman microscope system (LabRam HR Evolution, Horiba) equipped with a laser wavelength of 532 nm and laser power of 20 mW. The dispersions of GO and GO@PLLA in alcohol were observed via solubility test. 0.5 mg GO and GO@PLLA were, respectively, added into 50 mL alcohol to prepare homogenous suspension with stirring and ultrasonic. The suspension state was observed immediately and static after 12 hours.

*2.4. Preparation PLLA and Its Hybrid Scaffolds.* PLLA, PLLA/GO (1.0 wt.%), and PLLA/GO@PLLA (1.0 wt.%) composite powders were prepared through a series of processes involved dissolving, magnetic stirring, sonicating, centrifuging, and vacuum drying. A self-designed 3D printing system was used to prepare the scaffolds. The preparation procedure was as follows: the scaffold model was imported into 3D printing system after designing and then converted to STL files. Consequently, the laser beam scanned the printing area selectively layer by layer according to the scaffold model. The 3D printing was performed at a series of optimum parameters: laser power 3.5 W, scanning speed 180 mm/s, scanning interval of 0.1 mm, and powder-bed depth of 0.1 mm. The scaffolds were obtained with approximately 600 $\mu$m pore size and 450 $\mu$m strut size.

*2.5. Microstructural Characterization.* The crystallization of PLLA, PLLA/GO, and PLLA/GO@PLLA scaffolds were analyzed on a differential scanning calorimetry (DSC; 214Polyma, Netzsch) accompany with a 50 mL/min nitrogen pumping. The composites (about 10 mg) were heated from room temperature to 200°C at a heating rate of 10°C/min. X-ray diffraction spectra of PLLA, PLLA/GO, and PLLA/GO@PLLA composites were acquired by an X-ray diffractometer (XRD; X'Pert PRO MPD). In detail, the specimen of the scaffolds was cut to thin slices ($10 \times 20 \times 15\ mm^3$) and was scanned at the diffraction ranging from 10 to 80° at a scanning speed of 2°/min. Fourier-transform infrared (FTIR) spectra within a reflectance mode of 4000-400 $cm^{-1}$ were obtained to determine the surface properties of composite scaffolds. Raman spectrometer was used to detect the functional group of scaffolds with a wavelength of 532 nm at the range from 400 and 2500 $cm^{-1}$.

The brittle fracture surface morphologies of PLLA and its hybrid scaffolds were observed by scanning electron microscope (SEM; Nova 450). The specimens were coated with gold for 150 s using a high-vacuum sputter coater ion sputter before SEM observation.

*2.6. Mechanical Properties Evaluation.* The universal testing machine (WD-D1, LTD, China) was used to evaluate the mechanical properties of PLLA and its hybrid scaffolds. Tensile tests were performed at a speeding of 2 mm/min. All tensile specimens were manufactured to dumbbell shapes ($13 \times 5 \times 2\ mm^3$). Compression tests were detected at a speed

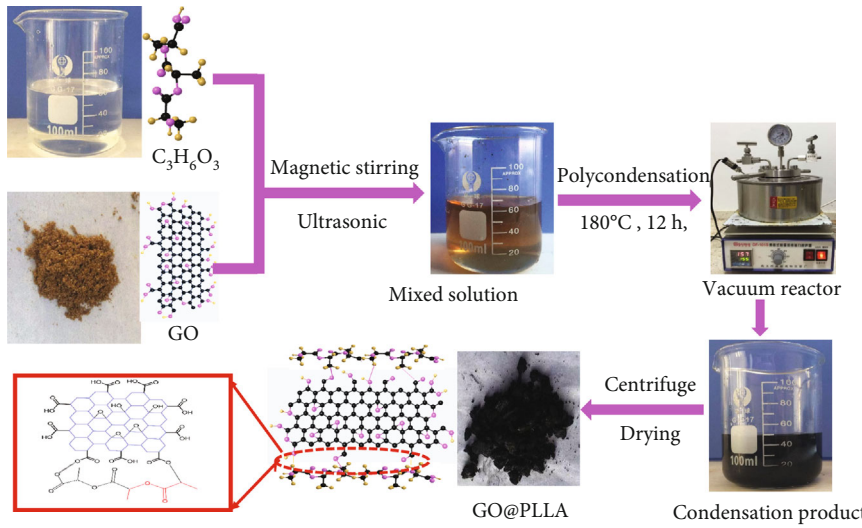


Figure 1: Flow diagram of synthesizing of GO@PLLA.

of 2 mm/min according to GB/T1041-92 standard. Accordingly, all compression specimens were printed to square shapes with 5 mm. Three times testing were performed during the measurement.

*2.7. In Vitro Degradation Measurement.* The degradation behavior of PLLA and its hybrid scaffold was evaluated in the phosphate-buffered saline (PBS) solution at room temperature. The initial specimens of PLLA and its hybrid scaffolds were weighed by a balancing scale as the control group. At 1, 2, 3, and 4 weeks, the specimens were taken out and washed with distilled water to erase the residual. After that, the specimens were dried in a vacuum oven at 55°C for 12 h and the residual weight of specimens was weighted. The residual weight fraction ($\Phi$) was calculated by the following:

$$\Phi = \frac{Wi}{Wr} \times 100\%, \quad (1)$$

where $W_i$ and $W_r$ are the initial weight and the residual weight of specimens after incubation, respectively.

*2.8. Cell Tests.* MG-63 cells were used to perform the cell culture experiments. In detail, the cells are maintained in Dulbecco's modified Eagle's medium at 37°C in a $CO_2$ condition. The culture medium was charged every 2 days. Prior to cell culture on the scaffolds, the scaffold samples ($10 \times 10 \times 2\,mm^3$) were washed with PBS solution and sterilized with ultraviolet light for 0.5 h and then placed in 12-well plates. After that, cell suspension at a density of $2 \times 10^5$ cells/mL was seeded on the surface of the scaffolds. Meanwhile, enough culture medium was added to each well of the plate. The medium was changed each day during culture period. After culturing for 1, 4, and 7 days, the samples were taken out and rinsed thrice with PBS to remove residue and then gradient dehydrated with ethanol. The dehydrated samples were dried in a vacuum oven at 55°C for 24 h. Finally, the cell-cultured samples were gold-coated for 2 min to observe cell morphology via SEM.

Live/dead cell staining assay was executed to evaluate cell spreading on the scaffold samples. After culturing for 1, 4, and 7 days, the samples were washed gently with PBS and immersed in 4% formaldehyde at 37°C for 20 min. The fixed cells were stained with 2 $\mu$g/mL calcein acetoxymethyl ester and 1 $\mu$g/mL ethidium homodimer at 37°C for 20 min, respectively. Then, the stained cells were dehydrated gradually with ethanol and dried under vacuum. Finally, the scaffolds fixed with stained cells were imaged by fluorescence microscope (Olympus, BX63).

Cell viability on PLLA and its hybrid scaffolds were evaluated through cell counting kit-8 assay (CCK-8). The MG-63 cell was cultured on the scaffolds for the desired time before the CCK-8 experiment. After the culture medium was removed, CCK-8 reagent was added into each plate. Cells were further incubated at 37°C for another 4 h. Finally, the optical density (OD) value at 450 nm was recorded by a spectrophotometric microplate reader.

*2.9. Statistical Analysis.* All the experiment was performed independently in triplicate to exhibit the difference between the different groups. The data was represented as means ± standard deviation with the one-way ANOVA. Data with $^*p < 0.05$ present significant difference.

## 3. Results and Discussion

*3.1. Characteristic of GO and GO@PLLA.* XPS was employed to corroborate the changes of chemical functional groups for GO@PLLA. The peeks of functional groups of GO were exhibited in Figure 2(a). There were five peaks at 284.5 eV, 285.3 eV, 287.0 eV, 288.2 eV, and 289.3 eV, which were assigned to the functional groups of C=C/C-C, C-OH, C-O, C=O, and O-C=O, respectively [24]. The spectrum of GO@PLLA was presented in Figure 2(b). There were six peaks. The component of -OH of GO was reduced

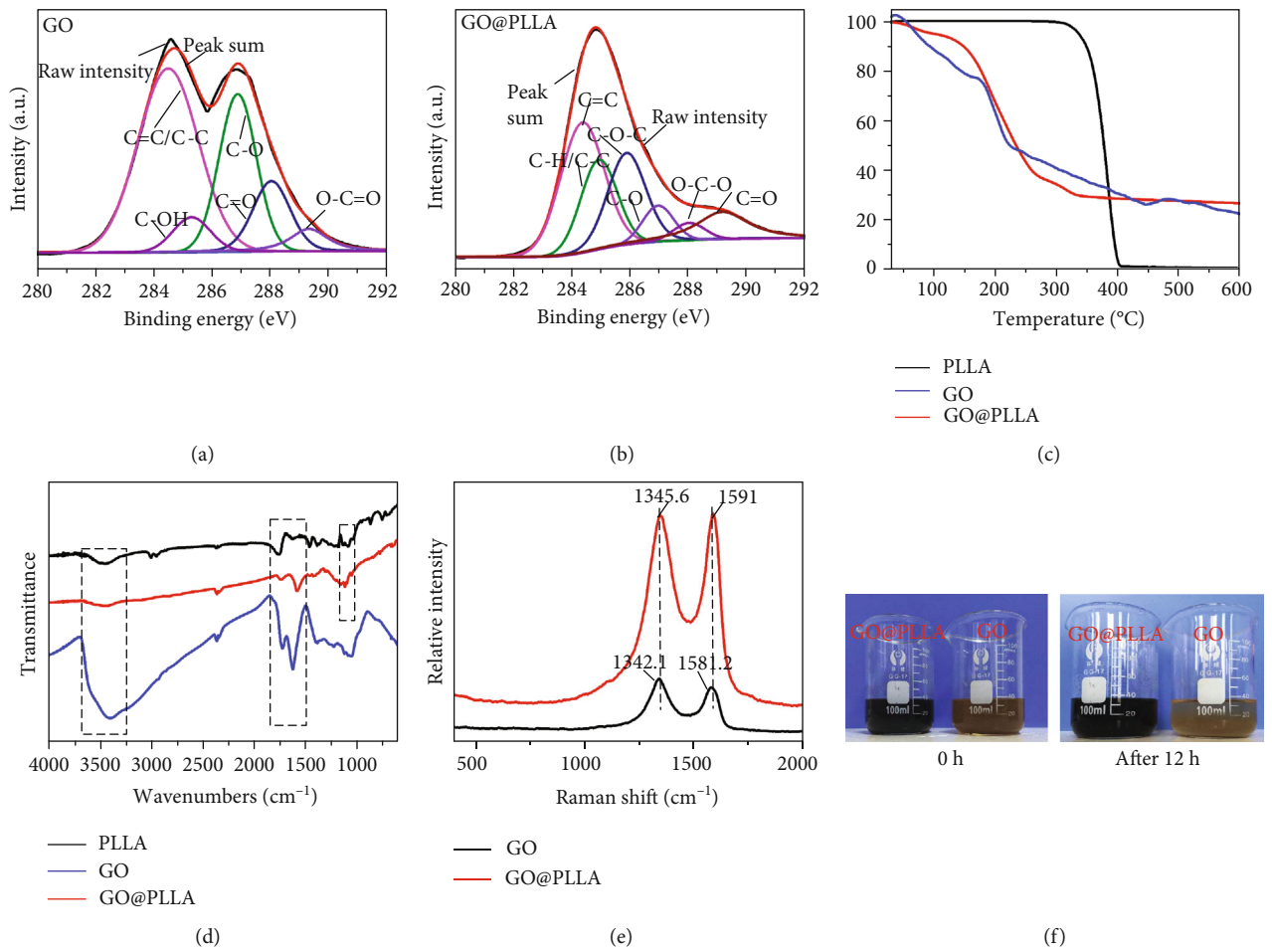


Figure 2: (a) XPS spectra of GO, (b) XPS spectra of GO@PLLA, (c) thermal degradation curves, (d) FTIR spectra, (e) Raman spectra of GO and GO@PLLA, and (f) photos of GO and GO@PLLA dispersed in ethanol after 12 h.

significantly. Conversely, the components of C-H and O=C-O of GO@PLLA were increased due to the grafted PLLA chains. Furthermore, the intensity of C-OH peak exhibited a relative decrease, while the intensity of C-H and O-C=O enhanced in some degree.

The thermal stabilities of GO, PLLA, and GO@PLLA were tested by TGA, as presented in Figure 2(c). For GO, the weight loss at the range of 50 to 150°C was ascribed to the evaporation of moisture content [35]. At the following stage, the mass loss was mainly attributed to that the surface functional groups decomposed into CO, $CO_2$, and $H_2O$ [36]. As for GO@PLLA, the weight loss of GO@PLLA which occurred at 50 to 160°C was caused by the evaporation of water. Subsequently, the pyrolysis turned slow due to the successfully grafted PLLA chain on graphene. In addition, it could be seen that the PLLA chain grafted on GO was pyrolyzed completely before 400°C, which is consistent with the obtained TGA curve.

Figure 2(d) exhibits the FTIR spectrum of PLLA, GO, and GO@PLLA. For the spectra of GO, the characteristic peaks located at 3430, 1728, and 1632 $cm^{-1}$ corresponded to the O-H, C=O, and C-O stretching vibrations, respectively [37]. As for GO@PLLA, the peak intensity around 3430 $cm^{-1}$ decreased significantly. It was believed that the esterification reaction between functional groups of L-lactic acid and GO resulted in the reduction of hydroxyl groups. At the same time, the peak position of C=O stretching vibrations was gradually blue shifted from 1728 to 1750 $cm^{-1}$, which could be ascribed to the increased ester groups caused by the graft of PLLA chains on GO. In addition, some typical resonances peaks of PLLA appeared at the spectrum of GO@PLLA. Therefore, it was demonstrated that PLLA chains in situ grafted on GO.

The conformational changes of GO@PLLA were assessed by Raman spectroscopy, as exhibited in Figure 2(e). For the Raman spectra of GO, the bands of D and G around 1342.1 and 1581.2 $cm^{-1}$ corresponded to the vibration of sp2 and sp3 bonded carbon atoms, respectively [38]. For GO@PLLA, the peaks located at 1345.6 and 1591 $cm^{-1}$ indicated a blue shift of 3.5 and 9.8 $cm^{-1}$, respectively, which was closely related with the reaction of PLLA chain and GO [39].

The sedimentation experiment was executed to test the dispersity of GO and GO@PLLA in anhydrous ethanol, with obtained images demonstrated in Figure 2(f). GO and GO@PLLA powders formed uniform dispersion in anhydrous ethanol after magnetic stirring and ultrasonic. However, GO precipitated from the solution and a layer of aggregation appeared after 12 h. As a comparison, GO@PLLA

still presented uniform dispersion state in suspension. This indicated that a strong interaction between organic solvent and GO@PLLA improved the dispersion.

Based on above results, it was confirmed that the PLLA chains in situ grafted on GO successfully. GO provided abundant active sites for the grafted process due to its two-dimensional nanosheet structure. Furthermore, GO served as initiator accelerated the reaction between macromolecule and surface-active groups. According to some literature, the monomer grafted on the GO surface induced by initiation or crystal during the initial step [36, 40]. Meanwhile, the formed free polycondensations coupled with the functional groups on GO. At last, GO was covered with PLLA chains with the continuous polycondensation reaction.

*3.2. PLLA and Nanohybrid Scaffolds Properties.* The SLS system and the as-prepared scaffold as shown in Figures 2(a) and 2(b). The uniform dispersion of the nanofiller and good interfacial compatibility between the nanofiller and the matrix play a positive role for the composites. In this study, dispersion of GO in matrix was observed via SEM, as shown in Figures 3(c)–3(f). The neat PLLA scaffold exhibited relatively smooth surface morphology, while PLLA hybrid scaffolds showed rougher surface morphologies. As showed in Figure 3(d), the aggregation of GO was observed and disjointed with the matrix, which might be attributed to the poor interfacial compatibility. For the PLLA/GO@PLLA scaffold, the well-distributed GO@PLLA firmly embedded in matrix, which exhibited enhanced interfacial bonding with PLLA matrix, as shown in Figure 3(e).

The FTIR spectrum of PLLA and hybrid scaffolds is presented Figure 4(a). The peak at 1753 $cm^{-1}$ was shifted to high wavenumber, indicating slightly interaction due to the intermolecular and intramolecular hydrogen bonding between GO and the PLLA matrix. In addition, the shift of the peak was more significant for PLLA/GO@PLLA as compared to PLLA/GO. Raman spectroscopy was used to diagnose the chemical structure, as shown in Figure 4(b). The prominent peaks of the PLLA scaffold at 1769, 1453, and 873 $cm^{-1}$ were observed, which assigned to C=O stretching, -CH3 asymmetric deformation mode, and the C-COO stretching, respectively. In PLLA hybrid scaffolds, the peak located at 1596 and 1345 $cm^{-1}$ represented an intense tangential mode and a disorder induced mode of GO. For the PLLA/GO scaffold, the peaks of C=O stretching and -CH3 asymmetric deformation mode shifted to 1772 and 1455 $cm^{-1}$, respectively. It might be ascribed to that strong hydrogen interaction between PLLA and GO [41]. Furthermore, the upper shift was observed in the PLLA/GO@PLLA scaffold, which was caused by the stronger interaction between PLLA and GO@PLLA.

DSC was employed to evaluate the crystallization behavior of PLLA and its nanohybrids under nonisothermal condition. The second heating range from 30 to 200°C at the heating rate of 10°C was displayed in Figure 4(c). The melting temperature ($T_m$) of PLLA, PLLA/GO, and PLLA/-GO@PLLA scaffolds was about 176.7, 178.5, and 180.1°C, respectively. Obviously, after incorporating the nanofiller, the location of endothermic peak was slightly shifted. It might be attributed to mobility of the PLLA chains was restrained due to the effective combination between PLLA and GO [42]. Moreover, the thermal stability of PLLA/-GO@PLLA was higher than PLLA/GO, which might be ascribed to uniform dispersion of GO@PLLA and interfacial bonding with PLLA matrix [43].

The influence of adding GO@PLLA on the crystalline structure of PLLA composites was analyzed by XRD, as presented in Figure 4(d). For the PLLA scaffold, two peaks typically located at 16.3° and 18.6° exhibited the crystallization in $\alpha$ form [44]. After incorporating the nanofiller into the PLLA scaffold, two peaks at 15.0 and 22.4° were observed, which belong to (001, 210) reflection peaks of GO, respectively. Interestingly, it could be observed that the diffraction peaks of the PLLA hybrid scaffold blue shifted with incorporation of GO and GO@PLLA [45]. Meanwhile, the intensity of characteristic peak at 16.8° increased for PLLA/-GO@PLLA, which indicated an improved crystallinity due to stronger bonding between GO@PLLA and PLLA matrix.

*3.3. Mechanical Properties.* Bone scaffolds should possess suitable mechanical properties to withstand stress conduction in bone defect so as to provide support for the new bone growth [46, 47]. In this study, the tensile and compressive experiments were conducted to evaluate the mechanical strength of PLLA and its hybrid scaffolds. The stress-strain curves and tensile properties of the scaffolds are presented in Figure 5(a). For the PLLA/GO scaffolds, the tensile strength increased from 8 to 16 MPa, and the tensile modulus increased from 100 to 120 MPa, respectively. As for PLLA/-GO@PLLA, the tensile strength and tensile modulus improved to 19 MPa and 170 MPa, respectively. For the compression tests, the compressive strength of the PLLA/GO scaffold improved from 6 to 8 MPa and the compression modulus increased to 80 MPa. More obviously, the compressive strength and modulus of the PLLA/GO@PLLA scaffold further improved to 16 MPa and 190 MPa, respectively.

The mechanical properties of the PLLA/GO@PLLA scaffold are affected by many factors. Firstly, the grafted PLLA chains promoted homogenous dispersion of GO in the PLLA/GO@PLLA scaffold. Furthermore, GO@PLLA intertwined with PLLA matrix to form mechanical interlock, which promoted the better interfacial bonding. As a result, it suppressed the crack extension during tensile process through transferring the interior stress to GO sheets [48, 49], which could effectively bear the external force. In addition, the crystallinity of the PLLA scaffold has been improved after adding the GO@PLLA. Base on the above, significant improvement of mechanical properties was acquired. In the PLLA/GO scaffold, the GO tended to aggregate in PLLA matrix due to its higher specific surface energy, which might be the main reason for the undesirable enhancement.

*3.4. In Vitro Degradation Behavior.* The in vitro degradation property of PLLA and its hybrid scaffolds were evaluated. Figure 6(a) exhibits residual weight fraction of the scaffold during immersion test. The mass loss of PLLA reached 7.95% after 4-week immersion. Compared with the PLLA scaffold, the hybrid scaffolds exhibit obviously promoted

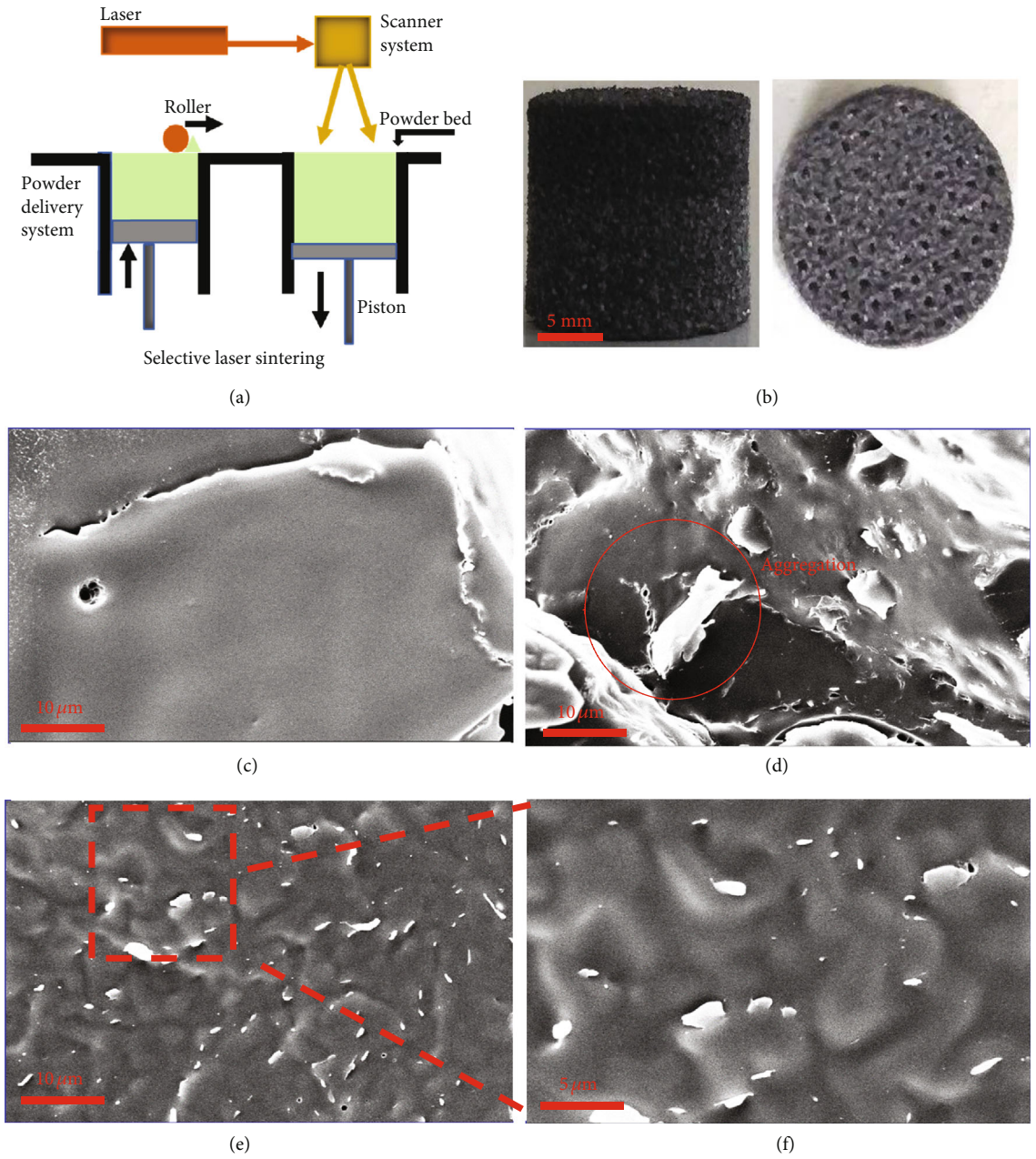


Figure 3: (a) The schematic diagram of SLS and (b) as-prepared scaffold. The brittle surface morphologies of (c) PLLA, (d) PLLA/GO, and (e) PLLA/GO@PLLA scaffolds. (f) Magnified image of (e).

degradation rate. The mass loss of PLLA/GO and PLLA/GO@PLLA scaffolds was 9.80% and 10.97%, respectively. The result indicated that GO expedited the degradation of the PLLA scaffold. The pH values of the residual PBS solution soaked with scaffolds were detected, with results shown in Figure 6(b). Corresponding to the initial PBS solution, the pH value decreased from 7.4 to 7.2, 7.12, and 7.1, respectively, for PLLA, PLLA/GO, and PLLA/GO@PLLA scaffolds.

The surface morphologies of the immersed scaffolds were observed via SEM to further characterize the degradation behavior. Figures 6(c)–6(e) show the surface morphologies of PLLA and its hybrid scaffolds after immersion for 4 weeks. The PLLA scaffold exhibited the relatively smooth surface with some tiny holes. The PLLA/GO scaffold shown relatively coarse surface. Some cracks concentrated in a relatively concentrated area, which may due to the aggregation of GO. Comparing with the PLLA/GO scaffold, the PLLA/GO@PLLA scaffold shown a relatively uniform corrosion morphology, and the erosion was much more serious. The in vitro degradation of scaffolds was accelerated after adding GO, which might be explained by the hydrophilicity of hybrid scaffolds [50]. The addition of GO improved the hydrophilicity of PLLA scaffold, thereby the surface wettability of scaffold becomes better. Furthermore, uniformly

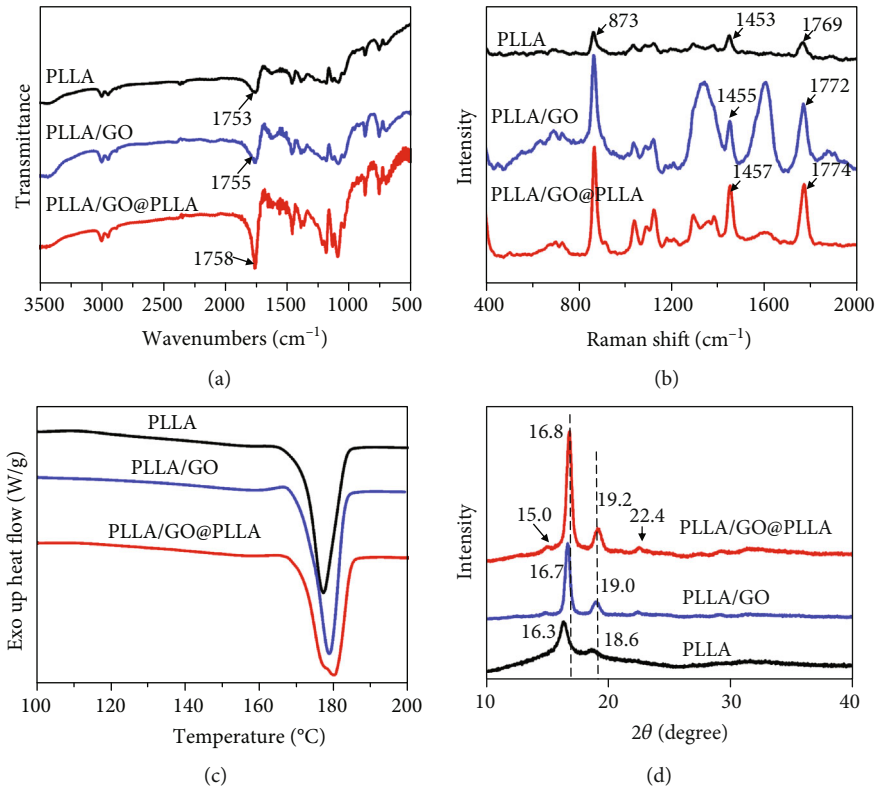


Figure 4: (a) FTIR, (b) Raman spectra, (c) DSC heating curves, and (d) XRD analysis of PLLA, PLLA/GO, and PLLA/GO@PLLA scaffolds.

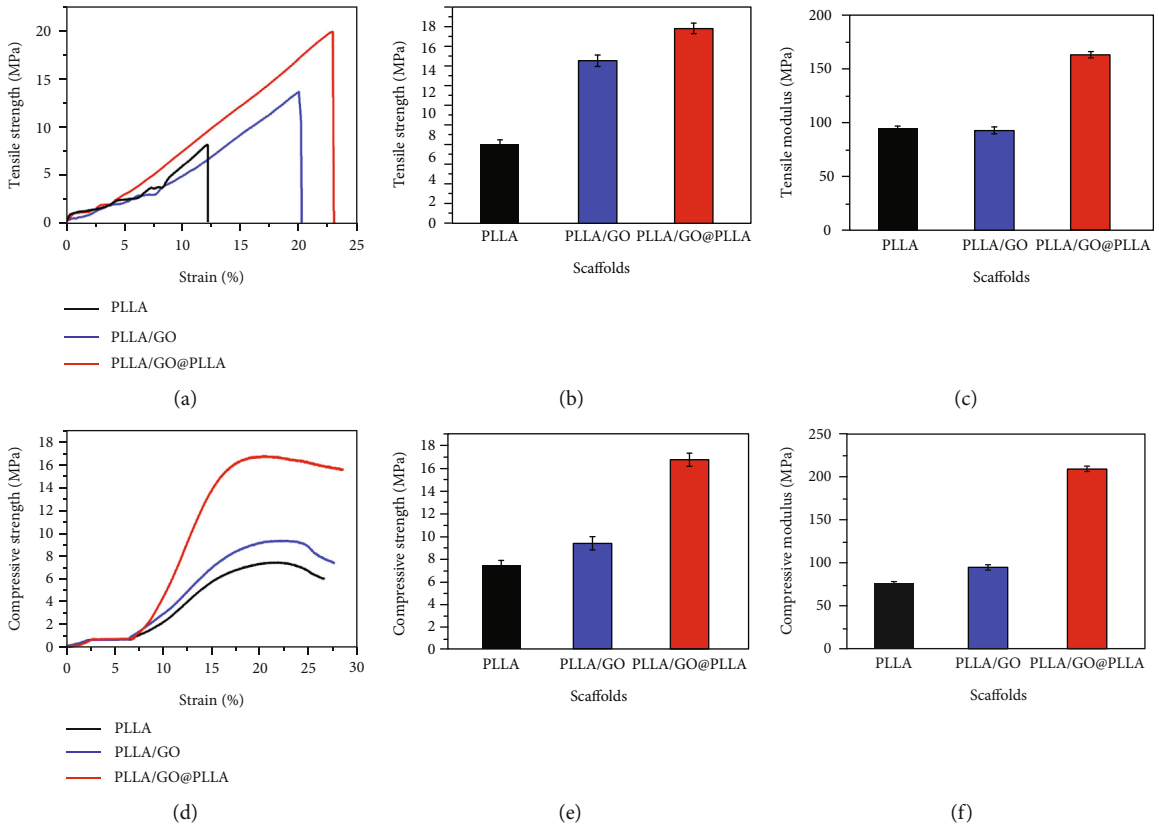


Figure 5: (a) Tensile stress-strain curves, (b) tensile strength, (c) tensile modulus, (d) compressive stress-strain curves, (e) compressive strength, and (f) compressive modulus of PLLA and its hybrid scaffolds.

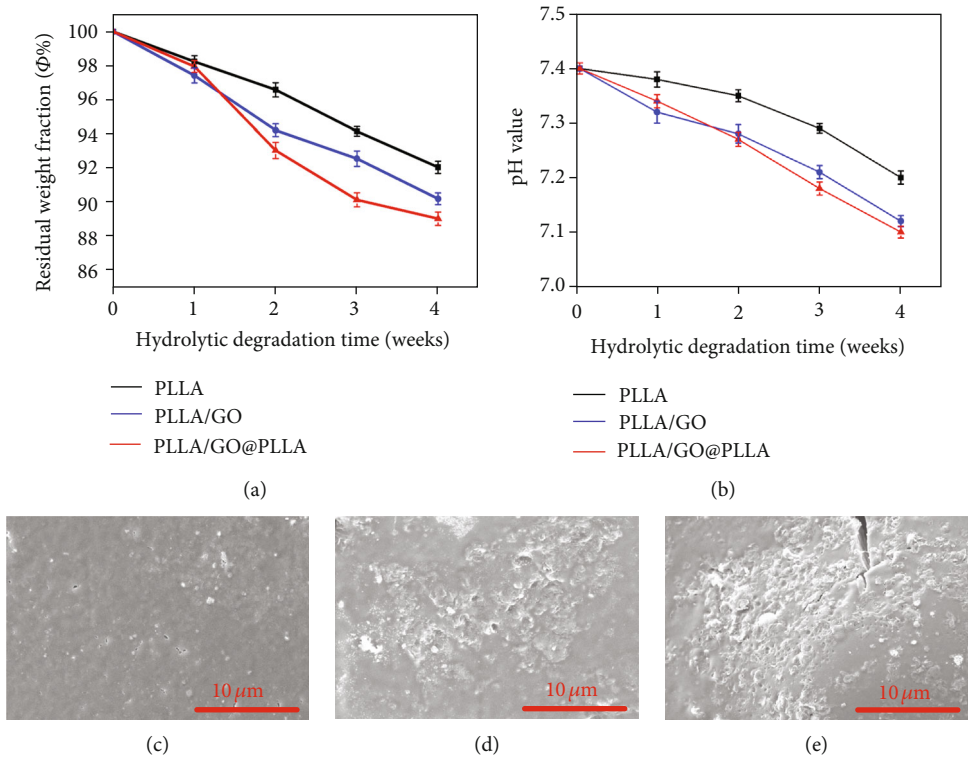


Figure 6: (a) Weight loss, (b) pH value, and SEM morphologies of (c) PLLA, (d) PLLA/GO, and (e) PLLA/GO@PLLA scaffolds after immersion in PBS solution.

dispersed GO and PLLA formed more two-phase interfaces in the scaffold, which provided more degrade sites and solution exchange channels for the PBS solution. It benefits the influx of the aqueous media into scaffolds [51, 52].

*3.5. Cytocompatibility.* The SEM images of cells adhesion on different PLLA scaffolds after 1, 4, and 7 days were present in Figure 7. It could be seen that the cells fixed and spread on the scaffolds with culture time increasing. After culturing for 4 days, more cells and extracellular matrix exhibited typical morphologies and covered the surface of hybrid scaffolds. With the culturing time increased to 7 days, the cells on the PLLA/GO@PLLA scaffolds appeared mature and plumper shape [53]. It was indicated that incorporating GO@PLLA into scaffolds benefited cell adhesion and spreading.

Live and dead staining experiment was performed to further evaluate the biocompatibility of the PLLA and its hybrid scaffolds. The fluorescence images were presented in Figure 8. Almost no dead cells were observed in all scaffolds. Compared to PLLA and PLLA/GO scaffolds, more live cells were found in the PLLA/GO@PLLA scaffolds during the same period. It was indicated that the incorporation of GO@PLLA exhibited beneficial factor for cell growth. The CCK-8 assay was performed to quantitatively investigate the osteoblasts proliferation on the scaffolds, the results were present Figure 8(b). Obviously, the OD values increased gradually with culture period increasing for all scaffolds, and the addition of GO promoted cells proliferation. Notably, the OD values of the PLLA/GO@PLLA scaffold have significant difference in comparison to the PLLA scaffold

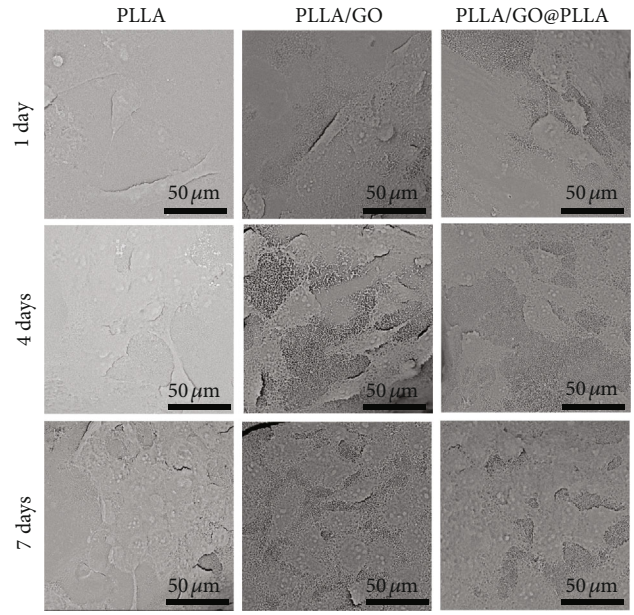


Figure 7: SEM micrographs of MG63 cells on PLLA and its hybrid scaffolds after 1, 4, and 7 days of culture.

throughout culture period, which showed higher cell viability. It was indicated that GO have intrinsic biocompatibility. Moreover, good dispersion in matrix after GO grafted with the PLLA chains, which may provide a suitable microenvironment for cells proliferation [54, 55].

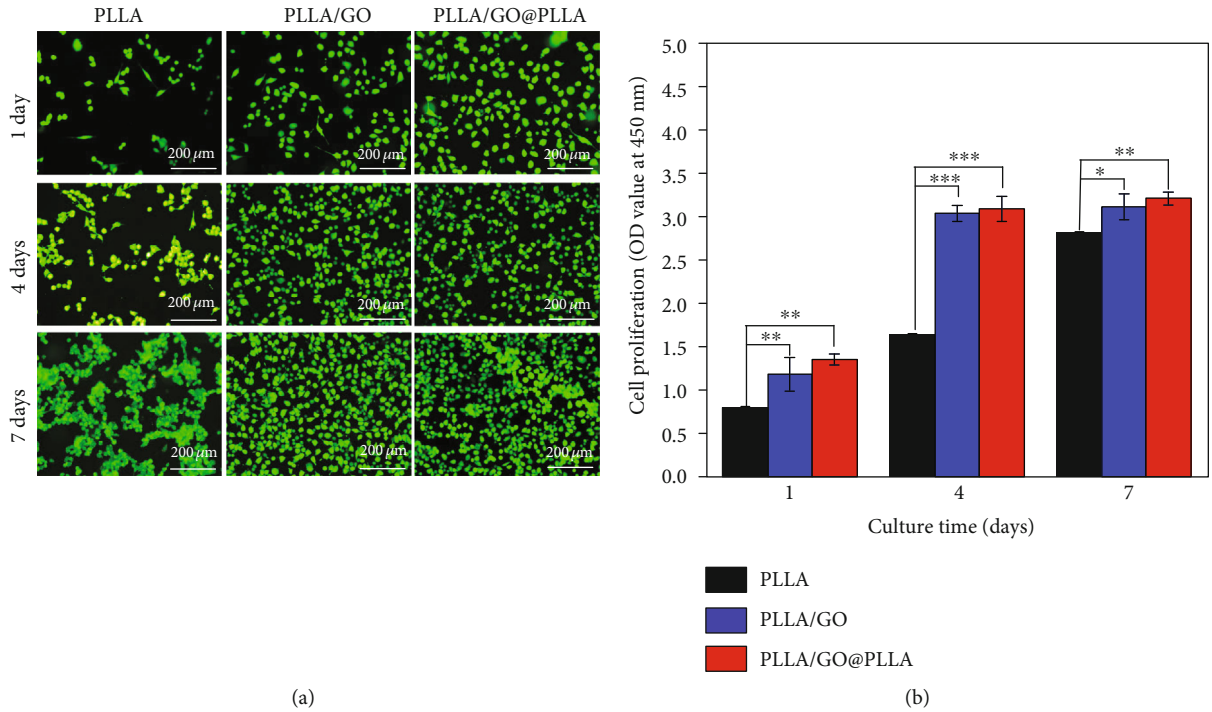


Figure 8: (a) Fluorescence images of MG-63 cells on PLLA and its hybrid scaffolds; and (b) OD determined by CCK-8 assays after culture for 1, 4 and 7 days.

## 4. Conclusions

In this study, GO@PLLA was prepared through in situ polycondensation. PLLA and its hybrid scaffolds were successfully fabricated via SLS. GO@PLLA could uniformly dispersed in PLLA matrix. Moreover, stronger interface bonding was formed between GO@PLLA and PLLA matrix. As a result, the mechanical properties of the PLLA/-GO@PLLA scaffold were significantly enhanced. Meanwhile, the weight loss tests indicated that GO enhanced the degradation rate of the PLLA scaffold. The cytocompatibility experiments showed that the PLLA/GO-*p*-PLLA scaffold exhibited favorable biological performance. Therefore, the PLLA/GO@PLLA scaffold was a potential substitute for bone tissue engineering.

## Data Availability

The data used to support the findings of this study are available from the corresponding author upon request.

## Conflicts of Interest

The authors declare that there are no conflicts of interest regarding the publication of this paper.

## Authors' Contributions

Guoyong Wang and Chongxian He contributed equally to this work.

## Acknowledgments

This study was supported by the following funds: (1) the Natural Science Foundation of China (51935014, 51905553, 81871494, 81871498, and 51705540); (2) Hunan Provincial Natural Science Foundation of China (2019JJ50774, 2018JJ3671, and 2019JJ50588); (3) Jiangxi Provincial Natural Science Foundation of China (20192ACB20005); (4) Guangdong Province Higher Vocational Colleges and Schools Pearl River Scholar Funded Scheme (2018); (5) the Open Sharing Fund for the Large-Scale Instruments and Equipments of Central South University; (6) the Project of Hunan Provincial Science and Technology Department (2017RS3008); and (7) the Project of Science and Technology of Jiangxi Provincial Education Department (GJJ190465).

## References

[1] M. Eleuteri, L. Pastorino, and O. Monticelli, "On the degradation properties of electrospun fibers based on PLLA: the effect of a drug model modification," *Polymer Degradation and Stability*, vol. 153, pp. 109–117, 2018.

[2] K. Zhang, J.-K. Peng, Y.-D. Shi, Y.-F. Chen, J.-B. Zeng, and M. Wang, "Control of the crystalline morphology of poly (L-lactide) by addition of high-melting-point poly (L-lactide) and its effect on the distribution of multiwalled carbon nanotubes," *The Journal of Physical Chemistry B*, vol. 120, no. 30, pp. 7423–7437, 2016.

[3] N. Cai, Q. Dai, Z. Wang, X. Luo, Y. Xue, and F. Yu, "Toughening of electrospun poly (L-lactic acid) nanofiber scaffolds with unidirectionally aligned halloysite nanotubes," *Journal of Materials Science*, vol. 50, no. 3, pp. 1435–1445, 2015.

[4] Q. Zhang, V. N. Mochalin, I. Neitzel et al., "Mechanical properties and biomineralization of multifunctional nanodiamond-PLLA composites for bone tissue engineering," *Biomaterials*, vol. 33, no. 20, pp. 5067–5075, 2012.

[5] X. Li, J. Wei, K. E. Aifantis et al., "Current investigations into magnetic nanoparticles for biomedical applications," *Journal of Biomedical Materials Research Part A*, vol. 104, no. 5, pp. 1285–1296, 2016.

[6] C. Gao, M. Yao, C. Shuai, S. Peng, and Y. Deng, "Nano-SiC reinforced Zn biocomposites prepared *via* laser melting: Microstructure, mechanical properties and biodegradability," *Journal of Materials Science & Technology*, vol. 35, no. 11, pp. 2608–2617, 2019.

[7] T. Qiao, P. Song, H. Guo, X. Song, B. Zhang, and X. Chen, "Reinforced electrospun PLLA fiber membrane via chemical crosslinking," *European Polymer Journal*, vol. 74, pp. 101–108, 2016.

[8] M. Mariano, F. Pilate, F. B. de Oliveira et al., "Preparation of cellulose nanocrystal-reinforced poly (lactic acid) nanocomposites through noncovalent modification with PLLA-based surfactants," *ACS Omega*, vol. 2, no. 6, pp. 2678–2688, 2017.

[9] A. M. Pinto, J. Cabral, D. A. P. Tanaka, A. M. Mendes, and F. D. Magalhães, "Effect of incorporation of graphene oxide and graphene nanoplatelets on mechanical and gas permeability properties of poly (lactic acid) films," *Polymer International*, vol. 62, no. 1, pp. 33–40, 2013.

[10] P. Feng, J. Jia, S. Peng, W. Yang, S. Bin, and C. Shuai, "Graphene oxide-driven interfacial coupling in laser 3D printed PEEK/PVA scaffolds for bone regeneration," *Virtual and Physical Prototyping*, pp. 1–16, 2020.

[11] G. Wang, F. Qi, W. Yang et al., "Crystallinity and reinforcement in poly-L-lactic acid scaffold induced by carbon nanotubes," *Advances in Polymer Technology*, vol. 2019, article 8625325, 10 pages, 2019.

[12] M. Kaseem, K. Hamad, F. Deri, and Y. G. Ko, "A review on recent researches on polylactic acid/carbon nanotube composites," *Polymer Bulletin*, vol. 74, no. 7, pp. 2921–2937, 2017.

[13] P. Feng, Y. Kong, L. Yu et al., "Molybdenum disulfide nanosheets embedded with nanodiamond particles: co- dispersion nanostructures as reinforcements for polymer scaffolds," *Applied Materials Today*, vol. 17, pp. 216–226, 2019.

[14] R. Aversa, R. V. V. Petrescu, A. Apicella, and F. I. T. Petrescu, "Nano-diamond hybrid materials for structural biomedical application," *American Journal of Biochemistry and Biotechnology*, vol. 13, no. 1, pp. 34–41, 2017.

[15] D. J. Hickey, B. Ercan, L. Sun, and T. J. Webster, "Adding MgO nanoparticles to hydroxyapatite-PLLA nanocomposites for improved bone tissue engineering applications," *Acta Biomaterialia*, vol. 14, pp. 175–184, 2015.

[16] Y. Yang, J. Zan, W. Yang et al., "Metal organic frameworks as a compatible reinforcement in a biopolymer bone scaffold," *Materials Chemistry Frontiers*, vol. 4, no. 3, pp. 973–984, 2020.

[17] C. Shuai, J. Zan, Y. Yang et al., "Surface modification enhances interfacial bonding in PLLA/MgO bone scaffold," *Materials Science and Engineering: C*, vol. 108, p. 110486, 2020.

[18] W. Huang, "Graphene nanopapers," in *Nanopapers*, pp. 27–58, Elsevier, 2018.

[19] X.-J. Shen, S. Yang, J.-X. Shen et al., "Improved mechanical and antibacterial properties of silver-graphene oxide hybrid/-polylactid acid composites by in-situ polymerization," *Industrial Crops and Products*, vol. 130, pp. 571–579, 2019.

[20] A. L. Rivera-Briso, F. L. Aachmann, V. Moreno-Manzano, and Á. Serrano-Aroca, "Graphene oxide nanosheets versus carbon nanofibers: Enhancement of physical and biological properties of poly(3-hydroxybutyrate-co-3-hydroxyvalerate) films for biomedical applications," *International Journal of Biological Macromolecules*, vol. 143, pp. 1000–1008, 2020.

[21] W. Li, T. Shang, W. Yang et al., "Effectively exerting the reinforcement of dopamine reduced graphene oxide on epoxy-based composites via strengthened interfacial bonding," *ACS Applied Materials & Interfaces*, vol. 8, no. 20, pp. 13037–13050, 2016.

[22] C. Wang, J. Li, S. Sun et al., "Electrophoretic deposition of graphene oxide on continuous carbon fibers for reinforcement of both tensile and interfacial strength," *Composites Science and Technology*, vol. 135, pp. 46–53, 2016.

[23] M. Xu, J. Zhu, F. Wang et al., "Improved in vitro and in vivo biocompatibility of graphene oxide through surface modification: poly (acrylic acid)-functionalization is superior to PEGylation," *ACS Nano*, vol. 10, no. 3, pp. 3267–3281, 2016.

[24] M. Yuan, Y. Chen, M. Yuan, H. Li, X. Xia, and C. Xiong, "Functionalization of graphene oxide with low molecular weight poly (lactic acid)," *Polymers*, vol. 10, no. 2, p. 177, 2018.

[25] C. Shuai, L. Yu, W. Yang, S. Peng, Y. Zhong, and P. Feng, "Phosphonic acid coupling agent modification of HAP nanoparticles: interfacial effects in PLLA/HAP bone scaffold," *Polymers*, vol. 12, no. 1, p. 199, 2020.

[26] L.-N. Wang, P.-Y. Guo Wang, and J.-C. Wei, "Graphene oxide-graft-poly (l-lactide)/poly (l-lactide) nanocomposites: mechanical and thermal properties," *Polymers*, vol. 9, no. 12, p. 429, 2017.

[27] W. Li, Z. Xu, L. Chen et al., "A facile method to produce graphene oxide- *g* -poly(L-lactic acid) as an promising reinforcement for PLLA nanocomposites," *Chemical Engineering Journal*, vol. 237, pp. 291–299, 2014.

[28] Y. Kang, C. Wang, X. Shi, G. Zhang, P. Chen, and J. Wang, "Crystallization, rheology behavior, and antibacterial application of graphene oxide- *graft* -poly (l-lactide)/poly (l-lactide) nanocomposites," *Applied Surface Science*, vol. 451, pp. 315–324, 2018.

[29] Y. Sun and C. He, "Synthesis and stereocomplex crystallization of poly (lactide)–graphene oxide nanocomposites," *ACS Macro Letters*, vol. 1, no. 6, pp. 709–713, 2012.

[30] C. Zhang, L. Wang, T. Zhai, X. Wang, Y. Dan, and L.-S. Turng, "The surface grafting of graphene oxide with poly (ethylene glycol) as a reinforcement for poly (lactic acid) nanocomposite scaffolds for potential tissue engineering applications," *Journal of the Mechanical Behavior of Biomedical Materials*, vol. 53, pp. 403–413, 2016.

[31] C. Shuai, W. Yang, Y. Yang et al., "Selective laser melted Fe-Mn bone scaffold: microstructure, corrosion behavior and cell response," *Materials Research Express*, vol. 7, no. 1, article 015404, 2020.

[32] M. C. Wurm, T. Möst, B. Bergauer et al., "In-vitro evaluation of Polylactic acid (PLA) manufactured by fused deposition modeling," *Journal of Biological Engineering*, vol. 11, no. 1, p. 29, 2017.

[33] F. Lopresti, F. Carfì Pavia, I. Vitrano, M. Kersaudy-Kerhoas, V. Brucato, and V. la Carrubba, "Effect of hydroxyapatite concentration and size on morpho-mechanical properties of PLA-based randomly oriented and aligned electrospun nanofibrous mats," *Journal of the Mechanical Behavior of Biomedical Materials*, vol. 101, article 103449, 2020.

[34] J. Ju, X. Peng, K. Huang et al., "High-performance porous PLLA-based scaffolds for bone tissue engineering: Preparation, characterization, and *in vitro* and *in vivo* evaluation," *Polymer*, vol. 180, article 121707, 2019.

[35] S. Cheng, X. Chen, Y. G. Hsuan, and C. Y. Li, "Reduced graphene oxide-induced polyethylene crystallization in solution and nanocomposites," *Macromolecules*, vol. 45, no. 2, pp. 993–1000, 2012.

[36] J.-H. Yang, S.-H. Lin, and Y.-D. Lee, "Preparation and characterization of poly (L-lactide)–graphene composites using the in situ ring-opening polymerization of PLLA with graphene as the initiator," *Journal of Materials Chemistry*, vol. 22, no. 21, pp. 10805–10815, 2012.

[37] G. Z. Papageorgiou, Z. Terzopoulou, D. Bikiaris et al., "Evaluation of the formed interface in biodegradable poly(l-lactic acid)/graphene oxide nanocomposites and the effect of nanofillers on mechanical and thermal properties," *Thermochimica Acta*, vol. 597, pp. 48–57, 2014.

[38] S. S. Nanda, D. K. Yi, and K. Kim, "Study of antibacterial mechanism of graphene oxide using Raman spectroscopy," *Scientific Reports*, vol. 6, no. 1, article 28443, 2016.

[39] W. Huang, S. Wang, C. Guo, X. Yang, Y. Li, and Y. Tu, "Synthesis and characterization of well-defined poly(l-lactide) functionalized graphene oxide sheets with high grafting ratio prepared through click chemistry and supramolecular interactions," *Polymer*, vol. 55, no. 18, pp. 4619–4626, 2014.

[40] Y. Cao, T. Shi, C. Jiao et al., "Fabrication and properties of zirconia/hydroxyapatite composite scaffold based on digital light processing," *Ceramics International*, vol. 46, no. 2, pp. 2300–2308, 2020.

[41] X. Meng, V. Bocharova, H. Tekinalp et al., "Toughening of nanocelluose/PLA composites via bio-epoxy interaction: mechanistic study," *Materials & Design*, vol. 139, pp. 188–197, 2018.

[42] J. Li, P. Xiao, H. Li et al., "Crystalline structures and crystallization behaviors of poly(l-lactide) in poly(l-lactide)/graphene nanosheet composites," *Polymer Chemistry*, vol. 6, no. 21, pp. 3988–4002, 2015.

[43] Q. Li, S. Qin, X. Tian et al., "Enhancement of the interface in poly(l-lactide) and poly(propylidene carbonate) blends by introducing of poly(l-lactide)-grafted graphene oxide to improve mechanical properties," *Applied Surface Science*, vol. 433, pp. 739–749, 2018.

[44] M. C. Righetti, M. Gazzano, M. L. Di Lorenzo, and R. Androsch, "Enthalpy of melting of $\alpha'$ - and $\alpha$-crystals of poly(l-lactic acid)," *European Polymer Journal*, vol. 70, pp. 215–220, 2015.

[45] J. Shi, W. Wang, Z. Feng, D. Zhang, Z. Zhou, and Q. Li, "Multiple influences of hydrogen bonding interactions on PLLA crystallization behaviors in PLLA/TSOS hybrid blending systems," *Polymer*, vol. 175, pp. 152–160, 2019.

[46] C. Shuai, Z. Zeng, Y. Yang et al., "Graphene oxide assists polyvinylidene fluoride scaffold to reconstruct electrical microenvironment of bone tissue," *Materials & Design*, vol. 190, article 108564, 2020.

[47] Y. Yang, C. He, Dianyu E et al., "Mg bone implant: features, developments and perspectives," *Materials & Design*, vol. 185, article 108259, 2020.

[48] D. Qian, E. C. Dickey, R. Andrews, and T. Rantell, "Load transfer and deformation mechanisms in carbon nanotube-polystyrene composites," *Applied Physics Letters*, vol. 76, no. 20, pp. 2868–2870, 2000.

[49] M. M. Gudarzi and F. Sharif, "Enhancement of dispersion and bonding of graphene-polymer through wet transfer of functionalized graphene oxide," *Express Polymer Letters*, vol. 6, no. 12, pp. 1017–1031, 2012.

[50] X.-c. Du, X.-l. Xu, X.-h. Liu, J.-h. Yang, Y. Wang, and X.-l. Gao, "Graphene oxide induced crystallization and hydrolytic degradation of poly(butylene succinate)," *Polymer Degradation and Stability*, vol. 123, pp. 94–104, 2016.

[51] J. Duan, Y.-n. Xie, J.-h. Yang et al., "Graphene oxide induced hydrolytic degradation behavior changes of poly(l-lactide) in different mediums," *Polymer Testing*, vol. 56, pp. 220–228, 2016.

[52] C. Shuai, Y. Cheng, Y. Yang, S. Peng, W. Yang, and F. Qi, "Laser additive manufacturing of Zn-2Al part for bone repair: formability, microstructure and properties," *Journal of Alloys and Compounds*, vol. 798, pp. 606–615, 2019.

[53] C. Gao, M. Yao, S. Li, P. Feng, S. Peng, and C. Shuai, "Highly biodegradable and bioactive Fe-Pd-bredigite biocomposites prepared by selective laser melting," *Journal of Advanced Research*, vol. 20, pp. 91–104, 2019.

[54] H. Liang, Y. Yang, D. Xie et al., "Trabecular-like Ti-6Al-4V scaffolds for orthopedic: fabrication by selective laser melting and *in vitro* biocompatibility," *Journal of Materials Science & Technology*, vol. 35, no. 7, pp. 1284–1297, 2019.

[55] S. He, S. Yang, Y. Zhang et al., "LncRNA ODIR1 inhibits osteogenic differentiation of hUC-MSCs through the FBXO25/H2B-K120ub/H3K4me3/OSX axis," *Cell Death & Disease*, vol. 10, no. 12, p. 947, 2019.